Theoretical and Computational Methods for Mesoscopic Textures in Nematic Liquid Crystals with Anisotropic Elasticity

A DISSERTATION
SUBMITTED TO THE FACULTY OF THE GRADUATE SCHOOL
OF THE UNIVERSITY OF MINNESOTA
BY

Cody Dylan Schimming

IN PARTIAL FULFILLMENT OF THE REQUIREMENTS
FOR THE DEGREE OF
DOCTOR OF PHILOSOPHY

Jorge Viñals

July, 2022

Acknowledgements

I am very grateful for the many people that have supported me throughout my time in graduate school. While this is not an exhaustive list of those that deserve my thanks, here are a few specific expressions of gratitude.

First, I want to thank my advisor, Jorge, for fostering a research environment in which I was able to explore and learn independently while also being available whenever I needed help understanding a particular topic or couldn't get a calculation or computation to work. I greatly appreciate the introduction to the fascinating world of liquid crystal physics and all of the important pieces of knowledge—both physics and non-physics—that he has imparted to me.

I also want to thank our collaborator, Shawn Walker, who I am eternally indebted to for his creation of the software packages that were invaluable to my thesis research. Shawn was always very helpful and approachable whenever I needed help with my computations.

I owe countless thanks to my family—my parents, brothers, grandparents, aunts, uncles, and cousins—whose support for me and patience with my schedule has been a tremendous help. I especially want to thank everyone that has taken the time to pick me up so that I could attend a family event.

My friends in grad school have been a constant source of happiness, support, and stability as well and I do not think I would have had any amount of success here had I not had their friendship. I particularly want to thank my roommates Mike and Paul who have always helped me when I've needed it and have been patient with all of my rants about my research.

Finally, I'd like to thank my thesis defense committee for taking the time to read through my dissertation and serve on the committee.

Abstract

Nematic liquid crystals are materials in which the underlying constituents are anisotropic which, in turn, leads to anisotropic properties and response at the meso and macro scales. As has been shown in recent experiments on nematic systems composed of complex aggregates, anisotropic polymers, and biologically inspired active materials, as the constituents become more complicated, the material properties become more anisotropic. Thus, nematic liquid crystals represent an interesting opportunity to probe the interplay between elasticity, anisotropy, geometry, and topology.

This dissertation focuses on these interplays in an effort to expand the understanding of the structure and dynamics of mesoscopic textures in nematics, particularly two phase domains and topological defects. To accomplish this, we review the shortcomings of the classical Landau-de Gennes theory when posed with the problem of anisotropic elasticity. We then develop a computational, self-consistent field theory to advance the state of computational mesoscale modelling of anisotropic nematics. We show that, despite the increased computational complexity, this theory can resolve three dimensional nematic configurations well. We apply it directly to the case of two phase domains and disclinations in systems of lyotropic chromonic liquid crystals, of which many recent experiments have demonstrated anisotropic properties and structures. We find good qualitative and quantitative agreement with the experiments, while positing new directions for further experimental research.

We also review existing theoretical gaps in the study of three dimensional nematic disclination lines and loops. These are much more complicated objects, both geometrically and topologically, than their two dimensional counterparts. We develop a mathematical construction of the disclination loop charge, which leads to the definition of a novel tensor which we call the "disclination density tensor." This tensor is locally defined in terms of the nematic tensor order parameter and can be used to identify both the location and geometric structure of line disclinations. We further show that the disclination density tensor is related to the conservation of topological charge, and this connection is used to derive a kinematic law of motion for nematic disclinations. We show with analytical calculation and numerical computation that the disclination

density tensor and the derived line velocity are important tools that give insight into the structure and dynamics that reflect the complex interplay between elasticity, anisotropy, geometry, and topology of disclination lines in three dimensional nematics. The results of this dissertation represent not only a new set of tools for future research and engineering endeavors, but also fundamental insights into the nature of complex structures in nematic liquid crystals.

Contents

List of Tables

List of Figures

Chapter 1

Introduction

1.1 Nematic Liquid Crystals

The oxymoronic term "liquid crystal" refers to a broad class of materials in which the internal microstructure leads to intermediate symmetry breaking. These materials are not disordered enough to be an isotropic liquid, nor are they ordered enough to be a crystalline solid. However, one of the most fascinating aspects of liquid crystals is that they do not exhibit just one phase of matter between the liquid and solid phase; there are many. Each phase has its own intermediate symmetry breaking. For example, the nematic phase breaks orientational symmetry and the material constituents align with one another, but the centers of mass of the constituents are still randomly distributed so many of the fluid-like properties of the material are retained. Smectic phases on the other hand do break translational symmetry in one dimension and hence form a layered fluid; while columnar phases break translational symmetry in two dimensions and hence form ordered "columns" of fluid [1].

Many of these phases may be exhibited by the same material, either by changing the temperature of the sample or the concentration of "nematogens" (i.e. the liquid crystal constituents). The types of phases, and the specific symmetries that are broken macroscopically, reflect the microscopic structure of the material. If the nematogens are symmetric about rotations by $2\pi/p$, the resulting nematic phase will be symmetric about $2\pi/p$. These are known as the p-atic phases [2, 3]. Similarly, if the nematogens are chiral (e.g. DNA) the corresponding nematic phase may also break chiral symmetry,

in which case we call these materials "cholesterics" [1].

In this dissertation we will focus on the 2-atic nematic phase. That is, material systems in which the nematogens are rod-like and tend to align with one another, but are otherwise translationally invariant. These systems exhibit anisotropic optical properties, namely birefringence, and so they are highly prevalent in technological applications such as liquid crystal displays (LCD) [4]. Further, as fluids, nematics have anisotropic viscosities which lead to interesting and unique transport properties [5, 6]. The continuous symmetry breaking of nematics also leads to elastic properties of the material [7]. Inhomogeneities in the orientation of nematogens result in stresses in the material that tend to force the system to a uniform state. In this sense, nematic liquid crystals can be thought of as a viscoelastic fluid.

One might ask, if a uniform state is elastically preferred, can inhomogeneities persist over observable time scales? And if so, what is their nature? The answer to the first question has been known for decades. Inhomogoneities in the orienational order can exist in the form of topological defects, much like many other systems with broken continuous symmetries [7–9]. They also exist when boundary conditions are stronger than the elastic stress created by the inhomogeneity. An interesting case occurs at the isotropic-nematic phase transition in which domains of nematic phase form and the nematogens have a preferred orientation at the interface [10, 11].

The second question is more complicated and has not been fully answered, although our general understanding has pointed to an incredibly interesting facet of liquid crystal physics: interplays between elasticity, anisotropy, geometry, and topology. The primary focus of this dissertation will be to develop computational models and analytic tools that probe the effect of these interplays on the structure and dynamics of domains and defects in nematics. This has been of recent interest to the liquid crystal community, especially within the rapidly growing active and biological matter communities. In the next section we highlight the specific experimental investigations and theoretical challenges motivating the work in this dissertation.

1.2 Motivation

Materials which form passive nematic phases broadly fall into two classes. "Thermotropics" are those in which the nematogens are small, elongated, organic molecules. The phase transition in these materials is controlled primarily by the system temperature, hence the name thermotropic [1]. The other class is "lyotropics," in which larger elongated constituents are dispersed in a solvent (such as tobacco mosaic virus in water). These materials' phase transitions are induced primarily by changing the concentration rather than the temperature.

Both types of nematic materials have a long history of experiments. Many of the more classic properties, such as the birefringence, underpin their technological applications, and were discovered in thermotropic systems long ago [1]. These systems are still employed in technological applications today. Topological defect cores in these systems are very small (on the order of the molecular size, $\approx 1 - 10$nm) and so experimental studies of topological defects in thermotropic nematics was limited to understanding the orientation of the nematogens far from the defect core, rather than understanding the mesoscopic structure of the core itself [1, 8]. Further, the isotropic-nematic phase transition is first order in three dimensions, fundamentally due to the symmetry of the nematogens. However, the transition in thermotropic systems is only of weakly first order, with a very small coexistence region, and thus experimentally observing domains in thermotropics is difficult.

Lyotropic liquid crystals, on the other hand, present new opportunities to experimentally study the mesoscopic structure of both topological defects and nematic domains at coexistence. Topological defect cores in these systems are typically larger, and the coexistence region of the nematic-isotropic phase transition is large enough for nematic and isotropic domains to form in experiments [1, 10, 12–15]. Further, because the structure of the nematogens in lyotropics can vary widely—i.e. in size, shape, chemistry, etc.—they are great candidates to probe the interplays between elasticity, anisotropy, geometry, and topology that are fundamental to the structure and dynamics of defects and domains.

For the purposes of this dissertation, we are primarily motivated by recent experiments performed in the so called "lyotropic chromonic liquid crystals," or "chromonics"

for short. Chromonics are interesting in a number of areas, ranging from nucleic acids, food additives, pharmaceuticals, advanced electronics components, and the fact that they are biocompatible and used to manipulate biological matter. The rod-like nematogens in a chromonic are formed by aggregates of disc-like molecules with hydrophobic interactions [16, 17]. That is, they are essentially rods of stacked discs, which have a relatively small scission energy and are even more anisotropic than traditionally studied liquid crystals [5, 18]. This additional anisotropy leads to anisotropic surface anchoring, causing either homeotropic (perpendicular) or tangential alignment at isotropic-nematic interfaces. It also leads to anisotropic elasticity, in that the elastic modes of the nematic have different energetic weights.

Recent experiments on chromonics have shown isotropic-nematic domains with anisotropic "spindle-shaped" morphologies and surface defects that appear as cusps at various points of the interface [10, 15]. Additionally, experiments on topological defects in thin films of chromonics have revealed cores as large as 20μm in diameter, several orders of magnitude larger than those observed in thermotropics. The reason behind this large core size is still not understood. Because of the large size, the mesoscopic properties of topological defect cores in chromonics can be directly studied via optical light experiments [10, 15]. For the defect cores, the fine structure is not isotropic, as one might expect, instead the core is highly anisotropic. One of the goals of this dissertation is to computationally and theoretically explore the effects of anisotropy on the mesoscopic domains and topological defect cores to help understand these experimental results and predict the structure and dynamics of these systems when anisotropy might be important.

While the experiments described above were performed in thin films, and so the system is effectively two dimensional, we are also motivated by fully three dimensional experiments. Topological defects in three dimensional nematics are lines or loops, and their geometric character plays an important role in their structure and dynamics. While line defects in nematics were discovered long ago [8], only recently there have been effective methods for experimentally studying them [19–21]. They have also been of interest recently in several different experimental contexts. In chromonics, it was observed that applying various type of flow to a sample can nucleate line defects [22, 23] while recent advances in the field of active nematics have allowed researchers to study fully three

dimensional active domains. In these three dimensional active domains, line defects are spontaneously nucleated due to active stresses in the medium [24]. Another goal of this dissertation is to advance the theoretical identification and understanding of line defects in nematics for the benefit of future experimental investigations.

We are not only motivated by recent experiments, but also some important gaps in the theoretical analysis of nematics, which we briefly review here. Although, the orientation of a nematic is apolar, it is typically described by a unit vector, $\hat{\mathbf{n}}$, called the director. It is understood that $\hat{\mathbf{n}}$ and $-\hat{\mathbf{n}}$ describe the same macroscopic state. For an inhomogeneous configuration, the director represents a local average of the orientation of nematogens and is taken to be a function of position, $\hat{\mathbf{n}} = \hat{\mathbf{n}}(\mathbf{r})$. One of the earliest theories used to describe the state of an inhomogeneous nematic is the Frank-Oseen elastic theory, in which the free energy of a configuration is given written in terms of four elastic modes: $(\nabla\cdot\hat{\mathbf{n}})^2$, $|\hat{\mathbf{n}}\cdot(\nabla\times\hat{\mathbf{n}})|^2$, $|\hat{\mathbf{n}}\times(\nabla\times\hat{\mathbf{n}})|^2$, and $\nabla\cdot[\mathbf{n}\,(\nabla\cdot\mathbf{n}) + \mathbf{n}\times(\nabla\times\mathbf{n})]$ [25]. Often, one makes the "one-constant" approximation in which each of these modes are weighted equal to one another in the free energy [1].

The Frank-Oseen theory works quite well to describe configurations deep in the nematic phase and when defects are small. However, when describing the isotropic-nematic phase transition, or when modelling the spatial extent of topological defects, the theory fails because the director is not defined in the isotropic phase or at the singular points of the defects. These pieces may be cut-out and treated as boundaries [1], but the structure must then be assumed. A more physically consistent way of addressing this problem is to introduce an order parameter. This was done by Leslie and Ericksen, where they introduced the scalar order parameter, S, which measures the local degree of order of the nematic [26,27]. Thus, the nematic can be everywhere described by two variables, S and $\hat{\mathbf{n}}$.

While domains and defects can be modelled with the Ericksen-Leslie formalism [28], there are nuances that detract from its appeal. The fundamental topological defects in nematics are disclinations, in which $\hat{\mathbf{n}}$ rotates around a singular point. Because of the apolar nature of the nematogens, the stable topological defects have half integer winding numbers, so that upon completion of a loop around the defect $\hat{\mathbf{n}} \to -\hat{\mathbf{n}}$. This leads to difficulties in theoretical modelling using the director $\hat{\mathbf{n}}$ since there is a discontinuity in the vector representation. Another issue is that S and $\hat{\mathbf{n}}$ fail to account for all types of

mesoscopic order that a nematic may exhibit. This is the issue of biaxiality, which we will discuss in more detail in future chapters. It has been shown that isotropic-nematic interfaces and disclinations can exhibit biaxiality [29, 30], yet S and $\hat{\mathbf{n}}$ cannot account for this degree of freedom.

These issues can be assuaged by introducing a new order parameter that is a traceless, symmetric tensor. It is typical to denote this tensor by $\mathbf{Q}$, and models that involve this will often be regarded simply as $\mathbf{Q}$-tensor models. Much like S, $\mathbf{Q}$ involves a local average of nematogen orientation (see e.g. Eq. (2.9)). Therefore, $\mathbf{Q}$ contains all the information given by S and $\hat{\mathbf{n}}$, in that S parameterizes one of the eigenvalues and $\hat{\mathbf{n}}$ gives one of the eigenvectors. However, $\mathbf{Q}$ also contains information about details of the distribution of nematogens and explicitly obeys the symmetry $\hat{\mathbf{n}} = -\hat{\mathbf{n}}$ since if $\hat{\mathbf{n}}$ is an eigenvector, then so is $-\hat{\mathbf{n}}$. For us, $\mathbf{Q}$ will be the primary mathematical object of study in this dissertation, though we will also refer to S and $\hat{\mathbf{n}}$ when necessary to visualize a nematic configuration.

The primary theory involving $\mathbf{Q}$ is the Landau-de Gennes theory in which the free energy is written as a polynomial expansion of $\mathbf{Q}$ [1]. The theory has had success in predicting some aspects of the isotropic-nematic phase transition, namely that it is first order [31]. Additionally, although the idea behind the theory is that the free energy should be analytic near the transition for small $\mathbf{Q}$, it is also the go-to theory to study the nematic phase itself, even though there are other theories, such as the theories of Maier and Saupe [32] or Onsager [33] that also describe the nematic phase. The appeal of the Landau-de Gennes theory is that it is relatively simple and not necessarily computationally taxing, and that it yields qualitative predictions that can be compared with experiments. However, it has been known that the Landau-de Gennes free energy does not remain bounded under all physical conditions [34–36]. In particular, for anisotropically elastic nematics, the Landau-de Gennes free energy is unbounded which can lead to numerical instability in the modelling of nematics. One of the primary motivations of this dissertation is to develop a computationally viable model involving $\mathbf{Q}$ that remains bounded when modelling anisotropically elastic configurations.

Further, in three dimensions, while $\mathbf{Q}$ and the Landau-de Gennes free energy can model disclination lines and loops when the system is elastically isotropic, the theoretical methods for identifying the lines and understanding their dynamics is lacking.

There have been recent efforts to understand disclination lines in terms of their orientation [37, 38]. However, no local measure of the geometry and topology has been established for these objects. Hence, another primary goal of this dissertation is to fill this theoretical gap by introducing local methods, that can be computed from $\mathbf{Q}$ (which is available experimentally and computationally), to identify and characterize disclinations nematics.

Our motivations in this dissertation are both in understanding and in aid of experiments as well as to advance the theoretical and computational methods of researchers studying nematics. In particular, we will use both continuum simulation and analytical calculation to make progress on the problems of Landau-de Gennes unboundedness, elastic and anisotropic interplay, disclination identification, and disclination kinematics. Additionally, we will show how these seemingly disparate problems all benefit from advances of one another.

1.3 Outline

This dissertation is organized as follows:

In Chapter 2 we review standard results from the Landau-de Gennes free energy before discussing the unboundedness caused by including anisotropic elasticity. We then adapt and develop a new model based on the Ball-Majumdar free energy [36]. Here we delineate the computational details as well as show several numerical examples of computations that demonstrate the computational viability and stability of the method. We conclude this chapter with a detailed discussion of the possible choices for elastic energies as a function of $\mathbf{Q}$, and how these are predicted to affect various properties of the nematic.

In Chapter 3 we apply the model and numerical method developed in Chapter 2 to domains that form during the isotopic-nematic phase transition. In particular we study the effect of anisotropic surface anchoring and elastic anisotropy on the morphology of the domains and the structure of surface defects. Additionally we study the growth and morphogenesis of domains under varying elastic energies.

In Chapter 4 we apply the model of Chapter 2 to two dimensional topological defect cores in nematics in order to study their fine structure. Here we probe the interplay

between anisotropic elasticity and topology to explain anisotropic and biaxial structures seen in experiments [15]. We further quantitatively compare our computational results with experimental data and find good agreement.

In Chapter 5 we first review the topological and geometric structure of line disclinations in three dimensional nematics. We then develop a topological index which results in a novel tensor that is locally defined in terms of the nematic order parameter $\mathbf{Q}$. We explore the properties of this tensor and show that it can be used to identify the complex geometric character of the line defects.

In Chapter 6 we show that the tensor introduced in Chapter 5 is a conserved quantity and that it can be related to the conservation of topological charge. We invoke the methods of Halperin and Mazenko [39–41] to relate this conservation of topological charge to a kinematic velocity that can be computed from the order parameter at the location of the disclination core in two or three dimensions.

In Chapter 7 we use the kinematic velocity derived in Chapter 6 to analytically understand the motion of defects that are interacting or influenced by external fields or flows. We further use the computational model of Chapter 2 to simulate the motion of defects in these scenarios and show that the analytical kinematic equation accurately predicts the motion of disclinations.

Finally, in Chapter 8 we reflect on the primary results of the dissertation, and then catalogue several future directions for the research presented here.

Chapter 2

Computational Self-Consistent Field Theory

2.1 Introduction

Widely used theories based on a tensor order parameter of nematic order, and the Landau-de Gennes free energy, have proven effective at mathematically modelling features related to the first order isotropic-nematic phase transition, nematic order, defects, and transport, as well as some aspects of topological defect core fine structure [1,29–31,42]. It has been relied upon to model and study systems of more traditional thermotropic liquid crystals where the elastic constants are roughly equal (isotropic elasticity), two phase domains are spherical, and topological defects can be regarded simply as point-like singularities. In recent years, however, experimental studies of more complex liquid crystals, such as lyotropic chromonics or active nematics composed of microtubules, have revealed large, anisotropic topological defect cores that cannot be modeled as point singularities [10, 15, 43]. This suggests that we may need more control of the elastic constants in our modeling, as well as the need for more physically realistic microscopic Hamiltonians.

In this chapter, we explore some of the theoretical and computational issues with using the Landau-de Gennes free energy to model systems with anisotropic elasticity. We then develop a self-consistent field theory based on the Maier-Saupe free energy

and a potential introduced by Ball and Majumdar [32, 34, 36]. We detail a computational implementation of this free energy and lay out the computational details for the numerical studies performed as a part of this dissertation. We then provide computational evidence of our method's importance to problems where Landau-de Gennes fails. Finally we summarize the effect of various elastic energy terms broken down into the categories of surface energy, surface anchoring, and Frank-Oseen bulk elasticity. To our knowledge, this decomposition of the elastic energy has not been done before and the primary motivation is to gain insight into the qualitative effects of each term since there is little physical intuition from the tensor order parameter $\mathbf{Q}$. As we will show in future chapters, this decomposition will lead to physically intuitive reasoning for the behavior and morphologies observed in the calculations. All of the elastic terms to cubic order in $\mathbf{Q}$ are analyzed.

2.2 Landau-de Gennes unboundedness

We begin with the Landau-de Gennes free energy [1, 31]:

$$F_{LdG} = \int_{\Omega} \left[f_b(\mathbf{Q}) + f_e(\mathbf{Q}, \nabla \mathbf{Q}) + f_H(\mathbf{Q}) \right] \, d\mathbf{r} + \int_{\partial\Omega} f_\partial(\mathbf{Q}) \, dS(\mathbf{r}) \tag{2.1}$$

where Ω is the system domain, and $\mathbf{Q}$, a symmetric and traceless rank two tensor, is the nematic tensor order parameter. The bulk free energy density is denoted as f_B, f_e is an elastic free energy density that depends on gradients of $\mathbf{Q}$, f_H is a free energy density that accounts for interactions with an external field, and f_∂ is a surface free energy density that accounts for weak anchoring [44]. In this dissertation, we will primarily focus on the terms f_B and f_e and will neglect the other two. That is, we will assume there are no external fields (except in Sec. 7.5) and there is no weak anchoring at the domain boundary.

For uniaxial nematogens, the bulk free energy density is

$$f_b(\mathbf{Q}) = \frac{1}{2} a (T - T^*) \mathrm{Tr}[\mathbf{Q}^2] + \frac{1}{3} B \mathrm{Tr}[\mathbf{Q}^3] + \frac{1}{4} C \left(\mathrm{Tr}[\mathbf{Q}^2] \right)^2 \tag{2.2}$$

where a, B, C are phenomenological material parameters and T^* is the temperature at which the isotropic phase loses its stability. The cubic order term ensures a first

order phase transition for a three dimensional system, and it is always zero for a purely two-dimensional system since $\mathbf{Q}$ is traceless. We will frequently parameterize $\mathbf{Q}$ as

$$\mathbf{Q} = S\left(\hat{\mathbf{n}} \otimes \hat{\mathbf{n}} - \frac{1}{3}\mathbf{I}\right) + P\left(\hat{\boldsymbol{m}} \otimes \hat{\boldsymbol{m}} - \hat{\boldsymbol{\ell}} \otimes \hat{\boldsymbol{\ell}}\right) \tag{2.3}$$

where $\hat{\mathbf{n}}$, $\hat{\boldsymbol{m}}$, $\hat{\boldsymbol{\ell}}$ form an orthonormal frame. S and P parameterize the eigenvalues of $\mathbf{Q}$ where S represents the uniaxial order and P represents the biaxial order. Since $\mathbf{Q}$ is traceless and symmetric it has 5 degrees of freedom in three dimensions. These are all captured by the parameterization Eq. (2.3): S and P are two degrees of freedom that describe the eigenvalues while the other three degrees of freedom go into the orthonormal frame $\hat{\mathbf{n}}$, $\hat{\boldsymbol{m}}$, $\hat{\boldsymbol{\ell}}$. Given a tensor $\mathbf{Q}$—which we often will be from the simulations described throughout this dissertation—one can determine S from its maximum eigenvalue via $S = (3/2)\lambda_{\max}$ ($\mathbf{Q}$ will always be diagonalizable since it is symmetric) and $\hat{\mathbf{n}}$ is the corresponding eigenvector. P can then be determined from the difference of the two smallest eigenvalues while $\hat{\boldsymbol{m}}$ and $\hat{\boldsymbol{\ell}}$ are the corresponding eigenvectors. The sign of P is arbitrary and just determines which eigenvector should be assigned to $\mathbf{m}$ and which should be assigned to $\boldsymbol{\ell}$. The bulk energy, Eq. (2.2), is symmetric under $P \to -P$.

For $a(T - T^*) > 0$ there is a local minimum of Eq. (2.2) at the isotropic phase, $S = 0$, $P = 0$. Additionally, if $a(T - T^*) < (1/24)(B^2/C)$ there will also be a local minimum for a uniaxial phase with $S = S_N$ where

$$S_N = -\frac{1}{4}\frac{B}{C} + \sqrt{\frac{1}{16}\frac{B^2}{C^2} - \frac{3}{2}\frac{a(T - T^*)}{C}}. \tag{2.4}$$

Thus there is a range of temperatures that have locally stable isotropic and nematic phases, which is characteristic of a first order phase transition. At $a(T - T^*) = (1/27)(B^2/C)$ the Landau-de Gennes energies of the isotropic phase and the nematic phase are equal, and both zero. Although the initial purpose of the Landau-de Gennes theory was to describe the isotropic-nematic phase transition, many studies allow for negative $a(T - T^*)$ to study a purely nematic phase. Then the only minimum of the free energy is the nematic phase with S_N given by Eq. (2.4). We note that, technically, there are three local minima in terms of S and P. These are at $\{S = S_N, P = 0\}$,

$\{S = P_N,\, P = P_N\}$, and $\{S = P_N,\, P = -P_N\}$ where

$$P_N = \frac{1}{8}\frac{B}{C} - \sqrt{\frac{1}{64}\frac{B^2}{C^2} - \frac{3}{8}\frac{a(T - T^*)}{C}}. \tag{2.5}$$

All three of these minima represent the nematic phase, however, the choice of minimum just results in a redefinition of the director (i.e. the dominant orientation) and so without loss of generality we will choose to represent the equilibrium nematic phase as a uniaxial state where $S = S_N$, $P = 0$. To describe systems whose minima are biaxial states, one needs to add higher order terms to the bulk free energy density [31].

Equation (2.2) is all one needs to describe uniform or homogeneous systems. The primary subject of this dissertation, however, is non-uniform configurations. To treat these one must add an elastic energy, f_e, to the free energy density, which penalizes spatial gradients in the order parameter. In the nematic phase, if the configuration is weakly non-uniform (i.e. the director changes on relatively large length scales) then only gradients in the director $\hat{\mathbf{n}}$ must be considered. The corresponding free energy is called the Frank-Oseen free energy and is written [25, 45]

$$\begin{aligned} f_e(\nabla\hat{\mathbf{n}}) = K_{11}\left(\nabla\cdot\hat{\mathbf{n}}\right)^2 + K_{22}|\hat{\mathbf{n}}\cdot(\nabla\times\hat{\mathbf{n}})\,|^2 + K_{33}|\hat{\mathbf{n}}\times(\nabla\times\hat{\mathbf{n}})\,|^2 \\ - K_{24}\nabla\cdot\left[\hat{\mathbf{n}}\left(\nabla\cdot\hat{\mathbf{n}}\right) + \hat{\mathbf{n}}\times(\nabla\times\hat{\mathbf{n}})\right] \end{aligned} \tag{2.6}$$

where K_{11}, K_{22}, K_{33}, and K_{24} are elastic constants related to the elastic modes called "splay," "twist," "bend," and "saddle-splay" respectively. We note that the saddle-splay term is a total divergence and so upon integration will not contribute to bulk deformations. Since we will not be concerned with domain boundary effects we will omit this term moving forward.

In the case of strongly non uniform configurations, such as near topological defects or isotropic-nematic interfaces, Eq. (2.6) is questionable since the state of order itself changes very rapidly, and $\hat{\mathbf{n}}$ may not even be properly defined. One alternative is to describe the configuration with a scalar order parameter S in addition to $\hat{\mathbf{n}}$, such as in the Ericksen-Leslie formulation [26, 27]. A second alternative is to consider a tensor order parameter $\mathbf{Q}$, with the added benefit that it is free of singularities at topological defects. The latter approach is the one we take in this dissertation. The elastic energy

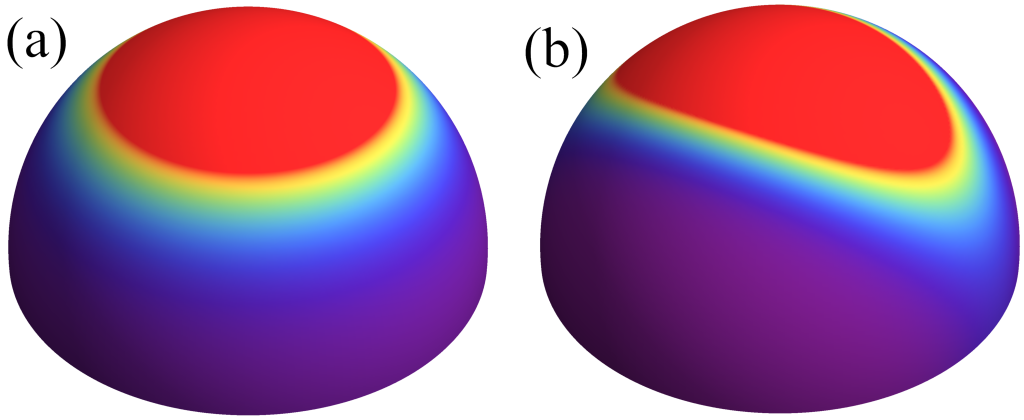

Figure 2.1: Example orientational probability distributions for nematogens, $p(\mathbf{u})$ plotted on the unit sphere for (a) a uniaxial configuration and (b) a biaxial configuration.

we will consider comprises up to cubic order in $\mathbf{Q}$, and it is given by,

$$f_e(\mathbf{Q}, \nabla\mathbf{Q}) = L_1\partial_k Q_{ij}\partial_k Q_{ij} + L_2\partial_j Q_{ij}\partial_k Q_{ik} + L_3 Q_{k\ell}\partial_k Q_{ij}\partial_\ell Q_{ij} + L_4 Q_{k\ell}\partial_i Q_{k\ell}\partial_j Q_{ij} \tag{2.7}$$

where L_i are elastic constants, $\partial_k \equiv \partial/\partial x_k$, and summation over repeated indices is assumed. The various reasons for focusing on these particular terms will be elaborated on in later sections and chapters, but the primary reason is to allow for independent control of the Frank-Oseen elastic constants K_{11}, K_{22}, and K_{33}. The L_i can be mapped to the K_{ii} in regions where the director changes slowly through the relations [15, 35]

$$\begin{aligned} K_{11} &= 2L_1S^2 + L_2S^2 - \frac{2}{3}L_3S^3 \\ K_{22} &= 2L_1S^2 - \frac{2}{3}L_3S^3 \\ K_{33} &= 2L_1S^2 + L_2S^2 + \frac{4}{3}L_3S^3. \end{aligned} \tag{2.8}$$

We note that if $L_3 = 0$ then $K_{11} = K_{33}$.

We describe next the properties of the tensor order parameter $\mathbf{Q}$. The discussion here relates to both the problem of the unboundedness of the Landau-de Gennes free energy and to its solution (Sec. 2.3). The order parameter may be defined microscopically as

the second moment of the canonical, equilibrium probability distribution p of molecular orientation $\mathbf{u}$ (assumed a unit vector),

$$\mathbf{Q}(\mathbf{r}) = \int_{S^2} \left(\mathbf{u} \otimes \mathbf{u} - \frac{1}{3}\mathbf{I} \right) p(\mathbf{u}, \mathbf{r}) \, dS(\mathbf{u}) \tag{2.9}$$

where the positional dependence introduced assumes that a mesoscopic, inhomogeneous configuration can be assumed to be in local equilibrium. This expression thus links the order parameter $\mathbf{Q}$, which can be related to macroscropic quantities such as the anisotropic susceptibility [46], to the microscopic orientation of the nematogens, $\mathbf{u}$. The integration is conducted over the unit sphere. The function $p(\mathbf{u}, \mathbf{r})$ is the local equilibrium distribution function of molecular orientation at constant temperature. The isotropic phase, when $\mathbf{Q} = 0$, corresponds to a uniformly distributed orientation $p = 1/(4\pi)$. A uniaxial configuration corresponds to a cylindrically symmetric, peaked distribution about a particular orientation, while the distribution for a biaxial configuration remains peaked, but loses its cylindrical symmetry. Fig. 2.1 shows a graphical illustration of $p(\mathbf{u})$ plotted on the unit sphere for both uniaxial and biaxial configurations.

The definition of Eq. (2.9) implies that there are bounds on the eigenvalues of $\mathbf{Q}$, namely $-1/3 \leq \lambda \leq 2/3$ which corresponds to the inequality relation $-1/2 \leq S \leq 1$. However, Eq. (2.4) places no such constrains on the eigenvalues, so that it is possible for the minima of Eq. (2.2) to be outside the bounds, and hence to correspond to a system that is no longer described by the thermal average introduced. In fact, Eq. (2.2) in principle allows for *any* value of S, and hence the physically motivated definition of $\mathbf{Q}$ from the thermal probability distribution function does not need to be consistent with the minimizer of the Landau-de Gennes energy.

This issue on its own does not lead to an unbounded free energy. However, when anisotropic elastic free energies are introduced the free energy can become unbounded below. To describe systems with anisotropic Frank-Oseen elasticity, that is $K_{11} \neq K_{22} \neq K_{33}$, one must use an elastic free energy in $\mathbf{Q}$ which is at least cubic in $\mathbf{Q}$, like that of Eq. (2.7). The inclusion of cubic terms in $\mathbf{Q}$ that contain gradients leads to an unbounded free energy if quartic order terms (or higher) are not included as well. Ref. [35] makes this clear by using a spherical tensor analysis to write all possible independent gradient

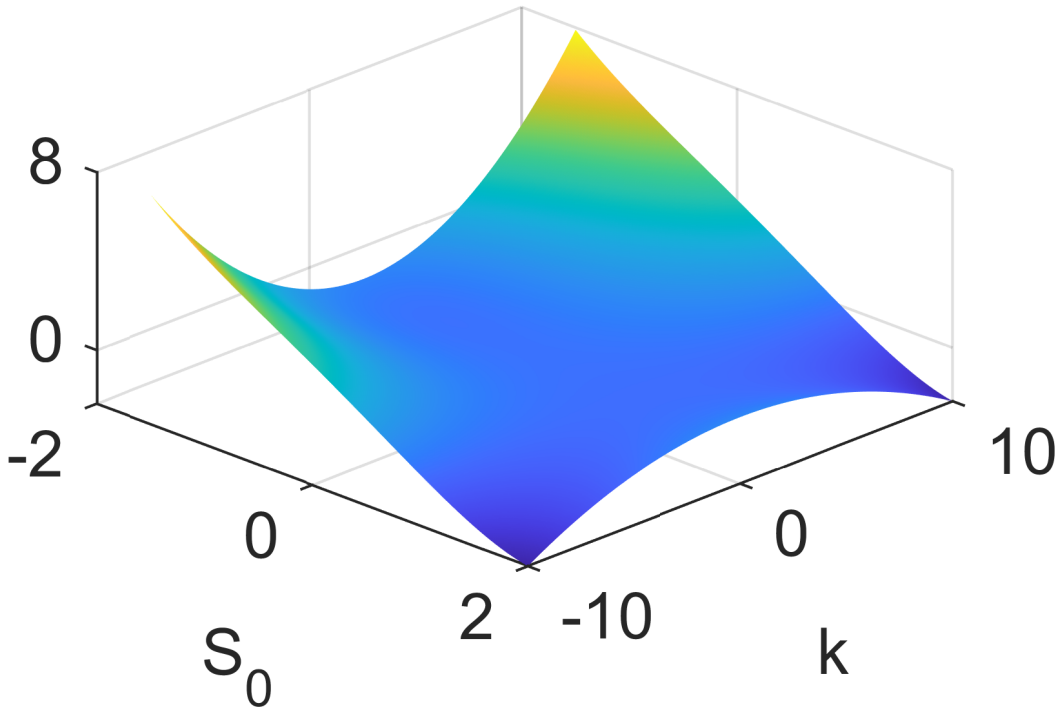

Figure 2.2: Average Landau-de Gennes energy of a perturbed uniaxial configuration such that $S = S_0 + 0.1 \sin \pi k x$ and $\hat{\mathbf{n}} = (0, 1, 0)$ as a function of S_0 and k, Eq. (2.11). The model parameters used are $a(T - T^*) = -1.26$, $B = 4$, $C = 1$, $L_1 = 1$, $L_3 = 3$, $L_2 = L_4 = 0$ corresponding to terms in Eqs. (2.2) and (2.7). The saddle point in the energy indicates it is not bounded from below.

terms to quadratic and cubic order (there are 2 to quadratic order and 6 to cubic order). The stability conditions on the L_i are summarized by the inequalities:

$$\begin{aligned} |\mathfrak{L}_8^{(3)}| &\geq 0 \\ \mathfrak{L}_1^{(2)} \pm \sqrt{\left(\mathfrak{L}_1^{(2)}\right)^2 + \left(\mathfrak{L}_3^{(3)}\right)^2 + \left(\mathfrak{L}_5^{(3)}\right)^2} &\geq 0 \\ \mathfrak{L}_2^{(2)} \pm \sqrt{\left(\mathfrak{L}_2^{(2)}\right)^2 + \left(\mathfrak{L}_4^{(3)}\right)^2 + \left(\mathfrak{L}_6^{(3)}\right)^2 + \left(\mathfrak{L}_6^{(3)}\right)^2} &\geq 0 \end{aligned} \tag{2.10}$$

where $\mathfrak{L}_i^{(k)}$ represents a linear combination of the L_i which are of order k in $\mathbf{Q}$ resulting from the spherical tensor decomposition. We note that *all* of the above inequalities must be satisfied for the Landau-de Gennes energy to be bounded, yet it is not possible for all of them to be satisfied if *any* cubic order coefficient is nonzero. Only adding quartic order terms can relieve the unboundedness. However, there are 14 quartic order terms allowed by symmetry, each with its own phenomenological coefficient [35]. The theory then becomes unwieldly, and not useful in practice. Further, including quartic order terms yields its own set of inequalities akin to Eq. (2.10) and, depending on the terms included, one is still not guaranteed to have a bounded free energy in the parameter space one wishes to study.

To illustrate the unboundedness of the Landau-de Gennes energy, we use a simple example in which a configuration $\mathbf{Q}(\mathbf{r})$ is perturbed about some uniaxial configuration of fixed S_0 known to be stable. Using the parameterization Eq. (2.3) we write $S = S_0 + \beta \sin \pi k x$, $\hat{\mathbf{n}} = (0, 1, 0)$ and $P = 0$. Using the elastic energy of Eq. (2.7) with $L_2 = L_4 = 0$, this leads to an average free energy quadratic in the wave number k

$$\begin{aligned} F(S_0, k) = \frac{1}{6} a \left(T - T^*\right) \left(2S_0^2 + \beta^2\right) + \frac{1}{27} B \left(2S_0^3 + 3S_0\beta^2\right) \\ + \frac{1}{18} C \left(2S_0^4 + 6S_0^2 + \frac{3}{4}\beta^4\right) + \frac{1}{2}\pi^2\beta^2 \left(L_1 - \frac{1}{3}S_0 L_3\right) k^2. \end{aligned} \tag{2.11}$$

The important point to note in this equation is in the coefficient of the term quadratic in k. If $L_3 > 0$, it is possible to make the free energy arbitrarily negative with large enough S_0 and k. We show in Fig. 2.2 a plot of Eq. (2.11) as a function of S_0 and k for $a(T - T^*) = -1.26$, $B = 4$, $C = 1$, $L_1 = 1$, $L_3 = 3$, and $\beta = 0.1$. The primary feature of Fig. 2.2 is the saddle point that shows for large S_0 and k an energy approaching

negative infinity. We will show in Sec. 2.5 that this unboundedness also manifests itself in a numerical instability for strongly non-uniform configurations. This feature of the Landau-de Gennes free energy has greatly limited the applicability of **Q**-tensor models as it has restricted their use to elastically isotropic systems.

2.3 Ball-Majumdar Singular Potential

To address the issues of the previous section, we adapt a description first proposed by Ball and Majumdar [36] based on the Maier-Saupe mean field theory. Instead of the typical Landau-de Gennes double well free energy, we employ a different bulk free energy density, $F_b = H(\mathbf{Q}) - T\Delta S$, where H is an interaction Hamiltonian for the nematogens and ΔS is the entropy relative to the isotropic phase [32]. Under the assumption of local equilibrium, we define the local entropy density per unit volume as

$$\Delta s(\mathbf{r}) = -nk_B \int_{S^2} p(\mathbf{u}, \mathbf{r}) \ln \left[4\pi p(\mathbf{u}, \mathbf{r})\right] \, dS(\mathbf{u}) \tag{2.12}$$

where n is the number density of nematogens, which we will assume is constant. We note that to consider non-uniform configurations we must allow the distribution $p(\mathbf{u}, \mathbf{r})$ to vary in space. The entropy of the system can then be computed as $\Delta S = \int_\Omega \Delta s(\mathbf{r}) \, d\mathbf{r}$

Because of the assumption of local equilibrium, we need only consider the equilibrium probability distribution function that maximizes the local entropy density. Additionally, we impose the self consistency condition that **Q** must also be defined by the same probability distribution, i.e. **Q** must be given by Eq. (2.9). That is, we are maximizing the entropy over the fixed *mesoscopic* **Q** manifold which constitutes a change in scale from microscopic to mesoscopic. Computing the first variation of Δs with the constraint we obtain

$$\begin{aligned} \frac{\delta}{\delta p}\left[-nk_B \int_{S^2} p \ln\left[4\pi p\right] \, dS(\mathbf{u}) - nk_B \mathbf{\Lambda} : \left(\mathbf{Q} - \int_{S^2} \left(\mathbf{u}\otimes\mathbf{u} - \frac{1}{3}\mathbf{I}\right) p \, dS(\mathbf{u})\right)\right] \\ = -nk_B \ln\left[4\pi p\right] - nk_B + nk_B \mathbf{\Lambda} : \left(\mathbf{u}\otimes\mathbf{u} - \frac{1}{3}\mathbf{I}\right) = 0 \end{aligned} \tag{2.13}$$

where $nk_B\mathbf{\Lambda}$ is a tensor of Lagrange multipliers and $\mathbf{A} : \mathbf{B} \equiv A_{ij}B_{ij}$ for tensors $\mathbf{A}$ and

B. Rearranging and normalizing we find the local equilibrium probability distribution,

$$p^*(\mathbf{u},\mathbf{r}) = \frac{\exp\left[\mathbf{\Lambda}(\mathbf{r}) : \mathbf{u}\otimes\mathbf{u}\right]}{Z\left[\mathbf{\Lambda}(\mathbf{r})\right]} \tag{2.14}$$

$$Z\left[\mathbf{\Lambda}(\mathbf{r})\right] = \int_{S^2} \exp\left[\mathbf{\Lambda}(\mathbf{r}) : \mathbf{u}\otimes\mathbf{u}\right]\, dS(\mathbf{u}) \tag{2.15}$$

where Z is interpreted as a single particle partition function in an external field defined by the Lagrange multiplier field $\mathbf{\Lambda}$.

The Lagrange multiplier $\mathbf{\Lambda}$ can be thought of as the thermodynamic conjugate variable to the order parameter $\mathbf{Q}$. The Lagrange multiplier is a functional of $\mathbf{Q}$, and as in density functional theory, the order parameter $\mathbf{Q}$ is a unique functional of $\mathbf{\Lambda}$. The definition of $\mathbf{Q}$, Eq. (2.9), can be recast so that $\mathbf{Q}$ is an average that is calculated self-consistently with Z,

$$\begin{aligned}\mathbf{Q} + \frac{1}{3}\mathbf{I} &= \frac{1}{Z\left[\mathbf{\Lambda}\right]}\int_{S^2} (\mathbf{u}\otimes\mathbf{u}) \exp\left[\mathbf{\Lambda} : \mathbf{u}\otimes\mathbf{u}\right]\, dS(\mathbf{u}) \\ &= \frac{1}{Z\left[\mathbf{\Lambda}\right]}\frac{\partial}{\partial\mathbf{\Lambda}}\int_{S^2} \exp\left[\mathbf{\Lambda} : \mathbf{u}\otimes\mathbf{u}\right]\, dS(\mathbf{u}) \\ &= \frac{1}{Z\left[\mathbf{\Lambda}\right]}\frac{\partial Z\left[\mathbf{\Lambda}\right]}{\partial\mathbf{\Lambda}} = \frac{\partial \ln Z\left[\mathbf{\Lambda}\right]}{\partial\mathbf{\Lambda}}.\end{aligned} \tag{2.16}$$

The last equation is a mean field self consistency condition (mean field as it only pertains to the average), and it has been shown to have a unique solution [47].

Therefore, the entropy density can then be rewritten as a functional solely of $\mathbf{Q}$ by inverting Eq. (2.16). We note that in general the single particle partition function cannot be computed analytically on the unit sphere, and hence an analytical inversion of this expression does not exist. Both the partition function and the inversion must be computed numerically. Considering $\mathbf{\Lambda}$ as a function of $\mathbf{Q}$, the entropy of a configuration is

$$\Delta S = \int_\Omega \left[\ln 4\pi + nk_BT\left(\mathbf{\Lambda}(\mathbf{Q}) : \left(\mathbf{Q} + \frac{1}{3}\mathbf{I}\right) - \ln Z\left[\mathbf{\Lambda}(\mathbf{Q})\right]\right)\right]\, d\mathbf{r}. \tag{2.17}$$

We introduce the Hamiltonian, $H = \int_\Omega\int_\Omega K\left[p^*(\mathbf{u}_1,\mathbf{r}_1), p^*(\mathbf{u}_2,\mathbf{r}_2)\right]\, d\mathbf{r}_1 d\mathbf{r}_2$ where K is an interaction kernel for molecules of orientation $\mathbf{u}_1$ and $\mathbf{u}_2$ at locations $\mathbf{r}_1$ and $\mathbf{r}_2$. One of the simplest interaction kernels is adapted from the Maier-Saupe [32, 34] free

energy:

$$K(\mathbf{r}_1,\mathbf{r}_2) = -\kappa\delta\left(\mathbf{r}_1-\mathbf{r}_2\right)\int_{S^2}\int_{S^2}\left[\left(\mathbf{u}_1\cdot\mathbf{u}_2\right)^2-\frac{1}{3}\right]p^*(\mathbf{u}_1,\mathbf{r}_1)p^*(\mathbf{u}_2,\mathbf{r}_2)\,dS(\mathbf{u}_1)dS(\mathbf{u}_2) \tag{2.18}$$

where κ is a phenomenological interaction strength coefficient. This interaction kernel can be significantly simplified by writing $\left[\left(\mathbf{u}_1\cdot\mathbf{u}_2\right)^2-1/3\right] = \mathbf{u}_1\otimes\mathbf{u}_1 : (\mathbf{u}_2\otimes\mathbf{u}_2-(1/3)\mathbf{I})$ and then separately performing the integrals, recalling the definition of $\mathbf{Q}$, Eq. (2.9). The kernel is then $K = -\kappa\delta(\mathbf{r_1}-\mathbf{r_2})\mathbf{Q}(\mathbf{r}_1):\mathbf{Q}(\mathbf{r}_2)$ so the Hamiltonian may be written as a function of $\mathbf{Q}$ only:

$$H(\mathbf{Q}) = -\kappa\int_\Omega \mathrm{Tr}\left[\mathbf{Q}(\mathbf{r})^2\right]\,d\mathbf{r}. \tag{2.19}$$

Putting this all together, we finally write the full bulk free energy, $H-T\Delta S$, for a configuration $\mathbf{Q}(\mathbf{r})$:

$$F_b(\mathbf{Q}) = \int_\Omega\left[-\kappa\mathrm{Tr}\left[\mathbf{Q}^2\right]+\ln 4\pi + nk_BT\left(\mathbf{\Lambda}(\mathbf{Q}):\left(\mathbf{Q}+\frac{1}{3}\mathbf{I}\right)-\ln Z[\mathbf{\Lambda}(\mathbf{Q})]\right)\right]\,d\mathbf{r} \tag{2.20}$$

where $\mathbf{\Lambda}$ is regarded as a function of $\mathbf{Q}$ through Eq. (2.16). Eq. (2.20) must be computed numerically because, in general, the partition function, Eq. (2.15), cannot be computed analytically. This also means that the inversion of Eq. (2.16) must be carried out numerically everywhere in the computational domain if the system is spatially heterogeneous. While this does increase the computational complexity of finding minimizers for this model, we show in later sections and chapters that even with modest computing resources we can fully simulate three-dimensional domains.

This bulk free energy captures all the properties of the nematic phase that the Landau-de Gennes bulk free energy describes. The minimizers of Eq. (2.20) are isotropic states with $\mathbf{Q}=\mathbf{0}$ or uniaxial states with $S = S_N^{\mathrm{BM}}$ (as well as $S = P = P_N^{\mathrm{BM}}$ and $S = -P = -P_N^{\mathrm{BM}}$) [36, 48] where the superscript BM denotes the fact that the equilibrium value of S for the Ball-Majumdar model is not given by Eq. (2.4), though we will drop this superscript subsequently for brevity.

The bulk free energy also leads to a first order phase transition. In Fig. 2.3 we plot the bulk free energy as a function of uniaxial order S for $\kappa/(nk_BT) = 3.3$, $\kappa/(nk_BT) =$

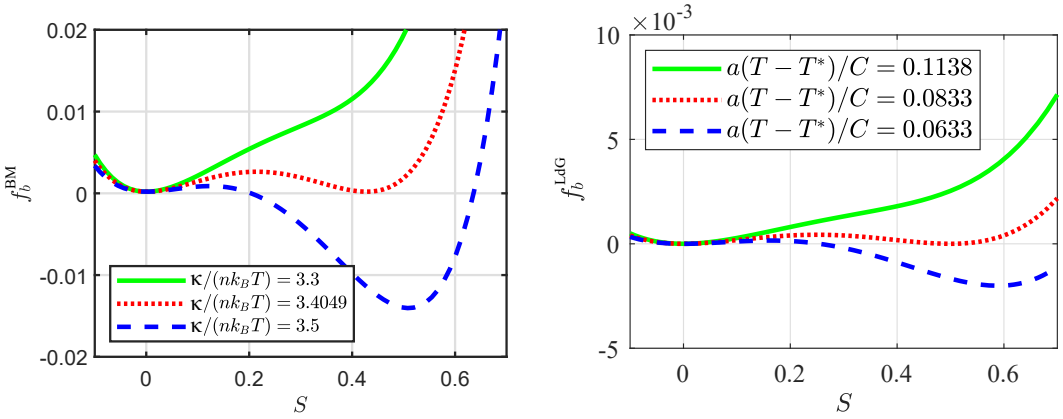

Figure 2.3: (left) Ball-Majumdar bulk free energy density as a function of uniaxial order S for $\kappa/(nk_BT) = 3.3$, $\kappa/(nk_BT) = 3.4049$, and $\kappa/(nk_BT) = 3.5$. (right) Landau-de Gennes bulk free energy density as a function of S for $B = -1.5$ and $a(T - T^*)/C = 0.1138$, $a(T - T^*)/C = 0.0833$, and $a(T - T^*)/C = 0.0633$.

3.4049, and $\kappa/(nk_BT) = 3.5$. This is plotted alongside the bulk free energy density given by the Landau-de Gennes model for parameters $B = -1.5$ and $a(T - T^*)/C = 0.1138$, $a(T - T^*)/C = 0.0833$, and $a(T - T^*)/C = 0.0633$. The double-well feature of the free energy is similar to that of the Landau-de Gennes bulk free energy as the temperature parameter is varied through exact coexistence between the isotropic and nematic phases, which occurs at $\kappa/(nk_BT) \simeq 3.4049$. Additionally, if $\kappa/(nk_BT) > 3.4016$ the nematic phase is stable while the isotropic phase ceases to be stable when $\kappa/(nk_BT) > 3.6683$. These values are consistent with previous studies of the Maier-Saupe free energy [1, 32, 49].

In Fig. 2.4 we plot the equilibrium values of S_N as a function of $\kappa/(nk_BT)$ where the shaded region represents the region in which isotropic and nematic phases are stable or metastable. Unlike the Landau-de Gennes bulk free energy, this region cannot be tuned since there is only one parameter controlling the phase behavior (as opposed to three in the latter case, a, B, and C). However, as we show in Sec. 2.8, different choices in the Hamiltonian will lead to different phase behavior. We also note that the equilibrium S_N does not scale as $(T - T^*)^{1/2}$ at low temperature as it does for the Landau-de Gennes bulk energy. Instead, $S_N \to 1$ as $\kappa/(nk_BT) \to \infty$.

The singular free energy self-consistently constrains the values of $\mathbf{Q}$ to be in the

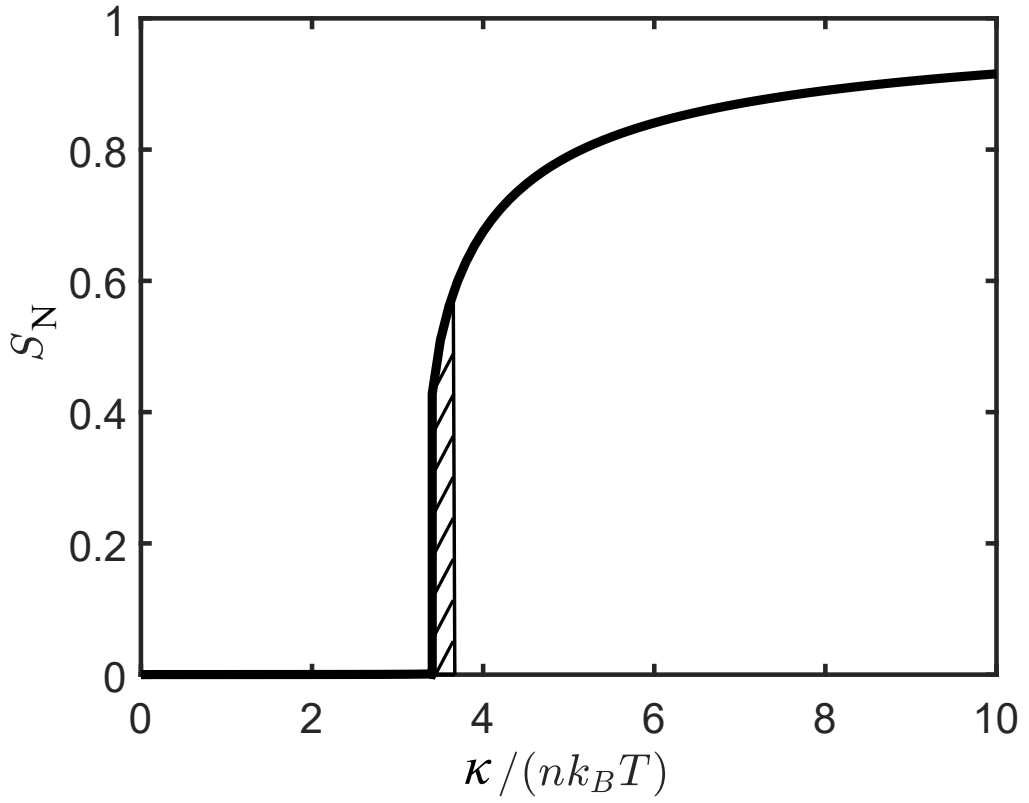

Figure 2.4: Equilibrium value of S, S_N, as a function of effective temperature parameter κ/nk_BT. The shaded region represents the region in which both isotropic and nematic phases are either stable or metastable.

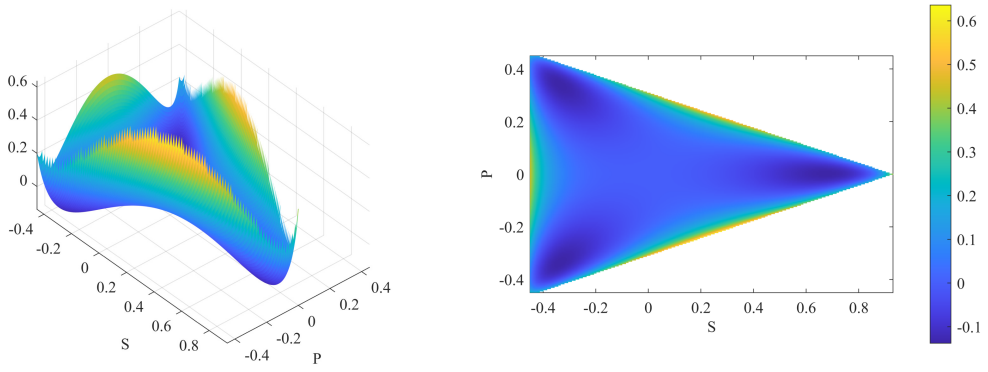

Figure 2.5: Bulk free energy as a function of S and P for the singular potential, Eq. (2.20), for $\kappa/nk_BT = 4$. As S and P go to their physical limits the energy diverges reflecting the constrained maximization. Outside the physically meaningful triangle the energy is undefined.

physically admissible range, and hence naturally cuts off the values of the eigenvalues so the unboundedness displayed in Fig. 2.2 does not occur when the elastic energy Eq. (2.7) is added to the full free energy. In fact, as $\mathbf{Q}$ approaches its physical limits, $\mathbf{\Lambda} \to \infty$ and hence the free energy diverges. Fig. 2.5 shows plots of Eq. (2.20) as a function of S and P with $\kappa/nk_BT = 4$ over the "physical triangle", defined by the limits of Eq. (2.9) [50]. Note that at these limits the energy diverges quickly.

We conclude this section by comparing the self-consistent free energy computed from the perturbation of Sec. 2.2 with the same elastic energy, Eq. (2.7). We consider $S = S_0 + 0.1 \sin \pi k x$ with $\hat{\mathbf{n}} = (0,\, 1,\, 0)$ and $P = 0$ which is then substituted into the free energy density and the average over a period is computed. Fig. 2.6 shows this average free energy, which must be computed numerically, plotted as a function of S_0 and k for $\kappa/nk_BT = 4$, $L_1 = 1$, $L_3 = 3$, and $L_2 = L_4 = 0$. As evident from the figure, the saddle point in the free energy no longer exists and the free energy remains bounded because the eigenvalues of $\mathbf{Q}$ (represented by S_0) are not allowed by the energy to go outside their physical bounds.

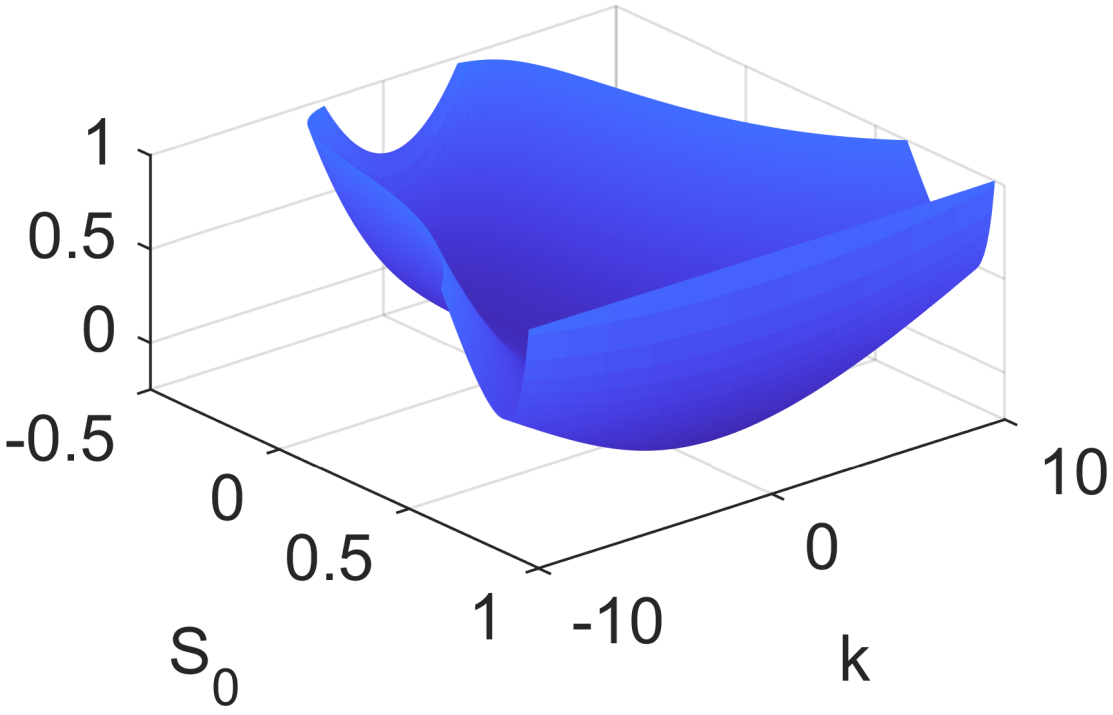

Figure 2.6: Average bulk free energy given by the singluar potential for the perturbed uniaxial configuration $S = S_0 + 0.1 \sin \pi kx$ and $\hat{\mathbf{n}} = (0, 1, 0)$ as introduced in Sec. 2.2. The model parameters used are $\kappa/nk_BT = 4$, $L_1 = 1$, $L_3 = 3$, $L_2 = L_4 = 0$. Unlike the Landau-de Gennes bulk free energy plotted in Fig. 2.2, the free energy plotted here remains bounded.

2.4 Computational Method

Here we detail the computational method employed throughout the rest of this dissertation. To find minimizers of the full free energy, we use a semi-implicit gradient flow algorithm. Given the convexity properties of both the Hamiltonian and of the entropy, we leverage the method of convex splitting [51–53] for stability with large time steps. The gradient flow equation is,

$$\frac{\partial \mathbf{Q}}{\partial t} = -\Gamma \frac{\delta F}{\delta \mathbf{Q}} \tag{2.21}$$

where Γ is a rotational viscosity and $\delta F/\delta \mathbf{Q}$ is the functional derivative of the full free energy F. We introduce dimensionless quantities by defining,

$$\tilde{\mathbf{r}} = \frac{\mathbf{r}}{\xi},\ \tilde{t} = \frac{t}{\tau},\ \tilde{F} = \frac{F}{\xi^3 n k_B T},\ \tilde{L}_{i\neq 1} = \frac{L_{i\neq 1}}{L_1} \tag{2.22}$$

where ξ and τ are characteristic length and time scales. This leaves each $\tilde{L}_i$, $\kappa/(nk_BT)$, $L_1/(\xi^2 nk_BT)$, and $\Gamma\xi^3\tau nk_BT$ as dimensionless control parameters for the system. However, because the latter two control the length and time scaling respectively, we will set these to unity unless otherwise specified. If we require parameters with physical dimensions (e.g. for comparison with experiment) we can find the appropriate length and time scales, ξ and τ, by fitting computational data to physical data. Additionally, $\kappa/(nk_BT)$ only controls the phase behavior of the system, as seen in Fig. 2.4, so we will adjust this parameter sparingly, only when we need the system to be in different parts of the phase diagram. The primary two values we will be concerned with are at isotropic-nematic coexistence, $\kappa/(nk_BT) = 3.4049$, and the globally stable nematic phase, for which we will use $\kappa/(nk_BT) = 4$. This leaves the $\tilde{L}_i$ as the primary control parameters that we shall study in subsequent chapters. We will also omit all tildes in subsequent quantities for simplicity.

Although the theory presented in the previous section has been written for the full tensor $\mathbf{Q}$, it is simpler in practice to first take advantage of the traceless and symmetric nature of $\mathbf{Q}$ and reduce the number of degrees of freedom. We decompose $\mathbf{Q}$ into an

appropriately normalized basis so that

$$\mathbf{Q} = \begin{pmatrix} \frac{2}{\sqrt{3}}q_1 & q_3 & q_4 \\ q_3 & -\frac{1}{\sqrt{3}}q_1 + q_2 & q_5 \\ q_4 & q_5 & -\frac{1}{\sqrt{3}}q_1 - q_2 \end{pmatrix}. \tag{2.23}$$

The system is then described by the five scalar fields $q_i(\mathbf{r}, t)$. Given each q_i one can extract the eigenvalues (or S and P) and eigenvectors of $\mathbf{Q}$ by constructing the matrix in Eq. (2.23).

Eq. (2.9) applies to each degree of freedom so that

$$\begin{aligned} q_1 + \frac{\sqrt{3}}{6} &= \frac{\sqrt{3}}{2}\int_{S^2} u_1^2 p(\mathbf{u})\, dS(\mathbf{u}) \\ q_2 + \frac{1}{2} &= \int_{S^2} \left(\frac{1}{2}u_1^2 + u_2^2\right) p(\mathbf{u})\, dS(\mathbf{u}) \\ q_3 &= \int_{S^2} u_1 u_2 p(\mathbf{u})\, dS(\mathbf{u}) \\ q_4 &= \int_{S^2} u_1 u_3 p(\mathbf{u})\, dS(\mathbf{u}) \\ q_5 &= \int_{S^2} u_2 u_3 p(\mathbf{u})\, dS(\mathbf{u}). \end{aligned} \tag{2.24}$$

In a similar manner to that presented in the previous section, we define Lagrange multipliers, Λ_i, that fix the relations of Eq. (2.24). Further, we derive the corresponding probability distribution and partition function

$$Z[\{\Lambda_i\}] = \int_{S^2} \exp\left[\Lambda_1\left(\frac{\sqrt{3}}{2}u_1^2\right) + \Lambda_2\left(\frac{1}{2}u_1^2 + u_2^2\right) + \Lambda_3 u_1 u_2 + \Lambda_4 u_1 u_3 + \Lambda_5 u_2 u_3\right] dS(\mathbf{u}) \tag{2.25}$$

so that each q_i is computed self-consistently with the partition function and

$$\begin{aligned} q_1 + \frac{\sqrt{3}}{6} &= \frac{\partial \ln Z}{\partial \Lambda_1} \\ q_2 + \frac{1}{2} &= \frac{\partial \ln Z}{\partial \Lambda_2} \\ q_{i=3,4,5} &= \frac{\partial \ln Z}{\partial \Lambda_{i=3,4,5}}. \end{aligned} \tag{2.26}$$

Substituting Eq. (2.23) for $\mathbf{Q}$ and Eq. (2.25) for Z and regarding each Λ_i as a function of each q_i through Eq. (2.26) we write the bulk free energy density as a function of q_i:

$$f_b(\mathbf{q}) = \left\{ \Lambda_1 \left(q_1 + \frac{\sqrt{3}}{6} \right) + \Lambda_2 \left(q_2 + \frac{1}{2} \right) + \sum_{i=3}^{5} \Lambda_i q_i + \ln 4\pi - \ln Z \left[\{\Lambda_i\} \right] \right\} - \left[2 \frac{\kappa}{n k_B T} \left(\sum_{i=1}^{5} q_i^2 \right) \right] \quad (2.27)$$

where $\mathbf{q} \equiv (q_1, q_2, q_3, q_4, q_5)$. We note that this energy can be written as the difference between two convex functions of $\mathbf{q}$: $f_b = \psi_0(\mathbf{q}) - \psi_1(\mathbf{q})$ where ψ_0 is the term in curly brackets and ψ_1 is the term in square brackets. This fact will be used when developing a computational algorithm for minimizing the energy as we will be able to apply the method of convex splitting to avoid a fully implicit algorithm.

We can also substitute Eq. (2.23) into the elastic free energy, Eq. (2.7), to find the

elastic energy density in terms of the q_i:

$$
\begin{aligned}
f_e(\mathbf{q},\nabla\mathbf{q}) = 2\sum_{i=1}^{5}|\nabla q_i|^2 + L_2\Bigg[&\left(\partial_y q_3 + \frac{2}{\sqrt{3}}\partial_x q_1 + \partial_z q_4\right)^2 \\
&+ \left(-\frac{1}{\sqrt{3}}\partial_y q_1 + \partial_y q_2 + \partial_x q_3 + \partial_z q_5\right)^2 + \left(-\frac{1}{\sqrt{3}}\partial_z q_1 - \partial_z q_2 + \partial_x q_4 + \partial_y q_5\right)^2\Bigg] \\
&+ 2L_3\Bigg[\frac{1}{\sqrt{3}}q_1\sum_{i=1}^{5}\left(2(\partial_x q_i)^2 - (\partial_y q_i)^2 - (\partial_z q_i)^2\right) + q_2\sum_{i=1}^{5}\left((\partial_y q_i)^2 - (\partial_z q_i)^2\right) \\
&\qquad + 2q_3\sum_{i=1}^{5}(\partial_x q_i\partial_y q_i) + q_4\sum_{i=1}^{5}(\partial_x q_i\partial_z q_i) + q_5\sum_{i=1}^{5}(\partial_y q_i\partial_z q_i)\Bigg] \\
+\frac{2}{3}L_4\Big\{&q_1\left[\partial_x q_1\left(2\sqrt{3}\partial_x q_1 + 3\partial_y q_3 + 3\partial_z q_4\right) + \partial_y q_1\left(-\sqrt{3}\partial_y q_1 + 3\partial_y q_2 + 3\partial_x q_3 + 3\partial_z q_5\right)\right. \\
&\left. + \partial_z q_1\left(-\sqrt{3}\partial_z q_1 - 3\partial_z q_2 + 3\partial_x q_4 + 3\partial_y q_5\right)\right] + q_2\left[\partial_x q_2\left(2\sqrt{3}\partial_x q_1 + 3\partial_y q_3 + 3\partial_z q_4\right)\right. \\
&\left. + \partial_y q_2\left(-\sqrt{3}\partial_y q_1 + 3\partial_y q_2 + 3\partial_x q_3 + 3\partial_z q_5\right) + \partial_z q_2\left(-\sqrt{3}\partial_z q_1 - 3\partial_z q_2 + 3\partial_x q_4 + 3\partial_y q_5\right)\right] \\
&+ q_3\left[\partial_x q_3\left(2\sqrt{3}\partial_x q_1 + 3\partial_z q_4\right) + \partial_y q_3\left(-\sqrt{3}\partial_y q_1 + 3\partial_y q_2 + 6\partial_x q_3 + 3\partial_z q_5\right)\right. \\
&\left. + \partial_z q_3\left(-\sqrt{3}\partial_z q_1 - 3\partial_z q_2 + 3\partial_x q_4 + 3\partial_y q_5\right)\right] + q_4\left[\partial_x q_4\left(2\sqrt{3}\partial_x q_1 + 3\partial_y q_3 + 6\partial_z q_4\right)\right. \\
&\left. + \partial_y q_4\left(-\sqrt{3}\partial_y q_1 + 3\partial_y q_2 + 3\partial_x q_3 + 3\partial_z q_5\right) + \partial_z q_5\left(-\sqrt{3}\partial_z q_1 - 3\partial_y q_2 + 3\partial_y q_5\right)\right] \\
&+ q_5\left[\partial_x q_5\left(2\sqrt{3}\partial_x q_1 + 3\partial_y q_3 + 3\partial_z q_4\right) + \partial_y q_5\left(-\sqrt{3}\partial_y q_1 + 3\partial_y q_2 + 3\partial_x q_3 + 6\partial_z q_5\right)\right. \\
&\left. + \partial_z q_5\left(-\sqrt{3}\partial_z q_1 - 3\partial_z q_2 + 3\partial_x q_4\right)\right]\Big\}. \qquad (2.28)
\end{aligned}
$$

Then, from the energy densities f_b and f_e, the gradient flow equations for each q_i are

$$
\frac{\partial q_i}{\partial t} = -\frac{\delta F}{\delta q_i} = -\frac{\partial f_b}{\partial q_i} - \frac{\partial f_e}{\partial q_i} + \nabla\cdot\frac{\partial f_e}{\partial \nabla q_i}. \qquad (2.29)
$$

The term $\partial f_b/\partial q_i$ turns out to have a relatively simple form:

$$\begin{aligned}\frac{\partial f_b}{\partial q_1} &= \frac{\partial \Lambda_1}{\partial q_1}\left(q_1 + \frac{\sqrt{3}}{6}\right) + \Lambda_1 + \frac{\partial \Lambda_2}{\partial q_1}\left(q_2 + \frac{1}{2}\right) + \sum_{i=3}^{5}\frac{\partial \Lambda_i}{\partial q_1}q_i - \frac{\partial \ln Z}{\partial q_1} - 4\frac{\kappa}{nk_BT}q_1 \\ &= \Lambda_1 - 4\frac{\kappa}{nk_BT}q_1 + \sum_{i=1}^{5}\frac{\partial \Lambda_i}{\partial q_1}\frac{\partial \ln Z}{\partial \Lambda_i} - \sum_{i=1}^{5}\frac{\partial \ln Z}{\partial \Lambda_i}\frac{\partial \Lambda_i}{\partial q_1} \\ &= \Lambda_1 - 4\frac{\kappa}{nk_BT}q_1\end{aligned} \tag{2.30}$$

where in the second line we have used Eq. (2.26) and the chain rule to show that the terms involving $\ln Z$ cancel. Eq. (2.30) was computed for q_1, but it is easy to show that an analogous result holds for all of the q_i. The terms involving f_e are not as simple and will be omitted here for brevity, however, we note that they can be simply derived from taking appropriate derivatives of Eq. (2.28). The weak formulation of the equations can be found in the code in Ref. [54].

To solve the equations of motion for each q_i we first discretize the system in time:

$$\begin{aligned}q_i^{(k+1)} - q_i^{(k)} = -\Delta t \Bigg[&\Lambda_i(\mathbf{q}^{(k+1)}) - 4\frac{\kappa}{nk_BT}q_i^{(k)} \\ &+ \frac{\partial f_e}{\partial q_i}\left(\mathbf{q}^{(k+1)}, \nabla\mathbf{q}^{(k+1)}\right) - \nabla\cdot\frac{\partial f_e}{\partial \nabla q_i}\left(\mathbf{q}^{(k+1)}, \nabla\mathbf{q}^{(k+1)}\right)\Bigg]\end{aligned} \tag{2.31}$$

where Δt is a time step parameter and $q_i^{(k)} \equiv q_i(\mathbf{r}, k\Delta t)$. We note that this is a semi-implicit time discretization since the second term on the right hand side is calculated at time step k while the rest are calculated at time step $k+1$. This takes advantage of the convex splitting of the bulk free energy discussed above. In essence, the convex splitting of the energy allows one to use a semi-implicit algorithm to solve the gradient flow equations and achieve the same level of precision and stability as if one was using a fully implicit algorithm [51–53].

At each time step, Eq. (2.31) is solved for $\mathbf{q}^{(k+1)}$. This is carried out by using either a finite difference or finite element approximation of the spatial dependence of $\mathbf{q}$. For the case of finite differences, we use lowest order stencils and square meshes to approximate first and second derivatives [55]. For the case of finite elements, we first rewrite the

equations in the weak formulation and introduce a test function $\mathbf{V}$:

$$\sum_{i=1}^{5}\left\langle q_i^{(k+1)}+\Delta t\left[\Lambda_i(\mathbf{q}^{(k+1)})+\frac{\partial f_e}{\partial q_i}^{(k+1)}\right],V_i\right\rangle + \sum_{i=1}^{5}\left\langle \Delta t\frac{\partial f_e}{\partial \nabla q_i}^{(k+1)},\nabla V_i\right\rangle = \sum_{i=1}^{5}\left\langle\left(1+4\Delta t\frac{\kappa}{nk_BT}\right)q_i^{(k)},V_i\right\rangle \quad (2.32)$$

where $\langle \mathbf{f},\mathbf{g}\rangle \equiv \int_\Omega \mathbf{f}(\mathbf{r})\cdot\mathbf{g}(\mathbf{r})\,d\mathbf{r}$. The domain is partitioned into separate pieces that form the mesh and are line segments in one dimension, triangles in two dimensions, or tetrahedra in three dimensions. Each q_i (which is the "trial function" in the language of finite elements) is then approximated by basis functions, which for us are linear functions, defined to be unity on a specific node of the mesh unique to the particular basis function and then continuous across element boundaries. The integrals in Eq. (2.32) are then performed over the domain, where the test functions are taken as convenient linear combinations of the basis functions, which yields an algebraic equation for the value of q_i on each node of the mesh. In general, Eq. (2.31) or Eq. (2.32) is nonlinear and so we must first linearize by replacing $\mathbf{q}^{(k+1)} \to \tilde{\mathbf{q}}^{(k+1)} + \delta\mathbf{q}$. Whether we use finite differences or finite elements, this leads to a linear equation for the value of $\delta\mathbf{q}$ at each node on the mesh, represented schematically by a matrix equation

$$\sum_{n=1}^{N} A_{mn}\delta\mathbf{q}_n = \mathbf{b}_m \quad (2.33)$$

where m and n index the node on the mesh and N is the total number of nodes on the mesh. Therefore, within each time step, we use Newton-Raphson's method [55] to find $\mathbf{q}^{(k+1)}$. This method is iterated until $|\delta\mathbf{q}| < 10^{-6}$. As mentioned, for finite differences, the matrix equation is generated using the appropriate lowest order stencils on square meshes for first and second order derivatives. For finite elements, we use the Matlab/C++ package FELICITY [56] to generate the matrices for the matrix equation. The matrix equations are then solved with the algebraic multi-grid solver (AGMG) [57–60] for 3D calculations, and the "backslash" command in Matlab for the 2D case.

An important feature of the numerical algorithm we employ is the evaluation of the Λ_i and the partition function Z. As mentioned above, Z cannot be evaluated analytically

and thus we must evaluate it numerically. Additionally, we must numerically invert Eq. (2.26) to find $\Lambda_i(\mathbf{q})$, because the solution of Eqs. (2.31) and (2.32) requires Λ_i at all points in the domain (and hence, at all points of the mesh). Also note that we must evaluate $\Lambda_i(\mathbf{q}^{(k+1)})$, i.e. we need Λ_i at the *next* time step, not the previous. Thus, upon linearization, this term becomes

$$\Lambda_i(\mathbf{q}^{(k+1)}) \to \Lambda_i(\tilde{\mathbf{q}}^{(k+1)}) + \sum_{j=1}^{5} \left.\frac{\partial \Lambda_i}{\partial q_j}\right|_{\tilde{\mathbf{q}}^{(k+1)}} \delta q_j \tag{2.34}$$

and so we also need $\partial \Lambda_i / \partial q_j$ for the Newton iteration solving for $\mathbf{q}^{(k+1)}$ in the discretization scheme.

To numerically evaluate Z (and all other integrals over the unit sphere, S^2) we use Lebedev quadrature which partitions the unit sphere into uniform points [61]. At each point on the mesh, we use this numerical evaluation and a Newton iteration (which starts at an initial guess $\Lambda_{i,0} = 0$ and terminates after $|\delta \Lambda_i| < 10^{-9}$) to invert Eq. (2.26) and find Λ_i given $\mathbf{q}$. To find $\partial \Lambda_i / \partial q_j$ we first regard Eq. (2.26) as a vector valued equation, and then note that taking a derivative of the left hand side with respect to q_j yields δ_{ij}:

$$\begin{aligned} \frac{\partial}{\partial q_j}\left(f_i(\mathbf{q}) = \frac{\partial \ln Z}{\partial \Lambda_i} \right) & \\ \Rightarrow \delta_{ij} &= \sum_{k=1}^{5} \frac{\partial^2 \ln Z}{\partial \Lambda_i \partial \Lambda_k} \frac{\partial \Lambda_k}{\partial q_j} \\ \Rightarrow \frac{\partial \Lambda_k}{\partial q_j} &= \left(\frac{\partial^2 \ln Z}{\partial \Lambda_k \partial \Lambda_j} \right)^{-1} \end{aligned} \tag{2.35}$$

where $\partial^2 \ln Z / \partial \Lambda_k \partial \Lambda_j$ can be computed from Eq. (2.25) and is required for the Newton iteration.

A computational challenge associated with this method is that this numerical inversion is required at all points in space, i.e. all nodes on the mesh, for every Newton step in determining $\mathbf{q}^{(k+1)}$. While this is a disadvantage compared to the Landau-de Gennes bulk free energy, we can improve the computational speed considerably by parallelizing the evaluation over the mesh, since Λ_i only depends on the value of $\mathbf{q}$ and not on its derivatives. Additionally, we can use the previous solution as the initial guess in the

Newton solver, which speeds up computation time significantly. We find in practice that the Newton iteration converges in only one or two steps.

For applications where we are looking for equilibrium solutions, we evolve the system in time and calculate the free energy of the configuration at each time step. We stop evolving when the energy fails to change within some tolerance. For systems where we are interested in the dynamics, such as in annihilating disclinations, we set a maximum time step and store the configuration $\mathbf{Q}$ for every time step. In subsequent sections, we will use the simpler tensor notation $\mathbf{Q}$ and $\mathbf{\Lambda}$ when discussing configurations, even though the actual computations involve the q_i and Λ_i. This notation is more in keeping with other literature on the topic, is more concise, and one can map directly from the q_i and Λ_i to $\mathbf{Q}$ and $\mathbf{\Lambda}$, which is how we extract the eigenvalues and eigenvectors of $\mathbf{Q}$.

We finish this section by mentioning a few considerations that may be implemented in future versions of the algorithm. First, $\mathbf{Q}$ and $\mathbf{\Lambda}$ can be simultaneously diagonalized since if $\mathbf{\Pi} = \mathbf{R}^T\mathbf{\Lambda}\mathbf{R}$ where $\mathbf{\Pi}$ is a diagonal matrix we may write

$$\begin{aligned} Z\mathbf{Q} &= \int_{S^2} \left(\mathbf{u}\mathbf{u}^T - \frac{1}{3}\mathbf{I}\right) \exp\left[\mathbf{u}^T\mathbf{\Lambda}\mathbf{u}\right]\, dS(\mathbf{u}) \\ &= \int_{S^2} \left(\mathbf{R}\mathbf{w}\mathbf{w}^T\mathbf{R}^T - \frac{1}{3}\mathbf{R}\mathbf{R}^T\right) \exp\left[\mathbf{w}^T\mathbf{R}^T\mathbf{\Lambda}\mathbf{R}\mathbf{w}\right]\, dS(\mathbf{w}) \\ &= \mathbf{R}\left[\int_{S^2} \left(\mathbf{w}\mathbf{w}^T - \frac{1}{3}\mathbf{I}\right) \exp\left[\mathbf{w}^T\mathbf{\Pi}\mathbf{w}\right]\, dS(\mathbf{w})\right]\mathbf{R}^T \end{aligned} \tag{2.36}$$

where in the second line we have redefined the variable of integration $\mathbf{u} \to \mathbf{R}\mathbf{w}$. Then

$$\mathbf{R}^T\mathbf{Q}\mathbf{R} = \frac{1}{Z}\int_{S^2} \left(\mathbf{w}\mathbf{w}^T - \frac{1}{3}\mathbf{I}\right) \exp\left[\sum_{i=1}^{3} \pi_i w_i^2\right]\, dS(\mathbf{w}) \tag{2.37}$$

which is itself a diagonal matrix since all the off diagonal terms are integrals of odd functions over the unit sphere, and hence vanish. A consequence of this fact is that the inversion of Eq. (2.26) may be carried out everywhere in the local eigenbasis of $\mathbf{Q}$ instead of the fixed frame, which would significantly reduce the amount of computation required. However, because we also need $\partial\Lambda_i/\partial q_j$ as part of the semi implicit algorithm it has turned out in practice that it is still faster to go through the procedure described above in the fixed basis. A significant improvement to future versions of the algorithm would be the introduction of a fast procedure for generating $\partial\Lambda_i/\partial q_j$ in the eigenbasis

of $\mathbf{Q}$.

Another consideration is the fact that if $\mathbf{\Lambda}$ becomes large (as it does when the eigenvalues of $\mathbf{Q}$ approach their physical limit) then the partition function Z becomes very large (since $\exp\left[\mathbf{u}^T\mathbf{\Lambda}\mathbf{u}\right]$ is very large) which may result in an overflow computation. A workaround here is to shift the exponential, since the trace of $\mathbf{\Lambda}$ is arbitrary and does not affect the probability distribution. Thus the exponential may be computed as $\exp\left[\mathbf{u}^T\mathbf{\Lambda}\mathbf{u} - C_0\right]$ where C_0 is chosen to avoid overflow computation. This would not be difficult to implement, but we have yet to come across the issue of overflow computations in practice. Finally, we mention that as the probability distribution becomes very peaked, that is, when S nears its physical limit of 1, the Lebedev quadrature (which is based on uniformly distributed points on the sphere) may fail or give highly inaccurate results. Again, we have not encountered this problem in practice, but a possible solution would be to use a more robust adaptive quadrature that increases the density of quadrature points near the peak of the distribution. Finally, we mention that a version of the code used for computations in this dissertation may be found in Ref. [54].

2.5 Computational Tests

Computations described here and in subsequent chapters were performed on various Matlab versions from R2017b to R2021b on a Haswell processor with a base clock of 2.5 Ghz at the Minnesota Supercomputing Institute. Newton iterations involving the determination of $\mathbf{\Lambda}$ (described above) were parallelized over 24 to 128 threads using Matlab's command parfor.

The first computational test we perform is a check on the accuracy of the Newton's method for evaluating $\mathbf{\Lambda}(\mathbf{Q})$. We test this using various tensors parametrized with $S_0 = 0.1, 0.6, 0.97, 0.995$ where $S_0 = 0.995$ is the largest value of S_0 for which the algorithm converges. As discussed in Sec. 2.3 if $S_0 = 1$ then $\mathbf{Q}$ is no longer physical and $\mathbf{\Lambda}$ diverges. Table 2.1 summarizes the results of the test in terms of the maximum component of the difference $\mathbf{\Lambda}_{max} - \mathbf{\Lambda}$ where $\mathbf{\Lambda}_{max}$ is the value of $\mathbf{\Lambda}$ given by the highest degree of quadrature tested, 5810. We find that for quadrature degrees below 500, the eigenvalues of $\mathbf{Q}$ must be relatively small to obtain accurate values of $\mathbf{\Lambda}$. For $\mathbf{Q}$ with eigenvalues close to the physical limit, the Lebedev quadrature degree must

Table 2.1: Maximum component of the difference $\mathbf{\Lambda}_{max} - \mathbf{\Lambda}$ for $\mathbf{\Lambda}$ given by Newton's method for various Lebedev quadrature degrees and maximum eigenvalue of $\mathbf{Q}$ parameterized by S_0. $\mathbf{\Lambda}_{max}$ is given by Newton's method with maximum quadrature degree 5810.

Quadrature Degree	$S_0 = 0.1$	$S_0 = 0.6$	$S_0 = 0.97$	$S_0 = 0.995$
14	0.04	1.4	49.6	No Convergence
86	3.2×10^{-9}	1.4×10^{-3}	31.2	No Convergence
590	1.8×10^{-15}	6.8×10^{-14}	7.1×10^{-3}	No Convergence
2030	7.2×10^{-15}	5.1×10^{-14}	5.1×10^{-12}	0.1
3470	2.3×10^{-14}	6.6×10^{-14}	1.9×10^{-12}	3.3×10^{-4}
$\lvert\mathbf{\Lambda}_{max}\rvert$	0.82	5.1	58.3	347

be sufficiently high to even converge. For most of our simulations, $S \lessapprox 0.8$ and so we use a quadrature degree of 590. For cases where S does get relatively large, we use a quadrature degree of 3470.

We next test the efficacy of the self-consistent bulk free energy in simulating spatially nonuniform configurations which are unstable in the Landau-de Gennes theory when f_e is cubic in $\mathbf{Q}$. In the first example, we choose a weakly perturbed configuration away from uniform. We take as initial condition a purely uniaxial configuration where $\mathbf{Q}$ is parameterized as in Eq. (2.3) with $\hat{\mathbf{n}} = (0, 1, 0)$, $S(x) = S_0 + 0.1 \sin \pi k x$, and $P = 0$. This is the configuration of Secs. 2.2 and 2.3 where the energies are plotted in Figs. 2.2 and 2.6. We further set the initial $k = 10$ and $S_0 = 0.6751$ and use elastic constants $L_3 = 3$, and $L_2 = L_4 = 0$. For the gradient flow we use a finite element discretization of space with square domain $[0, 1]^2$, a body centered mesh with 150×150 squares, and a time step $\Delta t = 4 \times 10^{-3}$.

We show in Fig. 2.7 the gradient flow of S during the minimization procedure described in Sec. 2.4 for both the singular bulk free energy and the usual Landau-de Gennes bulk free energy. The configuration iterated with the singular bulk free energy relaxes to a uniform configuration which is the correct behavior, while the configuration iterated with the Landau-de Gennes bulk free energy diverges in just 2 time steps. In the second example, we initialize the system with an adaptation from Ball and Majumdar [36] meant to demonstrate the stability of the singular bulk potential. We consider a cylindrically symmetric $\mathbf{Q} = S(r)(\hat{\mathbf{r}} \otimes \hat{\mathbf{r}} - 1/3\mathbf{I})$ where $\hat{\mathbf{r}}$ indicates the radial unit vector.

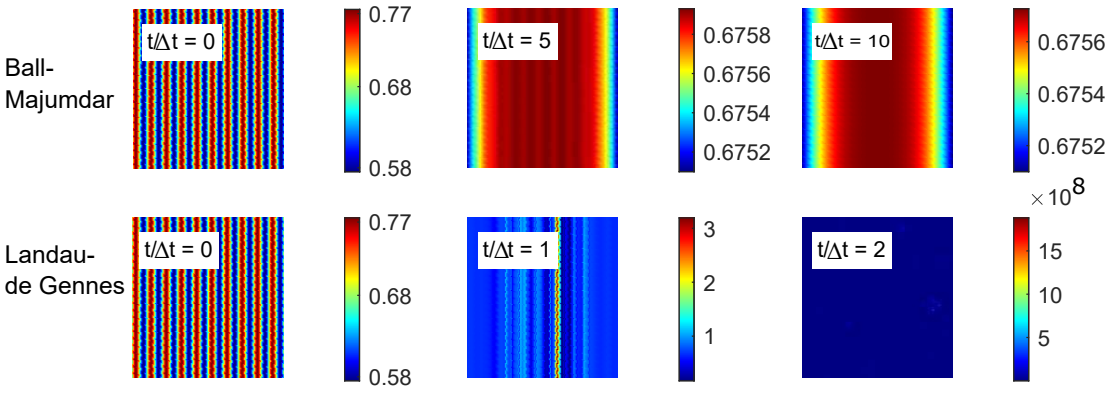

Figure 2.7: Comparison of the evolution of S between the Ball-Majumdar and Landau-de Gennes bulk free energies for a perturbed configuration with initial $S = S_0 + 0.1 \sin 10\pi x$ and elastic constants $L_3 = 3$, $L_2 = L_4 = 0$.

S is given by

$$S(r) = \begin{cases} S_0 \left(2 + \sin \frac{\pi k r}{5}\right) & 0 < r < 5 \\ 2S_0 \left(2 + \sin \pi k\right) \left(1 - \frac{r}{10}\right) & 5 < r < 10 \end{cases} \tag{2.38}$$

with $S_0 = 0.32$ and $k = 5$. We also set $\kappa / n k_B T = 3$ so that the bulk free energy is minimized by an isotropic configuration, so that the system will evolve to $S = 0$. As above, we use a body centered mesh on a square domain $[-10, 10]^2$ and time step $\Delta t = 4 \times 10^{-3}$. Fig. 2.8 shows several time steps in the gradient flow of S iterated with both the singular bulk free energy and the Landau-de Gennes bulk free energy. As in the previous example, the configuration iterated with the Landau-de Gennes bulk free energy diverges quickly while the configuration iterated with the singular bulk free energy evolves to a stable configuration with $S = 0$.

We finally test the feasibility of the computational method to handle systems in three dimensions. We consider three examples of spatially inhomogeneous structures: a hedgehog point defect (Fig. 2.9a), a half integer charge wedge line disclination (Fig. 2.9b), and a Saturn ring loop disclination (Fig. 2.9c). For these calculations we set $\kappa / n k_B T = 4$, $L_3 = 3$, and $L_2 = L_4 = 0$. For the point defect and line disclination we use a cubic domain $[-5, 5]^3$ with a uniform tetrahedral mesh with $41 \times 41 \times 41$ vertices. For the Saturn ring we use a cubic domain $[-30, 30]^3$ with a spherical cavity of radius

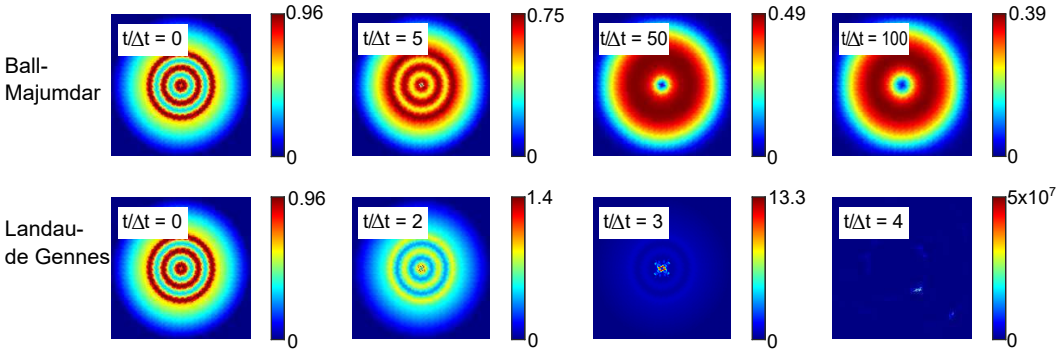

Figure 2.8: Comparison of the evolution of S between the Ball-Majumdar and Landau-de Gennes bulk free energies for the example of Eq. (2.38) adapted from an example from Ball and Majumdar.

7.5 and a body-centered-cubic mesh with 127108 vertices. We also set the time step $\Delta t = 5 \times 10^{-2}$. We iterate to equilibrium configurations when the free energy fails to change to within 10^{-6}. Initial conditions are set as $\mathbf{Q} = S_N(\hat{\mathbf{n}} \otimes \hat{\mathbf{n}} - 1/3\mathbf{I})$ with $\hat{\mathbf{n}}$ reflecting the defected configurations. These are given by

$$\begin{aligned}
\hat{\mathbf{n}}_{\text{Hedgehog}} &= \hat{\mathbf{r}} = (\cos\phi \sin\theta,\, \sin\phi \sin\theta,\, \cos\theta) \\
\hat{\mathbf{n}}_{\text{Disclination}} &= \left(\cos\frac{1}{2}\phi,\, -\sin\frac{1}{2}\phi,\, 0\right) \\
\hat{\mathbf{n}}_{\text{Saturn Ring}} &= \cos\alpha\hat{\boldsymbol{\rho}} + \sin\alpha\hat{\mathbf{z}} \\
\alpha &= \frac{\pi}{2} - \frac{1}{2}\arctan\left(\frac{z}{\rho - R}\right) - \frac{1}{2}\arctan\left(\frac{z}{\rho + R}\right) + \arctan\left(\frac{z}{\rho}\right)
\end{aligned} \tag{2.39}$$

where $\{r, \theta, \phi\}$ are the usual spherical coordinates and $\{\rho, \phi, z\}$ are cylindrical coordinates. On the boundaries, we use Neumann conditions for the point and line defects. For the Saturn ring, we use Dirichlet conditions setting a uniform boundary with $\hat{\mathbf{n}}_{\partial\Omega>} = (0,\, 0,\, 1)$ on the outer boundary and $\hat{\mathbf{n}}_{\partial\Omega<} = \hat{\mathbf{r}}$ on the inner sphere boundary to simulate strong homeotropic anchoring [62, 63].

Figs. 2.9a,b,c show equilibrium configurations for the point defect, line defect, and Saturn ring. The contours indicate surfaces of constant $S = 0.5S_N$ while the color represents the field S with the lines indicating the director $\hat{\mathbf{n}}$. These tests show that although the self-consistent model leads to a more complex numerical implementation

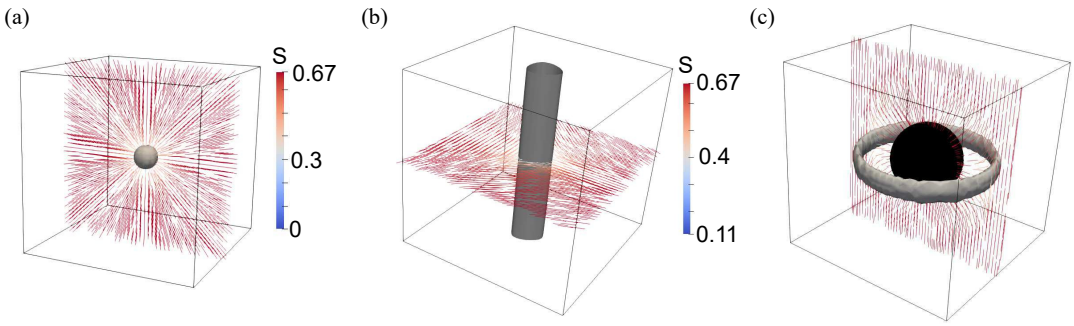

Figure 2.9: Examples of numerically computed equilibrium defect structures in three dimensional liquid crystals with $L_3 = 3$ using the singular bulk free energy and the computational method laid out in Sec. 2.4. The examples shown are (a) a hedgehog point defect, (b) a wedge line disclination, and (c) a Saturn ring loop disclination. Contours indicate surfaces of $S = 0.5S_N$, colors indicate S, and lines indicate the director orientation.

than the Landau-de Gennes free energy, we are able to obtain equilibrium configurations for complex heterogeneous configurations in nematics. Additionally, we are able to simulate configurations with large gradients in the order parameter even though the elastic energy is cubic in $\mathbf{Q}$ with large L_3. We note that the fine structure of topological defects, particularly line and loop disclinations, will be the focus of study in later chapters.

2.6 Elastic Energies

As previously mentioned, the functional form of the elastic energy that will be considered in this dissertation is given by Eq. (2.7) in terms of $\mathbf{Q}$ or Eq. (2.28) in terms of the degrees of freedom q_i. Here we discuss an analytic description of the various terms in the elastic energy that gives some intuition for their effect on heterogeneous systems in which the eigenvalues of $\mathbf{Q}$ change on mesoscopic scales (for example, two phase domains and topological defects).

Assume a uniaxial configuration $\mathbf{Q}(\mathbf{r}) = S(\mathbf{r})\left(\hat{\mathbf{n}}(\mathbf{r}) \otimes \hat{\mathbf{n}}(\mathbf{r}) - 1/3\mathbf{I}\right)$ with $P = 0$. Then quadratic combinations of $\nabla\mathbf{Q}$, which make up the elastic energy, can be organized in three categories: contributions to "surface tension" which are proportional to

Table 2.2: Categorization of contributions to surface tension, surface anchoring, and bulk elasticity of allowable terms in the Landau-de Gennes elastic energy up to cubic order in $\mathbf{Q}$.

Term	Surface Tension	Surface Anchoring	Bulk Elasticity
$L_1\partial_k Q_{ij}\partial_k Q_{ij}$	$\frac{2}{3}\lvert\nabla S\rvert^2$	0	$2S^2\left[(\nabla\cdot\hat{\mathbf{n}})^2+\lvert\hat{\mathbf{n}}\cdot(\nabla\times\hat{\mathbf{n}})\rvert^2 +\lvert(\hat{\mathbf{n}}\cdot\nabla)\hat{\mathbf{n}}\rvert^2\right]$
$L_2\partial_j Q_{ij}\partial_k Q_{ik}$	$\frac{1}{9}\lvert\nabla S\rvert^2$	$\frac{1}{3}(\hat{\mathbf{n}}\cdot\nabla S)^2$ $-\frac{2}{3}S\left[(\hat{\mathbf{n}}\cdot\nabla S)(\nabla\cdot\hat{\mathbf{n}})+(\hat{\mathbf{n}}\cdot\nabla)\hat{\mathbf{n}}\cdot\nabla S\right]$	$S^2\left[(\nabla\cdot\hat{\mathbf{n}})^2+\lvert(\hat{\mathbf{n}}\cdot\nabla)\hat{\mathbf{n}}\rvert^2\right]$
$L_3 Q_{k\ell}\partial_k Q_{ij}\partial_\ell Q_{ij}$	$-\frac{2}{9}S\lvert\nabla S\rvert^2$	$\frac{2}{3}S(\hat{\mathbf{n}}\cdot\nabla S)^2$	$\frac{2}{3}S^3\left[-(\nabla\cdot\hat{\mathbf{n}})^2-\lvert\hat{\mathbf{n}}\cdot(\nabla\times\hat{\mathbf{n}})\rvert^2 +2\lvert(\hat{\mathbf{n}}\cdot\nabla)\hat{\mathbf{n}}\rvert^2\right]$
$L_4 Q_{k\ell}\partial_i Q_{k\ell}\partial_j Q_{ij}$	$-\frac{2}{9}S\lvert\nabla S\rvert^2$	$\frac{2}{3}S(\hat{\mathbf{n}}\cdot\nabla S)^2$ $+\frac{2}{3}S^2\left[(\hat{\mathbf{n}}\cdot\nabla S)(\nabla\cdot\hat{\mathbf{n}})+(\hat{\mathbf{n}}\cdot\nabla)\hat{\mathbf{n}}\cdot\nabla S\right]$	0
$L_5 Q_{k\ell}\partial_\ell Q_{ki}\partial_j Q_{ij}$	$-\frac{1}{27}S\lvert\nabla S\rvert^2$	$\frac{1}{3}S(\hat{\mathbf{n}}\cdot\nabla S)^2$ $+\frac{1}{9}S^2\left[2(\hat{\mathbf{n}}\cdot\nabla S)(\nabla\cdot\hat{\mathbf{n}})-(\hat{\mathbf{n}}\cdot\nabla)\hat{\mathbf{n}}\cdot\nabla S\right]$	$\frac{1}{3}S^3\left[-(\nabla\cdot\hat{\mathbf{n}})^2+2\lvert(\hat{\mathbf{n}}\cdot\nabla)\hat{\mathbf{n}}\rvert^2\right]$
$L_6 Q_{k\ell}\partial_i Q_{ki}\partial_j Q_{\ell j}$	$-\frac{1}{27}S\lvert\nabla S\rvert^2$	$\frac{1}{3}S(\hat{\mathbf{n}}\cdot\nabla S)^2$ $+\frac{2}{9}S^2\left[4(\hat{\mathbf{n}}\cdot\nabla S)(\nabla\cdot\hat{\mathbf{n}})+(\hat{\mathbf{n}}\cdot\nabla)\hat{\mathbf{n}}\cdot\nabla S\right]$	$\frac{1}{3}S^3\left[2(\nabla\cdot\hat{\mathbf{n}})^2-\lvert(\hat{\mathbf{n}}\cdot\nabla)\hat{\mathbf{n}}\rvert^2\right]$
$L_7 Q_{k\ell}\partial_j Q_{ki}\partial_i Q_{\ell j}$	$-\frac{1}{27}S\lvert\nabla S\rvert^2$	$\frac{1}{3}S(\hat{\mathbf{n}}\cdot\nabla S)^2$ $+\frac{2}{9}S^2\left[(\hat{\mathbf{n}}\cdot\nabla S)(\nabla\cdot\hat{\mathbf{n}})+4(\hat{\mathbf{n}}\cdot\nabla)\hat{\mathbf{n}}\cdot\nabla S\right]$	$\frac{1}{3}S^3\left[2(\nabla\cdot\hat{\mathbf{n}})^2-\lvert(\hat{\mathbf{n}}\cdot\nabla)\hat{\mathbf{n}}\rvert^2\right]$
$L_8 Q_{k\ell}\partial_j Q_{ki}\partial_\ell Q_{ij}$	$-\frac{1}{27}S\lvert\nabla S\rvert^2$	$\frac{1}{3}S(\hat{\mathbf{n}}\cdot\nabla S)^2$ $+\frac{1}{9}S^2\left[-(\hat{\mathbf{n}}\cdot\nabla S)(\nabla\cdot\hat{\mathbf{n}})+2(\hat{\mathbf{n}}\cdot\nabla)\hat{\mathbf{n}}\cdot\nabla S\right]$	$\frac{1}{3}S^3\left[-(\nabla\cdot\hat{\mathbf{n}})^2+2\lvert(\hat{\mathbf{n}}\cdot\nabla)\hat{\mathbf{n}}\rvert^2\right]$

$|\nabla S|^2$; contributions to "surface anchoring" which involve terms related to the relative orientation of the director with gradients of S, for example $(\hat{\mathbf{n}}\cdot\nabla S)^2$; and contributions to "bulk elasticity" or "Frank-Oseen elasticity" which involve only gradients of the director and can be mapped to the Frank-Oseen elastic free energy in terms of splay, twist, and bend. These categorizations aid in the understanding of how various elastic constants affect the morphology and geometry of various configurations. We note that the terms "surface tension" and "surface anchoring" are usually reserved for their own definitions in the free energy (see f_∂ in Eq. (2.1)); however, here we regard gradients in S as "surfaces" in the sense that they will typically separate domains, either between phases (isotropic-nematic) or director orientation at the singular points of topological defects.

Table 2.6 shows this decomposition for all 8 elastic terms that are of quadratic and cubic order in $\mathbf{Q}$. Note that the terms cubic in $\mathbf{Q}$ all have a negative contribution to surface tension, which is another way to understand the instability described in Sec. 2.2. Additionally, from the contributions to bulk elasticity, it is immediately apparent that only taking L_1, L_2, $L_3 \neq 0$ the elastic energy can be mapped to the Frank-Oseen free energy and gives the relations in Eq. (2.8). For two dimensional systems, the subjects of Chaps. 3 and 4, the twist term will be zero since the director remains in plane. Thus,

for these systems, the measure of elastic anisotropy we use is

$$\varepsilon = \frac{K_{33} - K_{11}}{K_{33} + K_{11}} = \frac{3L_3 S}{6 + 3L_2 + L_3 S}. \tag{2.40}$$

$\varepsilon \in [-1, 1]$ and the limits $\varepsilon = 1, -1$ correspond to $K_{11} = 0$, $K_{33} = 0$, that is, bend or splay dominated anisotropy.

We finally note that the L_4 term in Table 2.6 has no contribution to bulk elasticity. Additionally, its contributions to surface tension and to surface anchoring are similar to that of the L_3 term. Thus it is a useful control term when studying separately the effects of bulk elastic anisotropy and surface anchoring on the morphology of nematic configurations.

2.7 Conclusion

Here we have described the primary model and computational method that will be used to simulate nematic configurations for the remainder of the dissertation. We have further developed the theory of Ball and Majumdar to be understood as a self-consistent field theory. This theory can be used to overcome known limitations of the Landau-de Gennes theory for elastically anisotropic nematics. Additionally, we presented numerical tests of the computational model which demonstrated the convergence of the method in cases where the Landau-de Gennes theory fails, as well as three dimensional configurations that attest to the viability of the method. Finally, we detailed an analytical decomposition of the elastic energy used to study nematic configurations in future chapters.

2.8 Appendix: Onsager Potential

Here we briefly demonstrate the possibility of using a different Hamiltonian in the bulk free energy while using the same method to constrain the values of $\mathbf{Q}$. Instead of the adapted Maier-Saupe potential used in the Ball-Majumdar free energy, one may choose

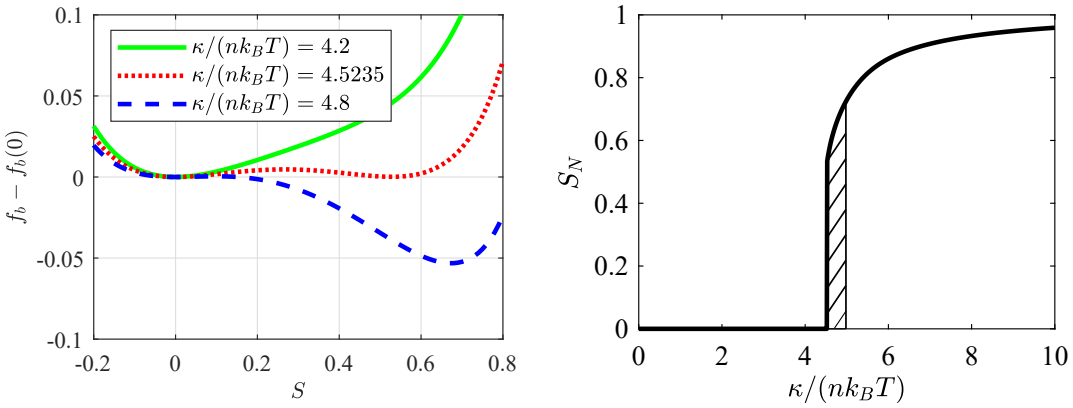

Figure 2.10: (left) Bulk free energy density $f_b - f_b(0)$ as a function of scalar order parameter S for the free energy computed with the Onsager potential. The free energy densities for $\kappa/(nk_BT) = 4.2$, $\kappa/(nk_BT) = 4.5235$, and $\kappa/(nk_BT) = 4.8$ are plotted. (right) Phase behavior for the Onsager potential. At $\kappa/(nk_BT) = 4.5235$ a first order phase transition occurs with $\Delta S_N = 0.529$. The shaded region shows the region of isotropic-nematic local stability.

an adapted Onsager potential [1, 33] with interaction kernel

$$K(\mathbf{r}_1, \mathbf{r}_2) = \kappa\delta(\mathbf{r}_1 - \mathbf{r}_2) \int_{S^2}\int_{S^2} \sqrt{1 - (\mathbf{u}_1 \cdot \mathbf{u}_2)^2}\, p^*(\mathbf{u}_1, \mathbf{r}_1) p^*(\mathbf{u}_2, \mathbf{r}_2)\, dS(\mathbf{u}_1) dS(\mathbf{u}_2). \tag{2.41}$$

This kernel cannot be explicitly written in terms of $\mathbf{Q}$ like the Maier-Saupe kernel can. Thus, its functional dependence on $\mathbf{Q}$ comes purely from $\mathbf{\Lambda}(\mathbf{Q})$ in the single particle probability distributions p^*. The Onsager definition of the interaction kernel comes from the excluded volume of two rods with orientations $\mathbf{u}_1$ and $\mathbf{u}_2$ with an aspect ratio such that $L \gg D$ where L is the length of the rod and D is the diameter. The parameter κ is a function of the rod aspect ratio and rod concentration.

Using the Onsager kernel, we may numerically compute the bulk free energy density as a function of S through inversion of the constraint equation, Eq. (2.16). We plot this for $\kappa/(nk_BT) = 4.2$, $\kappa/(nk_BT) = 4.5235$ and $\kappa/(nk_BT) = 4.8$ in Fig. 2.10. The isotropic phase energy is no longer always zero, since the kernel of Eq. (2.41) integrates to be nonzero when $p^* = 1/(4\pi)$. Thus in Fig. 2.10 we have subtracted the free energy at $S = 0$ to better compare the densities. We note that the bulk free energy with the Onsager potential displays the same double well behavior as the Landau-de Gennes

and Ball-Majumdar bulk free energies as the parameter $\kappa/(nk_BT)$ is varied through coexistence (see Fig. 2.3).

Additionally, we numerically determine that if $\kappa/(nk_BT) > 4.4875$ the nematic phase becomes stable, while exact coexistence occurs when $\kappa/(nk_BT) = 4.5235$. The value of the uniaxial order at coexistence is $S_N = 0.529$ and if $\kappa/(nk_BT) > 4.9799$ the isotropic phase is no longer stable. This coexistence region is larger than that for Ball-Majumdar bulk free energy. We remark that these values are different from previously reported values for the Onsager phase transition by de-Gennes [1] who used a variational approach to analytically approximate the properties of the transition. Here, we have used the approach of Sec. 2.3 to numerically compute the free energy.

Finally, we mention that to simulate inhomogeneous configurations with this bulk free energy, one would have to numerically compute the variation of Eq. (2.41) with respect to $\mathbf{Q}$ or $\mathbf{\Lambda}$ for each time step, since it would involve an integral that in general can only be computed numerically. While this is in theory possible, it would require even more computation than is already involved in the method. In this regard, the Maier-Saupe kernel is much more desirable since it can fully be written as a function of $\mathbf{Q}$.

Chapter 3

Equilibrium Structure and Growth of 2D Anisotropic Nematic Domains

3.1 Introduction

The isotropic-nematic phase transition is first order. Thus, for a range of temperatures and molecular concentrations, both phases can coexist, resulting in two-phase domains commonly refered to as "tactoids." Classically studied systems of thermotropic liquid crystals have a very small coexistence region and so, in these systems, tactoids are difficult to study experimentally. Lyotropic liquid crystals, on the other hand, exhibit a much larger coexistence region, and it is in these systems that tactoids have traditionally been observed and studied [64, 65]. Recent experiments [10, 11, 15] have shown anisotropic morphologies in both domains of isotropic phase surrounded by nematic phase ("negative" tactoids) and domains of nematic phase surrounded by isotropic phase ("positive" tactoids). The latter has been the subject of many theoretical and computational studies [28, 66–72] because of the distinct, anisotropic, spindle shaped structures. The anisotropy of the liquid crystal material, in terms of its surface tension, surface anchoring, and bulk elasticity, clearly plays a role in the overall morphology of these structures. Understanding the effects of these material parameters is paramount to

predicting the structure of engineered and biological materials in which the underlying complexity leads to anisotropic energies [6, 73–80].

Much of the modeling of positive tactoids has been through the use of the nematic director representation, $\hat{\mathbf{n}}$, because of the simplicity of the method. Often, the shape of the tactoid is assumed and held fixed and the director is frozen in various configurations while the energies of each configuration are compared [66–68]. Computational results can clarify the equilibrium structure of $\hat{\mathbf{n}}$ if the tactoid shape remains fixed [70, 72]. Methods that allow for the boundary to change, so as to allow the system to relax to a true equilibrium shape, are just starting to surface [81]. However, the isotropic matrix surrounding the nematic phase cannot be modeled by just $\hat{\mathbf{n}}$. The interface is therefore treated instead as a boundary of the domain, rather than a diffuse interface as seen in experiments.

Here, we model tactoids with the nematic tensor order parameter $\mathbf{Q}$. Because the eigenvalues of $\mathbf{Q}$ represent the degree of ordering, the diffuse interface can be fully resolved, and both phases can be simultaneously studied. In principle, the system can be allowed to relax to its equilibrium configuration, without the need for computationally complex boundary methods. Of course, the challenges of working with $\mathbf{Q}$ are that one needs to solve tensor valued equations. Additionally, lyotropic liquid crystals are naturally more anisotropically elastic than their thermotropic counterparts, and hence one encounters issues with the unboundedness of the Landau-de Gennes free energy when studying elastic anisotropy with the tensor $\mathbf{Q}$. Thus, to this point, studies using either the director, $\hat{\mathbf{n}}$ or $\mathbf{Q}$ have been inadequate to describe experimental systems.

In order to study the full effects of anisotropy, the model of Chapter 2 must be used. Additionally, the excess energy of the diffuse interface turns out to lead to the shrinking of tactoids in order to minimize this excess energy. This leads to tactoids that are smaller than those seen in experiment, and thus either an additional free energy stabilizing the domain must be added or a constraint must be placed on the system to conserve the volume of the nematic phase. Here we implement the latter approach by introducing a volume constraint and describing the mathematical and computational details associated with it. We study the properties of the diffuse interface as a function of anisotropic surface anchoring. We then computationally study the equilibrium morphologies of both negative and positive tactoids, varying both the surface anchoring and

bulk elasticity, to find shapes qualitatively similar to recent experiments. We end the chapter by examining the effect of the cubic order elastic constants from Eq. (2.7) on the growth of tactoids during a simulated quench to the nematic phase. We find that the resulting morphologies are highly sensitive to the elastic terms used.

3.2 Volume Constraint

We will study interface and tactoid morphology by solving Eqs. (2.29) for various values of L_3 and L_4 in Eq. (2.7). Before applying the model of Chapter 2 to these configurations we must first modify the theory to fix the volume of nematic phase in the system. The tactoid volume is an important variable in the determination of its equilibrium morphology. This is a simple matter in studies in which its boundary is given and fixed. However, since the interface in a **Q**-tensor description occurs naturally and **Q** is not a conserved order parameter, it is not possible to constrain the size of the tactoids directly. One possible solution is to couple a conserved phase field to the nematic and isotropic phases that varies from one phase to the other [82, 83]. This method does not appear to add any physical understanding and seems to the author too computationally cumbersome for the present study. Instead, we simply constrain the volume with a Lagrange multiplier in the free energy.

We first note that the matrix

$$\mathbf{A} = \frac{3}{S_N}\begin{pmatrix} 1 & 0 & 0 \\ 0 & 1 & 0 \\ 0 & 0 & 0 \end{pmatrix}, \tag{3.1}$$

where S_N is the equilibrium value of S, has the property that $\mathrm{Tr}\,[\mathbf{AQ}] = (S+3P)/S_N$ if we work in the eigenbasis of **Q** so that **Q** is diagonalized. This means that $\mathrm{Tr}\,[\mathbf{AQ}] = 1$ if the system is in the uniaxial nematic phase (i.e. $P = 0$ in Eq. (2.3)) and $\mathrm{Tr}\,[\mathbf{AQ}] = 0$ if the system is in the isotropic phase. Additionally, if we restrict our attention to systems that vary only in one or two spatial dimensions, which is motivated by configurations in thin films in experiments [10, 15], the director can be written as $\hat{\mathbf{n}} = (\cos\phi,\, \sin\phi,\, 0)$ where ϕ is the angle the director makes with the x-axis. We see, then, that the form of

$\mathbf{A}$ is the same if we change from the $\mathbf{Q}$ eigenbasis to the fixed lab frame:

$$\begin{gathered}\mathbf{R}\mathbf{A}\mathbf{R}^T = \mathbf{A} \\ \mathbf{R} = \begin{pmatrix} \cos\phi & -\sin\phi & 0 \\ \sin\phi & \cos\phi & 0 \\ 0 & 0 & 1 \end{pmatrix}.\end{gathered} \tag{3.2}$$

Thus, we may also write $\mathrm{Tr}\left[\mathbf{AQ}\right] = (\sqrt{3}q_1 + 3q_2)/S_N$ in terms of the degrees of freedom of $\mathbf{Q}$ defined in Eq. (2.23). We then obtain a proxy for the volume (area) of the nematic phase:

$$V_N = \frac{1}{S_N}\int_\Omega \left(\sqrt{3}q_1 + 3q_2\right)\, d\mathbf{r} \tag{3.3}$$

where Ω is the system domain.

Eq. (3.3) serves as a constraint on the tactoid volume and can be implemented with Lagrange multiplier μ. We define a new free energy $F^* = F - \mu\left(\int_\Omega \mathrm{Tr}\left[\mathbf{AQ}\right]\, d\mathbf{r} - V_N\right)$ so the gradient flow equations are

$$\frac{\partial q_i}{\partial t} = -\frac{\delta F}{\delta q_i} + \mu\frac{\partial \mathrm{Tr}\left[\mathbf{AQ}\right]}{\partial q_i}. \tag{3.4}$$

μ can be calculated at each discrete time step in the evolution in a similar fashion to Ref. [84] by taking a time derivative of the constraint equation, Eq. (3.3). This leads to

$$\begin{aligned} 0 &= \int_\Omega \left(\sqrt{3}\frac{\partial q_1}{\partial t} + 3\frac{\partial q_2}{\partial t}\right)\, d\mathbf{r} \\ &= \int_\Omega \left[\sqrt{3}\left(-\frac{\delta F}{\delta q_1} + \frac{\sqrt{3}}{S_N}\mu\right) + 3\left(-\frac{\delta F}{\delta q_2} + \frac{3}{S_N}\mu\right)\right]\, d\mathbf{r} \\ \Rightarrow \mu &= \frac{S_N}{12V_\Omega}\int_\Omega \left(\sqrt{3}\frac{\delta F}{\delta q_1} + 3\frac{\delta F}{\delta q_2}\right)\, d\mathbf{r} \end{aligned} \tag{3.5}$$

where V_Ω is the volume (area) of the system domain. We note that even though μ is recalculated at every time step, it converges to be approximately constant in only a few iterations.

As we show below, using this volume constraint we are able to fix the volume of both negative and positive tactoids. This is necessary to stabilize the positive tactoids

because even if the temperature is set to be exactly at coexistence between the phases, the positive tactoids tend to shrink due to the excess energy of the interface. Physically, the Lagrange multiplier μ may be thought of as a pressure or chemical potential for the nematic phase, that is set based on the tactoid volume.

We finally note that the volume constraint method is relatively simple for systems varying in one or two dimensions since the director can be fixed in the xy plane and $\mathbf{A}$ does not change form from the eigenbasis to the lab frame where the gradient flow is computed. In three dimensions, where the director now must be described by two angles, the change of base matrix is

$$\mathbf{R} = \begin{pmatrix} \cos\phi\sin\theta & -\sin\phi & \cos\phi\cos\theta \\ \sin\phi\sin\theta & \cos\phi & \sin\phi\cos\theta \\ \cos\theta & 0 & -\sin\theta \end{pmatrix} \tag{3.6}$$

and $\mathbf{RAR}^T \neq \mathbf{A}$. The corresponding nematic volume definition, akin to Eq. (3.3), is then a function of the angles θ and ϕ that define the director as well as the degrees of freedom of $\mathbf{Q}$. We therefore only consider cases in one or two spatial dimensions to avoid this complication.

3.3 Interfaces

We first consider isotropic-nematic interfaces in one spatial dimension. A primary goal is to study the dependence of interface width and energy on the elastic coefficient L_4, defined in Eq. (2.7). The one dimensional interface provides a useful case to test whether we can reasonably decompose the elastic terms as in Table 2.6, where the L_4 term should contribute to the surface anchoring and promote tangential alignment of the director with the interface.

To simulate the interface we use the computational method of Chapter 2 on a one dimensional domain with 1000 finite elements. We set $\Delta t = 0.1$ and $\kappa/nk_BT = 3.4049$ which is the value for exact coexistence between nematic and isotropic phases. Dirichlet conditions fix the left boundary to a nematic phase with $S_N = 0.4281$, the equilibrium value of S at this point of the phase diagram (see Fig. 2.4). We also fix the director to

tilt at angle ϕ_0 with respect to the interface normal so that $\phi_0 = 0$ corresponds to perpendicular (homeotropic) anchoring while $\phi_0 = \pi/2$ corresponds to parallel anchoring. The right boundary is fixed to the isotropic phase $\mathbf{Q} = \mathbf{0}$ so both domains far from the interface are thermodynamically stable. The gradient flow equations are iterated until the energy fails to change to within 10^{-6}. We solve for a range of 11 values of ϕ_0 equally spaced from $0 \leq \phi_0 \leq \pi/2$ and we vary the parameter L_4 from $L_4 = 0$ up to $L_4 = 4$.

Fig. 3.1 shows the results of the simulations. Fig. 3.1a shows S as a function of position for interfaces with various ϕ_0 and $L_4 = 4$. As the anchoring becomes more parallel, the interface becomes asymmetric about $x = 0$ and the width decreases. We expect the width of the interface to be proportional to the excess surface energy, since smaller gradients (larger widths) will cost less energy. Thus the width becoming smaller is understood as the effect of $L_4 \neq 0$, which favors parallel anchoring. We quantify the widths by defining the points x_1 and x_2 where $S = 0.9S_N$ and $S = 0.1S_N$ respectively, then define the width $W = x_2 - x_1$. Fig. 3.1b shows the width of the interface as a function of ϕ_0, normalized to the width at $\phi_0 = \pi/2$, for various values of L_4. If $L_4 = 0$ the width does not depend on ϕ_0. The normalized widths are displayed since the L_4 term also contributes to the overall surface tension (see Table 2.6), which also changes the width of the interface. Hence the normalization isolates the effect of surface anchoring.

Our hypothesis that the elastic terms can be decomposed into contributions to surface tension, surface anchoring, and bulk elasticity is tested in Fig. 3.1c. There we show the width difference $\Delta W = W(\phi_0 = 0) - W(\phi_0 = \pi/2)$ as a function of L_4. Since we expect the widths to be proportional to the excess energy of the interface, this indicates that as L_4 increases, the anchoring energy indeed increases proportionally. Hence the proposed decomposition in Sec. 2.6 is validated.

In Fig. 3.1d we examine the biaxiality at the interface for large anchoring. The appearance of biaxiality for elastically anisotropic nematics has been shown in previous computational studies of the interface [30], albeit using a Landau-de Gennes free energy. Along with S, we plot the biaxiality parameter

$$\beta^2 = 1 - 6\frac{\mathrm{Tr}\left[\mathbf{Q}^3\right]^2}{\mathrm{Tr}\left[\mathbf{Q}^2\right]^3} \tag{3.7}$$

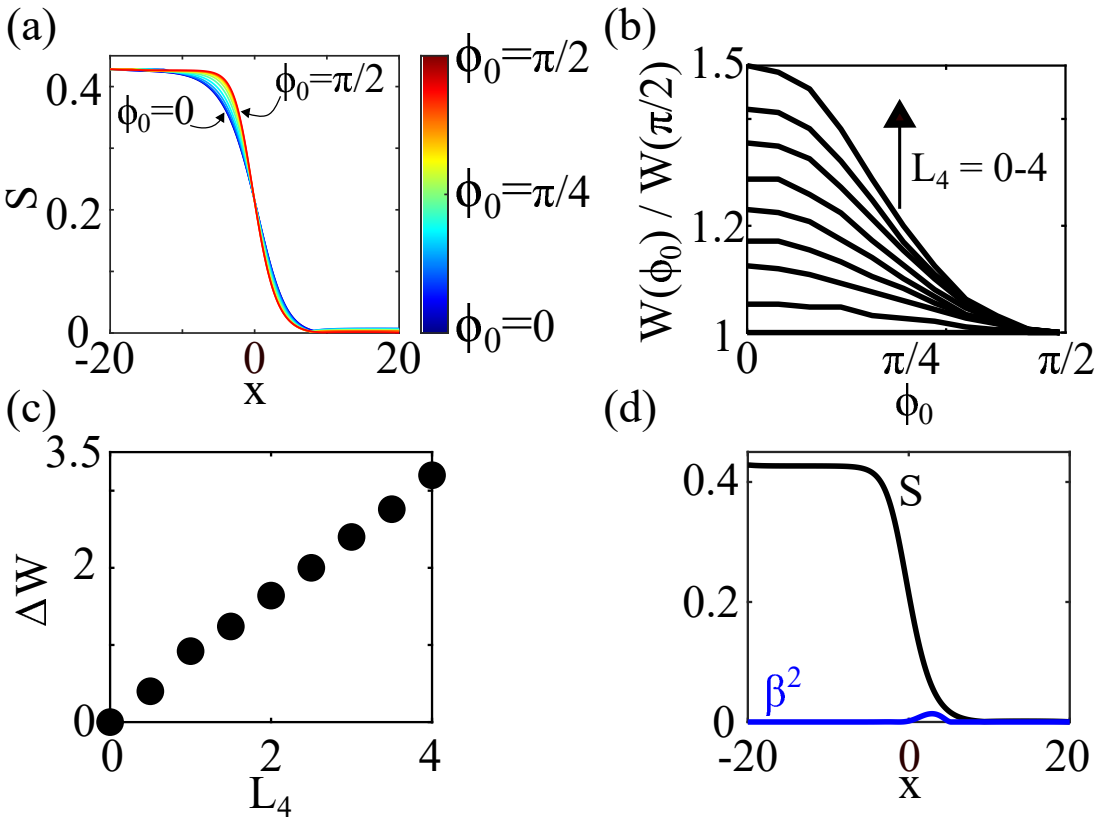

Figure 3.1: Numerical solution for a one-dimensional interface with varying anchoring angle ϕ_0 and elastic constant L_4. (a) Plots of scalar order parameter S versus position for $L_4 = 4$ and varying ϕ_0. As the anchoring goes from homeotropic to parallel the width of the interface gets smaller. (b) Interface width as a function of ϕ_0, normalized by its value at $\phi_0 = \pi/2$ for $L_4 \in [0, 4]$ (c) Width difference $\Delta W = W(\phi_0 = 0) - W(\phi_0 = \pi/2)$ as a function of L_4. (d) Nematic order S and biaxiality parameter β^2, defined in Eq. (3.7), across the interface for $\phi_0 = \pi/2$ and $L_4 = 4$.

for an interface with $L_4 = 4$ and $\phi_0 = \pi/2$. This parameter is a useful measure of biaxiality since it is unity when the order parameter is fully biaxial and zero when the order parameter is uniaxial or isotropic. $\beta^2 = 0$ for homeotropic anchoring as required by symmetry, however for parallel anchoring we see small amounts of biaxiality on the isotropic side of the interface. This is likely the cause of the asymmetric interface as the anchoring becomes parallel. We note that since our Hamiltonian promotes uniaxial alignment, Eq. (2.18), the appearance of biaxiality is purely entropic. We will return to the topic of biaxiality in Chapter 4 where we study the structure of disclination cores.

3.4 Negative Tactoids

We now focus on configurations where the order parameter is allowed to vary in two spatial dimensions, i.e. $\mathbf{Q} = \mathbf{Q}(x, y)$. This is motivated by experiments in thin films between treated glass plates [10, 15]. Here, we computationally study negative tactoids (isotropic domains surrounded by a nematic matrix).

In experiments, negative tactoids appear when a nematic phase is heated to coexistence. Typically, topological defects melt and produce domains of isotropic phase surrounded by a nematic matrix. As such, we consider tactoids that have director winding number $\pm 1/2$. Although other winding numbers are seen in experiment, these are the most likely since $\pm 1/2$ defects are the stable defects in the nematic phase. Recent experiments on lyotropic chromonic liquid crystals have reported pronounced cusps occurring where the director is homeotropic at the interface [10, 15]. These cusps are morphological manifestations of topological defects at the interface, known as "boojums," which nucleate due to the surface energy which promotes tangential director anchoring. The charge, or circulation, of these defects is related to the cusp angle τ_N:

$$m = \pm\frac{1}{2} - \frac{1}{2} + \frac{\tau_N}{2\pi}. \tag{3.8}$$

Thus, boojums are a result of frustration between a domain that energetically prefers tangential anchoring but must have points of homeotropic anchoring due to the topology of the surrounding nematic. Here we are concerned with understanding how anisotropic elasticity and surface anchoring affect the morphology of the boojums.

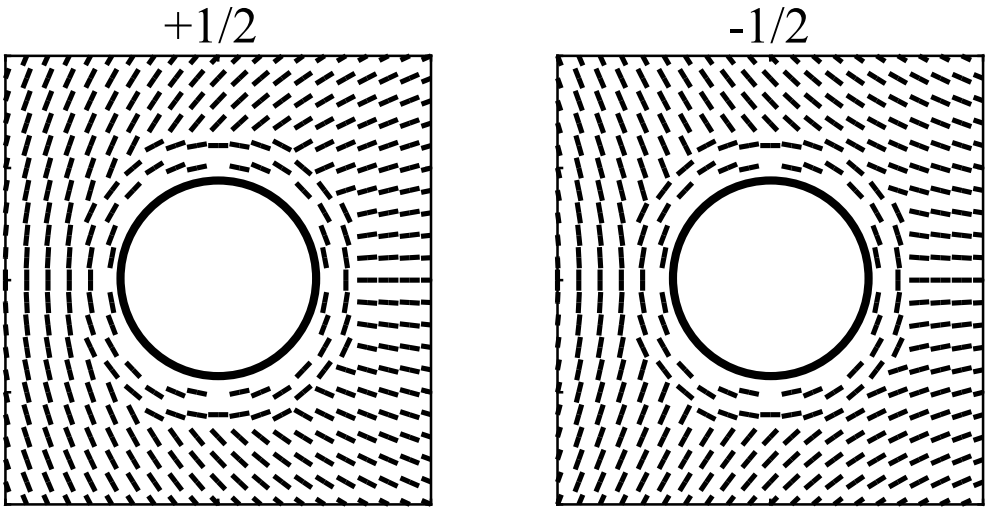

Figure 3.2: Initial condition for the director configuration for simulations of negative tactoids of $\pm 1/2$ topological charge with fixed volume. This initial condition promotes the formation of surface boojums.

Because we are considering tactoids with overall topological charge, the volume constraint of Sec. 3.2 is not strictly needed. However, we do fix the volume to roughly match the experimental value of the ratio of interface width to tactoid radius. Additionally, the surface boojums will not spontaneously nucleate in the simulation because of the energy cost of nucleation and the nature of the mean-field calculation. Therefore, to study them we use an initial condition with director fields shown in Fig. 3.2. This initial condition creates defects outside the tactoid, which eventually coalesce and form boojums on the surface.

Our numerical solution is obtained in a 150×150 body-centered square mesh with $\Delta t = 0.1$. We iterate until the energy fails to change to within 10^{-6}. As with the interface, the parameter $\kappa/nk_BT = 3.4049$. We use Neumann boundary conditions on the outer boundary and fix the tactoid volume to $40^2\pi$. For our computations, we vary both L_3 and L_4. From Eq. (2.40), the elastic anisotropy parameter ε is controlled via L_3 while both L_3 and L_4 contribute to surface anchoring (Table 2.6). For the simulations of negative tactoids, we fix $L_3 + L_4 = 5$ for strong surface anchoring, while varying L_3 to obtain the desired value of ε.

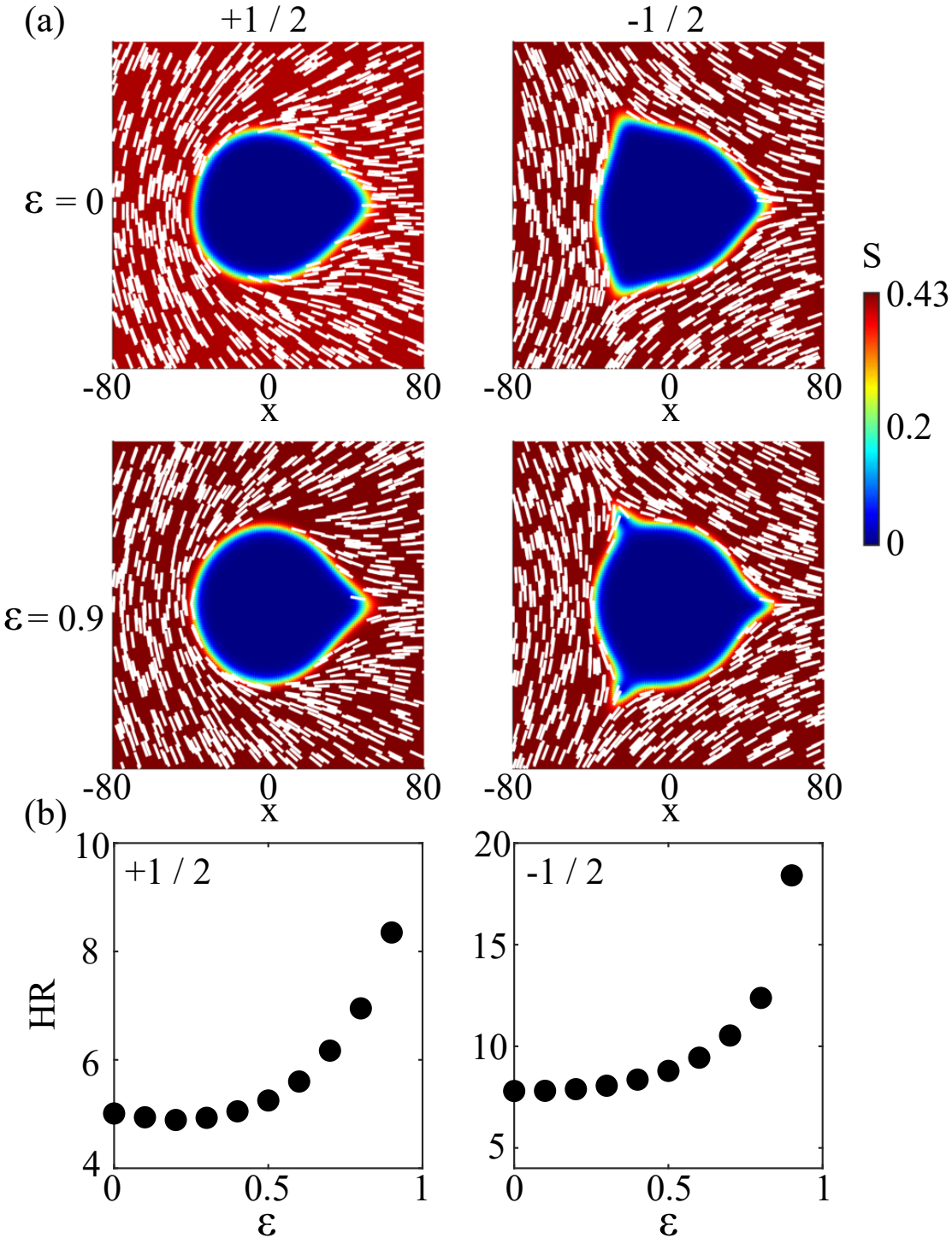

Figure 3.3: Simulated equilibrium morphology of negative tactoids with varying bulk elastic anisotropy. (a) Scalar order parameter S and director structure for example tactoids with topological character $+1/2$ (left) and $-1/2$ (right). The examples include the cases of no elastic anisotropy $\varepsilon = 0$ and large elastic anisotropy $\varepsilon = 0.9$. (b) Boojum curvature, H times average radius R as a function of elastic anisotropy ε.

Fig. 3.3 shows simulation results for $\pm 1/2$ negative tactoid equilibrium configurations. Fig. 3.3a displays S and the director profile for no elastic anisotropy $\varepsilon = 0$ and large elastic anisotropy $\varepsilon = 0.9$. Qualitatively, the cusps created by the boojums become sharper as anisotropy is increased, with the large anisotropy plots similar to those seen in the experiments of Ref. [15].

To quantify cusp sharpening, we plot in Fig. 3.3b the cusp curvature multiplied by average tactoid radius, HR, versus elastic anisotropy ε. Boojum curvature is computed by fitting a parabola to the points on the interface close to the boojum and then extracting the curvature of the fitted parabola. For $\varepsilon > 0.5$, the curvature rapidly increases. Thus we infer that the appearance of sharp cusps in tactoids is linked to the elastic anisotropy of the material. This can be understood as a balance between surface anchoring and bulk elasticity. If the splay constant is reduced ($\varepsilon > 0$) the tactoid may incur more splay distortion to maintain its tangential anchoring closer to the boojum, resulting in a sharper configuration.

3.5 Positive Tactoids

As mentioned in Sec. 3.1, positive tactoids have been more heavily studied than negative tactoids, both theoretically and experimentally. However, there are still only a handful of two-phase, continuum computational studies [28, 30, 85]. Here we apply our computational model as well as the volume constraint introduced in Sec. 3.2 to study the effect of elastic anisotropy and surface anchoring on equilibrium morphology and director fields of positive tactoids. We analyze the configurations in terms of parameters historically common to the study of tactoids [66–68].

We consider positive tactoids of spindle-like shape where the boundary is given by two arcs of a circle, giving rise to a long axis, R and short axis r. This is typically the assumed shape in other numerical studies and is seen in tactoids in experiments [10, 11, 66, 67, 72]. Additionally, we consider director fields that range continuously from uniform, where $\hat{\mathbf{n}}$ is a constant, to bipolar, where the director field is perfectly tangential to the interface and is characterized by defects at the ends of the domain. Configurations between the uniform and bipolar limits can be described by the location of "virtual" defects given by extending the director into the isotropic phase a distance R^* from the

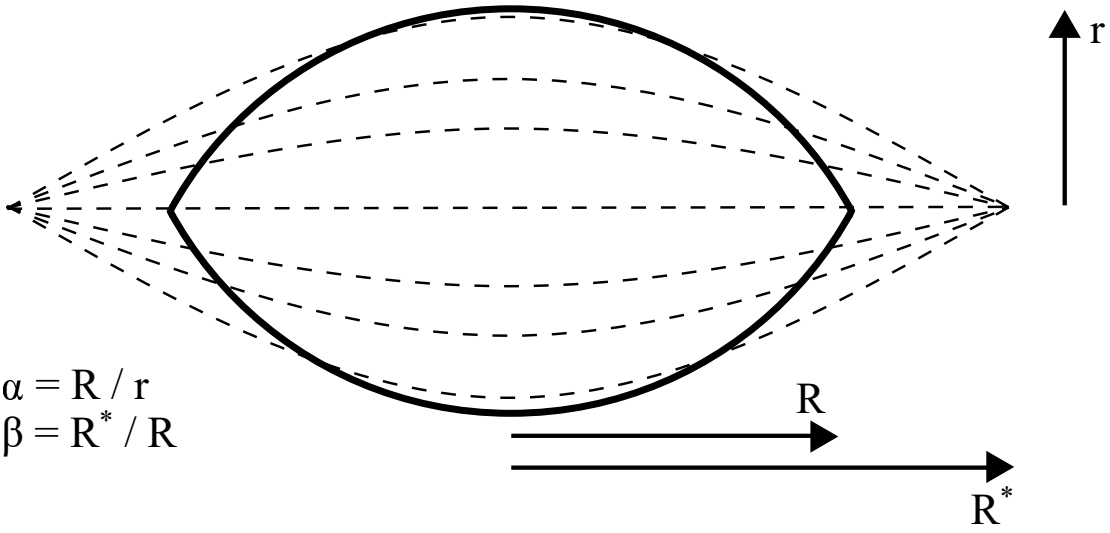

Figure 3.4: Sketch of the morphology and director structure of a positive tactoid. Solid lines represent the interface while dashed lines represent the director field which converges on virtual defects located outside the domain.

center of the tactoid. Hence, there are two dimensionless parameters that describe the shape and director fields

$$\begin{aligned} \alpha &\equiv \frac{R}{r} \\ \beta &\equiv \frac{R^*}{R} \end{aligned} \tag{3.9}$$

where $\alpha = 1$ represents a circular domain and $\beta \in [1, \infty)$, ranges from bipolar to homogeneous. A sketch of a tactoid with these parameters is shown in Fig. 3.4.

To investigate the effect of anisotropic elasticity and surface anchoring on these parameters, we numerically relax, in a similar manner as laid out in Sec. 3.4, from initial configurations given by these parameters for various $L_3 + L_4$ which controls the surface anchoring, and ε which controls the elastic anisotropy. Given α and β and the

Table 3.1: Parameters $\{\alpha, \beta\}$ of the minimum energy positive tactoid with anchoring strength measured by $L_3 + L_4$ and elastic anisotropy ε

$L_3 + L_4$	$\varepsilon = 0$	$\varepsilon = 0.2$	$\varepsilon = 0.4$	$\varepsilon = 0.6$	$\varepsilon = 0.8$
0	$\{1, \infty\}$	$\{1, \infty\}$	$\{1, \infty\}$	$\{1, \infty\}$	$\{1, \infty\}$
1	$\{1.2, 2\}$	$\{1.2, 2\}$	$\{1.2, 2\}$	$\{1.2, 1.5\}$	$\{1.2, 1.5\}$
2	$\{1.2, 1.5\}$	$\{1.2, 1.5\}$	$\{1.2, 1.5\}$	$\{1.2, 1.5\}$	$\{1.2, 1.5\}$
3	$\{1.4, 1.5\}$	$\{1.4, 1.2\}$	$\{1.4, 1.2\}$	$\{1.4, 1.2\}$	$\{1.4, 1.2\}$
4	$\{1.6, 1.2\}$	$\{1.6, 1.2\}$	$\{1.6, 1.1\}$	$\{1.6, 1.1\}$	$\{1.6, 1.1\}$
5	$\{1.6, 1.2\}$	$\{1.6, 1.2\}$	$\{1.8, 1.1\}$	$\{1.8, 1.1\}$	$\{1.8, 1.05\}$

nematic volume V_N, we can compute

$$\begin{aligned} r &= \sqrt{\frac{V_N}{\frac{(\alpha^2+1)^2}{2}\arctan\left(\frac{2\alpha}{\alpha^2-1}\right) - \alpha\left(\alpha^2-1\right)}} \\ R &= \alpha r \end{aligned} \tag{3.10}$$

with the director field in the top half of the tactoid given by

$$\begin{aligned} \hat{\mathbf{n}} &= \frac{\tilde{\mathbf{n}}}{|\tilde{\mathbf{n}}|} \\ \tilde{\mathbf{n}}(x,y) &= \left(\sqrt{R^{*2} - x^2},\ \frac{-y}{\sqrt{{R_C^*}^2 - x^2} - y_0}\right) \\ R^* &= \beta R \\ R_C^* &= \frac{R^{*2} + r^2}{2r} \\ y_0 &= \frac{R^2 - r^2}{2r} \end{aligned} \tag{3.11}$$

which is reflected across $y = 0$ to give the director in the bottom half. We set the tactoid volume to be $V_N = 120^2\pi$ and initialize configurations with varying $\{\alpha, \beta\}$ such that $\alpha \in \{1, 1.2, 1.4, 1.6, 1.8, 2\}$ and $\beta \in \{1, 1.05, 1.1, 1.2, 1.5, 2, \infty\}$. We note that roughly if $\beta > 3$ the director configuration is nearly indistinguishable from the uniform case.

We simulate from the described initial conditions until the free energy fails to change to within 10^{-6}, so that the configuration is at a minimum in the free energy. For each

pair of $L_3 + L_4$ and ε studied we find the set $\{\alpha, \beta\}$ that has the smallest computed energy. Table 3.1 summarizes the results. We find that as elastic anisotropy is increased, tactoids become more bipolar, that is, β decreases. We also find that increasing the anchoring strength is associated with increasing aspect ratio. Thus for materials with larger surface anchoring, the tactoids tend to be more anisotropic in shape. In Fig. 3.5a we show S and the director field for four different energy minimizers, while in Fig. 3.5b we plot an example energy landscape for $L_3 + L_4 = 5$ and $\varepsilon = 0.8$. The energy landscapes are typically flat, which is why we do not see much change in overall structure from the initial conditions during the numerical relaxation.

Finally, we note that while the shapes of the positive tactoids are similar to those seen in the experiments of Ref. [10], the energy minimizing configurations are slightly different. Tactoids appearing in Ref. [10] are more bipolar and have a smaller aspect ratio than the minimum energy configurations in our study. Based on the theoretical work of Ref. [70] this can be explained by a larger surface *tension* to bulk elasticity ratio in the experiments. This disparity highlights a shortcoming in the **Q**-tensor approach; namely, there are no elastic energy terms that only contribute to surface tension, thus making a study of the separate effect of surface tension difficult.

3.6 Tactoid Growth

Here we explore the effect of L_3 and L_4 on non-equilibrium tactoid growth kinetics. To do this, we remove the volume constraint of the previous sections and lower the effective temperature to simulate a quench into the nematic phase. Simulations are carried out in a similar manner to the previous sections, however, we do not have a stopping criteria and instead choose the total number of iterations to simulate. We set $\kappa/nk_BT = 3.6$, which corresponds to an equilibrium $S_N = 0.5609$. We initialize every system as a disc of radius $R = 20$ and a uniform director field, $\hat{\mathbf{n}} = (1, 0, 0)$. We then simulate 500 iterations of growth with $\Delta t = 0.2$.

Fig. 3.6 shows results for three sets of elastic constants: $\{L_3, L_4\} = \{0, 4\}, \{2, 2\}, \{4, 0\}$. Fig. 3.6a shows S and the director field after 500 iterations. We find that the director fields are markedly different in all three cases. If $L_3 > L_4$, the director develops a bipolar configuration with boojums at the ends of the tactoid, similar to the equilibrium shapes

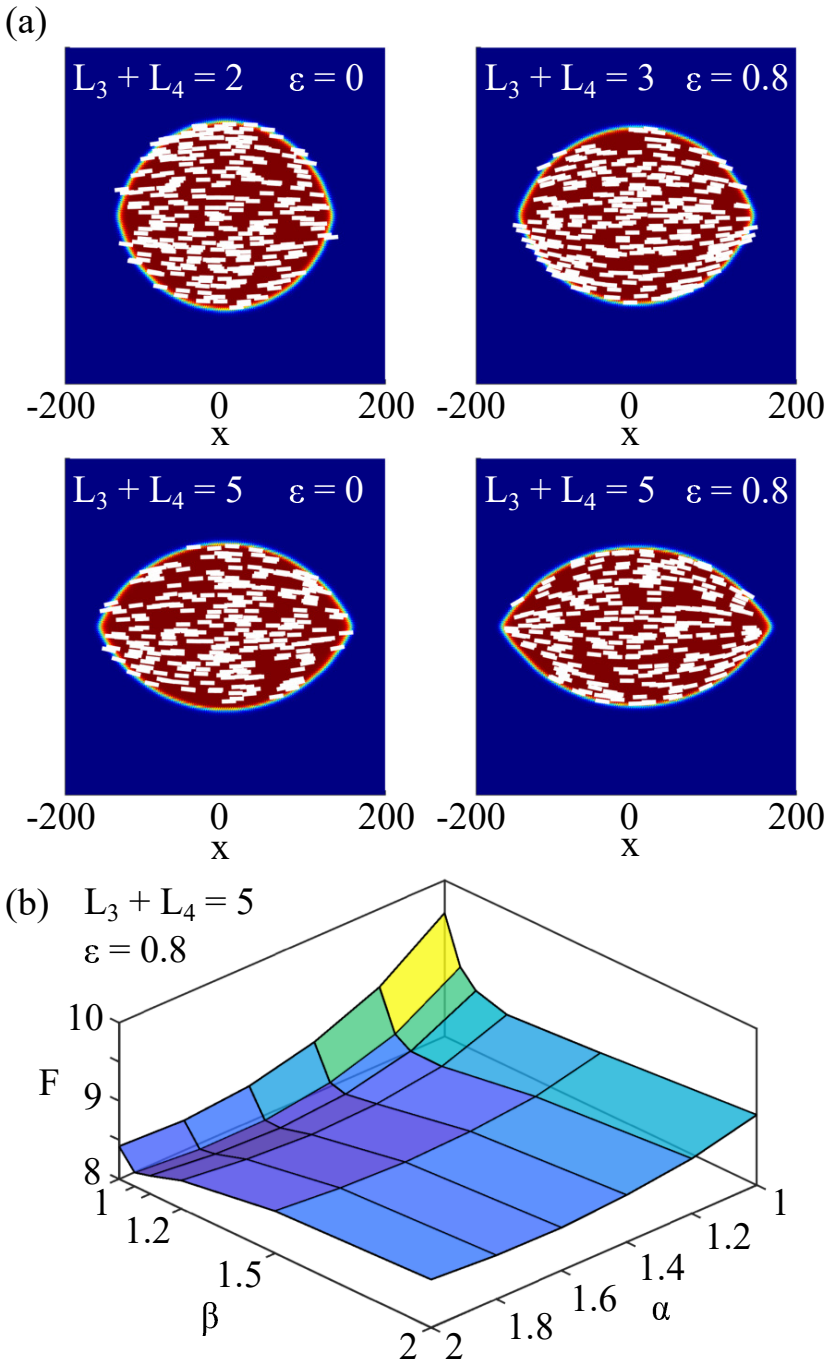

Figure 3.5: Example computations of equilibrium positive tactoids. (a) Scalar order parameter S and director structure for minimum energy positive tactoids for various values of surface anchoring, $L_3 + L_4$, and bulk elastic anisotropy, ε. (b) Example plot of the elastic free energy as a function of aspect ratio α and bipolarity β for $L_3 + L_4 = 5$ and $\varepsilon = 0.8$.

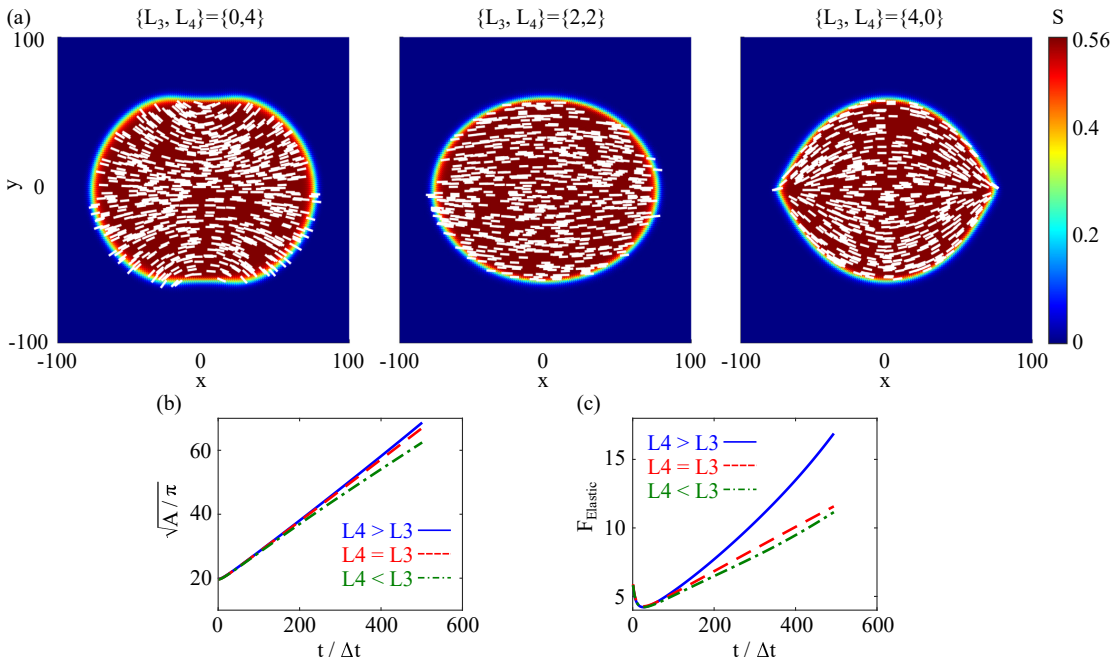

Figure 3.6: Results from simulated tactoid growth from initial uniform, circular configurations with $\{L_3, L_4\} = \{0, 4\}, \{2, 2\}, \{4, 0\}$. (a) Scalar order paramter S and director configuration at 500 iterations. The resulting configuration is seen to be highly sensitive to the choice of elastic constants. (b) $\sqrt{A/\pi}$ plotted as a function of iteration number $t/\Delta t$. A linear scaling is observed. (c) Plots of the elastic energy, Eq. (2.7), versus iteration number for each case simulated. The lowest energy configuration has $L_3 > L_4$.

studied in Sec. 3.5 and similar to shapes seen in experiments. On the other hand, if $L_4 > L_3$ the director tends to homeotropic alignment which, if simulated further, eventually forms defects on the top and bottom poles of the tactoid. If $L_3 = L_4$ these effects seemingly cancel, as the director remains uniform and the shape grows to be elliptical. In all three cases, the area of the tactoid grows like $A \sim t^2$ as shown in Fig. 3.6b. This behavior is expected for two dimensional domain growth driven by phase energy difference [7]. Fig. 3.6c show the elastic free energy, Eq. (2.7), as a function of iteration number for all three cases. We find that the configuration with the lowest elastic free energy is where $L_3 > L_4$ since anchoring energy is minimized while incurring a bulk elastic penalty. When $L_3 = L_4$ the energy is marginally higher, since there is no bulk elasticity, though anchoring energy is not minimized. The elastic energy for $L_3 < L_4$ is much higher than that of the other two configurations since homeotropic anchoring costs the most energy and there are bulk director distortions.

The results shown in Fig. 3.6 are similar to numerical results from Ref. [69]. There, the effect of the L_2 and L_3 terms was analyzed. However, the simulations of Ref. [69] were performed on a computational domain much smaller (500nm^2) than typical experiments and were performed with the unbounded Landau-de Gennes energy and hence did not use values of L_3 greater than 1. Here, we compute with system sizes and values of L_3 close to the experimental setups of Ref. [10] and since both L_3 and L_4 terms are cubic in $\mathbf{Q}$, their effects can be cancelled out by having equal coefficients. Hence, the L_4 term serves as a better control to understand the difference in growth. Because the functional derivative of $\mathbf{Q}$ drives the time evolution of the system, there should be terms in $\delta F_3/\delta\mathbf{Q}$ and $\delta F_4/\delta\mathbf{Q}$ that are exactly equal and opposite. Here F_3 and F_4 refer to the elastic energies from the L_3 and L_4 terms. We compute these functional derivatives

$$\begin{aligned}\frac{\delta F_3}{\delta Q_{k\ell}} &= \partial_k Q_{ij}\partial_\ell Q_{ij} - 2\partial_i Q_{k\ell}\partial_j Q_{ij} - 2Q_{ij}\partial_k\partial_\ell Q_{ij} \\ \frac{\delta F_4}{\delta Q_{k\ell}} &= -\partial_k Q_{ij}\partial_\ell Q_{ij} - Q_{ij}\partial_k\partial_\ell Q_{ij} - Q_{k\ell}\partial_i\partial_j Q_{ij}\end{aligned} \tag{3.12}$$

and find that the first term of either functional derivative is equal and opposite.

To investigate the effect of this term on the eigenvectors of $\mathbf{Q}$ we write $\mathbf{Q}$ as in Eq. (2.3) with $\hat{\mathbf{n}} = (\cos\phi, \sin\phi, 0)$, $\mathbf{m} = (-\sin\phi, \cos\phi, 0)$, and $\boldsymbol{\ell} = (0, 0, 1)$. Using this

parameterization we have

$$m_k \partial_t Q_{k\ell} n_\ell = S \partial_t \phi \tag{3.13}$$

$$m_k \partial_k Q_{ij} \partial_\ell Q_{ij} n_\ell = \frac{2}{3} m_k \partial_k S n_\ell \partial_\ell S + 2 m_k \partial_k P n_\ell \partial_\ell P + 2(S-P)^2 m_k \partial_k \phi n_\ell \partial_\ell \phi_\ell. \tag{3.14}$$

At the interface the second and third terms of Eq. (3.14) are small since the biaxiality, P, is small (Sec. 3.3) and $(S-P)^2$ is small compared to ∇S. ∇S is in the direction of the interface normal, the angle of which we denote with θ. Equating Eqs. (3.13) and (3.14), we have the dominant contribution to the time evolution of ϕ at the interface:

$$\partial_t \phi \sim (L_4 - L_3) \sin 2(\theta - \phi). \tag{3.15}$$

This contribution vanishes when $L_3 = L_4$ and when the director is tangential or perpendicular to the interface. However, if $L_3 < L_4$ it drives $\phi = \theta$, or homeotropic alignment, whereas if $L_3 > L_4$ it drives $\phi = \theta + \pi/2$, or tangential alignment. This is precisely the behavior observed in the simulations.

We emphasize that this process is of kinetic origin and does not drive the system to minimize the *elastic* free energy, since we see that tangential anchoring still minimizes the elastic energy for $L_3 < L_4$. Of course, the full free energy, that is bulk and elastic free energy, is still getting smaller at each time step since the nematic domain is growing. Thus we conclude that this effect is *not* related to bulk elastic anisotropy. The kinetic growth of the tactoids is dominated by bulk free energy minimization, while the elastic energy terms do not necessarily lead to elastic energy minimization. That is, the system is tending to evolve to a *local* minimum in the full free energy, but not necessarily the *global* minimum.

We finish this section by exploring the configurations that develop at long times with variable L_3, but $L_4 = 0$. If $L_3 > 0$, the tactoid develops a bipolar director configuration, leading to an anisotropic morphology with aspect ratio $\alpha > 1$ The aspect ratio continues to grow until boojums form, at which point the aspect ratio tends to stay constant since the director is tangent to the interface everywhere except the endpoints. Fig. 3.7 shows $(\alpha - 1)/L_3$ as a function of iteration number $t/\Delta t$. We find that the data collapses for various L_3, indicating that the growth of and final value of aspect ratio in tactoids is

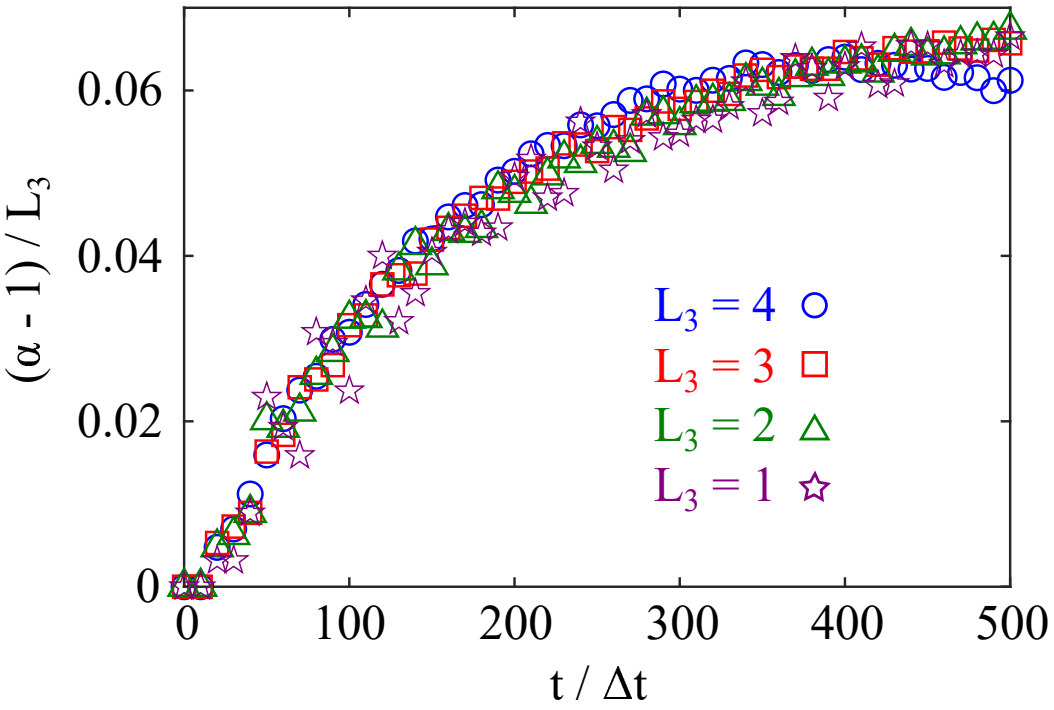

Figure 3.7: Tactoid aspect ratios, scaled as $(\alpha - 1)/L_3$, versus iteration number $t/\Delta t$ for various values of L_3. The data collapse indicates that both the transient and steady state aspect ratios scale linearly with L_3.

linearly proportional to L_3, which may suggest a method for experimentally determining the value of L_3.

3.7 Conclusion

Here we have described the numerical study of isotropic-nematic domains with the tensor order parameter $\mathbf{Q}$ for nematic liquid crystals. Using the self-consistent field theory of the Ball-Majumdar model, we have computationally obtained interface and tactoid configurations with varying contributions from surface anchoring and bulk elasticity. Additionally we have presented a method to computationally fix the volume of nematic phases in one and two dimensional systems, which allows the volume to be varied as a control parameter. The competition of surface anchoring and bulk elastic anisotropy leads to sharp boojums in negative tactoids, which are also seen in experiments. Postive tactoid morphology also becomes more anisotropic as these material parameters are varied. Finally, tactoid growth was numerically studied and it was found that the long time configurations are sensitively dependent on the elastic energy included in the model. This study should be important for future computational and experimental studies of tactoids, as well as in engineering liquid crystals materials with desired morphological properties. In particular, we note that the phenomenon described in Sec. 3.6 requires further study in liquid crystalline materials, but may also point to a general trend in the morphogenesis of other systems with viscoelastic properties. The long time morphologies in such systems may not be minimizers of the elastic energy, which is an important point to consider when attempting to understand natural morphologies by minimizing elastic energies (i.e. with the director representation, $\hat{\mathbf{n}}$, in liquid crystals).

Chapter 4

Equilibrium Structure of 2D Anisotropic Disclination Cores

4.1 Introduction

Topological defects in nematics are singularities where the orientation of the director cannot be defined. They can be formed from coalescing domains, patterning surfaces, or applying electromagnetic fields [1,10,62,86]. In traditional liquid crystal studies, the core of the defect has been treated as a singularity. In computational studies the singularity is regularized with ad-hoc methods, or is effectively "cut out" in favor of modeling the long range distortion in the director field [1, 87, 88]. However, recent experiments performed in lyotropic chromonic liquid crystals have revealed large, anisotropic cores and have proven that defect cores have a more nuanced fine structure that gives rise to a unique interplay between elasticity, anisotropy, and topology that is not present in other materials [10, 15]. Additionally, resolving the defect core structure is of fundamental importance for many contemporary applications including active and living nematics, biological tissue dynamics, surface actuation, curved films, or the transport of droplets and biological materials in nematics [6, 74, 77, 89–98].

The **Q**-tensor formalism thus becomes the description of choice to study core structure, since the singularity is eliminated and the core region can be modeled directly. Direct comparison between tensor and director models near singularities is difficult on account of the large gradients of order in those regions, and the underlying expansion

in gradients of both descriptions. Furthermore, numerical studies of the core structure using the **Q**-tensor have thus far been limited to isotropic elasticity in which the "one-constant" approximation is employed ($K_{11} = K_{22} = K_{33} = K$) [29]. However, the nematogens that beget these anisotropic structures are themselves complex and clearly display anisotropic elasticity [5, 18]. Hence, a more physically realistic modeling of the core structure should include this elastic anisotropy. Here, we study the effect of anisotropic elasticity on the equilibrium structure of the core of $\pm 1/2$ disclinations in the thin film setting. We show that previous results for the far-field director structure can be recovered which smoothly connect to a new near field solution based on the model of Chapter 2. These results are associated with anisotropic stresses near the defect that have important consequences for active nematics in particular. Further, we directly compare our results with experimental data and show that anisotropic elasticity leads to anisotropic defect core structures that are also highly biaxial.

4.2 One Elastic Constant Disclination Core Structure

Throughout this chapter, as in the previous chapter, we will assume the director lies in xy plane since we are primarily motivated by experiments performed in thin films [10,15]. Thus when considering the bulk elasticity of the liquid crystal, we do not include twist distortion (K_{22}). We can also parameterize the director as $\hat{\mathbf{n}} = (\cos\phi, \sin\phi, 0)$ so that there is one degree of orientational freedom only. In the case of the one-constant approximation, the Frank-Oseen free energy density is

$$f_{FO}(\phi) = K|\nabla\phi|^2. \tag{4.1}$$

The configuration with minimum energy is a uniform configuration with $\phi(x, y) = \phi_0$, such that ϕ_0 is a constant. Due to topological constraints on the system, however, configurations containing a disclination may represent a minimum in the constrained free energy landscape. To mathematically resolve the structure of the disclinations, the Euler-Lagrange equation resulting from Eq. (4.1) must be satisfied. In the one-constant approximation this is

$$\nabla^2\phi = 0. \tag{4.2}$$

In Cartesian coordinates, a solution to this (away from disclination core) describing a defect is

$$\phi(x,y) = m\theta + \phi_0 = m \arctan\left(\frac{y-y_0}{x-x_0}\right) + \phi_0 \tag{4.3}$$

where m is the winding number of the disclination, which for liquid crystals can be any half-integer, x_0 and y_0 are the x, y coordinates of the disclination, and ϕ_0 is an overall phase. The middle panel of Fig. 4.1 shows an example of this solution with $m = 1/2$ and $\phi_0 = 0$.

Eq. (4.3) is the standard description of the director away from a disclination in two dimensions. It is important as well to note that Eq. (4.2) is a linear partial differential equation, and hence the solution for *many* disclinations in a one-constant system is simply a sum of the single disclination solutions at the location of each disclination. The solution is not valid at the defect core as $\phi(x_0, y_0)$ is indeterminate. Thus for studies based on the director representation, one must "cut out" the core region in some way. To study the structure of the near core region, a regularized field must be used. One possible avenue is the tensor order parameter $\mathbf{Q}$ which has already been shown to be biaxial near the core of disclinations [29]. This biaxial fine structure will be discussed in greater detail in Sec. 4.5.

4.3 Anisotropic Elasticity: Far- and near-field solutions

For arbitrary K_{11} and K_{33} the Frank-Oseen free energy for a *uniaxial* nematic becomes

$$\begin{aligned} f_{FO}(\phi) = K_{11}\left[\sin^2\phi(\partial_x\phi)^2 + \cos^2\phi(\partial_y\phi)^2 - \sin 2\phi\partial_x\phi\partial_y\phi\right] \\ + K_{33}\left[\cos^2\phi(\partial_x\phi)^2 + \sin^2\phi(\partial_y\phi)^2 + \sin 2\phi\partial_x\phi\partial_y\phi\right]. \end{aligned} \tag{4.4}$$

In the limit $K_{11} = K_{33} = K$ this reduces to Eq. (4.1). To find far-field equilibrium defect solutions, Eq. (4.4) is recast in polar coordinates from the center of the defect, such that θ is the azimuthal angle, and the corresponding Euler-Lagrange equation is [88, 99]

$$\frac{\partial^2\phi}{\partial\theta^2}\left[1 - \varepsilon\cos 2(\phi-\theta)\right] - \left[2\frac{\partial\phi}{\partial\theta} - \left(\frac{\partial\phi}{\partial\theta}\right)^2\right]\varepsilon\sin 2(\phi-\theta) = 0 \tag{4.5}$$

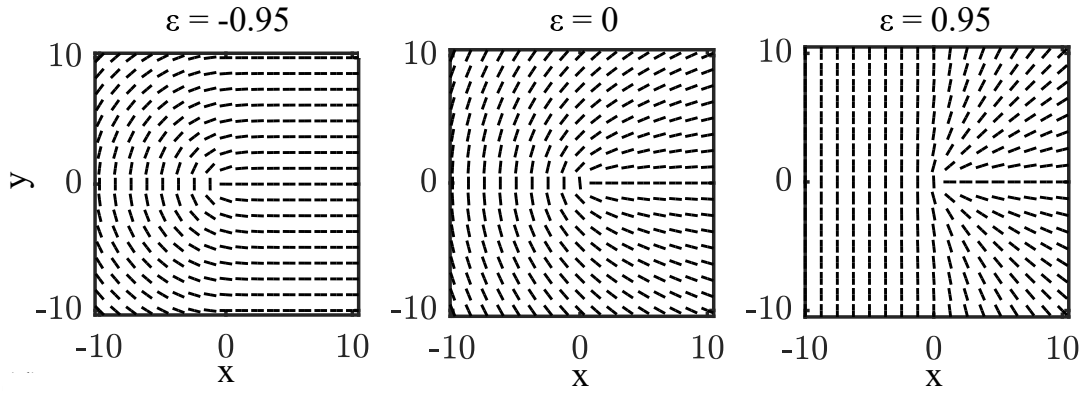

Figure 4.1: Equilibrium director configurations for $+1/2$ disclinations with $\varepsilon = -0.95$ (left), $\varepsilon = 0$ (middle), $\varepsilon = 0.95$ (right). These configurations are obtained via numerical simulation of the Ball-Majumdar model, described in Chapter 2.

where ε is the elastic anisotropy defined in Eq. (2.40). This equation was originally integrated by Dzyaloshinskii [99]. There is no closed form solution, but it can be expressed as the following integral relation

$$\begin{aligned} \theta &= p \int_0^{\phi(\theta)-\theta} \sqrt{\frac{1-\varepsilon\cos 2\xi}{1-p^2\varepsilon\cos 2\xi}}\, d\xi \\ \pi &= (m-1)p \int_0^{\pi} \sqrt{\frac{1-\varepsilon\cos 2\xi}{1-p^2\varepsilon\cos 2\xi}}\, d\xi \end{aligned} \tag{4.6}$$

where p depends on ε and m and can be determined from the second integral. The integral equations can be solved numerically, and yield solutions that deviate from the $\phi = m\theta$ behavior of the one constant approximation. These deviations can be quantified by decomposing ϕ into angular Fourier components,

$$\phi(\theta) = \pm\frac{1}{2}\theta + \sum_{n=1}^{\infty} \phi_n \sin n\theta. \tag{4.7}$$

There has been some success in using this solution and the Fourier decomposition to measure the elastic constants of liquid crystals by measuring ϕ near a defect [15, 88]. Importantly, the anisotropic elastic Euler-Lagrange equation is nonlinear and hence the solution for multiple defects is not simply the sum of the ϕ fields of each defect.

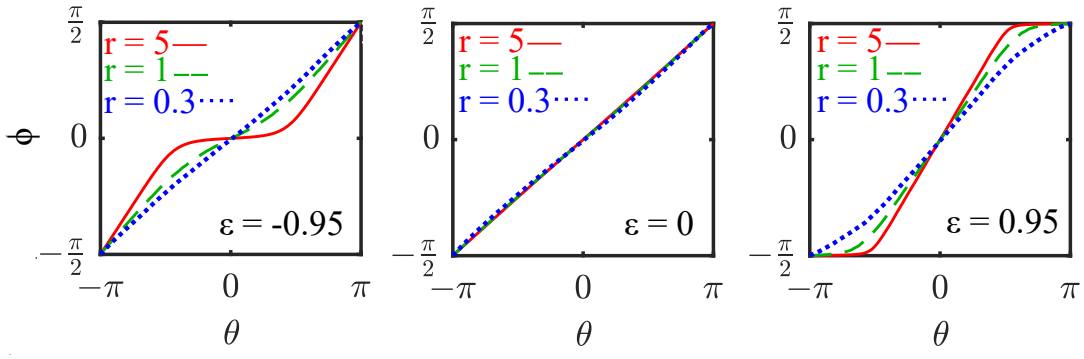

Figure 4.2: Director angle, ϕ, obtained from numerical solution of the Ball-Majumdar model, plotted against the azimuthal angle θ for $\varepsilon = -0.95$ (left), $\varepsilon = 0$ (middle), $\varepsilon = 0.95$ (right). For each value of ε three distances from the core are plotted, showing that the deviations from the one-constant solutions become small near the core.

In describing disclinations, as with the one constant case, the core region must be handled separately if $\hat{\mathbf{n}}$ or ϕ is used. In the tensor representation, on the other hand, the full set of equations for the components of $\mathbf{Q}$ are solved to give the structure of the core. We are also interested in solving the $\mathbf{Q}$ equations in order to interpolate between the far field Dzyaloshinskii solution (it is expected that the configuration is uniaxial far from the core) and the near field disclination core structure. We are also interested in verifying that indeed the far field solution agrees with the Dzyaloshinskii solution when using $\mathbf{Q}$ and the singular potential. To accomplish this, we solve the gradient flow equations, Eq. (2.29), using a finite difference scheme on a mesh with 257×257 vertices and Neumann conditions on the boundaries. We set $\kappa/(nk_BT) = 4$ and $\Delta t = 0.1$. We iterate until the total free energy fails to change to within 10^{-6} of its current value. We first report the differences in the director fields for large elastic anisotropy. Fig. 4.1 shows three director configurations for $+1/2$ disclinations with $\varepsilon = -0.95$, $\varepsilon = 0$, and $\varepsilon = 0.95$. When elastic anisotropy is large the director configuration evolves to remove one type of distortion: splay if $\varepsilon < 0$ and bend if $\varepsilon > 0$. This is because $K_{33} \to 0$ when $\varepsilon \to -1$ and $K_{11} \to 0$ when $\varepsilon \to 1$, so it energetically favorable to have configurations with only bend or only splay. For $-1/2$ disclinations the director cannot relax to remove all of one type of distortion because of its three-fold symmetry.

The far field solutions are precisely the Dzyaloshinskii solution. In Fig. 4.2 we show ϕ as a function of θ for the three cases in Fig. 4.1 which, when compared to previous

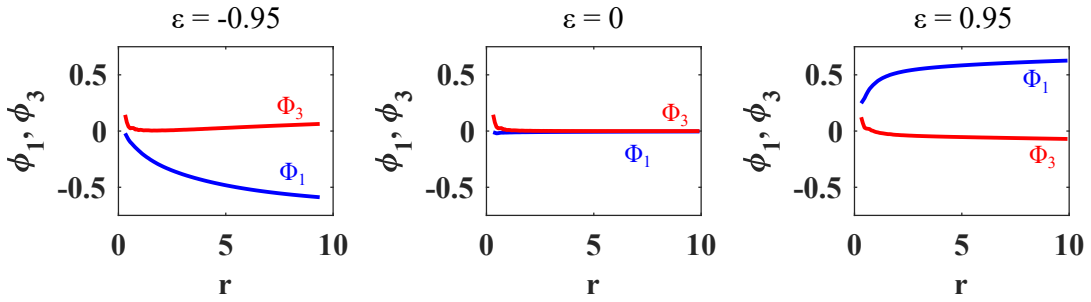

Figure 4.3: Fourier amplitudes, $\phi_1(r)$ and $\phi_3(r)$, computed using the Ball-Majumdar model of Chapter 2, of the deviation to $\phi = (1/2)\theta$ for a $+1/2$ disclination (see Eq. (4.7)), plotted as a function of radial distance from the core, for $\varepsilon = -0.95$ (left), $\varepsilon = 0$ (middle), and $\varepsilon = 0.95$ (right). ϕ_1 is represented by the blue curves, while ϕ_3 is represented by the red curves.

studies of the Dzyaloshinskii equations, show the same deviations from $\phi = (1/2)\theta$, the isotropic configuration [88]. However, as the core is approached, these deviations become smaller until they go to zero at the core. Fig. 4.2 also shows ϕ versus θ for distances near the core which show that the deviations from the isotropic limit vanish at the core. That is, in the asymptotic limit $\phi(r \to 0) = (1/2)\theta$. This is likely due to the elastic anisotropy's dependence on S (Eq. (2.40)). As we will show, S also becomes small near the core, hence the effective anisotropy near the core becomes small, leading to smaller deviations. Even though S does not go to zero at the core (see Sec. 4.5), the anisotropic component to the elasticity is proportional to S^3 (Eq. (2.8)) and hence this component effectively vanishes relative to its contribution far from the core. To characterize the deviations' dependence on radial distance, we use the Fourier decomposition in Eq. (4.7) and plot the primary amplitudes, $\phi_1(r)$ and $\phi_3(r)$ in Fig. 4.2 for the $+1/2$ defects of Fig. 4.1. As evidenced by the figure, the deviations go to zero at the core ($r = 0$) and go to the Dzyaloshinskii solution away from the core. For the $+1/2$ defects, the ϕ_1 Fourier mode is dominant, while the ϕ_3 mode is roughly zero even for cases with elastic anisotropy. For $-1/2$ disclinations the ϕ_3 mode is the dominant mode [15]. The length scale associated with the rising Fourier modes is roughly the core size, which is expected since this is the same scale S is changing on.

Finally, we investigate the effect of these anisotropic director configurations on the disclination polarization defined as $\nabla \cdot \mathbf{Q}$. This vector quantity is important in the fields

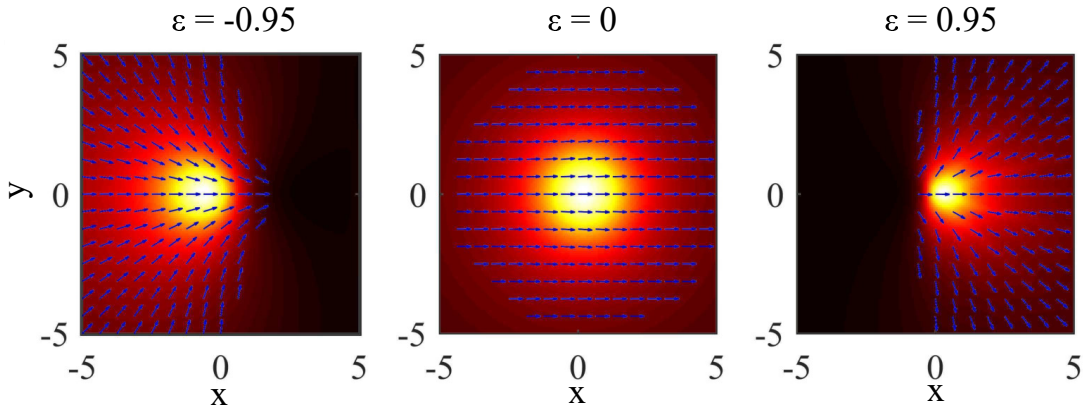

Figure 4.4: Disclination polarization, $\nabla \cdot \mathbf{Q}$, for $+1/2$ disclinations computed using the Ball-Majumdar model of Chapter 2, with $\varepsilon = -0.95$ (left), $\varepsilon = 0$ (middle), and $\varepsilon = 0.95$ (right). The arrows indicate the direction of the polarization while the black to red to white color scale represents the magnitude. For anisotropic elastic configurations the polarization is spatially anisotropic in magnitude and has a convergent (divergent) direction.

of active matter and surface actuation of liquid crystal elastomers, as it is proportional to the assumed force generated by the active nematogens, or the heating and cooling of the elastomer [76,100]. It is well known that $+1/2$ defects generate flows in active nematics due to this active force [95, 101]. However, many such models have neglected elastic anisotropy because of the difficulties associated with the Landau-de Gennes free energy. Here, we show in Fig. 4.4 that elastic anisotropy qualitatively changes the character of the polarization. The arrows in the plots show the direction of the polarization while the colormap shows the magnitude. While the magnitude is largest at the core of the defect, for the cases of $\varepsilon = -0.95$ and $\varepsilon = 0.95$ the polarization is asymmetric about reflections through the vertical axis. Additionally, for the anisotropic cases, the polarization near the core has nonzero divergence, (i.e. $\nabla \cdot (\nabla \cdot \mathbf{Q}) \neq 0$). This has implications for active materials with elastic anisotropy, as the force will be asymmetric and there will be an overall (positive or negative) divergence at the core of disclinations. It is our hypothesis that this is an important component in the mechanism of layer formation in bacterial colonies, cell extrusion in epithelial tissue, and swimmer saturation in living liquid crystals, which all show convergent and divergent behavior of the nematogens at defects [93, 94, 98].

4.4 Disclination Core Morphology

Here we compare the equilibrium morphology of disclinations in two dimensions computed using the model of Chapter 2 to that of the experiments in Ref. [15] performed in thin films. In order to directly compare with the experiments, we present results for the optical retardance, $\Gamma = \gamma(S - P)$, where γ is a constant of proportionality between Γ and $S - P$ [15]. This quantity is measured in experiments and is essentially a measure of the difference in speed of perpendicular polarizations of light passing through the liquid crystal, and thus is related to the birefringence. Specifically $\Gamma = d|\Delta n|$ where d is the film thickness ($d \approx 4.5\mu$m in the experiments [15]) and $|\Delta n|$ is the in-plane birefringence. It reveals where the system is orientationally ordered ($\Gamma \neq 0$) or disordered ($\Gamma = 0$) with respect to the system plane. For lyotropic chromonic liquid crystals, it can be used to image the morphology of defect cores which are as large as 20μm in diameter.

To understand the anisotropy of Γ induced by elastic anisotropy as a function of distance from the core, Γ is decomposed into its angular Fourier amplitudes

$$\Gamma(r, \theta) = \Gamma_0(r) + \sum_{n=1}^{\infty} \Gamma_n(r) \cos n\theta \tag{4.8}$$

where the coordinates r and θ are polar coordinates defined by the disclination core center. Elastic energies with no contribution to "surface anchoring" (see Table 2.6) and degenerate Frank-Oseen bulk elasticity ($\varepsilon = 0$) lead to an axisymmetric core with $\Gamma(r, \theta) = \Gamma_0(r)$ regardless of the topological charge of the defect. Thus, $\Gamma_{n\neq 0}(r)$ are quantitative measures of the morphological anisotropy of the core. To study the effect of elastic anisotropy we use nonzero L_2 and L_3 in Eq. (2.7) to set the surface anchoring and bulk elastic anisotropy.

Fig. 4.5a shows the computed spatial profile of Γ for $\pm 1/2$ disclinations as well as the surrounding director structure. Fig. 4.5b shows the numerically determined angular Fourier amplitudes of Γ (solid and dashed lines) as a function of radial distance from the core plotted alongside experimental data from Ref. [15] (dots and error bars). To determine the dimensional position and optical retardance we find ξ and γ by fitting the computed Γ_0 to the experiment for the $+1/2$ disclination. In fitting, we match the

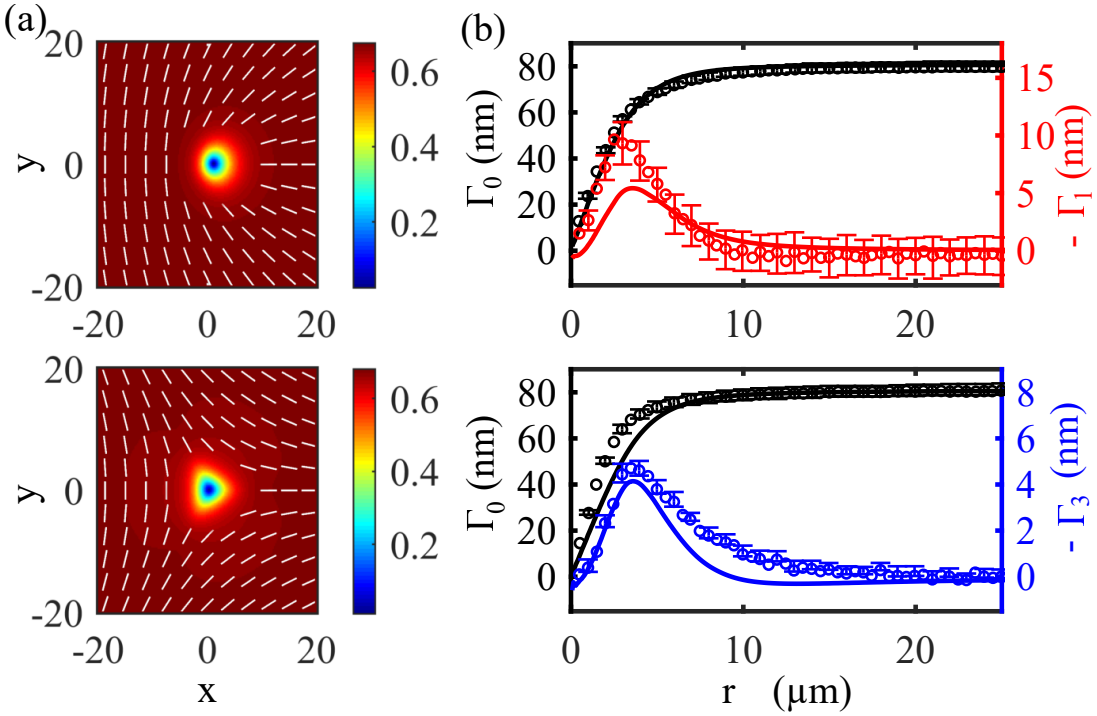

Figure 4.5: Spatial profile and director structure of $\pm 1/2$ disclinations modeled by the self-consistent theory of Chapter 2 with physically realistic elastic anisotropy. (a) Simulated optical retardance Γ and director. (b) Angular Fourier amplitudes of Γ plotted as a function of distance from the core. Solid and dashed lines come from the simulation shown in (a) while dots and error bars come from the experiment of Ref. [15]. For the $+1/2$ disclination, the dominant anisotropic Fourier amplitude is Γ_1 while for the $-1/2$ disclination it is Γ_3. The elastic constants used are $L_2 = 7$ and $L_3 = 5$ which maintain the experimental value of $\varepsilon = 0.4$.

saturation limit of the computed and experimental Γ_0 to find γ, and we adjust ξ until the computed and experimental Γ_0 coincide. We find $\gamma = 119.8$nm and $\xi = 1.2\mu$m. We note that we only fit these values for Γ_0 of the $+1/2$ disclination and use these values for the $-1/2$ disclination and all higher Fourier modes.

For the elastic constants, L_2 and L_3 are not chosen independently, but are constrained to maintain $\varepsilon = 0.4$ which is appropriate for the lyotropic chromonic liquid crystal used in the experiments [5, 15]. This effectively leaves a single elastic parameter that can be varied that is related to the contribution of surface anchoring. We thus choose the parameter set that best matches the peak height of the experimental $\Gamma_{n\neq 0}$, leading to $L_2 = 7$, $L_3 = 5$. We emphasize that the same parameter set was used to compute both defect configurations in Fig. 4.5 and that the minimal number of free parameters was used in the elastic energy. Despite these constraints on the model, it agrees well with the experimental data for both $\pm 1/2$ disclinations, indicating that simply allowing for elastic anisotropy yields physically accurate, qualitively different morphologies in disclination morphology. Just as in the experiments, we find that the maximal anisotropy occurs near the edge of the defect core region.

4.5 Disclination Core Biaxiality

We also study the biaxiality of the core region for anisotropic disclinations. While it is known that the defect core becomes biaxial for systems modelled with the Landau-de Gennes free energy with a one-constant elastic energy [29, 102], it has not been studied for systems with anisotropic elasticity, or for the self-consistent model presented in Chapter 2.

In Fig. 4.6 we show the biaxiality parameter β, defined in Eq. (3.7), for the $\pm 1/2$ disclinations of Fig. 4.5. We find that the configuration is uniaxial away from the core and then becomes maximally biaxial as the core is approached, until becoming uniaxial again, though with negative order parameter, at the center of the core. We also find that the biaxial structure away from the core is anisotropic, which is more prominently seen in the $-1/2$ configuration. The biaxiality extends further into the splay-dominated regions, likely because the splay constant is reduced and thus it is more favorable for biaxiality to develop there. Close to the core region, however, the biaxiality becomes

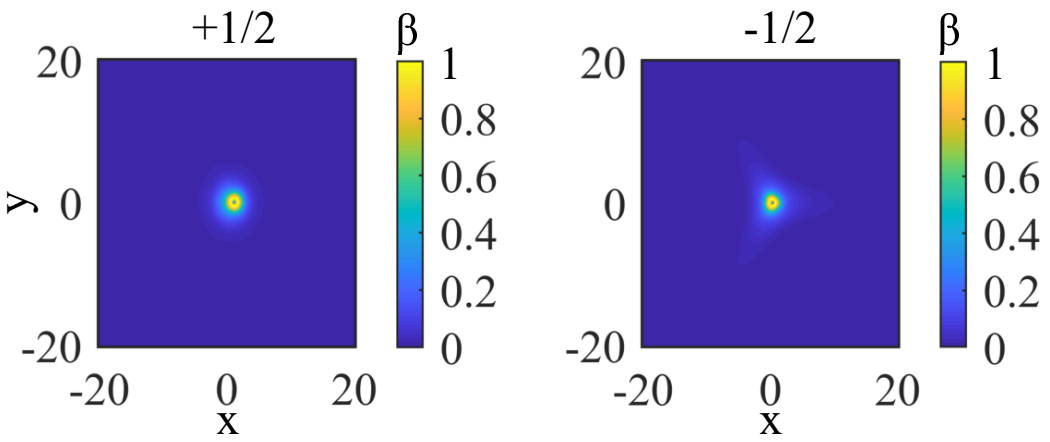

Figure 4.6: Biaxiality parameter β, defined in Eq. (3.7), for the simulated $\pm 1/2$ disclinations shown in Fig. 4.5. The core region transitions from uniaxial, to maximally biaxial, to uniaxial again at the center, where the eigenvalues of $\mathbf{Q}$ cross.

axisymmetric likely due to the reduction of S and hence the reduced elastic anisotropy.

To better understand the non-monotonicity of the biaxiality as the defect core is approached, we plot in Fig. 4.7 the orientational probability distributions as one moves across a $-1/2$ disclination. Far from the core the disclination is uniaxial, where $\mathbf{Q}$ has two degenerate eigenvalues and $P = 0$. At the maximally biaxial points, the distribution has spread out in the xy plane, but not along the z direction, which corresponds to a $\mathbf{Q}$ tensor with three distinct eigenvalues. At the center of the core the distribution is characterized by equally likely orientations in the xy plane and is again uniaxial, but now the eigenvalues of $\mathbf{Q}$ cross and $S = P$. The access to the probability distribution at all points in space shows another advantage of the self-consistent field theory of Chapter 2 in the sense that we are able to understand how a given $\mathbf{Q}$ relates to the microscopic probability distribution. This microscopic transition of uniaxial $\rightarrow$ biaxial $\rightarrow$ uniaxial distributions can be thought of as a mesoscopic transition from rod-like $\rightarrow$ plate-like $\rightarrow$ disc-like nematogens. It still remains to be seen experimentally if this biaxial transition occurs. Because the optical retardance $\Gamma \propto S - P$, it cannot distinguish between the states $S = P = 0$ and $S = P \neq 0$. For lyotropic chromonic liquid crystals, it has been proposed that instead of going through a biaxial transition, the enhanced elastic forces near the core tend to break the aggregates and melt the liquid crystaline order [10].

Finally, we remark that the presence of biaxiality in the simulations is interesting

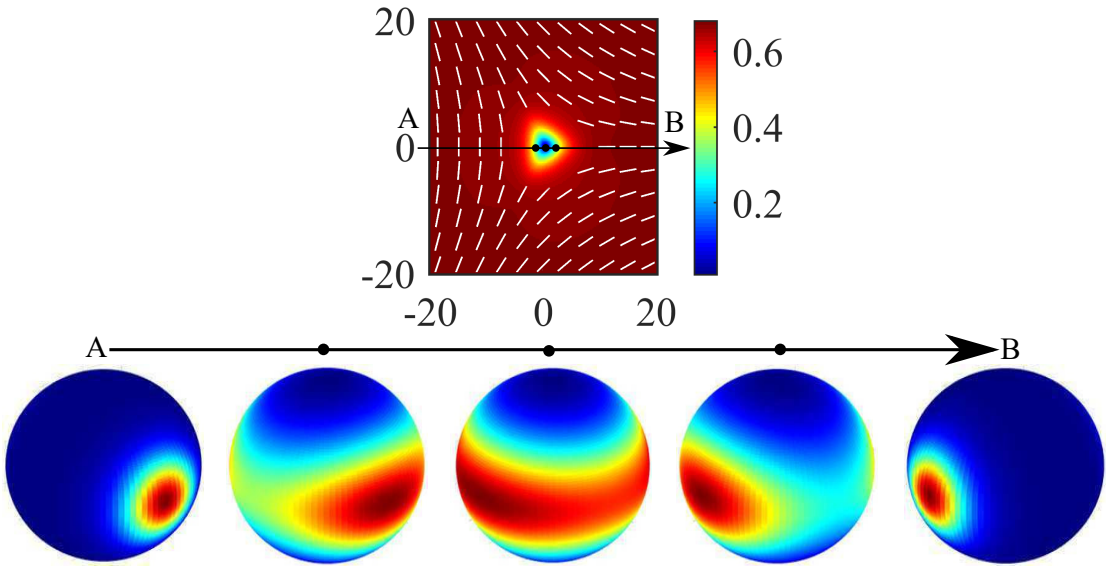

Figure 4.7: Orientational probability distribution function plotted on the unit sphere at various points throughout the $-1/2$ disclination simulated for Fig. 4.5. The nature of the biaxiality at the core is revealed as the spreading out of the distribution as the core is approached.

in and of itself. For the Landau-de Gennes theory, it can be shown that specifically the cubic term in the bulk free energy favors biaxiality when S is reduced [102]. However, the self-consistent Ball-Majumdar model does not have a term cubic in $\mathbf{Q}$. Indeed, the Hamiltonian only promotes uniaxial alignment of nematogens. This means that the appearance of biaxiality is purely entropic for the system and comes out of the numerical computation of the entropy. Thus it is difficult to compare the biaxial length scale as defined by the cubic coefficient in the Landau-de Gennes bulk free energy, Eq. (2.2), $r_B \sim \sqrt{K/BS^3}$ [102]. We note that the scale of biaxiality is roughly on the scale of defect core in our simulations.

4.6 Conclusion

Here we have presented numerical results related to the effect of elastic anisotropy on the equilibrium structure of $\pm 1/2$ disclinations in thin films. We showed that far from

the defect core, the self-consistent field theory developed in Chapter 2 reproduces previously known results given by the Dzyaloshinkii solution while continuously connecting to new results at the defect core for which a **Q** tensor description is required. Anisotropic elasticity also produces defect cores which are morphologically anisotropic and our calculations agree with experimentally studied disclinations. Further, we showed that the full, numerically computed, entropy causes defects to develop biaxial cores, which are also anisotropic. As the nematogens being studied become more complex, the models must adapt to take into account the more physically realistic elastic anisotropy of the materials. Thus the fact that the model reproduces experimental results shows that it will be useful in understanding more complicated phenomena in systems involving flows, activity, or heat induced structural change. The success of the model in capturing experimental systems is a good sign that the model can be used to study more complex systems in which defects play a prominent role.

Chapter 5

Disclination Line Identification in 3D Nematics

5.1 Introduction

In three dimensional nematics, disclinations are spatially extended line defects. Line disclinations have played an important role in our understanding of liquid crystalline systems, and have continued to be a significant source of research interest. Indeed, the observation of line disclinations led to the discovery and naming of the nematic phase ("nematic" comes from the Greek word for thread, $N\acute{\eta}\mu\alpha$) [1]. Disclinations are created when domains of mismatching orientation coalesce, when boundary conditions determine the overall topology of the sample, when external fields or shear flows are applied, or in active nematics where defects spontaneously nucleate [10, 21–24, 62].

Because of renewed interest in active and biological matter, there have been many recent efforts to characterize disclination lines. Ref. [38] shows that the geometric properties of disclination lines can be expressed through a series of tensors from ranks 1–3. These properties determine the force of one line on another as well as their active flow. Refs. [103, 104] have characterized disclinations in two dimensions as particles, and connected their velocity to a conserved topological charge density. These characterizations have important implications for identifying defect positions and velocities in both experimental systems and numerical investigations.

Here we extend this previous work by investigating the topological properties of

disclination lines and deriving a tensor field we call the "disclination density tensor." We first discuss the general structure of disclination lines and the topological considerations that go into their description. We then derive the disclination density tensor starting from the definition of the topological charge. Finally we present numerical examples of calculations of the disclination density tensor. These numerical examples show the potential for applications of the disclination density tensor to future experimental and computational studies of disclinations in nematics.

5.2 Disclination Line Structure

A major challenge with the description and analysis of disclination lines in three dimensions is their distinct topological character and complex geometry. Both aspects are qualitatively different than their two dimensional counterparts, which are point-like singularities (see Chapter 4). Here we introduce the basics of the topology and geometry of disclination lines to be able to facilitate the further discussion on defect identification and kinematics in terms of these topological and geometric descriptions.

To topologically describe defects in any system with continuous symmetry breaking, one starts with the "ground state manifold" [9,105]. This is the space that includes only the (bulk) energy minimizing states of an order parameter. For example, in an n-vector model—that is, a model in which the order parameter is an n-component vector—rotational symmetry is broken and the ground state is one in which all vectors point in a common direction. The ground state manifold of such a system is the space of possible directions that the vectors might point, or S^{n-1}, the unit sphere of dimension $n-1$. For liquid crystals in two dimensions, the ground state manifold is the real projective space, $\mathbb{RP}^1$, because of the apolar symmetry of the director. However, topologically, $\mathbb{RP}^1 \cong S^1$ and so the order parameter can be represented simply by a 2-vector or complex number. This is not the case in three dimensions. Here the ground state manifold is $\mathbb{RP}^2$, which is not isomorphic to the unit sphere S^2 and hence must be treated differently than, for example, a classical magnetic system.

To understand the allowable defects, one looks to the homotopy groups of the ground state manifold [9,105]. The homotopy groups of a manifold are concerned with characterizing the ability to continuously deform subsets of a manifold to a point. For example,

the "fundamental group," (the first homotopy group, denoted $\Pi_1(\cdot)$ where the argument is the ground state manifold) of a manifold is trivial ($\{0\}$) if every one-dimensional subspace (i.e. curve) of the manifold can be continuously deformed to a point; that is, it is simply connected. The mth homotopy group is then concerned with continuously deformed m-dimensional subsets of the manifold. If the mth homotopy group of the ground state manifold is nontrivial, then defects are topologically allowed. For liquid crystals in two dimensions, the fundamental group $\Pi_1(\mathbb{RP}^1) = \mathbb{Z}$, the integers [105]. This indicates that the defects that can occur have various charges and upon combining will add as integers (or semi-integers due to the apolar nature which allows semi-integer charges). One can think of a defect as an element of the homotopy group under some mapping (i.e. $+1/2$ disclination $\rightarrow 1 \in \mathbb{Z}$). For three dimensional liquid crystals, however, the fundamental group $\Pi_1(\mathbb{RP}^2) = \mathbb{Z}_2$ indicating that all disclinations have the same charge, since $\mathbb{Z}_2 = \{0, 1\}$, and that upon combination they will annihilate one another (since $1 + 1 = 0$ in $\mathbb{Z}_2$). Additionally, the second homotopy group, $\Pi_2(\mathbb{RP}^2)$, is also nontrivial, so point charge defects (commonly known as "hedgehogs" [105,106]) are also topologically allowed. The topological allowance of line defects is in stark contrast to 3-vector models, which only allow point defects and do not allow line defects (since $\Pi_1(S^2) = \{0\}$, that is "you can't lasso a basketball!" [107]). This topological uniqueness has been one of the primary reasons for the lack of a more rigorous mathematical treatment.

Another reason is the geometric complexity of line disclinations. In two dimensions, the geometry of a defect only appears in its orientation, which is an interesting aspect to study and has had more recent examinations [37,108,109]. However, for three dimensional nematics not only the orientation must be described, but also how the disclination line lies in space and how the nematic director is oriented around the defect. The description of how the disclination line lies in space is given by the tangent vector to the disclination line $\hat{\mathbf{T}}$. $\hat{\mathbf{T}}$ may change along the line which indicates curvature of the disclination line. The director distortion near the defect is characterized by the "rotation vector" $\hat{\mathbf{\Omega}}$. $\hat{\mathbf{\Omega}}$ is defined as the vector perpendicular to the director as it encircles the line. $\hat{\mathbf{T}}$ and $\hat{\mathbf{\Omega}}$ are independent from one another, and their relationship determines the type of line defect and how it interacts with other defects [24, 38]. For example, if $\hat{\mathbf{T}} = \hat{\mathbf{\Omega}}$, the director pattern will look like a $+1/2$ defect in two dimensions. On

the other hand, if $\hat{\mathbf{T}} = -\hat{\mathbf{\Omega}}$ the director pattern will look like a $-1/2$ defect. The cases where $\hat{\mathbf{T}} = \pm\hat{\mathbf{\Omega}}$ are typically referred to as "wedge" disclinations. A "twist" disclination occurs when $\hat{\mathbf{T}} \cdot \hat{\mathbf{\Omega}} = 0$ and the director twists as it goes around the line. Note that all of these cases are topologically equivalent and can be rotated into each other continuously.

For a single, straight ($\hat{\mathbf{T}}$ constant) disclination line the director field around the line can be explicitly written:

$$\hat{\mathbf{n}} = \hat{\mathbf{n}}_0 \cos\frac{1}{2}\phi + \hat{\mathbf{n}}_1 \sin\frac{1}{2}\phi \tag{5.1}$$

where $\hat{\mathbf{n}}_0$, $\hat{\mathbf{n}}_1$, $\hat{\mathbf{\Omega}}$ is an orthonormal triad of vectors, and ϕ represents the azimuthal angle around the disclination in the plane normal to $\hat{\mathbf{T}}$ with respect to some reference axis in the plane. Fig. 5.1 shows an example disclination defining $\hat{\mathbf{n}}_0$, $\hat{\mathbf{n}}_1$, and $\hat{\mathbf{\Omega}}$ as well as $\hat{\mathbf{T}}$ and ϕ. Eq. (5.1) is a useful expression for analytical approximations near the line, but it is not generally applicable far from the line. For systems with curved defects, multiple defects, or boundary conditions the director field may not obey Eq. (5.1) far from the defect core. Thus, identifying a disclination's rotation vector can prove troublesome if non-local methods are employed. We note that Eq. (5.1) holds asymptotically near the core because it minimizes the elastic energy while still producing a defect configuration. Of course far from the core the elastic energy is still minimized but due to the reasons noted above the minimum energy configuration may not be given by Eq. (5.1).

Finally, we note that because disclinations are topologically protected, they must either terminate at the boundary of the domain, or on itself in the form of a loop. Disclination loops arise in many scenarios, including active nematics, Saturn rings, and flow induced domain separation [22, 24, 62]. Defect loops are interesting objects because they carry two types of topological charge. They are disclinations, and hence represent an instance of the fundamental homotopy group having charge $1/2$. They also represent an instance of the second homotopy group since one can measure an overall *point* defect charge by covering the whole loop with a measuring surface. In this case, loops have integer (including zero) point charge. The examples in active nematics typically have zero point charge and have roughly constant $\hat{\mathbf{\Omega}}$ around the loop. The Saturn ring defect, on the other hand, has -1 point charge since it is induced by cancelling an overall $+1$ point charge created by homeotropic anchoring on a colloidal particle [62]. These loop

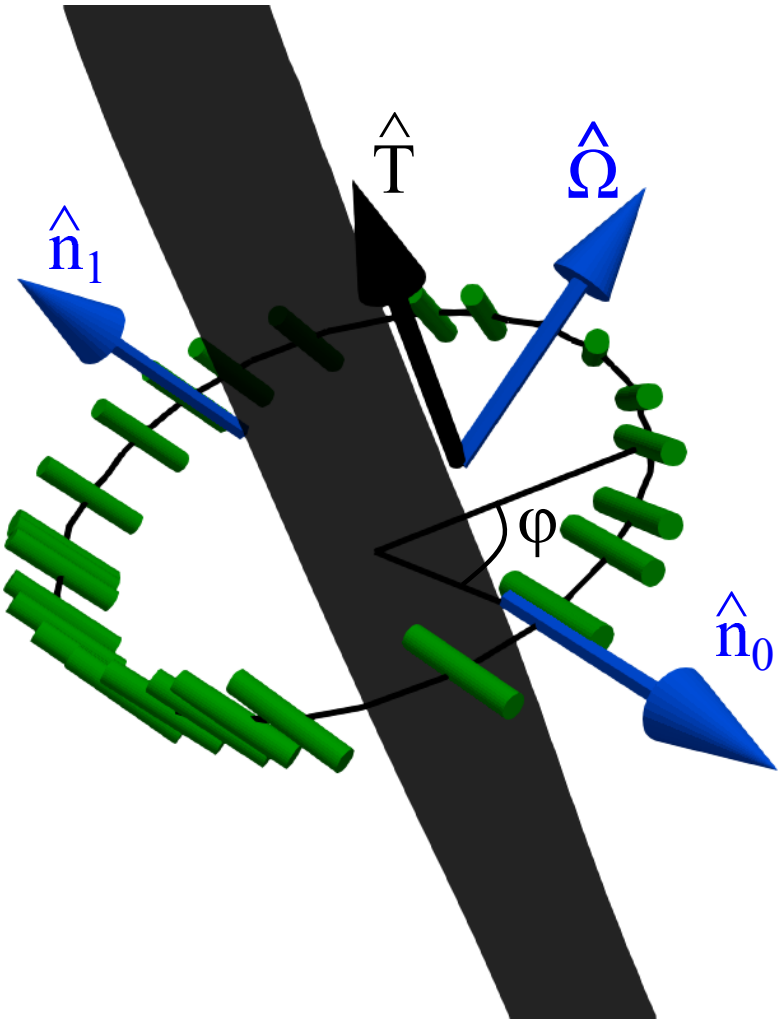

Figure 5.1: Schematic example of a disclination line showing its geometric features. $\hat{\mathbf{T}}$ is the unit tangent vector and $\{\hat{\mathbf{n}}_0, \hat{\mathbf{n}}_1, \hat{\mathbf{\Omega}}\}$ describes the orientation of nematogens (depicted as cylinders) as they encircle the defect core.

defects represent an interesting consequence of the fact that both the fundamental and second homotopy groups are nontrivial for three dimensional nematics.

5.3 Disclination Density Tensor

Our goal here will be to use the equations that give the topological charge as a starting point to derive a local topological measure for disclination lines. We will then show that this local topological measure also measures some geometrical aspects of the disclination line and can be used to identify defects in computational and experimental samples.

In two dimensions, the topological charge, m, of a defect in a nematic can be measured by integrating the change in angle of the director $\hat{\mathbf{n}}$ around a loop surrounding the defect:

$$2\pi m = \oint_C d\phi = \oint_C \nabla\phi \cdot d\boldsymbol{\ell}. \tag{5.2}$$

where m is a semi integer, the so called topological charge of the defect. Since $\hat{\mathbf{n}} = (\cos\phi, \sin\phi)$ in two dimensions, the charge can be written as

$$2\pi m = \oint_C \varepsilon_{\mu\nu}\hat{n}_\mu \partial_k \hat{n}_\nu \, d\ell_k, \tag{5.3}$$

where $\boldsymbol{\varepsilon}$ is the fully antisymmetric tensor in two dimensions. For three dimensional nematics, to our knowledge, there does not exist a generalization of Eq. (5.3) for line disclinations. An equivalent expression does exist for point defects (up to a sign ambiguity) [105]. The difficulty of generalizing to three dimensions can be exemplified with the following: Given a straight disclination with variable $\hat{\boldsymbol{\Omega}}$, so that Eq. (5.1) gives the director in each normal plane for a different triad $\hat{\mathbf{n}}_0$, $\hat{\mathbf{n}}_1$, $\hat{\boldsymbol{\Omega}}$, we would like a path integral that gives the same charge regardless of the measuring curve chosen.

This example is sketched in Fig. 5.2a where curves C_1 and C_2 are chosen to measure the charge of the defect. The naive extension of the measuring path integral in Eq. (5.3) would be

$$\oint_C |\hat{\mathbf{n}} \times \partial_k \hat{\mathbf{n}}| \, d\ell_k. \tag{5.4}$$

This gives the correct result for curve C_1 in Fig. 5.2a, but for curve C_2, which is out of the normal plane, it does not. To understand this, consider the path traced out in order parameter space by the two curves, shown in Fig. 5.2b. Integrating $|\hat{\mathbf{n}} \times \partial_k \hat{\mathbf{n}}|$

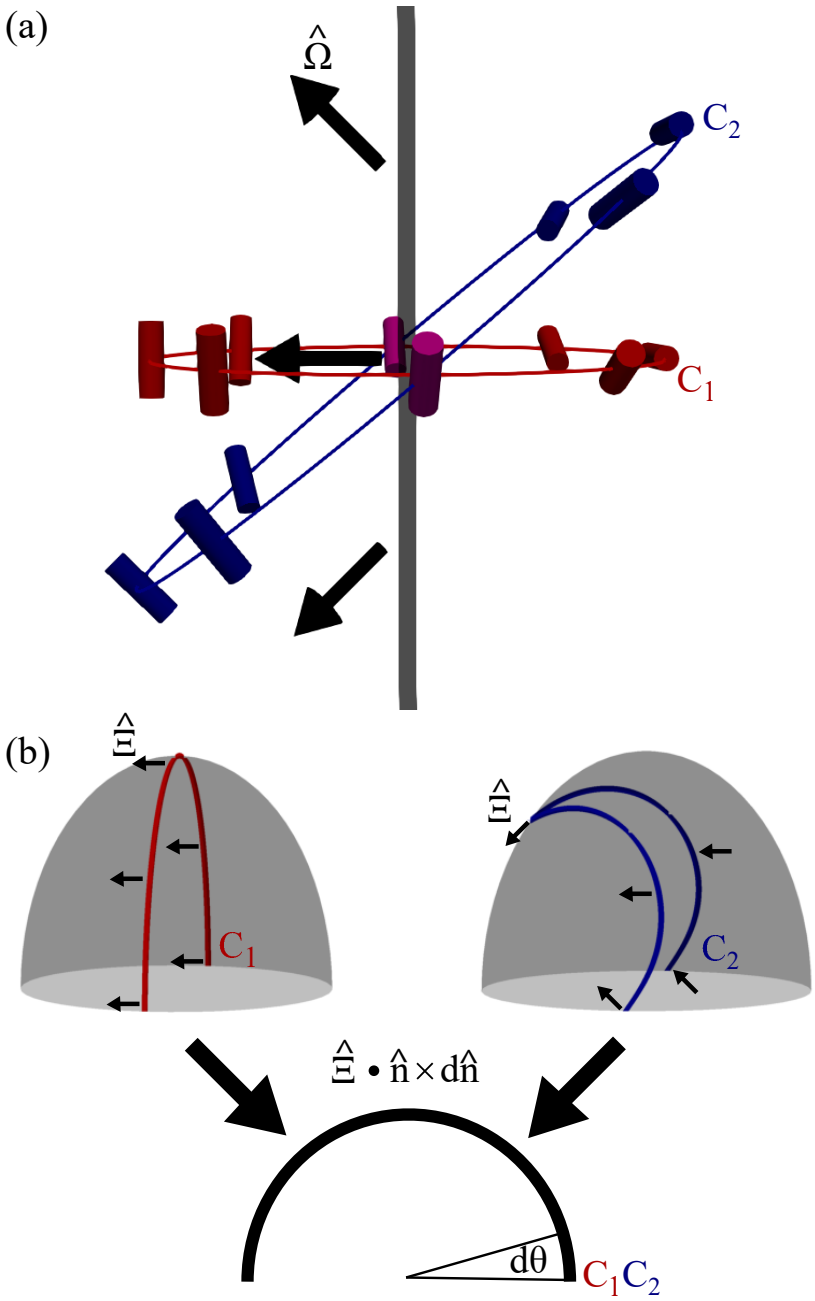

Figure 5.2: The charge of a disclination with varying $\hat{\mathbf{\Omega}}$ is measured with two curves C_1 and C_2. (a) C_1 remains in the normal plane to the disclination line where $\hat{\mathbf{\Omega}}$ is constant along the curve. C_2 is out of the normal plane. (b) Curves C_1 and C_2 in order parameter space. $\hat{\mathbf{\Xi}}$ is defined as the vector that projects the curve to a great circle, defined at each point along the curve. Integrating $\hat{\mathbf{\Xi}} \cdot (\hat{\mathbf{n}} \times d\hat{\mathbf{n}})$ yields the same charge for both curves since the projection collapses both curves onto the half circle with ends identified.

corresponds, in order parameter space, to integrating the arc length of the curve in this space, since

$$|\hat{\mathbf{n}} \times d\hat{\mathbf{n}}|^2 = \sin^2\theta d\phi^2 + d\theta^2 \tag{5.5}$$

which is the element of length squared written in terms of the metric on the unit sphere parameterized by spherical angles ϕ and θ. Thus, Eq. (5.4) depends on the path chosen and so does not give the topological charge of a defect if the curve in order parameter space is not a great circle. Further, if there is not a defect, the integral of Eq. (5.4) may still be nonzero.

Instead, we define a new integrand such that its integral gives the total topological charge of the the nematic it encircles. To do this, we construct a local unit vector, $\hat{\boldsymbol{\Xi}}$, so that $\hat{\boldsymbol{\Xi}} \cdot (\hat{\mathbf{n}} \times \partial_k \hat{\mathbf{n}})$ gives only the projected length of the curve in order parameter space along a great circle. The idea is that if one only integrates the contribution of arc length along a great circle, the total integral will either be the length of a great circle from opposite points on the equator (i.e. π) or zero if the curve does not pass through the equator, since equal contributions will move in opposite directions along the projection.

Explicitly, after mapping the measuring curve to order parameter space in the manner of Fig. 5.2, one fixes an arbitrary point on the curve in order parameter space that remains fixed throughout the calculation. Then, for each point on the curve, one computes

$$\hat{\boldsymbol{\Xi}} \equiv \hat{\mathbf{n}} \times d\hat{\mathbf{n}}'/|\hat{\mathbf{n}} \times d\hat{\mathbf{n}}'| \tag{5.6}$$

for every point along the curve. Here $d\hat{\mathbf{n}}'$ is the tangent vector for a great circle defined by the fixed point and the current point on the curve. From Eq. (5.6), it is straightforward to show that

$$\hat{\boldsymbol{\Xi}} \cdot (\hat{\mathbf{n}} \times d\hat{\mathbf{n}}) = \frac{d\hat{\mathbf{n}} \cdot d\hat{\mathbf{n}}'}{|\hat{\mathbf{n}} \times d\hat{\mathbf{n}}'|} \equiv d\varsigma \tag{5.7}$$

where we have introduced the notation ς to indicate the projected arclength along a great circle. This is illustrated in Fig. 5.2b, where the projection maps the curve in order parameter space to the half circle with ends identified. If a defect is present, the curve in order parameter space will have points on opposite sides of the equator, and the corresponding integral will be nonzero. However, if the curve does not contain points on the equator, the integral will yield zero as there will be equal parts positive

and negative projections along the half circle. We reiterate that the goal here is to show that

$$\oint_C d\varsigma = 0,\, \pi \tag{5.8}$$

independent of the curve, C, chosen to measure the charge.

We now prove this with the following argument. We first assume the curve in order parameter space is parameterized as $\hat{\mathbf{n}}(\tau)$ and does not pass through the equator (i.e., the curve in real space does not enclose a disclination). Let $\hat{\mathbf{n}}(0)$ be our fixed point on the curve, then let

$$\hat{\mathbf{V}}(\tau) = a(\tau)\hat{\mathbf{n}}(0) + b(\tau)\hat{\mathbf{n}}(\tau) \tag{5.9}$$

be such that $\hat{\mathbf{V}}(\tau) \cdot \hat{\mathbf{n}}(0) = 0$, which can be achieved via the Gram-Schmidt procedure. Then the curve

$$\hat{\mathbf{W}}(t, \tau) = \cos t\hat{\mathbf{n}}(0) + \sin t\hat{\mathbf{V}}(\tau) \tag{5.10}$$

parameterizes the great circle passing through $\hat{\mathbf{n}}(0)$ and $\hat{\mathbf{n}}(\tau)$ for any given τ. This is the case because, after some trigonometric manipulation, one can show that $\hat{\mathbf{W}}(t^*, \tau) = \hat{\mathbf{n}}(\tau)$ when $t^* = -\arctan(1/a(\tau))$. With these definitions, Eq. (5.7) can be written as

$$d\varsigma = \frac{d\hat{\mathbf{n}} \cdot d\hat{\mathbf{n}}'}{|\hat{\mathbf{n}} \times d\hat{\mathbf{n}}'|} = \left.\frac{d\hat{\mathbf{n}}/d\tau \cdot d\hat{\mathbf{W}}/dt}{|\hat{\mathbf{n}} \times d\hat{\mathbf{W}}/dt|}\right|_{t=t^*} d\tau. \tag{5.11}$$

Substituting Eq. (5.10) and integrating we find

$$\oint_C d\varsigma = \oint_C \frac{\hat{\mathbf{n}}(0) \cdot d\hat{\mathbf{n}}/d\tau}{|\hat{\mathbf{n}}(0) \times \hat{\mathbf{n}}(\tau)|}\, d\tau = \oint_C \frac{\hat{\mathbf{n}}(0) \cdot d\hat{\mathbf{n}}}{|\hat{\mathbf{n}}(0) \times \hat{\mathbf{n}}|}. \tag{5.12}$$

If the curve C does not cross the equator of the unit sphere the above integral is zero since the closed curve C traced by the directors $\hat{\mathbf{n}}(\tau)$ starts and ends at the same point.

Now, if the curve does cross the equator, then π must be added to the contour integral for each time the equator is crossed (since opposite points on the equator are identified). To show that exactly π must be added, consider a curve, C_1 such that $\hat{\mathbf{n}}(0)$ is on the equator and $\hat{\mathbf{n}}(1)$ is located on the opposite side of the equator, but let $\hat{\mathbf{n}}(\tau)$, $\tau \in (0, 1)$ be arbitrary (though still differentiable, of course). While this is not a closed curve on the unit sphere, it is a closed curve in our order parameter space. If we now add a curve C_2 that begins at $\hat{\mathbf{n}}(1)$ and ends at $\hat{\mathbf{n}}(0)$, but is specifically a great

circle, we may compute

$$\oint_{C_1+C_2} d\varsigma = 0 \tag{5.13}$$

from our arguments above. However, since C_2 is a great circle that moves "backwards" from $\tau = 1$ to $\tau = 0$ we have $\oint_{C_2} d\varsigma = -\pi$ so that

$$\oint_{C_1} d\varsigma = \pi. \tag{5.14}$$

A subtle point here is that if the equator is passed an even number of times, the configuration is topologically equivalent to a configuration with no defects. This is not reflected by our measure since we are representing the projective space with vectors, instead we manually take the result of the calculation modulo 2.

Thus, we can compute the defect charge through

$$\pi p = \oint_C \hat{\Xi}_\gamma \varepsilon_{\gamma\mu\nu} \hat{n}_\mu \partial_k \hat{n}_\nu \, d\ell_k \tag{5.15}$$

where $p \in \{0, 1\}$ is computed modulo 2 so that the defect charge is $m = p/2$ and $\hat{\mathbf{\Xi}}$ is not necessarily constant but defined locally on the curve C . We note that we must compute the final charge modulo 2 since an even number of defects can be topologically removed by annihilating the defects, or a defect that would have integer charge in two dimensions can be removed by local rotations in three dimensions.

As the measuring curve C is taken to be smaller and smaller, the resulting curve in order parameter space approaches a great circle (since near the defect $\hat{\mathbf{n}}$ approaches Eq. (5.1)) and hence, $\hat{\mathbf{\Xi}} \to \hat{\mathbf{\Omega}}$. Therefore, it will be useful to identify $\hat{\mathbf{\Omega}}$ as a geometric property of the defect core. We further note that the integrands of Eqs. (5.3) and (5.15) are similar to the disclination effective strain, defined in Ref. [38]. Since near the defect core $\hat{\mathbf{n}}$ can be taken as in Eq. (5.1), we find $\hat{\Omega}_\gamma \varepsilon_{\gamma\mu\nu} \hat{n}_\mu \partial_k \hat{n}_\nu = (1/2)\partial_k \phi$. For a two dimensional nematic, the effective disclination strain is $m\nabla\phi$ where m is the disclination charge. Hence the similarity in the expressions.

We now derive an expression for the disclination charge in terms of the tensor order parameter, $\mathbf{Q}$, rather than the director. $\mathbf{Q}$ is often the quantity that is worked with when studying disclinations since it regularizes the singularity at the core. To do this, we must be careful since the defect cores are spatially extended, with the order parameter

becoming biaxial around the center in order to regularize the singularity (see Chapter 4). If the order parameter is uniaxial, we find

$$\varepsilon_{\gamma\mu\nu}Q_{\mu\alpha}\partial_k Q_{\nu\alpha} = S_N^2\varepsilon_{\gamma\mu\nu}\hat{n}_\mu\partial_k\hat{n}_\nu. \tag{5.16}$$

Therefore, if one restricts the measuring curve C to only pass through points of constant S_N, which we denote as C_N, the charge may be obtained via the relation

$$S_0^2\pi p = \oint_{C_N} \hat{\Xi}_\gamma\varepsilon_{\gamma\mu\nu}Q_{\mu\alpha}\partial_k Q_{\nu\alpha}\, d\ell_k. \tag{5.17}$$

This generalizes Eq. (5.15) in terms of the tensor order parameter. Eq. (5.17) may be used to detect line disclinations, however, in practice it is complicated to compute $\hat{\mathbf{\Xi}}$ for various curves. Additionally, many curves must be constructed to measure the full extent of a disclination line. Therefore, we instead use Eq. (5.17) as a starting point to derive a local quantity that is much more useful in practice.

To find a locally defined quantity, we first apply Stokes' theorem to Eq. (5.17), which yields

$$S_0^2\pi p = \int_{\Gamma_N} \varepsilon_{i\ell k}\partial_\ell\left(\hat{\Xi}_\gamma\varepsilon_{\gamma\mu\nu}Q_{\mu\alpha}\partial_k Q_{\nu\alpha}\right)\, da_i \tag{5.18}$$

where Γ_N is a surface bounded by curve C_N, da_i is an element of area on the surface, and $\hat{\mathbf{\Xi}}$ is extended to be defined over the surface. The integrand in Eq. (5.18) is a vector comprised of three terms:

$$\varepsilon_{i\ell k}\left(\partial_\ell\hat{\Xi}_\gamma\varepsilon_{\gamma\mu\nu}Q_{\mu\alpha}\partial_k Q_{\nu\alpha} + \hat{\Xi}_\gamma\varepsilon_{\gamma\mu\nu}\partial_\ell Q_{\mu\alpha}\partial_k Q_{\nu\alpha} + \hat{\Xi}_\gamma\varepsilon_{\gamma\mu\nu}Q_{\mu\alpha}\partial_\ell\partial_k Q_{\nu\alpha}\right). \tag{5.19}$$

The third term is trivially zero since $\mathbf{Q}$ is a regular quantity with no singularities. The first term is zero near defects since $\hat{\mathbf{\Xi}} \to \hat{\mathbf{\Omega}}$ and $\varepsilon_{\gamma\mu\nu}Q_{\mu\alpha}\partial_k Q_{\nu\alpha} \propto \hat{\Omega}_\gamma$ near the defect core. Thus, since $\hat{\mathbf{\Omega}}$ is a unit vector its derivative will be perpendicular to itself and the first term above will be zero. Away from the core this quantity may not go to zero, and in fact must be nonzero to give zero total charge for some configurations, such as those containing double-splay or double-twist [45], which we discuss in more detail in Sec. 5.6. However, numerically we find that this term is zero for most director configurations that involve disclinations. This leaves a single nonzero term near defects and leads to our

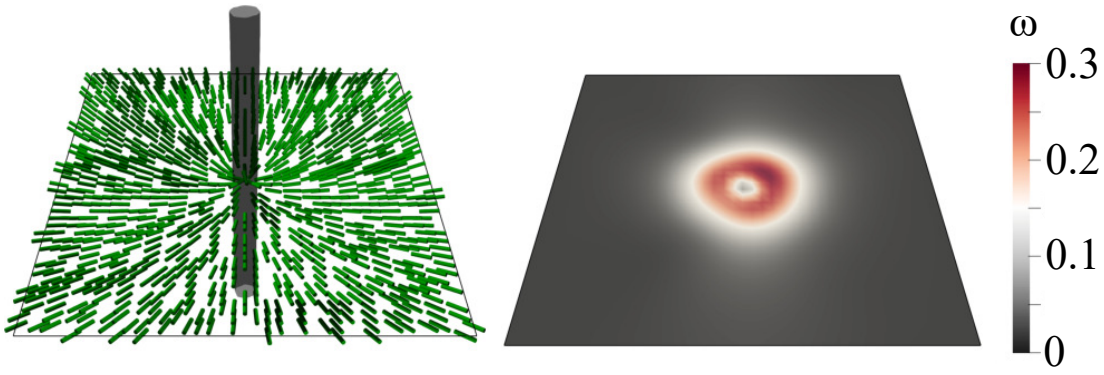

Figure 5.3: (Left) Cylinders depict the director orientation for a +1 simulated line defect. The contour shows where the scalar order parameter $S = 0.3S_N$. (Right) Magnitude of $\mathbf{D}$, ω, for the +1 line defect. Note that at the center of the defect, $\omega = 0$.

primary result, which we call the disclination density tensor,

$$D_{\gamma i} := \varepsilon_{\gamma\mu\nu}\varepsilon_{ik\ell}\partial_k Q_{\mu\alpha}\partial_\ell Q_{\nu\alpha}. \tag{5.20}$$

We remark that for two-dimensional configurations, the appropriate quantity that identifies disclinations is D_{33}, which has been used in previous studies to track and identify defects [110, 111]. Thus, this tensor goes to the correct limit in the two dimensional case.

The disclination density tensor may be computed directly from the nematic order parameter and hence it is locally defined and continuous. Further, $\mathbf{D} \neq 0$ for nonsingular distortions when S is constant, except for a few special cases such as double-splay and double-twist, which are not topologically protected and cost a large amount of energy. This can be seen by using the parameterization Eq. (2.3) for a constant $S = S_N$ and a uniaxial nematic:

$$D_{i\gamma} = S_N^2\varepsilon_{ik\ell}\varepsilon_{\gamma\mu\nu}\partial_k\hat{n}_\mu\partial_\ell\hat{n}_\nu \tag{5.21}$$

which is zero for director distortions with no double-splay or double-twist (see Sec. 5.6). Thus the tensor $\mathbf{D}$ may be used as a local identifier of disclinations.

Additionally, the eigenvector structure of $\mathbf{D}$ may also be used to identify the geometric properties of disclination lines. To first gain some analytical intuition about the structure of $\mathbf{D}$ at disclinations, we seek an approximation of $\mathbf{Q}$ near the defect

core. Taking a point on a disclination located at $\mathbf{r} = (0, 0, 0)$, if we are close to the core, but far enough away so that the distribution is uniaxial and we can write $\mathbf{Q} = S_N\left(\hat{\mathbf{n}} \otimes \hat{\mathbf{n}} - (1/3)\mathbf{I}\right)$. Taking $\hat{\mathbf{n}}$ as in Eq. (5.1), and substituting $\hat{\mathbf{n}}$ in the uniaxial form of $\mathbf{Q}$ gives

$$\begin{aligned}
\mathbf{Q} &= S_N\left[\cos^2\frac{1}{2}\phi\hat{\mathbf{n}}_0 \otimes \hat{\mathbf{n}}_0 + \sin^2\frac{1}{2}\phi\hat{\mathbf{n}}_1 \otimes \hat{\mathbf{n}}_1 + \cos\frac{1}{2}\phi\sin\frac{1}{2}\phi\left(\hat{\mathbf{n}}_0 \otimes \hat{\mathbf{n}}_1 + \hat{\mathbf{n}}_1 \otimes \hat{\mathbf{n}}_0\right) - \frac{1}{3}\mathbf{I}\right] \\
&= S_N\left[\cos^2\frac{1}{2}\phi\left(\hat{\mathbf{n}}_0 \otimes \hat{\mathbf{n}}_0 - \hat{\mathbf{n}}_1 \otimes \hat{\mathbf{n}}_1\right) + \frac{1}{2}\sin\phi\left(\hat{\mathbf{n}}_0 \otimes \hat{\mathbf{n}}_1 + \hat{\mathbf{n}}_1 \otimes \hat{\mathbf{n}}_0\right)\right. \\
&\qquad\qquad \left. + \left(-\frac{1}{3}\hat{\mathbf{n}}_0 \otimes \hat{\mathbf{n}}_0 + \frac{2}{3}\hat{\mathbf{n}}_1 \otimes \hat{\mathbf{n}}_1 - \frac{1}{3}\hat{\mathbf{\Omega}} \otimes \hat{\mathbf{\Omega}}\right)\right] \\
&= S_N\left[\frac{1}{6}\mathbf{I} - \frac{1}{2}\hat{\mathbf{\Omega}} \otimes \hat{\mathbf{\Omega}} + \frac{1}{2}\cos\phi\left(\hat{\mathbf{n}}_0 \otimes \hat{\mathbf{n}}_0 - \hat{\mathbf{n}}_1 \otimes \hat{\mathbf{n}}_1\right) + \frac{1}{2}\sin\phi\left(\hat{\mathbf{n}}_0 \otimes \hat{\mathbf{n}}_1 + \hat{\mathbf{n}}_1 \otimes \hat{\mathbf{n}}_0\right)\right]
\end{aligned} \tag{5.22}$$

where we have used familiar trigonometric identities and the fact that $\{\hat{\mathbf{n}}_0, \hat{\mathbf{n}}_1, \hat{\mathbf{\Omega}}\}$ form an orthonormal triad so that $\mathbf{I} = \hat{\mathbf{n}}_0 \otimes \hat{\mathbf{n}}_0 + \hat{\mathbf{n}}_1 \otimes \hat{\mathbf{n}}_1 + \hat{\mathbf{\Omega}} \otimes \hat{\mathbf{\Omega}}$. If we now take an orthonormal triad representing the orientation of the disclination line, $\{\hat{\boldsymbol{\nu}}_0, \hat{\boldsymbol{\nu}}_1, \hat{\mathbf{T}}\}$, we note that

$$\begin{aligned}
\cos\phi &= \frac{\hat{\boldsymbol{\nu}}_0 \cdot \mathbf{r}}{|\hat{\mathbf{T}} \times \mathbf{r}|} \\
\sin\phi &= \frac{\hat{\boldsymbol{\nu}}_1 \cdot \mathbf{r}}{|\hat{\mathbf{T}} \times \mathbf{r}|}.
\end{aligned} \tag{5.23}$$

This description of $\mathbf{Q}$ is valid for $|\hat{\mathbf{T}} \times \mathbf{r}| > a$ where a is the radius of the disclination core. For $|\hat{\mathbf{T}} \times \mathbf{r}| < a$, the inner core region, the eigenvalues of $\mathbf{Q}$ are not constant. We approximate the inner core region by linearly extrapolating in $\mathbf{r}$ to $\mathbf{r} = 0$, that is

$$\begin{aligned}
\cos\phi &\to \frac{\hat{\boldsymbol{\nu}}_0 \cdot \mathbf{r}}{a} \\
\sin\phi &\to \frac{\hat{\boldsymbol{\nu}}_1 \cdot \mathbf{r}}{a},
\end{aligned} \tag{5.24}$$

so that

$$\mathbf{Q} \approx S_N \left[\frac{1}{6}\mathbf{I} - \frac{1}{2}\hat{\mathbf{\Omega}} \otimes \hat{\mathbf{\Omega}} + \frac{\hat{\boldsymbol{\nu}}_0 \cdot \mathbf{r}}{2a} \left(\hat{\mathbf{n}}_0 \otimes \hat{\mathbf{n}}_0 - \hat{\mathbf{n}}_1 \otimes \hat{\mathbf{n}}_1 \right) + \frac{\hat{\boldsymbol{\nu}}_1 \cdot \mathbf{r}}{2a} \left(\hat{\mathbf{n}}_0 \otimes \hat{\mathbf{n}}_1 + \hat{\mathbf{n}}_1 \otimes \hat{\mathbf{n}}_0 \right) \right]. \tag{5.25}$$

This linear core approximation was introduced in Ref. [38] and is actually quite a close approximation to simulation and experiments, particularly near the core. Remarkably, even though far from the core $\mathbf{Q}$ is uniaxial, as the core is approached the approximation becomes biaxial and the eigenvalues cross at the core, just as one expects (see Sec. 4.5). We will use this approximation throughout the rest of this dissertation and we will often align our axes so that $\hat{\boldsymbol{\nu}}_1 = \hat{\mathbf{x}}$, $\hat{\boldsymbol{\nu}}_1 = \hat{\mathbf{y}}$, and $\hat{\mathbf{T}} = \hat{\mathbf{z}}$.

Using this approximation, we compute $\mathbf{D}$ from Eq. (5.20) so that, near the defect, $\mathbf{D}$ decomposes as

$$\mathbf{D}(\mathbf{r}) = \omega(\mathbf{r}) \left(\hat{\mathbf{\Omega}} \otimes \hat{\mathbf{T}} \right) \tag{5.26}$$

where $\omega(\mathbf{r})$ is a non-negative scalar field which is at its maximum at the disclination core with $\omega(0) = S_N^2/a^2$. In typical cases, ω is non-zero only inside a diffuse core (on the order of the biaxiality length), and is zero far from defect cores where the order parameter is uniaxial.

The linear core approximation used above does break down away from the core of the defect, yet, as we show later in Sec. 5.4, the decomposition of Eq. (5.26) holds. We also find that ω goes to zero at the core of integer line defects, shown in Fig. 5.3. This is a nice result since in three dimensions integer line defects are unstable, since they can be rotated into the third dimension to continuously remove the defect line (see e.g. the discussion in Sec. 5.2). This is called the "escape to the third dimension" and can result in a system with no defect, or one or more hedgehog defects along the original line [1].

Another useful property of $\mathbf{D}$ is that it inherently fixes the sign of $\hat{\mathbf{\Omega}} \cdot \hat{\mathbf{T}}$. A common issue with determining the character of a disclination line is that the independent vectors $\hat{\mathbf{\Omega}}$ and $\hat{\mathbf{T}}$ are defined only up to a sign, and it is the sign of their scalar product that determines the winding character of the disclination (the winding character refers to whether the disclination is of type "wedge", "twist", or a combination of the two). The scalar product is proportional to the trace of $\mathbf{D}$ and, hence, once a direction for $\hat{\mathbf{T}}$ (or $\hat{\mathbf{\Omega}}$) is chosen the sign of the other vector is fixed by definition. If one is only interested in the winding character of the line one only needs to compute the trace of $\mathbf{D}$.

Because the disclination density tensor can be computed from only the first derivative of the order parameter, this method of identifying defects and obtaining geometric information is powerful and should prove useful in both computational and experimental studies. In the next section we show how $\hat{\mathbf{\Omega}}$ and $\hat{\mathbf{T}}$ can be numerically determined from $\mathbf{Q}$ for various simulated defect configurations. Before we do this, we first note that we do not expect the construction of $\mathbf{D}$ to hold for strongly curved defects such as in the transient stages of defect nucleation or annihilation. By strongly curved, we mean that $\kappa a \gtrsim 1$ where κ is the disclination line curvature and a is the radius of the defect core. For curvatures this large, the continuum description of the disclination breaks down and hence the definition of $\mathbf{D}$ is no longer valid.

5.4 Numerical Examples

We now present several examples of the practical application of $\mathbf{D}$ on several numerical examples of various defect configurations in three dimensions. First, to determine ω, $\hat{\mathbf{\Omega}}$, and $\hat{\mathbf{T}}$ one computes $\mathbf{D}$ from the first derivatives of $\mathbf{Q}$ and Eq. (5.20). ω is computed as the Frobenius norm of $\mathbf{D}$ ($\omega = \sqrt{D_{\gamma i} D_{\gamma i}}$). $\hat{\mathbf{\Omega}}$ is the non-degenerate eigenvector of the product $\mathbf{D}\mathbf{D}^T$ while $\hat{\mathbf{T}}$ is that of $\mathbf{D}^T\mathbf{D}$. Finally, one must ensure that both $\hat{\mathbf{T}}$ and $\hat{\mathbf{\Omega}}$ are continuous along the disclination line. This can be accomplished by fixing the direction of the tangent vector (in our experience, this is the easier vector to fix) and then fixing $\hat{\mathbf{\Omega}}$ everywhere by enforcing $\text{sgn}\left(\hat{\mathbf{\Omega}} \cdot \hat{\mathbf{T}}\right) = \text{sgn}\left(\text{Tr}\left[\mathbf{D}\right]\right)$.

The examples shown in this section were computed using the self-consistent model of Chapter 2, and a finite element discretization. In all calculations $\kappa/nk_BT = 4$ and $\Delta t = 0.1$. We use a standard tetrahedral mesh with varying numbers of vertices depending on the defect configuration.

We first show simple examples in which $\hat{\mathbf{\Omega}}$ and $\hat{\mathbf{T}}$ are known *a priori*. Fig. 5.4a shows a straight line defect with varying $\hat{\mathbf{\Omega}}$ along its length. The left figure shows the director configuration in three different planes while the right figure shows the field ω along with the computed $\hat{\mathbf{\Omega}}$ and $\hat{\mathbf{T}}$ at the center of the defect. Fig. 5.4b shows an example with multiple line defects. One defect has $\hat{\mathbf{\Omega}} = -\hat{z}$ while the other has $\hat{\mathbf{\Omega}} = \hat{y}$ and hence they are perpendicular. It was shown in Ref. [38] (and will be derived in another way in Chapter 7) that straight defects with perpendicular $\hat{\mathbf{\Omega}}$s do not interact with one

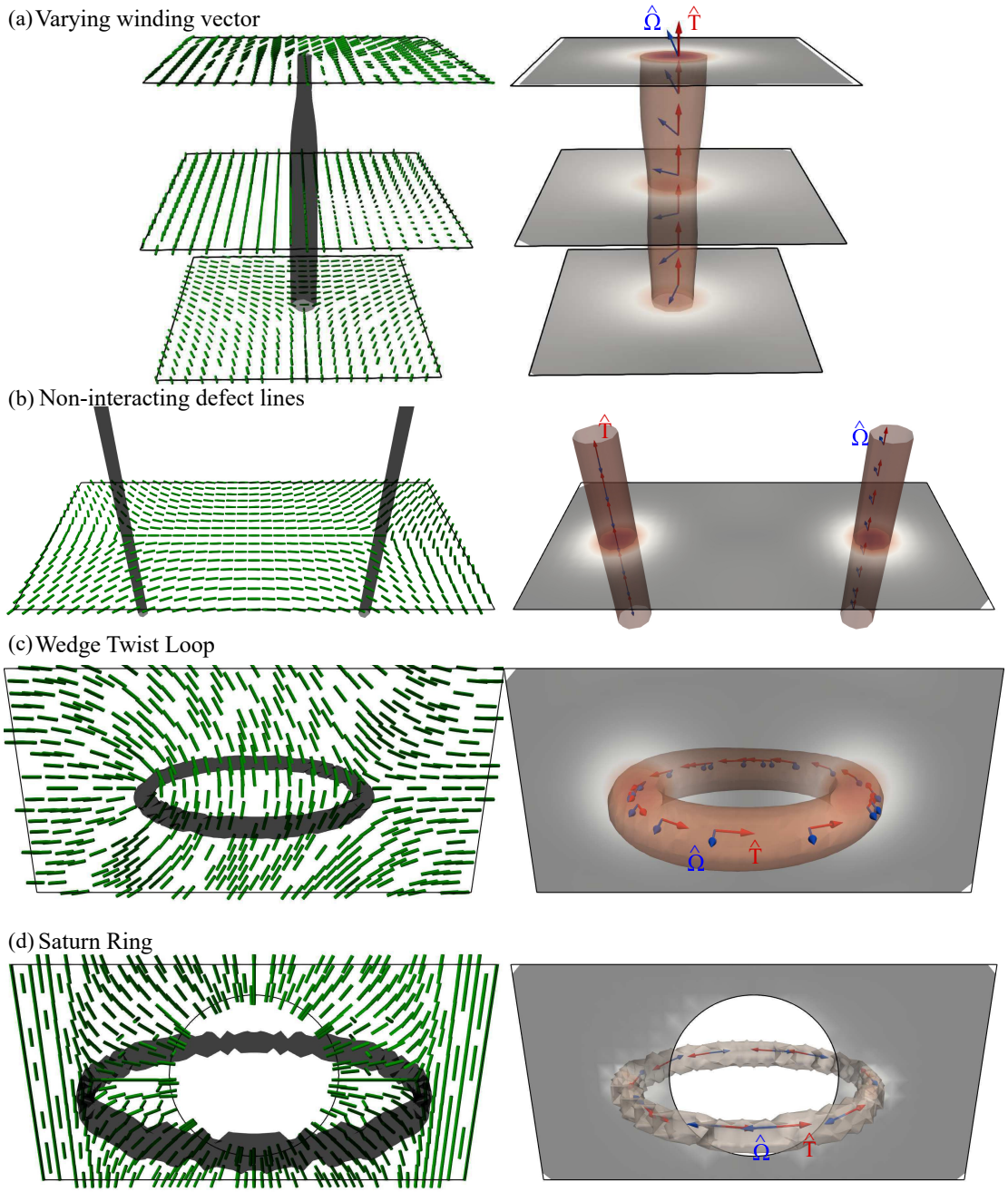

Figure 5.4: Various simulated defect director configurations (left) and the corresponding computed decomposition of the disclination density tensor (right). On the left, cylinders represent the director orientation while contours show where $S = 0.3S_N$. On the right, the grey to red color scale shows ω with contours indicating where $\omega = 0.7\omega_{\max}$ while blue vectors indicate computed $\hat{\mathbf{\Omega}}$ and red vectors are $\hat{\mathbf{T}}$. The examples shown are (a) a straight disclination line with varying $\hat{\mathbf{\Omega}}$, (b) two non-interacting defect lines with perpendicular $\hat{\mathbf{\Omega}}$s, (c) a snapshot of a wedge twist loop disclination, and (d) a Saturn ring loop disclination.

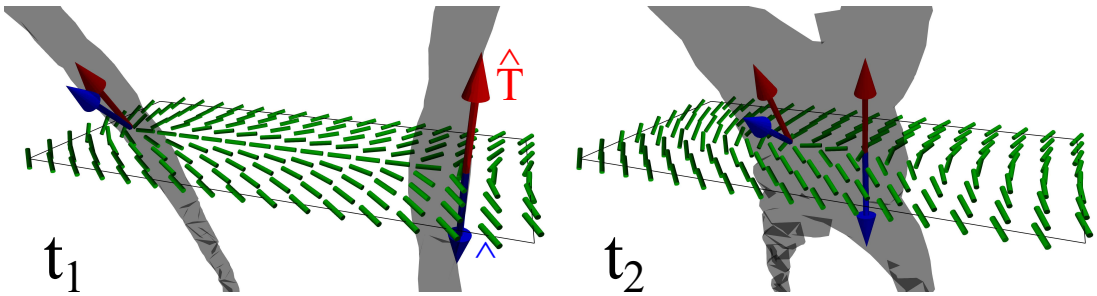

Figure 5.5: Time snapshots of simulated annihilating disclination which are initially straight and have constant $\hat{\mathbf{\Omega}}$, but have non-parallel tangent and rotation vectors. The snapshot at the right occurs near annihilation at the closest point between the lines. The cylinders represent the director orientation while the contour shows where $S = 0.3S_N$. The blue vectors show $\hat{\mathbf{\Omega}}$ for each defect while the red vectors show $\hat{\mathbf{T}}$.

another, hence we find two straight line defects that do not move. Fig. 5.4c shows a snapshot of a self-annihilating wedge-twist loop defect, showing that the construction of $\mathbf{D}$ can also be used for weakly curved defects. In this configuration, $\hat{\mathbf{\Omega}}$ is constant along the loop and lies in the plane of the loop. Fig. 5.4d shows a Saturn ring configuration where homeotropic anchoring on a colloidal particle induces a disclination loop where $\hat{\mathbf{\Omega}} \cdot \hat{\mathbf{T}} = -1$ along the loop. The loop defects show that it is particularly important to be able to identify $\hat{\mathbf{\Omega}} \cdot \hat{\mathbf{T}}$ to understand the defect structure. We also note that the loop of Fig. 5.4c has a point charge of 0 while the Saturn ring loop defect in Fig. 5.4d has a point charge of -1, showing that $\mathbf{D}$ can be used for either case.

We now display a couple of examples where the director configuration is not known *a priori* but needs to be computed, in this case by relaxation driven by energy minimization e.g. Eq. (2.21). First, we consider the case of line disclination annihilation (sometimes referred to as disclination "recombination" [21]). Fig. 5.5 shows two snapshots in time of the disclination line geometry as given by $\mathbf{D}$ as two disclinations with non-parallel initial tangent vectors and rotation vectors are close to annihilating. Here, both $\hat{\mathbf{T}}$ and $\hat{\mathbf{\Omega}}$ change during the annihilation, and each defect develops curvature near the point closest to the other defect. $\hat{\mathbf{T}}$ and $\hat{\mathbf{\Omega}}$ can be computed up to the annihilation event, and while only shown for a single point, $\hat{\mathbf{T}}$ and $\hat{\mathbf{\Omega}}$ can be computed along the entire defect line. We will more systematically analyze the annihilation of defect lines in Chapter 7.

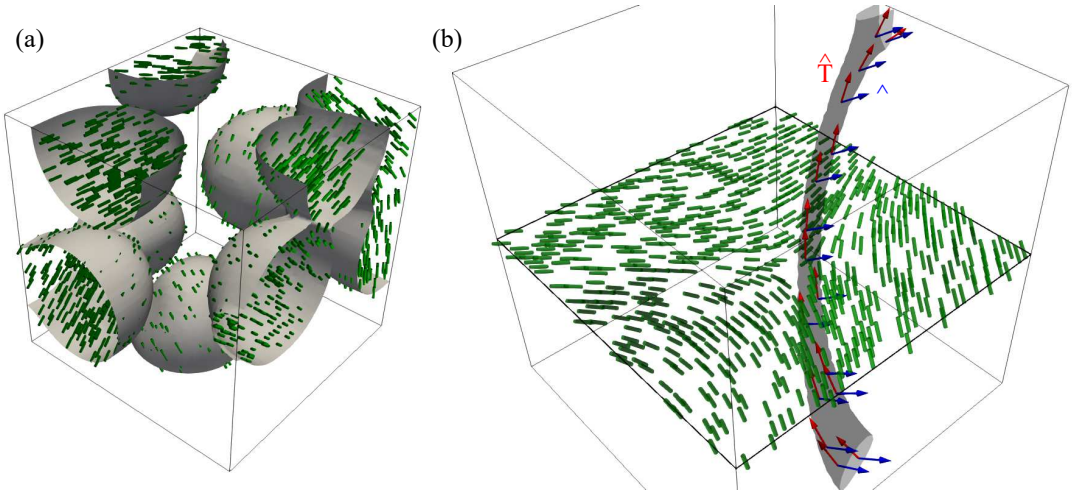

Figure 5.6: Simulated quench into the nematic phase from randomly generated domains with randomly generated director orientation. (a) Initial condition with 12 randomly generated domains of uniform director orientation. The green cylinders represent the director orientation while the contours show where $S = 0.5S_N$. (b) Relaxed configuration after 60 iterations which resulted in the nucleation of a disclination line. $\mathbf{D}$ is computed and decomposed into $\hat{\mathbf{\Omega}}$ and $\hat{\mathbf{T}}$ along the line with each being shown in blue vectors and red vectors respectively.

The second complex example we show is the formation of a line disclination from the coalescence of domains with random uniform orientation. Fig. 5.6a shows the initial condition with randomly generated domains all with randomly generated director orientation. Since we simulate a quench into the nematic phase, the domains grow until they coalesce. This coalescence can cause a defect to form if there is a large enough mismatch in director orientation. Fig. 5.6b shows the configuration after 60 iterations where a line disclination has formed. We compute $\mathbf{D}$ and the resulting $\hat{\mathbf{\Omega}}$ and $\hat{\mathbf{T}}$ and find that the nucleated disclination is weakly curved and has a roughly constant $\hat{\mathbf{\Omega}}$ which is close to perpendicular to $\hat{\mathbf{T}}$. This shows an example of the Kibble mechanism of line defect formation, which has been argued to be analogous to domain coalescence in the case of nematics [112, 113].

Both of the previous sets of examples display the power of the disclination density tensor method in defect identification and characterization. We conclude this section by commenting on the methods for determining $\hat{\mathbf{\Omega}}$ laid out in the supplementary information of Ref. [24] and how they compare to our methods presented here. First, the local formula, $\tilde{\mathbf{\Omega}} = \hat{\mathbf{n}} \times (\hat{\mathbf{n}} \cdot \nabla)\, \hat{\mathbf{n}}$ is similar to the definition of $\hat{\mathbf{\Xi}}$, except there is no reference to a measuring curve and the directional derivative is in the direction of $\hat{\mathbf{n}}$ rather than the direction of the great circle as described in Sec. 5.3. Thus $\tilde{\mathbf{\Omega}}$ is proportional to $\hat{\mathbf{\Omega}}$ at the disclination core since $\hat{\mathbf{\Xi}} \to \hat{\mathbf{\Omega}}$ but goes to zero for pure twist disclinations. The other method described in Ref. [24] is a non-local construction where a curve surrounding a disclination line in real space is mapped to the corresponding curve in order parameter space. $\hat{\mathbf{\Omega}}$ is then the normal vector to the curve in order parameter space. This gives the correct $\hat{\mathbf{\Omega}}$ as long as $\hat{\mathbf{n}}$ is as in Eq. (5.1). However, since $\hat{\mathbf{n}}$ may deviate from Eq. (5.1) due to external constraints, curvature of the defect, or the presence of other defects one is not guaranteed to obtain an accurate $\hat{\mathbf{\Omega}}$. Additionally, it is computationally taxing, since a new curve must be generated for every point along the disclination. Thus, the local method of determining $\hat{\mathbf{\Omega}}$ and $\hat{\mathbf{T}}$ from $\mathbf{D}$ is more robust and computationally viable for large systems.

5.5 Conclusion

Here we have reviewed the structure and geometric description of disclination lines in three dimensional nematics. The uniqueness and complexity of the topology and geometry of the lines has made it difficult to come up with mathematical tools that identify defect locations and geometry. We have thus contributed to recent efforts to fundamentally understand the nature of defect lines and loops in nematics. By introducing the disclination density tensor, $\mathbf{D}$, we have introduced a computationally feasible way to identify disclination line properties in computational and experimental systems. The complex examples of defect annihilation and nucleation shown here exemplify the usefulness in systems such as active nematics where defects are the generators of motion in the system, and are constantly nucleating and recombining.

There is still more theoretical work that can be done as well. It will be useful to have a more rigorous mathematical analysis of the disclination density tensor $\mathbf{D}$. As we show in the next chapter, $\mathbf{D}$ can also be related to the Jacobian of the map from real space to order parameter space in some situations. Understanding this connection more broadly is important. Additionally, as mentioned, $\mathbf{D}$ is nonzero in the presence of double-splay and double-bend distortions, even when there are no disclinations. We expand on this case in the following appendix; however, we note that there is still much work that can be done in understanding how $\mathbf{D}$ may be used in these contexts.

5.6 Appendix: Disclination Density Tensor for Double-Splay Configurations

As previously mentioned, $\mathbf{D}$ may be nonzero in specific configurations that do not contain a topological defect; for example in configurations with double-splay or double-twist distortion. We can explicitly calculate $\mathbf{D}$ in this case by considering $\hat{\mathbf{n}} = \cos k\rho\hat{\mathbf{z}} + \sin k\rho\hat{\boldsymbol{\rho}}$ in cylindrical coordinates. The resulting configuration is shown in Fig. 5.7. This is a "double-splay" configuration where the director is splayed in both directions and k characterizes the inverse length scale of the distortion. A double-twist configuration can be obtained by replacing $\hat{\boldsymbol{\rho}} \to \hat{\boldsymbol{\theta}}$ in the equation for $\hat{\mathbf{n}}$.

Given the double-splay configuration above we compute $\mathbf{D}$ at $\rho = 0$ using Eq. (5.21),

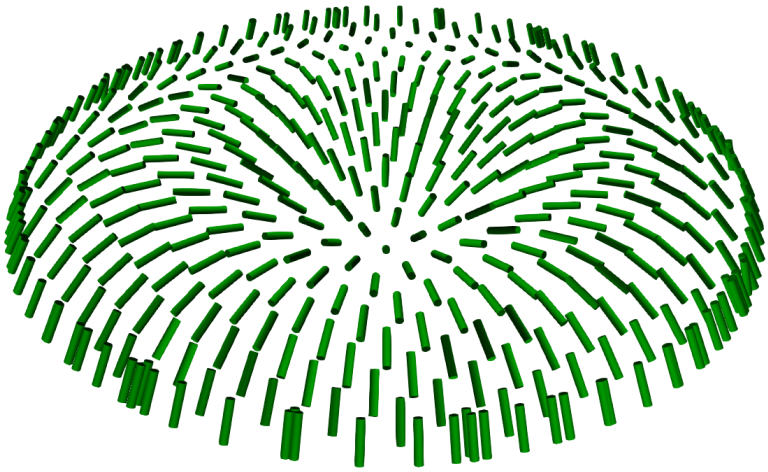

Figure 5.7: Example configuration in which the director exhibits double-splay.

and find,

$$\mathbf{D} = S_N^2 k^2 \left(\hat{\mathbf{z}} \otimes \hat{\mathbf{z}}\right). \tag{5.27}$$

We note that the result is the same for a double twist configuration. Thus, for these configurations $\mathbf{D} \neq 0$. However, we note that computing the charge defined in Eq. (5.15) along *any* curve C in this configuration, the charge is zero. This is because the corresponding curve in order parameter space will either not pass through the equator, or will do so an even number of times giving zero modulo two. This implies that it is possible to continuously remove the distortions to yield an undefected configuration. In experiments, such a relaxation will happen rapidly in systems in which the free energy penalizes such elastic distortions, e.g., the systems we are concerned with in this dissertation. This is why we do not observe them in the simulations presented here.

Nevertheless, there are several liquid crystal systems which do support these distortions energetically. These are primarily cholesterics, in which the nematogens break chiral symmetry and in turn support spontaneous twist deformations [1]. These systems have been shown to exhibit spontaneous double-twist separated by disclinations, known as "blue phases" [87, 114]. Additionally, and more recently, lyotropic chromonics have been shown to exhibit double-twist configurations in tubes [115]. Further, for liquid

crystals that have a strong response to external fields, topological defects known as "Skyrmions" may form when an external field is introduced [116, 117]. These defects are not disclinations, and instead share properties with skyrmions in magnetic systems [118]. In all such cases, namely systems in which elasticty or confinement promote double-splay or double-twist configurations, one would need the tensor order parameter, $\mathbf{Q}$, in addition to $\mathbf{D}$ to fully characterize regions where $\mathbf{D}$ is nonzero. This is not a problem, however, since $\mathbf{D}$ is computed from $\mathbf{Q}$ in the first place. Alternatively, formally, one may use the contour integral methodology as laid out in Sec. 5.3 to identify the existence of a disclination or not. $\mathbf{D}$ being nonzero for configurations such as Skyrmions and blue phases raises interesting possible future avenues in using $\mathbf{D}$ to study these systems as well.

Chapter 6

Kinematics of Disclinations

6.1 Introduction

In addition to the identification of defects in physical systems, understanding their dynamics has been of interest in a wide variety of fields including cosmology, superconductivity, metallurgy, and, of course, liquid crystals [7, 9, 24, 96, 113, 119, 120]. This has been the focus more recently in the burgeoning field of active nematics. This is because defects in active nematics drive local flows, and hence can be viewed as the fundamental "particles" (or excitations) that keep the system out of equilibrium [103, 104]. For engineered materials, defect dynamics is important for understanding how applying external stresses and flows will affect the shape and structure of defect lines [86]. Additionally, there are more advanced experimental techniques being developed that allow us to image and analyze the coarsening of defects in nematics and gain an understanding of the complex annihilation of loops and lines in three dimensions [19–21].

In two dimensions, the dynamics of disclinations is that of point objects. Much work has already been carried out in understanding the dynamics of these point-like defects. The dynamics of annihilation has been studied thoroughly for $\pm 1/2$ defects for the cases of passive, relaxational dynamics and for hydrodynamic coupling to backflows [9, 121, 122]. Additionally, the unbinding of defects in two dimensional active nematics has been likened to the Berezinskii-Kosterlitz-Thouless transition of the XY model [7, 103]. There are also reports of static and dynamic defect states that have been compared with vortex lattices in type-II superconductors [100, 123]. To understand the dynamics

of these systems, there have been recent studies that have shifted the focus from the nematogens to the defects themselves [103, 104].

For three dimensional disclinations there has been less theoretical investigation, likely due to the higher complexity of the system as described in Sec. 5.2. For disclination annihilation, one can rely on energetic arguments to predict the time dependence of recombination [21]. Further, analogies with dislocations in solid systems can allow one to define an "effective stress" imposed by disclinations on one another [38]. Recent efforts have also been made to understand the evolution of defect loops in active nematics [96, 120]. In this chapter, we relate the disclination line density to the disclination density tensor introduced in Sec. 5.3 by proving that it is related to the Jacobian matrix relating real space and order parameter space near defects. We then invoke the Halperin-Mazenko formalism [39–41, 124] to use the topological charge conservation and derive a kinematic law for disclination lines in three-dimensional nematics. This kinematic law applies regardless of the type of dynamics imposed on the system, i.e. whether the system is governed by relaxation, hydrodynamics, or active stresses.

6.2 Defect Line Densities

To derive a kinematic equation for the velocity of disclination lines we must first derive the associated disclination line density from the tensor order parameter, $\mathbf{Q}$. Because disclinations are lines, the defect density is a vector, directed along the tangent line to the disclination. If there are N distinct disclinations, the disclination line density is [124]

$$\boldsymbol{\rho}(\mathbf{r}) = \frac{1}{2}\sum_{j}^{N}\int_{C_j}\frac{d\mathbf{R}_j}{ds}\delta\left[\mathbf{r}-\mathbf{R}_j(s)\right]\,ds \tag{6.1}$$

where $\mathbf{r}$ is the position, C_j denotes the curve traced out by the jth disclination line (it does not denote the circuit of the previous chapter to define topological charge), and $\mathbf{R}_j(s)$ is the position of the jth line at point s along the curve, and the factor of $1/2$ comes from the charge of the defect. This expression is clearly directed along the tangent line to the disclination since $d\mathbf{R}_j/ds \propto \hat{\mathbf{T}}_j$. Integrating the line density over the system yields $(1/2)\sum L_j$, where L_j is the length of the jth disclination line. We also note that the charge of the disclination is always $1/2$, hence the factor of $1/2$ in front

of the right hand side of Eq. (6.1).

In the Halperin-Mazenko formalism, developed for superfluids and n-vector models [40, 41], the defect density is also defined by an order parameter that goes to zero at defect locations. For two dimensional nematics, $\mathbf{Q}$ goes to zero at defect locations, and one writes [104]

$$\begin{aligned} \rho^{2\mathrm{D}}(\mathbf{r}) &= \delta\left[\mathbf{Q}(\mathbf{r})\right] D(\mathbf{r}) \\ D &= \varepsilon_{\mu\nu}\varepsilon_{k\ell}\partial_k Q_{\mu\alpha}\partial_\ell Q_{\nu\alpha} \end{aligned} \tag{6.2}$$

where D is the Jacobian that relates order parameter space to real space.

In three dimensions, however, the order parameter $\mathbf{Q}$ does *not* go to zero at defect locations (see Sec. 4.5). Instead, its eigenvalues cross and $S = P$ at the core of the line. Thus one cannot directly use the full order parameter to locate the disclination, nor to define the disclination density in three dimensions. However, at the core we do have $S - P = 0$. Thus, we formulate the problem of singularity identification to finding zeros of the two-dimensional subspace of order parameter space defined by $S - P$. To find the corresponding Jacobian relating this subspace to real space we must know how the degrees of freedom are changing near the core of a disclination. We note that $\hat{\mathbf{n}}$ is orthogonal to $\hat{\mathbf{\Omega}}$ everywhere near the core so there is only one degree of freedom describing the orientation of $\hat{\mathbf{n}}$. Hence, our subspace only has two degrees of freedom that change near the disclination core, namely $S - P$ and ϕ, where ϕ is the angle of the nematogens with respect to a reference axis in the plane perpendicular to $\hat{\mathbf{\Omega}}$. Symbolically, we denote the corresponding delta function on this two dimensional subspace as $\delta\left[\mathbf{Q}_\perp\right]$. Fig. 6.1 shows this subspace schematically.

To compute the Jacobian relating this subspace to real space we first compute, using Eq. (2.3) with $\hat{\mathbf{n}} = (\cos\phi, \sin\phi, 0)$ and $\mathbf{m} = (-\sin\phi, \cos\phi, 0)$, that near the core of a defect with rotation vector $\hat{\mathbf{\Omega}}$

$$\hat{\Omega}_\gamma \varepsilon_{\gamma\mu\nu} Q_{\mu\alpha}\partial_k Q_{\nu\alpha} = (S - P)^2 \partial_k \phi \tag{6.3}$$

where again ϕ represents the orientation of the nematogens in the plane perpendicular to $\hat{\mathbf{\Omega}}$. This suggests viewing $(S-P)^2$ and ϕ as polar coordinates for our two dimensional subspace of order parameter space. In conventional polar coordinates, the Jacobian for

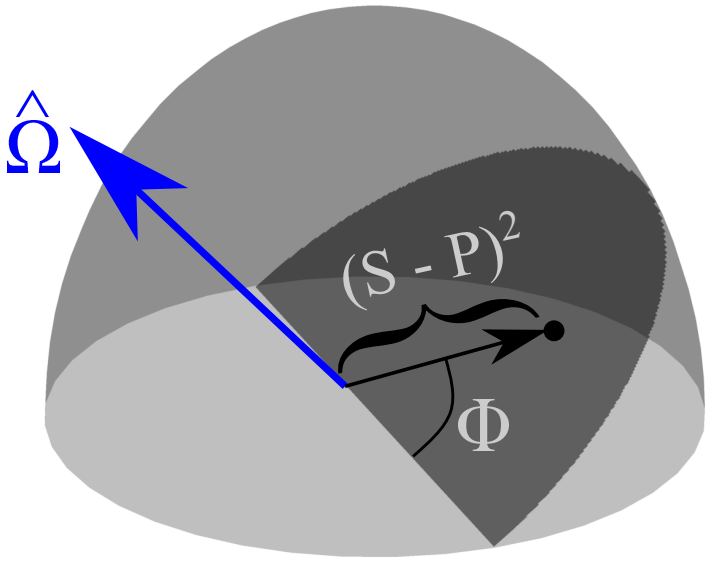

Figure 6.1: Schematic representation of the two dimensional subspace of the order parameter space near disclinations. A point in the subspace can be represented in polar coordinates by the distance from the origin $(S - P)^2$ and director orientation ϕ.

the transformation from polar to Cartesian can be computed as $\nabla \times (r\nabla\varphi)$. Thus, taking the curl of Eq. (6.3) and noting that $\varepsilon_{\gamma\mu\nu}Q_{\mu\alpha}\partial_k Q_{\nu\alpha}$ is parallel to $\hat{\Omega}_\gamma$ near the defect core (see Sec. 5.3), we find

$$\boldsymbol{\rho}(\mathbf{r}) = \delta\left[\mathbf{Q}_\perp(\mathbf{r})\right]\hat{\boldsymbol{\Omega}}\cdot\mathbf{D} \tag{6.4}$$

where $\mathbf{D}$ is the disclination density tensor introduced in Sec. 5.3. From the decomposition of $\mathbf{D}$, Eq. (5.26), $\boldsymbol{\rho}$ is parallel to the tangent vector of the disclination line, just as the density defined in Eq. (6.1). Note that the charge (of (1/2)) is included in the definition of $\mathbf{D}$. Also note that the units of $\boldsymbol{\rho}$ should be length^{-2} which is the case in Eq. (6.1). $\boldsymbol{\rho}$ defined in Eq. (6.4) also has units of length^{-2} since these are the units of $\mathbf{D}$ in Eq. (5.20). Additionally, this Jacobian reduces to the Jacobian D for two dimensional nematics in Eq. (6.2), where $\hat{\boldsymbol{\Omega}} = \pm\hat{\mathbf{z}}$ and $\hat{\mathbf{T}} = \hat{\mathbf{z}}$.

6.3 Velocity of Disclinations Lines

We now use the results derived for the defect densities in the previous section to derive a kinematic law for disclination lines in three dimensional nematics. Here we use methods established by Halperin and Mazenko for the dynamics of defects in n-vector models [39–41, 124]. The idea is to map the defect in order parameter space (using $\delta\left[\mathbf{Q}_\perp\right]$) to its location in real space (i.e. $\delta(\mathbf{r}-\mathbf{r}_0)$) and rely on the transformation properties of the δ-function. This will reveal a defect current, written as a function of the nematic order parameter, $\mathbf{Q}$, and its spatial and time derivatives, which can then be related to the disclination line velocity, $\mathbf{v} = d\mathbf{R}/dt$.

We begin by showing that the disclination density tensor, $\mathbf{D}$, is a conserved quantity and that it satisfies a continuity equation:

$$\begin{aligned}
\partial_t D_{\gamma i} &= \varepsilon_{\gamma\mu\nu}\varepsilon_{ik\ell}\left[\partial_k\partial_t Q_{\mu\alpha}\partial_\ell Q_{\nu\alpha} + \partial_k Q_{\mu\alpha}\partial_\ell\partial_t Q_{\nu\alpha}\right] \\
&= \varepsilon_{\gamma\mu\nu}\varepsilon_{ik\ell}\left[\partial_k\left(\partial_t Q_{\mu\alpha}\partial_\ell Q_{\nu\alpha}\right) + \partial_\ell\left(\partial_t Q_{\nu\alpha}\partial_k Q_{\mu\alpha}\right)\right] \\
&= 2\partial_k\left[\varepsilon_{\gamma\mu\nu}\varepsilon_{ik\ell}\partial_t Q_{\mu\alpha}\partial_\ell Q_{\nu\alpha}\right] \\
&\equiv 2\partial_k J_{\gamma ik}
\end{aligned} \tag{6.5}$$

where in the second line we have used the fact that the $\varepsilon_{ik\ell}\partial_k\partial_\ell Q_{\mu\alpha} = 0$, as $\mathbf{Q}$ is regular

around the disclination line, and in the third line we have redefined the indices on the second term so that $(\ell \leftrightarrow k)$ and $(\mu \leftrightarrow \nu)$. The tensor $\mathbf{J}$ is the current associated with the disclination density tensor $\mathbf{D}$. Using properties of delta functions we write

$$\begin{aligned} \partial_t \mathbf{D}\delta\left[\mathbf{Q}_\perp\right] &= 2\nabla\cdot\mathbf{J}\delta\left[\mathbf{Q}_\perp\right] \\ \Leftrightarrow \mathbf{D}\partial_t\delta\left[\mathbf{Q}_\perp\right] &= 2\mathbf{J}\cdot\nabla\delta\left[\mathbf{Q}_\perp\right]. \end{aligned} \tag{6.6}$$

Now we wish to write a continuity equation for the disclination density ρ. Taking a time derivative of Eq. (6.4) we obtain

$$\begin{aligned} \partial_t\rho_i &= \partial_t\delta\left[\mathbf{Q}_\perp\right]\hat{\Omega}_\gamma D_{\gamma i} + \delta\left[\mathbf{Q}_\perp\right]\partial_t\hat{\Omega}_\gamma D_{\gamma i} + \delta\left[\mathbf{Q}_\perp\right]\hat{\Omega}_\gamma\partial_t D_{\gamma i} \\ &= 2\partial_k\delta\left[\mathbf{Q}_\perp\right]\hat{\Omega}_\gamma J_{\gamma ik} + 2\delta\left[\mathbf{Q}_\perp\right]\hat{\Omega}_{\gamma ik}\partial_k J_{\gamma ik} \\ &= 2\partial_k\left(\delta\left[\mathbf{Q}_\perp\right]\hat{\Omega}_\gamma J_{\gamma ik}\right) \end{aligned} \tag{6.7}$$

where we have used the fact that $\partial_t\hat{\mathbf{\Omega}}\cdot\mathbf{D} = 0$ since $\hat{\mathbf{\Omega}}$ is a unit vector and the first vector component of $\mathbf{D}$ is proportional to $\hat{\mathbf{\Omega}}$. A similar argument holds for terms involving $\nabla\hat{\mathbf{\Omega}}$. Eq. (6.7) has the standard form of a continuity equation, and allows us to determine the conserved current associated with the disclination density. Thus the disclination density current can be written in terms of the nematic order parameter via the definition of the current $\mathbf{J}$, Eq. (6.5), at the location of the disclination core. Importantly, we only need to calculate $\mathbf{Q}$ and its derivatives, as given in the definition of $\mathbf{J}$ in Eq. (6.5) at the core to compute this current.

We now compute this disclination current from the definition of the line, Eq. (6.1). For brevity in the notation, we work this out for a single disclination line and assume the disclination line is parameterized by arc length. Taking a time derivative of Eq. (6.1) yields

$$\partial_t\rho_i(\mathbf{r}) = \frac{1}{2}\int_C \frac{dv_i}{ds}\delta\left[\mathbf{r}-\mathbf{R}\right]\,ds + \frac{1}{2}\int_C \hat{T}_i\partial_t\delta\left[\mathbf{r}-\mathbf{R}\right]\,ds \tag{6.8}$$

where we have used $d\mathbf{R}/ds = \hat{\mathbf{T}}$ since s is an arc length parameterization. Integrating the first term by parts and using the chain rule to compute the time derivative in the

second term yields

$$\begin{aligned}\partial_t \rho_i(\mathbf{r}) &= \frac{1}{2}\int_C v_i \left(\hat{T}_k \partial_k \delta\left[\mathbf{r}-\mathbf{R}\right]\right)\, ds - \frac{1}{2}\int_C \hat{T}_i \left(v_k \partial_k \delta\left[\mathbf{r}-\mathbf{R}\right]\right)\, ds \\ &= \frac{1}{2}\partial_k \left(\int_C v_i \hat{T}_k \delta\left[\mathbf{r}-\mathbf{R}\right]\, ds - \int_C v_k \hat{T}_i \delta\left[\mathbf{r}-\mathbf{R}\right]\, ds\right)\end{aligned} \tag{6.9}$$

where the boundary terms in the integration by parts are zero since they are either at infinity for lines or are the same point on a loop. In the second line we pull the derivative out since $\mathbf{v}$ and $\hat{\mathbf{T}}$ are functions of s and so the time derivative of ρ may be written as a total divergence. To make progress, we change variables from the paramterization s to the disclination coordinate $\mathbf{R}$ so $\hat{\mathbf{T}}ds = d\mathbf{R}$ and $\mathbf{v}(s) \to \mathbf{v}(\mathbf{R})$. We then have

$$\partial_t \rho_i(\mathbf{r}) = \frac{1}{2}\partial_k \left(\int_C v_i \delta\left[\mathbf{r}-\mathbf{R}\right]\, dR_k - \int_C v_k \delta\left[\mathbf{r}-\mathbf{R}\right]\, dR_i\right). \tag{6.10}$$

Finally, we use the property of the delta functions in the integrals to replace $\mathbf{v}(\mathbf{R})$ with $\mathbf{v}(\mathbf{r})$ and pull the velocity out of the integrals. The final result is then

$$\begin{aligned}\partial_t \rho_i(\mathbf{r}) &= \frac{1}{2}\partial_k \left(v_i \int_C \delta\left[\mathbf{r}-\mathbf{R}\right]\, dR_k - v_k \int_C \delta\left[\mathbf{r}-\mathbf{R}\right]\, dR_i\right) \\ &= \partial_k \left(v_i \rho_k - v_k \rho_i\right).\end{aligned} \tag{6.11}$$

We note that this expression is antisymmetric, so the velocity will be perpendicular to $\boldsymbol{\rho}$, and hence perpendicular to the disclination line, as it should.

We may then compare Eqs. (6.7) and (6.11) to relate the topological density current to the velocity (up to the curl of a vector field):

$$2\hat{\Omega}_\tau J_{\tau ik} \delta\left[\mathbf{Q}_\perp\right] = \hat{\Omega}_\gamma \left(v_i D_{\gamma k} - v_k D_{\gamma i}\right) \delta\left[\mathbf{Q}_\perp\right]. \tag{6.12}$$

Similar to Mazenko, we write $J_{\gamma ik} = \varepsilon_{ik\ell} g_{\gamma \ell}$ which serves as the definition of the tensor $\mathbf{g}$, which is more useful for actual calculations and cleans up the notation. Rearranging Eq. (6.12), substituting Eq. (5.26) for $\mathbf{D}$, and understanding that the delta function

means we only compute quantities *at* the defect core we obtain

$$\begin{aligned} \mathbf{v} &= 2\left.\frac{\hat{\mathbf{T}}\times\left(\hat{\mathbf{\Omega}}\cdot\mathbf{g}\right)}{\omega}\right|_{\mathbf{r}=\mathbf{R}} \\ g_{\gamma k} &= \varepsilon_{\gamma\mu\nu}\partial_t Q_{\mu\alpha}\partial_k Q_{\nu\alpha} \end{aligned} \tag{6.13}$$

where $\mathbf{v}$ is understood to vary along the defect line.

Eq. (6.13) is the primary result of this chapter. We note that this equation is a result of topological charge conservation and hence it applies regardless of the dynamical model chosen to govern the evolution of $\mathbf{Q}$. That is, this expression is equally valid for nematics undergoing relaxational dynamics or active nematics with mass transport. The dynamical information only enters the tensor $\mathbf{g}$. In the next chapter we will use this equation to aid in the analysis of numerical solutions of disclination motion. To end this chapter, however, we give some basic results that come from Eq. (6.13).

First, if the configuration is two dimensional we may take $\hat{\mathbf{T}} = \hat{\mathbf{z}}$ and $\hat{\mathbf{\Omega}} = \pm\hat{\mathbf{z}}$ so that the velocity may be written

$$v_i = \mp 2\frac{\varepsilon_{3ik}\varepsilon_{3\mu\nu}\partial_t Q_{\mu\alpha}\partial_k Q_{\nu\alpha}}{\varepsilon_{3\ell p}\varepsilon_{3\tau\xi}\partial_\ell Q_{\tau\beta}\partial_p Q_{\xi\beta}}. \tag{6.14}$$

This is equivalent to previous results derived for the defect velocity in two dimensions [104] and is useful to derive results in two dimensional systems.

If the system's evolution is governed by relaxational dynamics, then $\partial_t\mathbf{Q} = -\delta F/\delta\mathbf{Q}$ where F is the free energy of the system. If F has a functional derivative whose bulk (non-gradient) term is analytic in $\mathbf{Q}$ at the core—such as the Landau-de Gennes free energy or the self-consistent theory of Chapter 2—then we may ignore the contribution of the bulk free energy in the time derivative of $\mathbf{Q}$. To show this, we use the near core linear approximation of $\mathbf{Q}$ introduced in Eq. (5.25) and compute

$$\begin{aligned} \mathbf{Q} &= S_N\left(\frac{1}{6}\mathbf{I} - \frac{1}{2}\hat{\mathbf{\Omega}}\otimes\hat{\mathbf{\Omega}}\right) \\ \nabla\mathbf{Q} &= S_N\left[\frac{\hat{\mathbf{x}}}{2a}\otimes(\hat{\mathbf{n}}_0\otimes\hat{\mathbf{n}}_0 - \hat{\mathbf{n}}_1\otimes\hat{\mathbf{n}}_1) + \frac{\hat{\mathbf{y}}}{2a}\otimes(\hat{\mathbf{n}}_0\otimes\hat{\mathbf{n}}_1 + \hat{\mathbf{n}}_1\otimes\hat{\mathbf{n}}_0)\right] \end{aligned} \tag{6.15}$$

where we have aligned the local tangent vector with the z-axis, a is the core radius, and

$\hat{\mathbf{n}}_0$ and $\hat{\mathbf{n}}_1$ are defined as in Eq. (5.1). Then $\mathbf{g}$ is calculated as

$$\begin{aligned}
&\varepsilon_{\gamma\mu\nu}(Q^n)_{\mu\alpha}\nabla Q_{\nu\alpha} \\
&\qquad = \varepsilon_{\gamma\mu\nu}S_N^n\left[\left(\frac{1}{6}\right)^n\delta_{\mu\alpha}+\left(\sum_{m=0}^{n-1}\binom{n}{m}\left(\frac{1}{6}\right)^m\left(-\frac{1}{2}\right)^{n-m}\right)\hat{\Omega}_\mu\hat{\Omega}_\alpha\right] \\
&\qquad\qquad \cdot\left[\frac{\hat{\mathbf{x}}}{2a}\left(\hat{n}_{0\nu}\hat{n}_{0\alpha}-\hat{n}_{1\nu}\hat{n}_{1\alpha}\right)+\frac{\hat{\mathbf{y}}}{2a}\left(\hat{n}_{0\nu}\hat{n}_{1\alpha}+\hat{n}_{1\nu}\hat{n}_{0\alpha}\right)\right] \\
&\qquad = \left(\frac{S_N}{6}\right)^n\varepsilon_{\gamma\mu\nu}\left[\frac{\hat{\mathbf{x}}}{2a}\left(\hat{n}_{0\mu}\hat{n}_{0\nu}-\hat{n}_{1\mu}\hat{n}_{1\nu}\right)+\frac{\hat{\mathbf{y}}}{2a}\left(\hat{n}_{0\mu}\hat{n}_{1\nu}+\hat{n}_{1\mu}\hat{n}_{0\nu}\right)\right]=0 \quad (6.16)
\end{aligned}$$

at the core of the defect for any power n. Thus, any analytic bulk contribution in the free energy to $\partial_t\mathbf{Q}$ in Eq. (6.13) will be zero. This simplifies calculations since we must only consider the effect of the elastic free energy in the time derivative of $\mathbf{Q}$. In the specific case of the one-constant approximation, we may replace $\partial_t\mathbf{Q}\to\nabla^2\mathbf{Q}$.

Another simple result is the advection of a line defect under an imposed flow $\mathbf{u}$. Here we just take the time evolution of $\mathbf{Q}$ given by advection of the nematogens, $\partial_t\mathbf{Q} = (\mathbf{u}\cdot\nabla)\,\mathbf{Q}$. At the core, this is

$$(\mathbf{u}\cdot\nabla)\,\mathbf{Q} = S_N\left[\frac{u_x}{2a}\left(\hat{\mathbf{n}}_0\otimes\hat{\mathbf{n}}_0-\hat{\mathbf{n}}_1\otimes\hat{\mathbf{n}}_1\right)+\frac{u_y}{2a}\left(\hat{\mathbf{n}}_0\otimes\hat{\mathbf{n}}_1+\hat{\mathbf{n}}_1\otimes\hat{\mathbf{n}}_0\right)\right] \quad (6.17)$$

where we have again aligned the local tangent vector with the z-axis. Computing the tensor $\mathbf{g}$ and generalizing to a tangent vector in any direction, we have

$$\mathbf{g} = S_N^2\left(\frac{\mathbf{u}\times\hat{\mathbf{T}}}{a^2}\right) \quad (6.18)$$

so that the velocity as computed from Eq. (6.13) is

$$\mathbf{v} = 2S_N^2\frac{\hat{\mathbf{T}}\times(\mathbf{u}\times\hat{\mathbf{T}})}{a^2\omega} = \frac{2S_N^2}{a^2\omega}\left(\mathbf{u}-\left(\mathbf{u}\cdot\hat{\mathbf{T}}\right)\hat{\mathbf{T}}\right). \quad (6.19)$$

Thus, the disclination line is advected in the direction perpendicular to $\hat{\mathbf{T}}$ with the speed reduced by the amount that $\hat{\mathbf{T}}$ and $\mathbf{u}$ overlap, which is the expected result. These simple examples prove the immediate usefulness of the velocity equation, and we show in the next chapter more complicated examples that yet still yield analytical insight.

6.4 Conclusion

Here we have derived a kinematic law for the velocity of disclination lines, which can be computed as a function of the disclination density tensor $\mathbf{D}$ and the order parameter $\mathbf{Q}$. This kinematic law applies regardless of the dynamical model chosen for the order parameter and should prove useful to future studies where the dynamics of disclination lines is important, such as in defect annihilation, applied flows, or active nematics. There is still more work to be done in understanding disclination dynamics. The velocity, as demonstrated by Eq. (6.13), depends on its instantaneous rotation vector, $\hat{\mathbf{\Omega}}$. The issue of understanding how the rotation vector evolves in time remains a challenge. Recent theory and experiment have begun to explore this issue [21, 96, 120].

Chapter 7

Disclination Motion: Annihilation and Flows

7.1 Introduction

We use in this chapter the analytic results of the previous chapter in tandem with numerical computation to analyze qualitative but generic aspects of the motion of disclinations. We start by outlining the analytical approximations used and discussing the general results for motion of a disclination under a small applied distortion. The interaction between two defects can be approximated as one defect creating a distortion field that acts on the other and so this general result is used to understand the interaction between disclinations in both two and three dimensions. We also study elastically anisotropic conditions, which have so far been neglected by much of the theory and computation because of the unboundedness of Landau-de Gennes. Finally, we discuss some simple results involving applying fields and flows to the nematic, and their effect on disclination motion.

7.2 Analytical Approximations

In order to examine the consequences of Eq. (6.13) analytically, one needs to make some approximations about a given configuration $\mathbf{Q}$, and about its evolution. A useful property of the kinematic velocity equation Eq. (6.13) is that the quantities appearing

in the formula need only be computed at the disclination core, where the eigenvalues of $\mathbf{Q}$ cross. Thus, we may take advantage of the near core, linear approximation of $\mathbf{Q}$ discussed in Chapter 5 and given in Eq. (5.25). Throughout this chapter we will align our axes so that the tangent vector of the disclination of interest is $\hat{\mathbf{T}} = \hat{\mathbf{z}}$ with the vectors (defined in Eq. (5.25)) $\hat{\boldsymbol{\nu}}_0 = \hat{\mathbf{x}}$ and $\hat{\boldsymbol{\nu}}_1 = \hat{\mathbf{y}}$.

First, it is simple to evaluate the velocity of a single straight line disclination. In the isotropic limit, $\nabla^2\mathbf{Q} = 0$ at the core of the disclination and the tensor $\mathbf{g} = 0$ in Eq. (6.13); hence $\mathbf{v} = 0$. This is the correct stationary state for a single straight line disclination.

One of the ways in which disclinations can move is through an externally imposed distortion of the director field. We consider the general case of a small, non singular, perturbation of the director near the core. We take this perturbation to be a rotation by $\tilde{\varphi}$ about some axis $\hat{\mathbf{q}}$:

$$\hat{\mathbf{n}} \to \mathbf{R}(\hat{\mathbf{q}}, \tilde{\varphi})\hat{\mathbf{n}} = \cos\tilde{\varphi}\hat{\mathbf{n}} + \sin\tilde{\varphi}(\hat{\mathbf{q}} \times \hat{\mathbf{n}}) + (1 - \cos\tilde{\varphi})(\hat{\mathbf{q}} \cdot \hat{\mathbf{n}})\hat{\mathbf{q}} \equiv \tilde{\mathbf{n}}. \tag{7.1}$$

We assume $\tilde{\varphi}$ is small near the core and, importantly, that $\nabla\tilde{\varphi} \neq 0$ at the disclination core as well. Since $\tilde{\varphi}$ is small, we introduce the approximation $\tilde{\mathbf{n}} \approx \hat{\mathbf{n}} + \tilde{\varphi}(\hat{\mathbf{q}} \times \hat{\mathbf{n}})$. Thus, using Eq. (5.1) to express the director near the disclination core, we write

$$\tilde{\mathbf{n}} \approx \cos\frac{1}{2}\phi\left(\hat{\mathbf{n}}_0 + \tilde{\varphi}\left(\hat{\mathbf{q}} \times \hat{\mathbf{n}}_0\right)\right) + \sin\frac{1}{2}\phi\left(\hat{\mathbf{n}}_1 + \tilde{\varphi}\left(\hat{\mathbf{q}} \times \hat{\mathbf{n}}_1\right)\right) \equiv \cos\frac{1}{2}\phi\tilde{\mathbf{n}}_0 + \sin\frac{1}{2}\phi\tilde{\mathbf{n}}_1. \tag{7.2}$$

where $\tilde{\mathbf{n}}_0$ and $\tilde{\mathbf{n}}_1$ are defined analogously to $\tilde{\mathbf{n}}$. Applying the linear core approximation to this expression in the same way as in Sec. 5.3, we write $\mathbf{Q}$ close to the core as

$$Q_{\mu\nu} \approx S_N\left[\frac{1}{6}\delta_{\mu\nu} - \frac{1}{2}\hat{\Omega}_\mu\hat{\Omega}_\nu + \frac{x}{2a}\left(\tilde{n}_{0\mu}\tilde{n}_{0\nu} - \tilde{n}_{1\mu}\tilde{n}_{1\nu}\right) + \frac{y}{2a}\left(\tilde{n}_{0\mu}\tilde{n}_{1\nu} + \tilde{n}_{1\mu}\tilde{n}_{0\nu}\right)\right]. \tag{7.3}$$

so that

$$\begin{aligned}\nabla Q_{\mu\nu} = S_N\Bigg[&\frac{\hat{\mathbf{x}}}{2a}\left(\tilde{n}_{0\mu}\tilde{n}_{0\nu} - \tilde{n}_{1\mu}\tilde{n}_{1\nu}\right) + \frac{x}{2a}\nabla\tilde{\varphi}\left(p_{0\mu}\tilde{n}_{0\nu} + \tilde{n}_{0\mu}p_{0\nu} - p_{1\mu}\tilde{n}_{1\nu} - \tilde{n}_{1\mu}p_{1\nu}\right)\\ &+ \frac{\hat{\mathbf{y}}}{2a}\left(\tilde{n}_{0\mu}\tilde{n}_{1\nu} + \tilde{n}_{1\mu}\tilde{n}_{0\nu}\right) + \frac{y}{2a}\nabla\tilde{\varphi}\left(p_{0\mu}\tilde{n}_{1\nu} + \tilde{n}_{0\mu}p_{1\nu} + p_{1\mu}\tilde{n}_{0\nu} + \tilde{n}_{1\mu}p_{0\nu}\right)\Bigg]\end{aligned} \tag{7.4}$$

where we have introduced the notation $\mathbf{p}_k \equiv \hat{\mathbf{q}} \times \hat{\mathbf{n}}_k$. We then compute $\nabla^2\mathbf{Q}$ at the defect core, which no longer vanishes if $\nabla\tilde{\varphi} \neq 0$:

$$\nabla^2 Q_{\mu\nu}\big|_{x=y=0} = S_N \left[\frac{\partial_x \tilde{\varphi}}{a} \left(p_{0\mu}\tilde{n}_{0\nu} + \tilde{n}_{0\mu}p_{0\nu} - p_{1\mu}\tilde{n}_{1\nu} - \tilde{n}_{1\mu}p_{1\nu} \right) + \frac{\partial_y \tilde{\varphi}}{a} \left(p_{0\mu}\tilde{n}_{1\nu} + \tilde{n}_{0\mu}p_{1\nu} + p_{1\mu}\tilde{n}_{0\nu} + \tilde{n}_{1\mu}p_{0\nu} \right) \right]. \quad (7.5)$$

Then, taking only terms to $O(\tilde{\varphi})$ and using the relations

$$\begin{aligned}
\tilde{\mathbf{n}}_0 \cdot \tilde{\mathbf{n}}_1 &= 0 \\
\tilde{\mathbf{n}}_0 \cdot \tilde{\mathbf{n}}_0 &= \tilde{\mathbf{n}}_1 \cdot \tilde{\mathbf{n}}_1 = 1 \\
\mathbf{p}_0 \cdot \tilde{\mathbf{n}}_0 &= \tilde{\varphi} |\hat{\mathbf{q}} \times \hat{\mathbf{n}}_0|^2 \\
\mathbf{p}_1 \cdot \tilde{\mathbf{n}}_1 &= \tilde{\varphi} |\hat{\mathbf{q}} \times \hat{\mathbf{n}}_1|^2 \\
\mathbf{p}_0 \cdot \tilde{\mathbf{n}}_1 &= \hat{\mathbf{q}} \cdot \hat{\mathbf{\Omega}} - \tilde{\varphi} (\hat{\mathbf{q}} \cdot \hat{\mathbf{n}}_0)(\hat{\mathbf{q}} \cdot \hat{\mathbf{n}}_1) \\
\mathbf{p}_1 \cdot \tilde{\mathbf{n}}_0 &= -\hat{\mathbf{q}} \cdot \hat{\mathbf{\Omega}} - \tilde{\varphi} (\hat{\mathbf{q}} \cdot \hat{\mathbf{n}}_0)(\hat{\mathbf{q}} \cdot \hat{\mathbf{n}}_1) \\
\tilde{\mathbf{n}}_0 \times \tilde{\mathbf{n}}_1 &= \hat{\mathbf{\Omega}} \\
\mathbf{p}_0 \times \tilde{\mathbf{n}}_0 &= -\hat{\mathbf{q}} + \hat{\mathbf{n}}_0 (\hat{\mathbf{q}} \cdot \hat{\mathbf{n}}_0) \\
\mathbf{p}_1 \times \tilde{\mathbf{n}}_1 &= -\hat{\mathbf{q}} + \hat{\mathbf{n}}_1 (\hat{\mathbf{q}} \cdot \hat{\mathbf{n}}_1) \\
\mathbf{p}_0 \times \tilde{\mathbf{n}}_1 &= \hat{\mathbf{n}}_0 (\hat{\mathbf{q}} \cdot \hat{\mathbf{n}}_1) - \tilde{\varphi} \mathbf{p}_1 (\hat{\mathbf{q}} \cdot \hat{\mathbf{n}}_0) \\
\mathbf{p}_1 \times \tilde{\mathbf{n}}_0 &= \hat{\mathbf{n}}_1 (\hat{\mathbf{q}} \cdot \hat{\mathbf{n}}_0) + \tilde{\varphi} \mathbf{p}_1 (\hat{\mathbf{q}} \cdot \hat{\mathbf{n}}_1)
\end{aligned} \quad (7.6)$$

we compute $\hat{\mathbf{\Omega}} \cdot \mathbf{g} = \hat{\Omega}_\gamma \varepsilon_{\gamma\mu\nu} \nabla^2 Q_{\mu\alpha} \nabla Q_{\nu\alpha}$ after some lengthy algebra:

$$\hat{\mathbf{\Omega}} \cdot \mathbf{g} = \frac{2S_N^2 (\hat{\mathbf{q}} \cdot \hat{\mathbf{\Omega}})}{a^2} \hat{\mathbf{z}} \times (\hat{\mathbf{z}} \times \nabla\tilde{\varphi}) \,. \quad (7.7)$$

Substituting this in Eq. (6.13), generalizing to any tangent vector (i.e. $\hat{\mathbf{z}} \to \hat{\mathbf{T}}$), and computing $\omega = S_N^2/a^2$ at the core from Eq. (5.25), we find

$$\mathbf{v} = -4(\hat{\mathbf{q}} \cdot \hat{\mathbf{\Omega}})(\hat{\mathbf{T}} \times \nabla\tilde{\varphi}). \quad (7.8)$$

In two dimensions, we take $\hat{\mathbf{T}} = \hat{\mathbf{z}}$, $\hat{\mathbf{q}} = \hat{\mathbf{z}}$, and $\hat{\mathbf{\Omega}} = \pm\hat{\mathbf{z}}$ so that

$$\mathbf{v}^{2\mathrm{D}} = \mp(\hat{\mathbf{z}} \times \nabla\tilde{\varphi}). \tag{7.9}$$

We note that the result of Eq. (7.8) shows that the velocity will vanish if $\hat{\mathbf{q}} \perp \hat{\mathbf{\Omega}}$ or $\nabla\tilde{\varphi} \parallel \hat{\mathbf{T}}$, cases we will explore in Sec. 7.4.

While we have approximated the external distortion as a small planar rotation of $\hat{\mathbf{n}}$ near the core of the disclination, this approximation will prove particularly useful for the case of disclination annihilation, which we will focus on in Secs. 7.3 and 7.4 for the two dimensional and three dimensional cases respectively. Another area where this approximation may be used is in the physical rotation of sample boundaries in order to apply a torque on the disclinations. There has been some investigation of this case by using a Peach-Koehler "effective stress" approach and in experimental samples with photo-patterned boundaries to induce movement of disclination lines [38, 86]. We finally remark that the above calculation reflects the case of one elastic constant, that is $K_{11} = K_{22} = K_{33} = K$. To analyze cases of anisotropic elasticity one must include more terms in the elastic energy contribution of $\partial_t\mathbf{Q}$ in Eq. (6.13) (i.e. the L_2 and L_3 terms in Eq. (2.7)). We will do this as needed moving forward to analyze each case.

7.3 Two Dimensional Disclination Annihilation

Disclination interactions in two dimensions have been extensively studied for a variety of cases involving complex geometries, hydrodynamics, and activity [95, 103, 121, 122, 125,126]. However, there are very few studies that deal with the influence of anisotropic elasticity, likely due to the unboundedness of the Landau-de Gennes free energy under the addition of higher order gradients necessary to break isotropy. Additionally, recent work has shown non-standard dynamics of disclinations that have a twisted orientation with respect to one another [37,108,109]. Here we study both of these effects, anisotropic elasticity and twisted orientation, on the dynamics of disclination annihilation. Both of these have very important implications for non-equilibrium systems where defects are constantly nucleated and annihilated.

7.3.1 Optimal orientation

We focus on defects with charge $\pm 1/2$. These are the energetically stable defects that form in two dimensions [1]. These defects have a geometric orientation associated with them since the $+1/2$ disclinations have polar symmetry while the $-1/2$ disclinations have three-fold symmetry. Recent research has shown that these orientations can be described with either a vector, $\mathbf{b}$, for both disclinations, or a vector for the $+1/2$ disclination and a third rank tensor for the $-1/2$ disclination [37, 38, 108]. In either case, since we are in two dimensions, the orientation of both $\pm 1/2$ disclinations can be given by some angle ψ with respect to the x-axis. The director configuration of a single defect at position $\mathbf{r}_0 = (x_0, y_0)$ can then be written in terms of the director orientation as,

$$\phi(x, y) = \pm \frac{1}{2} \arctan\left(\frac{y - y_0}{x - x_0}\right) + \frac{\psi}{2}. \tag{7.10}$$

As discussed in Chapter 4, in the one elastic constant approximation, the Euler-Lagrange equation for ϕ which minimizes the Frank-Oseen free energy is linear, and hence the director configuration for many defects is given by the sum of defect solutions given by Eq. (7.10),

$$\phi(x, y) = \sum_{i=1}^{N} m_i \arctan\left(\frac{y - y_i}{x - x_i}\right) + \phi_0 \tag{7.11}$$

where N is the number of defects in the system, $m_i = \pm 1/2$ is the charge of the ith defect and ϕ_0 is an overall phase factor determined by the orientations of all the defects. For a one elastic constant system, if the director angle is given by Eq. (7.11) then we will say that system has "optimal orientation." We focus now on the case $N = 2$ and $m_1 = -m_2 = 1/2$, that is the case of oppositely charged disclinations. For this case, a configuration with optimal orientation has a constant ϕ on the line segment connecting both disclinations. Fig. 7.1 shows an example of two disclinations with optimal orientation and $\phi_0 = 0$ alongside an example with "twisted" orientation, a case we will discuss later.

The one-constant, Frank-Oseen interaction between the two disclination optimal

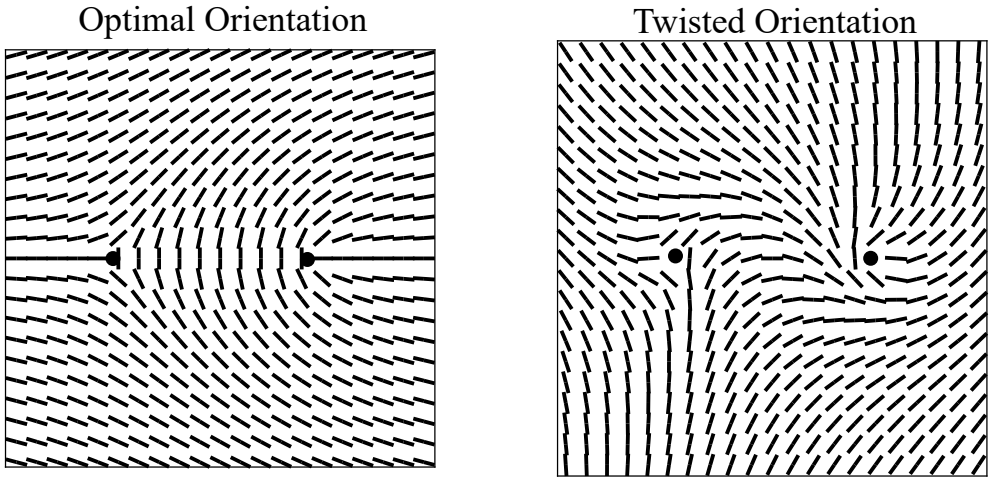

Figure 7.1: (left) A pair of oppositely charged disclinations with optimal orientation given by Eq. (7.11) with $\phi_0 = 0$. (right) A pair of oppositely charged disclinations with twisted orientation given by Eq. (7.22) with $\delta\phi = \pi$ and $\phi_0 = 0$.

orientation solution is [1]

$$F_{12} = \frac{\pi K}{2} \ln\left(\frac{|\mathbf{r}_1 - \mathbf{r}_2|}{a}\right) \tag{7.12}$$

where a is the defect core radius. Hence the force on, say, disclination 2 from disclination 1 is given by

$$\mathbf{f}_2 = -\frac{\partial F_{12}}{\partial \mathbf{r}_2} = -\frac{\pi K}{2} \frac{\hat{\mathbf{r}}_{21}}{|\mathbf{r}_1 - \mathbf{r}_2|} \tag{7.13}$$

where $\hat{\mathbf{r}}_{21}$ is the unit vector directed from $\mathbf{r}_1$ to $\mathbf{r}_2$. This is the familiar "Coulomb-like" attraction between oppositely charged defects in two dimensions. We note that the force is directed along the line segment between the defects, which intuitively leads to their annihilation. Additionally, there is no dependence on the overall phase factor ϕ_0.

If we view this configuration as one in which disclination 1 is imposing an inhomogeneous distortion on disclination 2, we may calculate the expected velocity of the defect from Eq. (7.9) by taking

$$\tilde{\varphi} = \frac{1}{2} \arctan\left(\frac{y - y_1}{x - x_1}\right) + \frac{\psi_1}{2} \tag{7.14}$$

i.e., the director distortion from disclination 1. This is precisely $\tilde{\varphi}$ as described in the previous section because the effect of adding a defect to the configuration is to rotate the director everywhere around the new defect. In two dimensions, this is the same as adding up all of the individual ϕ_i as in Eq. (7.11). Differentiating Eq. (7.14) and evaluating at the core of defect 2 gives

$$\nabla\tilde{\varphi} = \frac{1}{2}\left(\frac{y_1 - y_2}{|\mathbf{r}_1 - \mathbf{r}_2|^2}\hat{\mathbf{x}} - \frac{x_1 - x_2}{|\mathbf{r}_1 - \mathbf{r}_2|^2}\hat{\mathbf{y}}\right) \tag{7.15}$$

so that, from Eq. (7.9),

$$\mathbf{v}_2 = -2\frac{\hat{\mathbf{r}}_{21}}{|\mathbf{r}_1 - \mathbf{r}_2|} \tag{7.16}$$

which shows that the disclinations will annihilate, with their relative motion being along the line segment which joins them. Note that the velocity is proportional to the force in Eq. (7.13). The proportionality between the force and the velocity is the expected result for an over-damped system; however, we shall see that for twisted defects, the two calculations will differ.

Given the velocity in Eq. (7.16), we define the distance between the disclinations to be $R = |\mathbf{r_1} - \mathbf{r_2}|$ so that $dR/dt = \hat{\mathbf{r}}_{21} \cdot (\mathbf{v}_2 - \mathbf{v}_1)$. Then

$$\begin{aligned} \frac{dR}{dt} &= -\frac{4}{R} \\ \Rightarrow R(t) &= \sqrt{R_0^2 - 8t} \end{aligned} \tag{7.17}$$

where R_0 is the initial separation of the disclinations. The scaling of $R \sim t^{1/2}$ is the standard result for disclination annihilation [1].

We use this result to check our numerical code based on the singular potential as it will be used later in this chapter in anisotropic and three dimensional cases. For all calculations performed in this section, we use the finite element method and the singular free energy described in Chapter 2. We use a 150×150 body-centered square mesh and set $\Delta t = 0.2$. For all calculations in this chapter we set $\kappa/(nk_BT) = 4$ which corresponds to an equilibrium $S_N = 0.6751$. In Fig. 7.2 we show our results for the case of a single elastic constant ($L_2 = L_3 = L_4 = 0$) with $R_0 = 5$. We plot both disclination position x and x^2 for the $+1/2$ and $-1/2$ disclinations as a function of iteration number

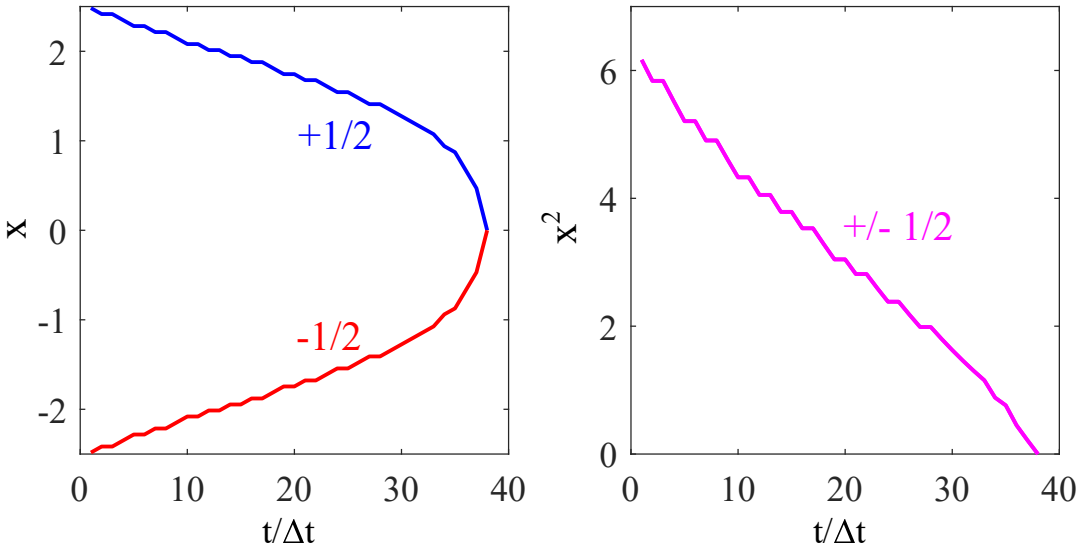

Figure 7.2: (left) Disclination position, x, as a function of iteration number $t/\Delta t$ for optimally oriented, one elastic constant annihilation of a $+1/2$ and $-1/2$ disclination. (right) x^2 plotted as a function of iteration number $t/\Delta t$. Both the $+1/2$ and $-1/2$ disclinations have the same squared position trajectory and hence their curves overlap. Note that the squared position is linear in time.

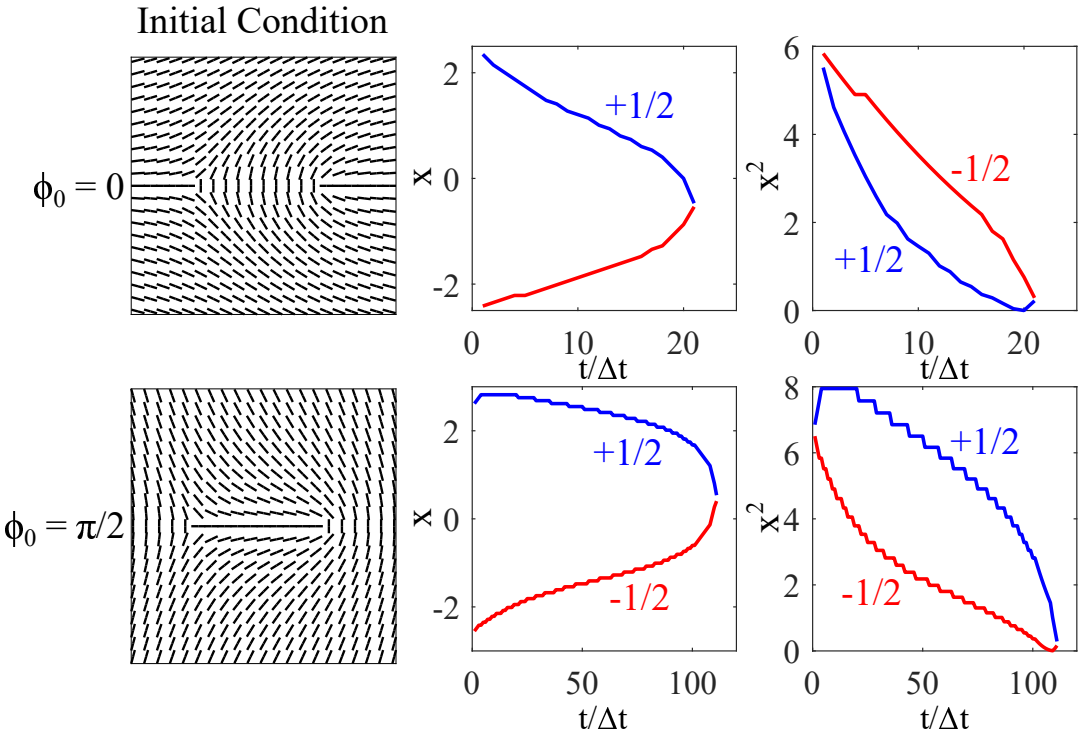

Figure 7.3: Simulated positions, x, and squared positions, x^2, as a function of iteration number $t/\Delta t$ for annihilating $\pm 1/2$ disclinations with anisotropic elasticity. In the simulations $L_3 = 3$ and $\Delta t = 0.2$. (top) Initial configuration with $\phi_0 = 0$. (bottom) Initial configuration with $\phi_0 = \pi/2$. In both cases, there is asymmetry between the motion of $+1/2$ and $-1/2$ disclinations, and the squared position no longer scales linearly.

$t/\Delta t$. These results confirm the scaling and symmetry of two disclination velocities predicted by Eq. (7.16) since x^2 is the same for both disclinations and is linear in time.

We study next the effect of anisotropic elasticity on the annihilation of disclinations. As discussed in Chapter 4, the Frank-Oseen energy for liquid crystals with anisotropic elasticity leads to nonlinear Euler-Lagrange equations for the director configuration. This means that the Dzyaloshinkii solutions of Chapter 4 cannot simply be summed to give the configuration of two oppositely charged disclinations with anisotropic elasticity. Since we do not know the director configuration *a priori* we cannot compute the energy of two disclinations analytically as we did above in Eq. (7.12). Instead, we will present qualitative arguments based on the Frank-Oseen elastic energy to interpret the results.

In Fig. 7.3 we show plots of the position of each defect, x, and the position squared, x^2, versus the iteration number $t/\Delta t$, for two configurations with $R_0 = 5$ but now with anisotropic elasticity, $L_3 = 3 \Rightarrow \varepsilon = 0.75$. In the first calculation we set $\phi_0 = 0$ while in the second we set $\phi_0 = \pi/2$. The annihilation occurs much faster for the case when $\phi_0 = 0$—note the difference in scales on the $t/\Delta t$ axis—and there is an asymmetry between the defects as well. In the $\phi_0 = 0$ case, the $+1/2$ disclination moves faster than the $-1/2$ disclination, while the opposite occurs in the $\phi_0 = \pi/2$ case. Further, the plots of x^2 in Fig. 7.3 do not scale as $-t$. This is in contrast with the case of one constant elasticity where disclination annihilation is symmetric between defects, and the velocity does not depend on the overall phase ϕ_0. We may understand this heuristically from the fact that for our choice of L_3 bend distortion now costs more energy than splay distortion. In the case where $\phi_0 = 0$, as seen in the initial condition plotted in Fig. 7.3, there is predominantly bend between the two defects, and hence it is more favorable to annihilate in this region to remove the bend distortion. On the other hand, if $\phi_0 = \pi/2$ there is splay distortion between the defects, so annihilating does not reduce the energy of the configuration as much.

To gain some analytical insight we now turn to Eq. (7.9). We must first extend this equation to include terms involving anisotropic elasticity. As we computed in Chapter 3 (Eq. (3.12)), the elastic contribution to the time dependence of $\mathbf{Q}$ resulting from a nonzero L_3 term is

$$\partial_t Q_{\mu\nu} = \nabla^2 Q_{\mu\nu} + L_3 \left(-\partial_\mu Q_{ij} \partial_\nu Q_{ij} + 2\partial_i Q_{\mu\nu} \partial_j Q_{ij} + 2Q_{ij} \partial_\mu \partial_\nu Q_{ij}\right). \tag{7.18}$$

To compute $\mathbf{v}$ from this we will use the approximation for $\mathbf{Q}$ near the core given by Eq. (5.25). As we showed in Chapter 4, since S is small near the core, the solution becomes increasingly similar to the case with isotropic elasticity, hence Eq. (5.25) remains a good approximation of $\mathbf{Q}$, but only at the core of a single defect. If we assume that the influence of the other defect is to rotate the director by an angle $\tilde{\varphi}$, then we may use the same approach as in Sec. 7.2, where now we must compute $\hat{\mathbf{\Omega}} \cdot \mathbf{g}$ for each term in

Eq. (7.18). For a $+1/2$ defect this works out to be

$$\begin{aligned}
&\hat{\Omega}_\gamma \varepsilon_{\gamma\mu\nu} \partial_\mu Q_{ij} \partial_\alpha Q_{ij} \nabla Q_{\nu\alpha} = 0 \\
&\hat{\Omega}_\gamma \varepsilon_{\gamma\mu\nu} \partial_i Q_{\mu\alpha} \partial_j Q_{ij} \nabla Q_{\nu\alpha} = \frac{S_N^3}{2a^3} \left[-4\hat{\mathbf{x}} \left(\hat{n}_{0x} \hat{n}_{0y} \right) + 2\hat{\mathbf{y}} \left(\hat{n}_{0x}^2 - \hat{n}_{0y}^2 \right) \right] \\
&\hat{\Omega}_\gamma \varepsilon_{\gamma\mu\nu} Q_{ij} \partial_\mu \partial_\alpha Q_{ij} \nabla Q_{\nu\alpha} = 0
\end{aligned} \tag{7.19}$$

where $\hat{n}_{0x}$ and $\hat{n}_{0y}$ are the x and y components of $\hat{\mathbf{n}}_0$. The second of the L_3 terms is the only one that survives and interestingly does *not* depend on $\tilde{\varphi}$. Instead, it only depends on the orientation of the defect through the components of the vector $\hat{\mathbf{n}}_0$. Using this to calculate the velocity of the $+1/2$ disclination we have

$$\mathbf{v}^+ = 4(\hat{\mathbf{z}} \times \nabla \tilde{\varphi}^-) - \frac{2L_3 S_N}{a} \left[\hat{\mathbf{x}} \left(\hat{n}_{0x}^2 - \hat{n}_{0y}^2 \right) + 2\hat{\mathbf{y}} \left(\hat{n}_{0x} \hat{n}_{0y} \right) \right]. \tag{7.20}$$

where $\tilde{\varphi}^-$ is the perturbation of the director from the $-1/2$ disclination. If we perform the same calculation for the velocity of the $-1/2$ disclination we find

$$\mathbf{v}^- = 4(\hat{\mathbf{z}} \times \nabla \tilde{\varphi}^+) \tag{7.21}$$

where $\tilde{\varphi}^+$ is the perturbation of the director from the $+1/2$ disclination. Note that the L_3 term drops out entirely for the $-1/2$ disclination.

Eqs. (7.20) and (7.21) give analytical rationale for both the asymmetry between the defects and how the overall phase affects the motion. The velocities are explicitly asymmetric as the L_3 term only appears in the $+1/2$ disclination velocity. The L_3 term in Eq. (7.20) predicts that a $+1/2$ disclination will be biased to move towards the bend distortion if $L_3 > 0$ or towards the splay distortion if $L_3 < 0$. On the other hand, there is no such bias for the $-1/2$ disclination. There is also an implicit asymmetry in the first terms of Eqs. (7.20) and (7.21) in that in general $\tilde{\varphi}^- \neq -\tilde{\varphi}^+$ which is the case for a one-constant elasticity. This is because the Euler-Lagrange equations from the Frank-Oseen elastic energy are nonlinear for the case of anisotropic elasticity. Our velocity equation has thus given us some analytic intuition that supports our heuristic intuition above for the differences in the results shown in Fig. 7.3.

Beyond the differences in the case of $\phi_0 = 0$ and $\phi_0 = \pi/2$, Eqs. (7.20) and (7.21) also allow us to predict the motion of cases between these two. In fact, Eq. (7.20)

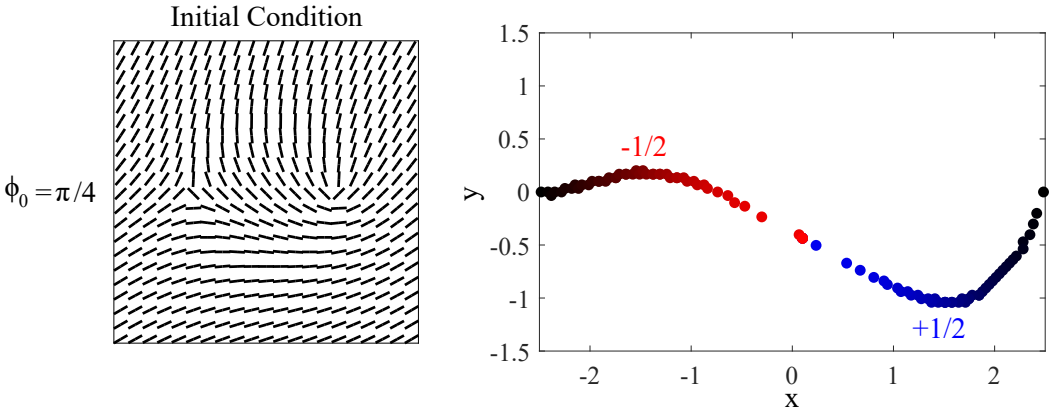

Figure 7.4: Plots of the (x, y) position of disclinations during annihilation for an initial condition with $\phi_0 = \pi/4$ and anisotropic elasticity $L_3 = 3$. Positions appear as dots which get brighter indicating later times in the simulation.

predicts that if the defects are aligned along the x-axis and $\phi_0 \neq 0, \pi/2$, the $+1/2$ disclination should have a component of its velocity transverse to the direction between the defects, at least early in the annihilation before the first term becomes dominant. To test this, we study numerically the case $\phi_0 = \pi/4$. We show in Fig. 7.4 plots of the (x, y) positions of the $\pm 1/2$ disclinations as they annihilate when the initial configuration has $\phi_0 = \pi/4$ and $L_3 = 3$. In the figure, the positions appear as dots which become brighter, indicating later times. Early in the simulation, the $+1/2$ disclination has a component of its velocity in the $-\hat{\mathbf{y}}$ direction, while the $-1/2$ disclination has a small transverse velocity component, but primarily moves along the line segment connecting the two disclinations.

We finally comment on the usefulness of the disclination velocity equation even in cases where an exact analytical solution is difficult (or impossible) to compute. While for the one-constant case, the Frank-Oseen energy for a two defect system can be computed analytically, this is not the case for a system with anisotropic elasticity. Yet, the velocity equation allows us to analytically predict the qualitative features of such systems, usually with relatively simple calculations. Also, as we will see in Sec. 7.3.2, even if the energy is analytically computable, the corresponding force is not guaranteed to yield the correct motion of the defects due to topological constraints on the system.

7.3.2 Twisted defect orientation

Because disclinations have an orientational degree of freedom, one can ask whether these degrees of freedom can be independently manipulated within a configuration containing multiple defects. As shown in Fig. 7.1, this is possible for configurations with two defects and it introduces another system variable, $\delta\phi$, which gives the relative orientation of the defects. Since the configuration involves rotating defects independently of one another, we call the type of configuration "twisted." Twisted defect configurations have been studied recently due to their unique dynamics and appearance in active systems [37,108,109]. Here we apply the velocity equation derived in Sec. 7.2 to twisted defects in a system with one elastic constant to give an analytic expression for the velocity and we show qualitatively different results from those expected from energy minimization. We then consider the effect of anisotropic elasticity on the motion of annihilating twisted defects.

The authors of Ref. [37] determined that for defects at fixed locations with fixed amount of twist $\delta\phi$, the Frank-Oseen energy is minimized by the following configuration:

$$\phi(x,y) = \frac{1}{2}\arctan\left(\frac{y-y_1}{x-x_1}\right) - \frac{1}{2}\arctan\left(\frac{y-y_2}{x-x_2}\right) + \frac{\delta\phi}{2}\left[1 + \frac{\ln\left(|\mathbf{r}-\mathbf{r}_1|^2\right) - \ln\left(|\mathbf{r}-\mathbf{r}_2|^2\right)}{\ln\left(|\mathbf{r}_1-\mathbf{r}_2|^2\right) - \ln\left(a^2\right)}\right] + \phi_0 \quad (7.22)$$

where $\mathbf{r}_i = (x_i, y_i)$ are the locations of the disclinations, and a is the defect core radius. If $\delta\phi = 0$ Eq. (7.22) reduces to the optimal orientation solution given in Eq. (7.11) for $N = 2$. The interaction terms in the one-constant Frank-Oseen elastic energy of this configuration can be computed as [37]

$$F_{12} = \frac{\pi K}{2}\ln\left(\frac{R}{a}\right) + \frac{\pi K \delta\phi^2}{2}\frac{\ln\left(R/(2a)\right)}{\ln\left(R/a\right)^2} \quad (7.23)$$

where we have again defined $R \equiv |\mathbf{r}_1 - \mathbf{r}_2|$. Importantly, the energy only depends on the distance between the defects and the twistedness of the configuration. Thus, the force that one defect exerts on the other will be directed along the line segment that joins them; that is $\mathbf{f}_2 \propto \hat{\mathbf{r}}_{12}$. There will also be a restoring torque that drives the defects to

rotate independently to restore the optimal orientation:

$$\tau(R,\delta\phi) = -\frac{\partial F_{12}}{\partial \delta\phi} = -\pi K \delta\phi \frac{\ln\left(R/(2a)\right)}{\ln\left(R/a\right)^2}. \tag{7.24}$$

While the force between disclinations is directed along the line segment that joins them, the defects actually take transverse trajectories in the course of annihilation. There have been several computational studies of this [37, 108, 109] and we have also analyzed twisted defect configurations, using the same methods as described for the optimal orientation defects, except we now initialize the system with Eq. (7.22) for given ϕ_0 and $\delta\phi$. Fig. 7.5 shows the initial conditions alongside the (x, y) positions of the $+1/2$ and $-1/2$ disclinations of several simulations for various $\delta\phi$ with the one-constant approximation, $L_2 = L_3 = L_4 = 0$, and $\phi_0 = 0$. As in other studies, there is an antisymmetric, transverse component to the velocity of the defects which increases as $\delta\phi$ increases. Thus, the force obtained by differentiating the energy does not explain the actual motion of the defects. Intuitively, this is because of the restoring torque that drives the defects to rotate. One way to rotate a defect is by uniformly rotating all of the nematogens in the system. However, doing this would rotate both defects in the same direction, and so would not reduce the amount of twist in the system. Thus the nematogens must rotate locally, near each defect inhomogeneously. The only way to accomplish this is by having the defects move transverse to one another. From this perspective, the nematogens try to most efficiently remove the twist from the configurations, and the defects move as a result of this.

On the other hand, we can use the disclination velocity equation, Eq. (7.9), to shift perspective to the defects and seek an analytic expression for their velocities. To do this, we write the perturbation $\tilde{\varphi}_i = \phi - \phi_i$, where ϕ_i denotes the terms that diverge at $\mathbf{r}_i$, so that it is the rotation of the director field caused by the other defect and the twist in the configuration. For the $+1/2$ disclination we find

$$\nabla\tilde{\varphi}|_{\mathbf{r}=\mathbf{r}_1} = -\frac{1}{2R}\left(\hat{\mathbf{z}} \times \hat{\mathbf{r}}_{12}\right) - \frac{\delta\phi}{2R\ln(R/a)}\hat{\mathbf{r}}_{12} \tag{7.25}$$

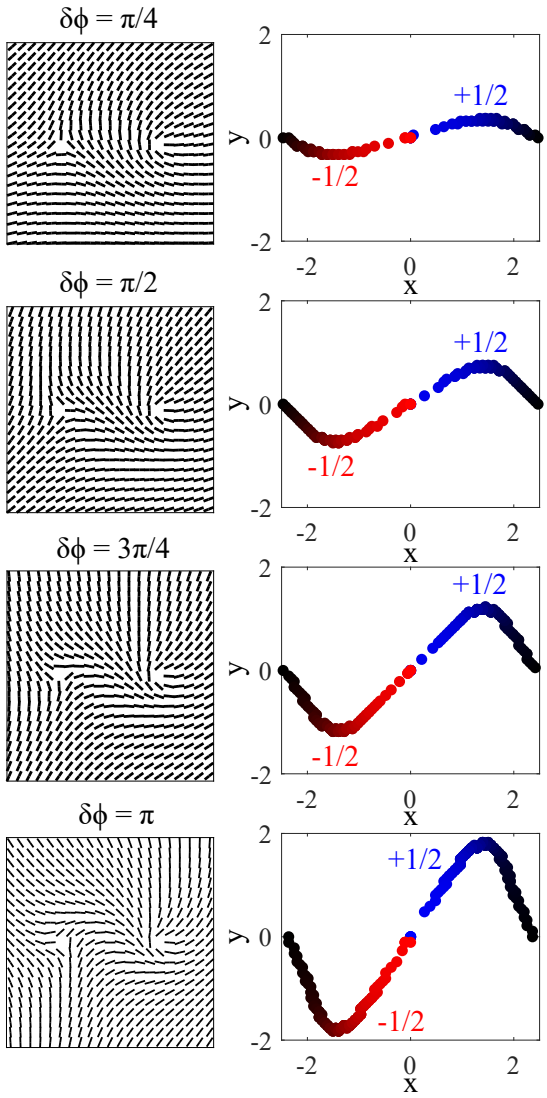

Figure 7.5: Initial conditions alongside simulated disclination (x, y) position for initially twisted $\pm 1/2$ defects with $\phi_0 = 0$ and $L_2 = L_3 = L_4 = 0$. The positions appear as dots in which the brighter dots indicate a later simulation time. Note that as $\delta\phi$ increases the transverse component of the velocity also increases.

so that the velocity is given by

$$\mathbf{v}^{+} = -2\left[\frac{1}{R}\hat{\mathbf{r}}_{12} - \frac{\delta\phi}{R\ln(R/a)}\left(\hat{\mathbf{z}}\times\hat{\mathbf{r}}_{12}\right)\right]. \tag{7.26}$$

Eq. (7.26) explicitly gives a component of the velocity perpendicular to $\hat{\mathbf{r}}_{12}$ if $\delta\phi \neq 0$ which is precisely what is observed in the simulations. We can similarly derive the velocity for the negative disclination

$$\mathbf{v}^{-} = 2\left[\frac{1}{R}\hat{\mathbf{r}}_{12} - \frac{\delta\phi}{R\ln(R/a)}\left(\hat{\mathbf{z}}\times\hat{\mathbf{r}}_{12}\right)\right] \tag{7.27}$$

which is opposite that of the positive disclination as expected for a one-constant system.

That the disclination velocity gives the correct qualitative velocity of the twisted defects, whereas an overdamped velocity proportional to the force as derived from the free energy does not, is a non-trivial result, and it implies a tensorial effective mobility linking velocity and driving force of topological origin. As discussed above, from the perspective of the nematogens, we may think of the motion as a geometric constraint that forces the nematogens to rotate locally while remaining continuous. On the other hand, if we shift our perspective to the defects as the primary objects in the system we can think of this as a topological constraint that the dynamics must obey while it drives the system to minimize its energy. This notion of regarding the disclinations as effective particles is analogous to many areas of condensed matter and high energy physics where there are multiple perspectives of which to understand the physical system [9].

We conclude this section by introducing anisotropic elasticity into the energy and studying the resulting motion. We first study disclination annihilation with twisted initial condition such that $\delta\phi = \pi$, $\phi_0 = 0$ and $R_0 = 5$. We explore the three cases of $L_3 = -1$ ($\varepsilon = -0.38$), $L_3 = 0$ and $L_3 = 3$ ($\varepsilon = 0.75$). In Fig. 7.6 we plot the trajectories in the form of (x, y) values of the annihilating defects. In all three cases, the motion of the $-1/2$ disclinations are relatively similar, with all three going through the same "apex" point of the trajectory, while the $+1/2$ defects display wildly different trajectories. If $L_3 = 3$ the $+1/2$ disclination does not move much from its starting position until $\delta\phi = 0$, while if $L_3 = -1$ the $+1/2$ disclination moves much faster and farther from its starting position. This behavior can be understood by the discussion in

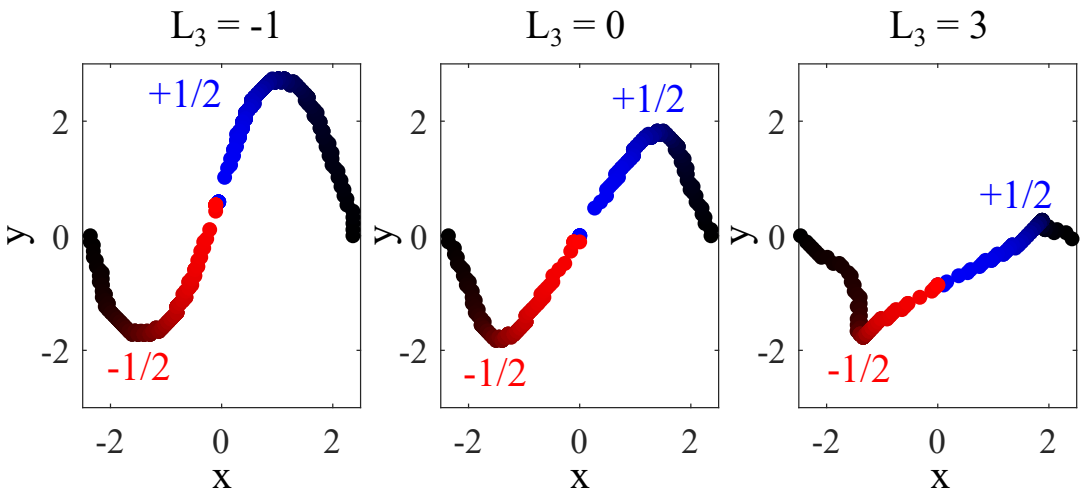

Figure 7.6: Disclination (x, y) positions during annihilation for a twisted configuration with initial $\delta\phi = \pi$ for various anisotropic elastic situations: $L_3 = -1$, $L_3 = 0$, and $L_3 = 3$. Dots indicate the position of defects while the brighter dots indicate later simulation time.

Sec. 7.3.1. From the calculation resulting in Eqs. (7.20) and (7.21) we see that the $+1/2$ disclination should move towards the bend region if $L_3 > 0$ or the splay region if $L_3 < 0$ while the $-1/2$ disclination should not be biased toward any direction. The twisted configuration in Fig. 7.1 shows the initial condition for all three anisotropic cases and we note that the $+1/2$ disclination does indeed have motion biased toward the splay or bend regions depending on the sign of L_3.

Here we have characterized the annihilation dynamics for two defects in two dimensions. We have shown that including anisotropic elasticity changes the dynamics so that it depends on the overall phase of the system as well. This has implications for defect coarsening in both passive and active systems in that coarsening in systems with anisotropic elasticity will be coupled to the boundary conditions and the conditions at the time of disclination nucleation. Additionally we have proven the usefulness of the velocity equation derived in Chapter 6 in not only analyzing motion but also predicting the motion of defects given the configuration. In later sections we will show that the predictive power can be used for even more complicated systems. This has implications for engineered systems in which directed motion of defects or particles is the desired outcome.

7.4 Three Dimensional Disclination Annihilation

We now turn our attention to the annihilation or "recombination" of disclination lines in three dimensions. We study two configurations specifically: two initially straight, uniform $\hat{\mathbf{\Omega}}$, disclination lines but of arbitrary tangent and rotation vectors, and initially circular loop disclinations. To initialize the computations as well as to analyze their motion with the kinematic velocity equation of Chapter 6, for the two line disclinations we set our coordinate system so that disclination 1 is located at $\mathbf{r}_1(z) = (-R/2, 0, z)$ with tangent vector $\hat{\mathbf{T}}_1 = \hat{\mathbf{z}}$. We further orient the coordinate system so that the closest point between the two disclinations lies on the x axis and the tangent vector of disclination 2 lies in the y-z plane so that the location of disclination 2 is given by $\mathbf{r}_2(z) = \Big(R/2, |\hat{\mathbf{z}} \times \hat{\mathbf{T}}_2|z, (\hat{\mathbf{z}} \cdot \hat{\mathbf{T}}_2)z\Big)$.

While we have Eq. (7.11) for the director configuration in two dimensions for a system with N defects, there is no equivalent in three dimensions, even for the simplest case of straight lines with constant $\hat{\mathbf{\Omega}}$. This is due to the fact that the Euler-Lagrange equations corresponding to the Frank-Oseen free energy in three dimensions are no longer linear. To see this, we may write the director as $\hat{\mathbf{n}} = (\cos\phi\sin\theta, \sin\phi\sin\theta, \cos\theta)$ and then the one-constant Frank-Oseen free energy density is

$$f(\nabla\phi, \nabla\theta) = K\left(\sin^2\theta|\nabla\phi|^2 + |\nabla\theta|^2\right). \tag{7.28}$$

The corresponding Euler-Lagrange equations are then

$$\begin{aligned} \sin 2\theta \nabla\phi \cdot \nabla\theta + \sin^2\theta\nabla^2\phi = 0 \\ \sin 2\theta|\nabla\phi|^2 - 2\nabla^2\theta = 0. \end{aligned} \tag{7.29}$$

Because of the nonlinearity in the Euler-Lagrange equations, it is possible that unique director solutions do not exist for $N \geq 2$ line disclinations. That is to say, given the disclination positions, orientations, and rotation vectors, we may not be able to uniquely describe the nematic configuration as we can with a two dimensional system with optimal orientation.

As one populates the system with defects, it becomes clear that after there are two disclination lines the interpretation (which holds in 2D) that subsequent defects just add

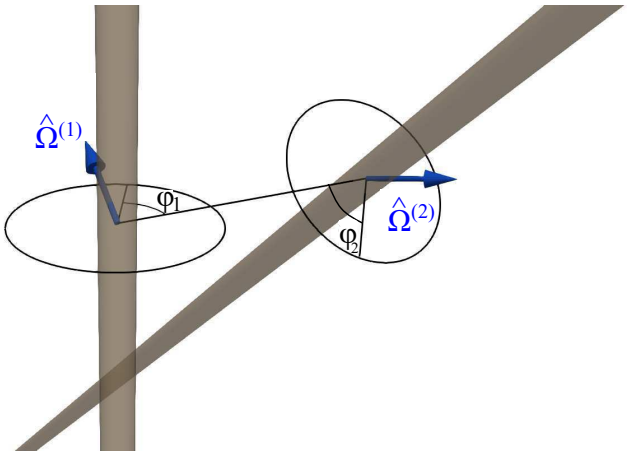

Figure 7.7: Diagram of two straight, interacting disclination lines. φ_1 represents the azimuthal angle in the normal plane of disclination 1 while φ_2 represents the azimuthal angle in the normal plane of disclination 2.

a rotation to the current director field breaks down since rotation in three dimensions is not commutative (so the order in which defects populate the system matters). Thus we might expect multiple configurations that satisfy Eq. (7.29) for a given set of rotation vectors. As an aside, this problem does not appear for loop defects (as long as they are sufficiently far from one another) because in the far field the director distortion that is characteristic of a loop disclination appears as a hedgehog of integer charge (see the discussion in Sec. 5.2) which can be added as multipoles of the director field [120]. While, there is still much work that needs to be done in understanding the coarsening dynamics of many line defects, here we focus on the simpler (but still complex) configuration with only two lines (or single loop).

7.4.1 One Constant Approximation

For two disclinations we can estimate the effect of one disclination on the other. To do this, we first define two fields, $\varphi_1(x, y, z)$ and $\varphi_2(x, y, z)$ which give the azimuthal angle

with respect to the normal planes of disclinations 1 and 2 in isolation,

$$\begin{aligned}\varphi_1(x,y,z) &= \arctan\left(\frac{y}{x+R/2}\right)\\ \varphi_2(x,y,z) &= \arctan\left(\frac{-\left(\hat{\mathbf{z}}\cdot\hat{\mathbf{T}}_2\right)y+\left|\hat{\mathbf{z}}\times\hat{\mathbf{T}}_2\right|z}{R/2-x}\right).\end{aligned} \tag{7.30}$$

Throughout this section, we assume that the two line defects (or single loop) have "optimal" orientation as discussed in Sec. 7.3.1, and so we have defined φ_1 and φ_2 so that they are both zero along the line segment connecting the closest points between the lines and, importantly, they share $\hat{\mathbf{n}}_0$ (so that $\hat{\mathbf{\Omega}}_1\cdot\hat{\mathbf{n}}_0=\hat{\mathbf{\Omega}}_2\cdot\hat{\mathbf{n}}_0=0$). A sketch of this configuration is shown in Fig. 7.7 with φ_1 and φ_2 visually depicted. We then assume the director field near disclination 1 is given by a small rotation of the director with respect to the axis $\hat{\mathbf{\Omega}}_2$. This allows us to apply Eq. (7.1) near the disclination with $\tilde{\varphi}=(1/2)\varphi_2$ and $\hat{\mathbf{q}}=\hat{\mathbf{\Omega}}_2$.

Using Eq. (7.8), we can predict the velocity of disclination 1 in the presence of disclination 2. To do this, we calculate $\nabla\tilde{\varphi}$ (with $\tilde{\varphi}=(1/2)\varphi_2$ in Eq. (7.30)) at the location of the disclination core, $\mathbf{r}_1$:

$$\begin{aligned}\nabla\tilde{\varphi}\big|_{\mathbf{r}=\mathbf{r}_1} = \frac{1}{2}\frac{|\hat{\mathbf{z}}\times\hat{\mathbf{T}}_2|z}{R^2+|\hat{\mathbf{z}}\times\hat{\mathbf{T}}_2|^2z^2}\hat{\mathbf{x}}\\ -\frac{1}{2}\frac{(\hat{\mathbf{z}}\cdot\hat{\mathbf{T}}_2)R}{R^2+|\hat{\mathbf{z}}\times\hat{\mathbf{T}}_2|^2z^2}\hat{\mathbf{y}}+\frac{1}{2}\frac{|\hat{\mathbf{z}}\times\hat{\mathbf{T}}_2|R}{R^2+|\hat{\mathbf{z}}\times\hat{\mathbf{T}}_2|^2z^2}\hat{\mathbf{z}}.\end{aligned} \tag{7.31}$$

Taking $\hat{\mathbf{q}}=\hat{\mathbf{\Omega}}_2$ in Eq. (7.8), the predicted velocity of disclination 1 is

$$\mathbf{v}_1(z) = -2\left(\hat{\mathbf{\Omega}}_1\cdot\hat{\mathbf{\Omega}}_2\right)\left[\frac{|\hat{\mathbf{z}}\times\hat{\mathbf{T}}_2|z}{R^2+|\hat{\mathbf{z}}\times\hat{\mathbf{T}}_2|^2z^2}\hat{\mathbf{y}}+\frac{(\hat{\mathbf{z}}\cdot\hat{\mathbf{T}}_2)R}{R^2+|\hat{\mathbf{z}}\times\hat{\mathbf{T}}_2|^2z^2}\hat{\mathbf{x}}\right]. \tag{7.32}$$

Eq. (7.32) yields several predictions about the motion of annihilating disclination lines. First, the velocity is largest at $z=0$, which is the closest point between the lines, and this point moves directly toward the opposite disclination. Additionally, if the lines are not parallel, then there is a component of the velocity for points $z\neq 0$ that is transverse to the direction between the defects. This component is odd in z,

and thus indicates that non-parallel lines will rotate to become parallel. If we focus on the closest points between defects and generalize to an arbitrary $\hat{\mathbf{T}}_1$, we find that the velocity of this point is

$$\mathbf{v}_1(0) = 2S_N^2 \left(\hat{\mathbf{\Omega}}_1 \cdot \hat{\mathbf{\Omega}}_2\right) \left(\hat{\mathbf{T}}_1 \cdot \hat{\mathbf{T}}_2\right) \frac{\hat{\mathbf{r}}_{12}}{R^2} \tag{7.33}$$

so that the closest point between disclinations does not move if the tangent vectors *or* rotation vectors are perpendicular to each other. Additionally if $\hat{\mathbf{\Omega}}_1 \cdot \hat{\mathbf{\Omega}}_2 \neq 0$ and $\hat{\mathbf{T}}_1 \cdot \hat{\mathbf{T}}_2 \neq 0$ we expect the distance between disclinations to scale as $R \sim t^{1/2}$ just as with two dimensional disclinations. We note that Eq. (7.33) is proportional to the force between two disclinations derived in Ref. [38] by using the effective Peach-Koehler force between disclinations. Here, however, we do not integrate the force between two disclinations over the disclinations as is done in Ref. [38]. Instead, Eq. (7.32) gives the velocity at points along the disclination line, which we are able to find since we are locally approximating the fully three dimensional configuration $\mathbf{Q}$ at the disclination core. This highlights the power of the method, given that one is able to reasonably approximate $\mathbf{Q}$.

To test these velocity predictions we numerically study the motion of annihilating disclination lines such that $\hat{\mathbf{\Omega}}_1 = \hat{\mathbf{z}}$ and $\hat{\mathbf{T}}_1 = \hat{\mathbf{z}}$ with varying $\hat{\mathbf{\Omega}}_2$ ($\hat{\mathbf{\Omega}}_2$ is always chosen so $\hat{\mathbf{\Omega}}_1 \cdot \hat{\mathbf{\Omega}}_2 < 0$) and $\hat{\mathbf{T}}_2$. We use the finite element method described in Chapter 2 with $\Delta t = 0.1$ and set $\kappa/(nk_BT) = 4$ so $S_N = 0.6751$ and $L_2 = L_3 = L_4 = 0$. We use a standard tetrahedral mesh with $41 \times 41 \times 41$ vertices. In Fig. 7.8a we plot several time slices of a typical simulation. The contour shows the extent of the defects (surfaces of constant $S = 0.3S_N$), while the cylinders show the director orientations. We find that the initially straight defects bend inward near the closest points. This is because the velocity is largest in these regions as discussed above. As the defects recombine, they leave behind horseshoe like structures that continue to annihilate. This behavior is similar to recent experimental results in Ref. [21] who studied the recombination of disclination lines in a nematic. In Fig. 7.8b we plot $\mathbf{v} \cdot \hat{\mathbf{r}}_{12}$ as a function of varying $\hat{\mathbf{T}}_1 \cdot \hat{\mathbf{T}}_2$ and $\hat{\mathbf{\Omega}}_1 \cdot \hat{\mathbf{\Omega}}_2$ to test the prediction of Eq. (7.33). We find that $\mathbf{v} \cdot \hat{\mathbf{r}}_{12}$ scales linearly with $\hat{\mathbf{\Omega}}_1 \cdot \hat{\mathbf{\Omega}}_2$ which is predicted by Eq. (7.33); however we only find a linear scaling with $\hat{\mathbf{T}}_1 \cdot \hat{\mathbf{T}}_2$ early in the simulations while the disclinations are straight. This is

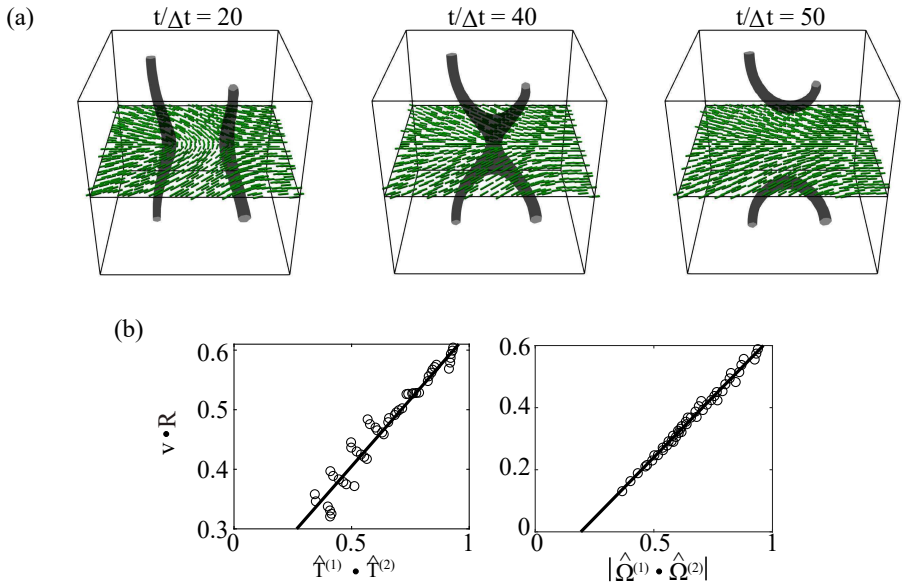

Figure 7.8: (a) Time slices of the configuration with two initially straight line disclinations with $\hat{\mathbf{T}}_1 \cdot \hat{\mathbf{T}}_2 = 0.3$ and $\hat{\mathbf{\Omega}}_1 \cdot \hat{\mathbf{\Omega}}_2 = -1$ at iteration numbers $t/\Delta t = 20$, 40, and 50. Contours represent surfaces of constant $S = 0.3S_N$ while cylinders represent the director configuration in the plane $z = 0$. The disclinations bend early in the simulation near their closes points as this is the point on the line that moves the fastest. After recombining, the disclinations continue to annihilate in horseshoe structures. (b) Instantaneous $\mathbf{v} \cdot \mathbf{r}_{12}$ plotted against instantaneous $\hat{\mathbf{T}}_1 \cdot \hat{\mathbf{T}}_2$ (left) and $\hat{\mathbf{\Omega}}_1 \cdot \hat{\mathbf{\Omega}}_2$ (right) for various simulations. We find that the relationship is linear as predicted by Eq. (7.33). We note that the points displayed in the figure for $\hat{\mathbf{T}}_1 \cdot \hat{\mathbf{T}}_2$ all come from early in the simulation, before the disclinations begin to curve as Eq. (7.33) only applies to this situation.

likely due to the fact that the disclinations develop curvature, which is not taken into account in the above calculation and results in changing the velocity slightly.

While we find agreement with the dependence of the velocity on $\hat{\mathbf{\Omega}}_1 \cdot \hat{\mathbf{\Omega}}_2$ and $\hat{\mathbf{T}}_1 \cdot \hat{\mathbf{T}}_2$ we do not find the expected scaling of $R \sim t^{1/2}$, particularly early in the simulations. This is due to two factors: the defects develop curvature, and thus a line tension slows them down [1,127] and the defects rotate to be parallel, increasing their speed since the velocity is proportional to $\hat{\mathbf{T}}_1 \cdot \hat{\mathbf{T}}_2$. To investigate the rotation of defects and the effect this has on their motion, we go back to Eq. (7.32) for the full velocity as a function of z. We now use two variables to characterize the system at a given point in time: the distance between the defects R and the angle between tangent vectors at the closest point between defects, ψ. We derive an equation for the time evolution of ψ by first noting that

$$\begin{aligned} \hat{\mathbf{T}}_1 \cdot \hat{\mathbf{T}}_2 &= \cos\psi \\ \Rightarrow \frac{d\hat{\mathbf{T}}_1}{dt} \cdot \hat{\mathbf{T}}_2 + \hat{\mathbf{T}}_1 \cdot \frac{d\hat{\mathbf{T}}_2}{dt} &= -\sin\psi \frac{d\psi}{dt} \end{aligned} \tag{7.34}$$

and

$$\frac{d\hat{\mathbf{T}}_1}{dt} = \frac{d}{dt}\frac{d\mathbf{r}_1}{dz} = \frac{d}{dz}\frac{d\mathbf{r}_1}{dt} = \frac{d\mathbf{v}_1}{dz}. \tag{7.35}$$

We can also derive a similar result for $d\hat{\mathbf{T}}_2/dt$. We then we find

$$\left.\frac{d\psi}{dt}\right|_{z=0} = -\frac{1}{\sin\psi}\left(\left.\frac{d\mathbf{v}_1}{dz} \cdot \hat{\mathbf{T}}_2\right|_{z=0} + \hat{\mathbf{T}}_1 \cdot \left.\frac{d\mathbf{v}_2}{dz}\right|_{z=0}\right) = \frac{4(\hat{\mathbf{\Omega}}_1 \cdot \hat{\mathbf{\Omega}}_2)\sin\psi}{R^2}. \tag{7.36}$$

We can also derive an equation for the distance between defects at their closest point by finding dR/dt:

$$\left.\frac{dR}{dt}\right|_{z=0} = \frac{4(\hat{\mathbf{\Omega}}_1 \cdot \hat{\mathbf{\Omega}}_2)\cos\psi}{R}. \tag{7.37}$$

Eqs. (7.36) and (7.37) constitute a system of coupled first order ordinary differential equations that characterize the motion of the two disclination system. Of course, these are just an approximation and we are still assuming the disclinations remain straight. Nevertheless, we note a few key details about the predictions they make. First, as previously noted, if the disclinations are perpendicular and $\cos\psi = 0$ the distance between the defects does not change. This does not mean the disclinations do not

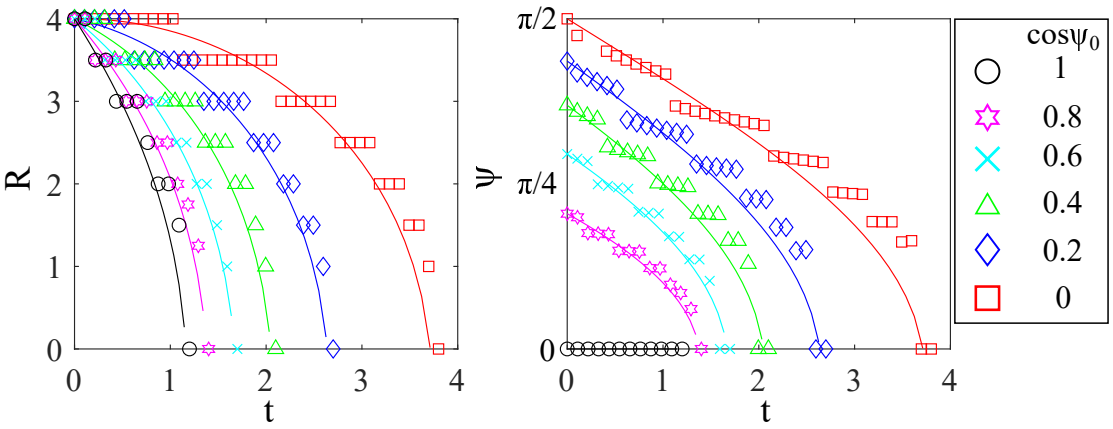

Figure 7.9: Line separation, R (left), and angle between disclinations, ψ (right), as a function of time for the full **Q**-tensor simulation (dots) and the forward Euler numerical solution to the ODE defined by Eqs. (7.36) and (7.37) (solid lines) for a variety of initial angles between disclinations, ψ_0, and initial separation $R_0 = 4$. The time is scaled for the ODE solutions to coincide with annihilation in the **Q**-tensor simulation, but there is no fit between the two. Good agreement is found between both solutions.

move, however. In this case $\sin\psi = 1$ and so ψ changes, i.e. the disclinations rotate. Additionally, the rotation rate is proportional to $1/R^2$ and so this rotation may take much longer if the defects are initially far apart.

To test the predictions of Eqs. (7.36) and (7.37), we solve them using a simple forward Euler method [55] in which we take the time step $\Delta t = 0.1$. In Fig. 7.9 we plot $R(t)$ for the numerical solution to Eqs. (7.36) and (7.37) as well as the results for the full **Q**-tensor simulations. In these plots, the solid lines are the Euler solution, while the individual points are R and ψ determined from the computation based on the **Q**-tensor. We use $R_0 = 4$ and a variety of ψ_0 to highlight the rotation of the disclinations as well. We emphasize that the solid lines in Fig. 7.9 are not fits, they are solutions to Eqs. (7.36) and (7.37); however, the time is scaled so that the Euler solutions annihilate at the same time as the **Q**-tensor computations. We find good agreement between the two methods, which highlights the power of using the kinematic velocity equation in analyzing and predicting disclination motion since the ODE defined by Eqs. (7.36) and (7.37) is much simpler to solve. We also note that the results of Ref. [38] predict that the force between two perpendicular disclinations should be zero, yet we find that there

is a restoring torque that causes the defects to rotate and still eventually annihilate.

As an aside, we have not considered the possibility of $\hat{\mathbf{\Omega}}_1 \cdot \hat{\mathbf{\Omega}}_2$ changing during the course of annihilation. While we do not observe this happening much in the one constant approximation simulations, there have been experiments that suggest it does indeed happen [21]. To derive an equation of motion for the $\hat{\mathbf{\Omega}}$s, however, one would need to analyze the time dependence of $\mathbf{Q}$ directly, which is outside the scope of this dissertation.

We now seek to study the relaxation of circular disclination loops in nematics. For loop disclinations we approximate the director in cylindrical coordinates such that it gives a two-defect configuration in every normal plane:

$$\begin{aligned} \hat{\mathbf{n}} &= \cos\left(\frac{1}{2}\varphi_1 + \frac{1}{2}\varphi_2\right)\hat{\mathbf{n}}_0 + \sin\left(\frac{1}{2}\varphi_1 + \frac{1}{2}\varphi_2\right)\hat{\mathbf{n}}_1 \\ \varphi_1(\rho,\theta,z) &= \arctan\left(\frac{z}{R-\rho}\right) \\ \varphi_2(\rho,\theta,z) &= \arctan\left(\frac{z}{R+\rho}\right) \end{aligned} \tag{7.38}$$

where R is the loop radius and φ_2 represents the rotation in the director field coming from the opposite side of the loop. We note that in Eq. (7.38), $\hat{\mathbf{n}}_0$ and $\hat{\mathbf{n}}_1$ may be functions of ρ and θ themselves if $\hat{\mathbf{\Omega}}$ is changing along the loop. Thus, near the defect core we can slightly modify our linear approximation of $\mathbf{Q}$ to be written in cylindrical coordinates so that

$$\mathbf{Q} \approx S_N\left[\frac{1}{6}\mathbf{I} - \frac{1}{2}\hat{\mathbf{\Omega}}\otimes\hat{\mathbf{\Omega}} + \frac{R-\rho}{2a}\left(\tilde{\mathbf{n}}_0\otimes\tilde{\mathbf{n}}_0 - \tilde{\mathbf{n}}_1\otimes\tilde{\mathbf{n}}_1\right) + \frac{z}{2a}\left(\tilde{\mathbf{n}}_0\otimes\tilde{\mathbf{n}}_1 + \tilde{\mathbf{n}}_1\otimes\tilde{\mathbf{n}}_0\right)\right] \tag{7.39}$$

where $\tilde{\mathbf{n}}_i = \hat{\mathbf{n}}_i + (1/2)\varphi_2\left[\hat{\mathbf{\Omega}}(-R)\times\hat{\mathbf{n}}_i\right]$ and $\hat{\mathbf{\Omega}}(-R)$ denotes $\hat{\mathbf{\Omega}}$ at the opposite side of the loop. While this approximation only gives the perturbation resulting from the opposite side of the loop, we show below that this is both analytically calculable and close to the numerical solution given by full $\mathbf{Q}$-tensor computations.

We first consider the case where $\hat{\mathbf{\Omega}}$ is constant along the loop. These are loops of zero point charge, as discussed in Sec. 5.2, and are commonly found experimentally in three dimensional active nematic systems [24]. To predict the velocity of the loops we use the approximation of Eq. (7.39). Here, however, we cannot just apply the velocity

of Eq. (7.8) since the line is not straight, and the curvature of the loop will add to the velocity. We thus calculate

$$\hat{\mathbf{\Omega}} \cdot \mathbf{g}\Big|_{\rho=R,\, z=0} = -\frac{S_N^2}{2a^2}\left[\frac{\partial \varphi_2}{\partial \rho}\hat{\boldsymbol{\rho}} + \left(\frac{\partial \varphi_2}{\partial z} + \frac{1}{R}\right)\hat{\mathbf{z}}\right] \tag{7.40}$$

where φ_2 is given in Eq. (7.38). We note that the terms including the derivative of φ_2 come from the interaction with the opposite side of the loop while the $1/R$ term comes from the curvature of the loop. Computing the derivative of φ_2 at the location of the loop we find

$$\begin{aligned} \frac{\partial \varphi_2}{\partial \rho}\bigg|_{\rho=R,\, z=0} &= 0 \\ \frac{\partial \varphi_2}{\partial z}\bigg|_{\rho=R,\, z=0} &= \frac{1}{2R} \end{aligned} \tag{7.41}$$

and taking the tangent vector of the loop to be $\hat{\mathbf{T}} = \hat{\boldsymbol{\theta}}$ we find the velocity at a point on the loop to be

$$\mathbf{v} = -\frac{3}{2R}\hat{\boldsymbol{\rho}}. \tag{7.42}$$

We note that Eq. (7.42) does not depend on $\hat{\mathbf{\Omega}}$ which makes sense from an energetic perspective since the energy of a loop disclination (within a one-constant approximation) does not depend on $\hat{\mathbf{\Omega}}$. Additionally, this velocity predicts that the loop shrinks at a constant rate everywhere until it annihilates itself, which is possible because the overall point charge is zero. Much like the disclinations in two dimensions, the radius of the loop is predicted to scale as $R^2 \sim -t$. We reiterate that this method does not require an integration about the loop to predict the velocity. Rather, we simply approximate the configuration $\mathbf{Q}$ at points along the loop, which then leads to an expression for the velocity at points along the loop.

To test the analytic prediction of Eq. (7.42) we numerically compute the motion of a disclination loop in a similar manner as laid out above. In Fig. 7.10a we show a snapshot of the director configuration of a twist disclination loop self-annihilating while in Fig. 7.10b we show the radius as a function of time while the inset shows the radius squared as a function of time. We find that $R^2 \sim -t$ as expected. Further, Eq. (7.42) predicts that the loop should annihilate faster than two straight line disclinations with

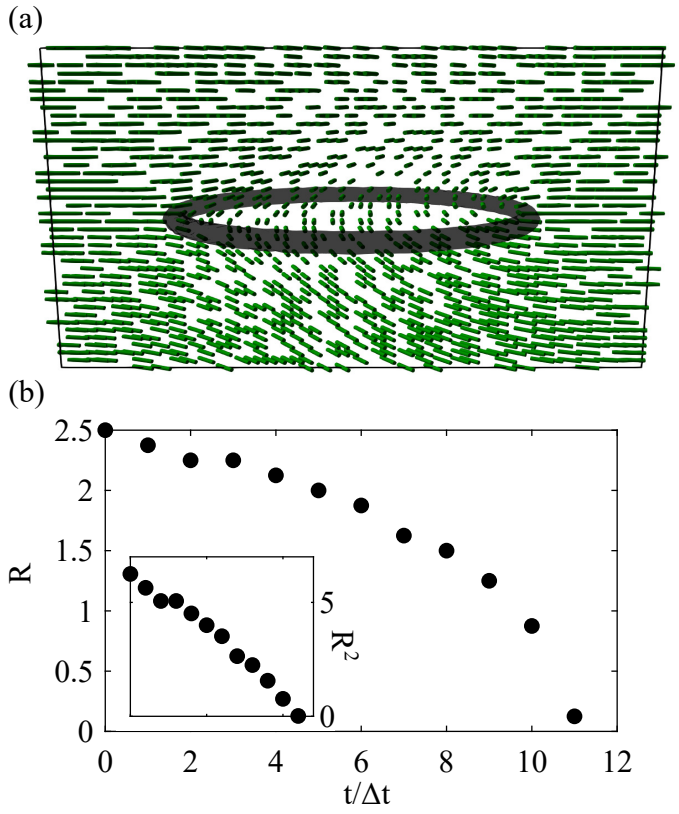

Figure 7.10: Self-annihilating twist loop. (a) Snapshot at $t/\Delta t = 5$ of the director configuration of the loop. The contour represents a surface of constant $S = 0.3S_N$. (b) Loop radius R plotted against iteration number. The inset shows R^2 versus $t/\Delta t$, demonstrating the scaling $R^2 \sim -t$.

$\hat{\mathbf{\Omega}}_1 \cdot \hat{\mathbf{\Omega}}_2 = -1$ and $\hat{\mathbf{T}}_1 \cdot \hat{\mathbf{T}}_2 = 1$. In particular, we calculate that for the same parameters the time of annihilation for the loop disclination should be $2/3$ smaller than the time for the line defects to annihilate. Comparing with a simulation of line disclinations with separation $R_0 = 5$ which annihilate at iteration number $T/\Delta t = 21$ we find that the loop disclination annihilates at iteration $T/\Delta t = 12$ which is very close to the predicted factor of $2/3$ given by the velocity equation.

We can also predict the velocity for loop disclinations with non-constant $\hat{\mathbf{\Omega}}$. These disclinations will have a total nonzero point charge. The most common disclination loop of this type is the Saturn ring configuration in which a particle with homeotropic anchoring is placed within a liquid crystal [62]. The anchoring condition necessitates a $1/2$ disclination loop with negative point charge to balance the induced charge from the particle (see e.g. Fig. 5.1) (topologically equivalent to a hyperbolic hedgehog). The analytic calculation is more difficult than above since now $\hat{\mathbf{\Omega}}$, $\hat{\mathbf{n}}_0$, and $\hat{\mathbf{n}}_1$ may vary along the loop. For concreteness, we take $\hat{\mathbf{\Omega}} = \hat{\mathbf{T}} = \hat{\boldsymbol{\theta}}$, $\hat{\mathbf{n}}_0 = \hat{\mathbf{z}}$, and $\hat{\mathbf{n}}_1 = \hat{\boldsymbol{\rho}}$ so that

$$\frac{\partial \hat{\mathbf{\Omega}}}{\partial \theta} = -\hat{\boldsymbol{\rho}},\ \frac{\partial \hat{\mathbf{n}}_0}{\partial \theta} = 0,\ \frac{\partial \hat{\mathbf{n}}_1}{\partial \theta} = \hat{\boldsymbol{\theta}}. \tag{7.43}$$

Then, after similar calculations to the rest of this chapter we find

$$\hat{\mathbf{\Omega}} \cdot \mathbf{g}\Big|_{\rho=R,\, z=0} = \frac{S_N^2}{2a^2}\frac{\partial \varphi_2}{\partial \rho}\hat{\boldsymbol{\rho}} + S_N^2\left[-\frac{1}{2a^2 R} + \frac{1}{2aR^2} + \frac{1}{2a^2}\frac{\partial \varphi_2}{\partial z}\right]\hat{\mathbf{z}}. \tag{7.44}$$

Much like the constant $\hat{\mathbf{\Omega}}$ loop, there are contributions from the curvature of the loop and the interaction between opposite sides of the loop. The terms involving derivatives of φ_2 are the interaction terms while the terms without derivatives come from the curvature. We note that there are two competing terms of different orders of R from the curvature. The negative term to $O(1/R)$ will tend to promote shrinking while the positive term to $O(1/R^2)$ will promote expanding. Also, when comparing to Eq. (7.40) note the difference in sign on the derivative terms. This is because the interaction between opposite sides is that of repulsion and not attraction.

Finally, computing the velocity we find,

$$\mathbf{v} = \left[-\frac{1}{2R} + \frac{a}{R^2}\right]\hat{\boldsymbol{\rho}}. \tag{7.45}$$

Eq. (7.45) predicts that if $R > 2a$ the loop disclination will shrink, similar to the constant $\hat{\mathbf{\Omega}}$ loop. However, if $R < 2a$ Eq. (7.45) predicts that the loop disclination will expand. Hence the prediction is that there is a stable defect size $R = 2a$ for disclination loops of this type. A consequence of this prediction is that hyperbolic hedgehog defects are actually small loops when viewed in the **Q**-tensor representation. This hypothesis has been explored analytically using the free energy and has been observed in some computational settings as well [128, 129].

7.4.2 Reduced Twist Constant

We now study the effect of anisotropic elasticity on three dimensional configurations containing disclinations. In particular we focus on the effect of lowering the twist elastic constant, K_{22}, relative to the splay and bend constants. In three dimensions the twist elastic mode is allowed, and it has been observed experimentally that many liquid crystals have a twist constant that is up to an order of magnitude smaller than the other two [5, 17, 18, 23]. Changing the relative twist constant in the **Q**-tensor field theory amounts to setting $L_2 \neq 0$. Thus to predict the motion of disclinations with the kinematic velocity equation we must first compute the contribution of the Ł$_2$ term to $\partial_t \mathbf{Q}$ in its gradient flow relaxation. We calculate,

$$-\frac{\delta F_2}{\delta Q_{\mu\nu}} = L_2 \partial_\nu \partial_k Q_{\mu k}, \tag{7.46}$$

where F_2 represents the corresponding term in the elastic energy (Eq. (2.7)) for which the coefficient is L_2.

For the case of two straight disclination lines we repeat the previous calculations to predict the component of the velocity resulting from nonzero L_2. To do this we assume that the linear approximation of **Q** near the core, Eq. (5.25), is still valid, which was the case near the core in our previous investigation of the equilibrium core structures in Chapter 4. We also assume that the rotation of the director near the core can be approximated in the same manner as above. This is also likely since, in contrast to the case of unequal splay and bend constants, twist defects appear to have an isotropic distribution of twist distortion around the disclination.

We first compute $\hat{\mathbf{\Omega}}_1 \cdot \mathbf{g}$ for arbitrary $\hat{\mathbf{n}}_0$, $\hat{\mathbf{n}}_1$, $\hat{\mathbf{\Omega}}_1$, and $\hat{\mathbf{\Omega}}_2$:

$$\begin{aligned}\hat{\mathbf{\Omega}}_1 \cdot \mathbf{g} = \frac{L_2 S_N^2}{8a^2} \Big[&-(\hat{\mathbf{\Omega}}_1 \cdot \hat{\mathbf{\Omega}}_2) \left(\hat{n}_{0x}(\hat{\mathbf{n}}_0 \cdot \nabla\tilde{\varphi}) + \hat{n}_{0x}^2 \partial_x \tilde{\varphi} + \hat{n}_{1x}(\hat{\mathbf{n}}_1 \cdot \nabla\tilde{\varphi}) + \hat{n}_{1x}^2 \partial_x \tilde{\varphi} \right. \\ &\left. + \hat{n}_{1y}(\hat{\mathbf{n}}_0 \cdot \nabla\tilde{\varphi}) - \hat{n}_{0y}(\hat{\mathbf{n}}_1 \cdot \nabla\tilde{\varphi}) \right) - p_{0x}(\hat{\mathbf{n}}_1 \cdot \nabla\tilde{\varphi}) - p_{0x}\hat{n}_{1x}\partial_x\tilde{\varphi} + p_{1x}(\hat{\mathbf{n}}_0 \cdot \nabla\tilde{\varphi}) + p_{1x}\hat{n}_{0x}\partial_x\tilde{\varphi} \\ &- p_{1y}(\hat{\mathbf{n}}_1 \cdot \nabla\tilde{\varphi}) - p_{1y}\hat{n}_{1y}\partial_y\nabla\tilde{\varphi} - p_{0y}(\hat{\mathbf{n}}_0 \cdot \nabla\tilde{\varphi}) - p_{0y}\hat{n}_{0y}\partial_y\tilde{\varphi} \Big] \hat{\mathbf{x}} \\ &+ \frac{1}{8a^2} \Big[-(\hat{\mathbf{\Omega}}_1 \cdot \hat{\mathbf{\Omega}}_2) \left(\hat{n}_{0x}(\hat{\mathbf{n}}_1 \cdot \nabla\tilde{\varphi}) - \hat{n}_{1x}(\hat{\mathbf{n}}_0 \cdot \nabla\tilde{\varphi}) + \hat{n}_{1y}(\hat{\mathbf{n}}_1 \cdot \nabla\tilde{\varphi}) + \hat{n}_{1y}^2 \partial_y \tilde{\varphi} \right. \\ &\left. + \hat{n}_{0y}(\hat{\mathbf{n}}_0 \cdot \nabla\tilde{\varphi}) + \hat{n}_{0y}^2 \partial_y \tilde{\varphi}) \right) + p_{0x}(\hat{\mathbf{n}}_0 \cdot \nabla\tilde{\varphi}) + p_{0x}\hat{n}_{0x}\partial_x\tilde{\varphi} + p_{1x}(\hat{\mathbf{n}}_1 \cdot \nabla\tilde{\varphi}) + p_{1x}\hat{n}_{1x}\partial_x\tilde{\varphi} \\ &+ p_{1y}(\hat{\mathbf{n}}_0 \cdot \nabla\tilde{\varphi}) + p_{1y}\hat{n}_{0y}\partial_y\tilde{\varphi} - p_{0y}(\hat{\mathbf{n}}_1 \cdot \nabla\tilde{\varphi}) - p_{0y}\hat{n}_{1y}\partial_y\tilde{\varphi} \Big] \hat{\mathbf{y}} \end{aligned} \quad (7.47)$$

where $\mathbf{p}_i = \hat{\mathbf{\Omega}}_2 \times \hat{\mathbf{n}}_i$. While Eq. (7.47) is not particularly useful for understanding the general behavior of disclination lines with reduced twist, we can analyze some specific cases. If we take $\hat{\mathbf{\Omega}}_1 = -\hat{\mathbf{z}}$, $\hat{\mathbf{\Omega}}_2 = \hat{\mathbf{z}}$, and $\hat{\mathbf{n}}_0 = \hat{\mathbf{x}}$ so that disclination 1 is a wedge disclination, we find,

$$\hat{\mathbf{\Omega}} \cdot \mathbf{g} = \frac{L_2 S_N^2}{4a^2} \left(\partial_x \tilde{\varphi} \hat{\mathbf{x}} + \partial_y \tilde{\varphi} \hat{\mathbf{y}} \right). \quad (7.48)$$

The velocity at the closest point between disclinations ($z = 0$) is then

$$\mathbf{v} = \left(\hat{\mathbf{T}}_1 \cdot \hat{\mathbf{T}}_2 \right) \left(2 + \frac{L_2}{2} \right) \frac{\hat{\mathbf{r}}_{12}}{R}. \quad (7.49)$$

Comparing this to Eq. (7.33) we find that the wedge disclination's speed is just enhanced by increasing L_2, which makes sense from an energetic perspective as we are increasing the bend and splay constants, so wedge disclinations cost more energy and hence will annihilate faster. On the other hand, if disclination 1 is a twist disclination and we take $\hat{\mathbf{\Omega}}_1 = \hat{\mathbf{y}}$, $\hat{\mathbf{\Omega}}_2 = -\hat{\mathbf{y}}$ and $\hat{\mathbf{n}}_0 = \hat{\mathbf{x}}$ the velocity at the closest points becomes

$$\mathbf{v} = \left[2 \left(\hat{\mathbf{T}}_1 \cdot \hat{\mathbf{T}}_2 \right) + \frac{L_2}{2} \left| \hat{\mathbf{T}}_1 \times \hat{\mathbf{T}}_2 \right| \right] \frac{\hat{\mathbf{r}}_{12}}{R}. \quad (7.50)$$

In this case, $L_2 \neq 0$ leads to an enhancement in the velocity if the disclinations are *not* parallel and, importantly, predicts that defects will be attracted regardless of their relative orientation. If $\hat{\mathbf{T}}_1 \parallel \hat{\mathbf{T}}_2$ we note that Eq. (7.50) predicts that there should be no difference in the annihilation as the case one elastic constant case, Eq. (7.33). This

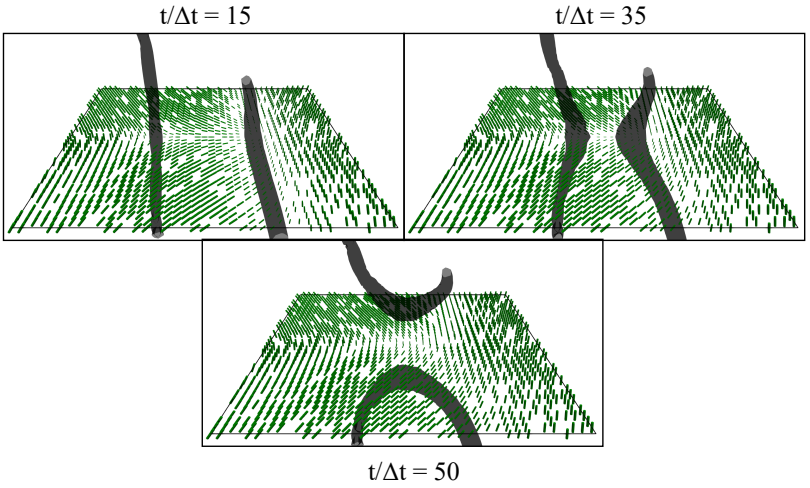

Figure 7.11: Recombination of initially perpendicular disclination lines with initial $\hat{\mathbf{\Omega}}_1 = \hat{\mathbf{y}}$ and $\hat{\mathbf{\Omega}}_2 = -\hat{\mathbf{y}}$ and reduced twist constant relative to splay and bend ($L_2 = 2$). Plots show director configurations in the plane $z = 0$ with contours that represent surfaces of constant $S = 0.3S_N$. The three plots are time slices of the configuration at $t/\Delta t = 15$, $t/\Delta t = 35$, and $t/\Delta t = 50$.

also makes sense from an energetic perspective since for $L_2 \neq 0$ the twist constant is unchanged and the case with $\hat{\mathbf{\Omega}}_1 = \hat{\mathbf{y}}$ and $\hat{\mathbf{\Omega}}_2 = -\hat{\mathbf{y}}$ with $\hat{\mathbf{T}}_1 = \hat{\mathbf{T}}_2 = \hat{\mathbf{z}}$ is a case of two twist disclinations, hence the system is dominated by twist distortion.

The velocity equation predicts interesting behavior in cases where $\hat{\mathbf{\Omega}}_1 \cdot \hat{\mathbf{\Omega}}_2 = 0$ as well. If we take $\hat{\mathbf{\Omega}}_1 = -\hat{\mathbf{y}}$, $\hat{\mathbf{\Omega}}_2 = \hat{\mathbf{z}}$, and $\hat{\mathbf{n}}_0 = \hat{\mathbf{x}}$ we find the velocity of the closest points on the disclination to be

$$\mathbf{v} = \frac{L_2 \left| \hat{\mathbf{T}}_1 \times \hat{\mathbf{T}}_2 \right|}{4} \frac{\mathbf{r}_{12}}{R} \tag{7.51}$$

so that perpendicular oriented disclinations will interact, but parallel disclinations will not. In a similar case, where we rotate $\hat{\mathbf{\Omega}}_1$ and $\hat{\mathbf{\Omega}}_2$ so that $\hat{\mathbf{\Omega}}_1 = \hat{\mathbf{z}}$ and $\hat{\mathbf{\Omega}}_2 = \hat{\mathbf{y}}$, we find

$$\mathbf{v} = \mathbf{0} \tag{7.52}$$

and hence, there is no interaction between disclinations in this case.

To test the analytic predictions for the above cases, we perform simulations similar

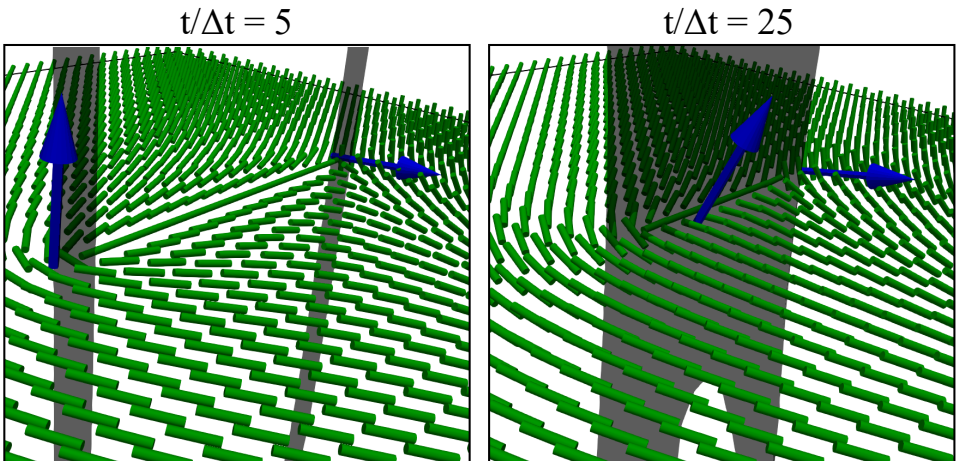

Figure 7.12: Disclination configurations and rotation vectors for two parallel disclinations with initial $\hat{\mathbf{\Omega}}_1 = -\hat{\mathbf{y}}$ and $\hat{\mathbf{\Omega}}_2 = \hat{\mathbf{z}}$ and reduced twist constant ($L_2 = 2$) for time slices at iteration numbers $t/\Delta t = 5$ and $t/\Delta t = 25$. Green cylinders indicate director orientation, contours represent surfaces of constant $S = 0.3S_N$, and blue vectors represent $\hat{\mathbf{\Omega}}_1$ and $\hat{\mathbf{\Omega}}_2$. As the simulation goes on, $\hat{\mathbf{\Omega}}_1$ and $\hat{\mathbf{\Omega}}_2$ tend to rotate towards one another.

to those described above, using the full relaxation equations for $\mathbf{Q}$, except we set $L_2 = 2$ to study the behavior of disclinations in a system with a reduced twist constant ($K_{11}/K_{22} = 2$). For these simulations we set $\Delta t = 0.1$ and the initial separation, $R_0 = 5$. We first compute two parallel lines with $\hat{\mathbf{\Omega}}_1 \cdot \hat{\mathbf{\Omega}}_2 = -1$. In the case of wedge disclinations, $\hat{\mathbf{\Omega}}_1 = -\hat{\mathbf{z}}$ and $\hat{\mathbf{\Omega}}_2 = \hat{\mathbf{z}}$, we find the two disclinations annihilate in 14 iterations. Note that this is faster than the case when $L_2 = 0$ (which annihilate in 21 iterations). If the disclinations are twist disclinations, $\hat{\mathbf{\Omega}}_1 = \hat{\mathbf{y}}$ and $\hat{\mathbf{\Omega}}_2 = -\hat{\mathbf{y}}$, then the disclinations annihilate in 24 iterations. As predicted by Eqs. (7.49) and (7.50) the parallel wedge disclinations annihilate faster than the twist disclinations. We also show in Fig. 7.11 time slices of a configuration with initially perpendicular disclinations where $\hat{\mathbf{\Omega}}_1 = \hat{\mathbf{y}}$ and $\hat{\mathbf{\Omega}}_2 = -\hat{\mathbf{y}}$. In this case the disclinations do interact and annihilate after 48 iterations, exactly twice as long as the parallel disclinations, which is also predicted by Eq. (7.50).

The behavior of disclinations with $\hat{\mathbf{\Omega}}_1 \cdot \hat{\mathbf{\Omega}}_2 = 0$ does not follow the predictions of Eqs. (7.51) and (7.52), however. In the case of $\hat{\mathbf{\Omega}}_1 = -\hat{\mathbf{y}}$ and $\hat{\mathbf{\Omega}}_2 = \hat{\mathbf{z}}$ we find that

perpendicular lines do interact, which is predicted by Eq. (7.51). However, we also find that parallel lines do eventually annihilate, which is a case that Eq. (7.51) predicts should not interact at all. Additionally, we find that when $\hat{\mathbf{\Omega}}_1 = \hat{\mathbf{z}}$ and $\hat{\mathbf{\Omega}}_2 = \hat{\mathbf{y}}$, there is an attraction between lines of any orientation which contradicts the prediction of $\mathbf{v} = 0$. We suspect the primary reason for the differing behavior is that $\hat{\mathbf{\Omega}}_1$ and $\hat{\mathbf{\Omega}}_2$ change throughout the computation as well, which is not accounted for by the above analytic predictions. In Fig. 7.12 we show an example of this by computing $\hat{\mathbf{\Omega}}_1$ and $\hat{\mathbf{\Omega}}_2$ at different times in the simulations for initially parallel disclinations with $\hat{\mathbf{\Omega}}_1 = -\hat{\mathbf{y}}$ and $\hat{\mathbf{\Omega}}_2 = \hat{\mathbf{z}}$. As evidenced by the figure, $\hat{\mathbf{\Omega}}_1$ and $\hat{\mathbf{\Omega}}_2$ rotate over the course of the simulation, which causes an attraction between the disclinations. Interestingly, in this particular case $\hat{\mathbf{\Omega}}_1$ and $\hat{\mathbf{\Omega}}_2$ tend to rotate toward each other, and hence $\hat{\mathbf{\Omega}}_1 \cdot \hat{\mathbf{\Omega}}_2 > 0$ which would result in a repulsion in the one constant case. The time dependence of $\hat{\mathbf{\Omega}}$ in the case of interacting disclinations still requires further study.

Finally, we study the motion of circular loop disclinations with nonzero L_2. In particular, we study the behavior of wedge-twist loops, since pure twist loops (which have twist distortion everywhere) will not qualitatively change with reduced twist constant. For definiteness, we set $\hat{\mathbf{\Omega}} = \hat{\mathbf{x}}$ and $\hat{\mathbf{n}}_0 = \hat{\mathbf{y}}$ along the loop. To obtain a prediction for the velocity, we use the same approximations for the loop as in the previous section and calculate the velocity of a point on the loop to be

$$\mathbf{v}(\theta) = -\frac{1}{2R}\left[3 + L_2\left(4 + 4\cos^2\theta - 2\sin\theta\right)\right]\hat{\boldsymbol{\rho}}. \tag{7.53}$$

We note that now the velocity is a function of the azimuthal angle θ. For the wedge-twist loop described, the twist portions occur at $\theta = 0,\ \pi$ while the $+1/2$ wedge portion occurs at $\theta = \pi/2$ and the $-1/2$ wedge portion occurs at $\theta = 3\pi/2$. If $L_2 \neq 0$, Eq. (7.53) predicts significant asymmetry in the evolution of the loop. The fastest portion of the loop turns out to be the twist portions, which is counter-intuitive from the results for straight line disclinations above, where the *wedge* disclinations annihilate faster when $L_2 > 0$. This is due to the $\cos^2\theta$ term in Eq. (7.53), which is the curvature coupling term (i.e. it does *not* come from derivatives of $\tilde{\varphi}$) when $L_2 \neq 0$. There is additional asymmetry predicted in the wedge portions of the loop due to the $\sin\theta$ term. This predicts that the $-1/2$ segment moves faster than the $+1/2$ segment if $L_2 > 0$. This

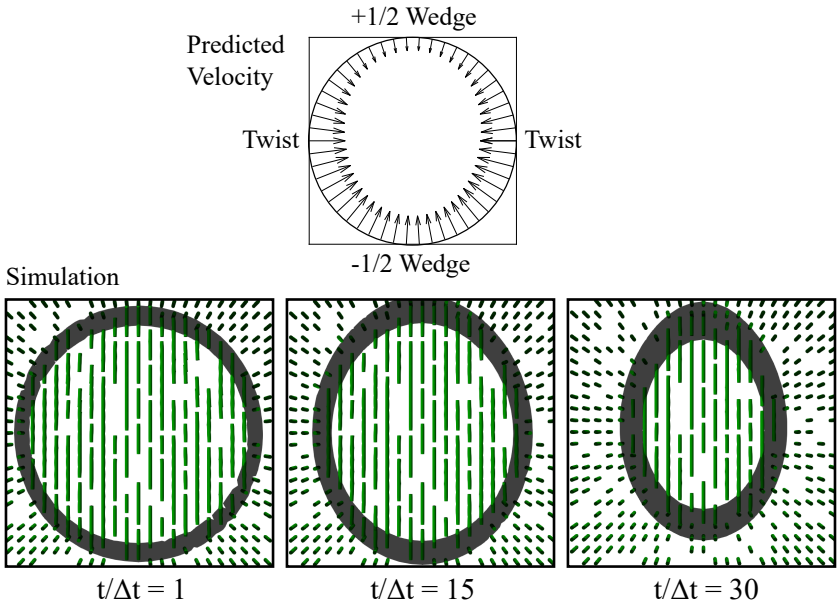

Figure 7.13: Self-annihilating wedge twist line with $L_2 = 2$. The top plot shows the analytical predicted velocity from Eq. (7.53) while the bottom plots show the configuration from the full **Q**-tensor simulation at iteration numbers $t/\Delta t = 1$, 15, and 30. The green cylinders represent the director orientation while the contour represents a surface of constant $S = 0.3S_N$ which indicates the disclination location.

is again against our intuition from the above discussion of straight lines, where wedge disclinations still annihilated symmetrically.

We test the velocity prediction equation against a simulation of an initially circular wedge twist disclination loop, using similar methods as described earlier in the chapter, except we now set $L_2 = 2$. Fig. 7.13 shows the predicted velocity, Eq. (7.53) alongside several time slices of the simulation results. The predicted velocity almost exactly captures the qualitative behavior of the self-annihilating loop disclination: the twist portions move fastest and there is asymmetry between the $+1/2$ and $-1/2$ wedge portions of the loop. This is another example of the velocity equation yielding accurate, qualitative, analytic predictions for the velocity of the loop.

Throughout this and the previous sections we have demonstrated analytical understanding as well as full scale **Q**-tensor numerical calculation of the qualitative and

quantitative annihilation of disclinations for a variety of complex scenarios. For almost all of the cases, the kinematic velocity equation proved to give accurate predictions and important understanding for the behavior of the disclinations lines in three dimensions. In the next two sections we show that the kinematic law can also give understanding in situations where there is an external field or flow.

7.5 Defect sorting by applied external electric or magnetic fields

We describe in this section and the next how the methodology developed thus far can be used to study some of the effects on disclination motion brought about by coupling to external fields or hydrodynamic flows in a nematic liquid crystal. These are two common situations studied in experiments on nematics [22, 23, 127, 130], and are important in technical and biological applications as well as in the context of active nematics [4,24,95]. The primary goal of these sections is to demonstrate the ability of the kinematic velocity equation to predict interesting defect phenomena when coupled to external degrees of freedom. We will return to two spatial dimensions for the examples shown here.

We begin by introducing a simple free energy coupling associated with an external field $\mathbf{H}$. Here we use the symbol $\mathbf{H}$ to denote a generic field that could be either electric or magnetic. Depending on the chemical structure of the liquid crystal, molecules in a sample may tend to align with or be perpendicular to an applied electric or magnetic field. For simplicity we will assume the molecules tend to align with the applied field. Then the simplest interaction free energy density is [1]

$$f_H = -|\epsilon_H| H_\mu Q_{\mu\nu} H_\nu \tag{7.54}$$

where ϵ_H is the anisotropic part of the electromagnetic permittivity or permeability of the liquid crystal associated with the field $\mathbf{H}$. The energy is minimized when $(\hat{\mathbf{n}} \cdot \mathbf{H})^2 = |\mathbf{H}|^2$, i.e. when the director aligns or anti-aligns with the field.

The contribution to $\partial_t \mathbf{Q}$ arising from Eq. (7.54) is given by

$$\partial_t Q_{\mu\nu} = |\epsilon_H| H_\mu H_\nu. \tag{7.55}$$

Given the approximation of $\mathbf{Q}$ at the core, Eq. (5.25), and if we write $\mathbf{H} = H\hat{\mathbf{H}}$ where $\hat{\mathbf{H}} = (\cos\chi, \sin\chi, 0)$ and χ is the angle the field makes with the x-axis, it is straightforward to compute

$$\hat{\mathbf{\Omega}} \cdot \mathbf{g} = \frac{|\epsilon_H| S_N H^2}{2a} \left[-2\hat{\mathbf{x}} \left(\hat{\mathbf{H}} \cdot \hat{\mathbf{n}}_0 \right) \left(\hat{\mathbf{H}} \cdot \hat{\mathbf{n}}_1 \right) + \hat{\mathbf{y}} \left(\left(\hat{\mathbf{H}} \cdot \hat{\mathbf{n}}_0 \right)^2 - \left(\hat{\mathbf{H}} \cdot \hat{\mathbf{n}}_1 \right)^2 \right) \right]. \quad (7.56)$$

The velocity of a single disclination with $\phi_0 = 0$ is then given by

$$\mathbf{v}^H = -\frac{|\epsilon_H| H^2 a}{S_N} \left[\cos 2\chi \hat{\mathbf{x}} + 2m \sin 2\chi \hat{\mathbf{y}} \right] \quad (7.57)$$

where m is the disclination charge ($m = \pm 1/2$ in two dimensions). Eq. (7.57) predicts that if the field is aligned or anti-aligned with $\hat{\mathbf{x}}$ the disclination will move in the $-\hat{\mathbf{x}}$ direction. On the other hand, if the field is aligned or anti-aligned with $\hat{\mathbf{y}}$ the field will move in the $\hat{\mathbf{x}}$ direction. This behavior is predicted to be the same regardless of the charge of the defect. However, if $\hat{\mathbf{H}}$ is skewed from these two alignments there is a predicted component of the velocity along $\hat{\mathbf{y}}$ that is proportional to the charge and, hence, there will be different motion for $\pm 1/2$ disclinations.

We have tested this prediction computationally by simulating disclinations in two dimensions in a similar manner as laid out in Sec. 7.3, except we now add the free energy density in Eq. (7.54) and the corresponding functional derivative to the time evolution. For the simulations we set $\Delta t = 0.5$, $|\epsilon_H| = 1$, and $H = 0.5$ In Fig. 7.14 we show the results of the simulations in the form of the trajectories of $\pm 1/2$ disclinations with $\hat{\mathbf{n}}_0 = \hat{\mathbf{x}}$ and $\chi = 0, \pi/4, \pi/2$. We find that the velocity of Eq. (7.57) correctly predicts the direction of motion for the defects in these cases. In particular, when $\chi = \pi/4$ the motion of the $+1/2$ and $-1/2$ disclinations is opposite one another, and so one could say that the effect of this skewed field is to sort the defects by topological charge. This fact may lead to a number of applications in which different type disclinations may correspond to different active nematic or biological motifs, or correspond to locations in which particles (or cells) preferentially accumulate, and hence allow particle and cell sorting. We note that the velocity given by Eq. (7.57) could also have been predicted from the energy directly, since the effect of the field is to align the director. However, having the analytical tool is useful for more complex scenarios where energy methods may not be

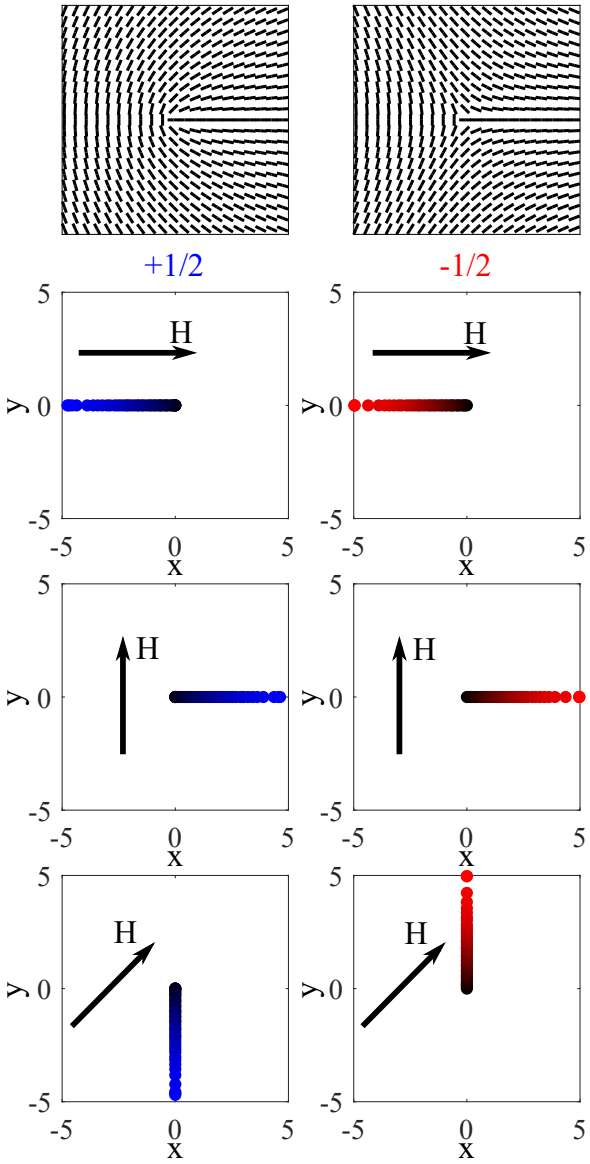

Figure 7.14: Effect of external field $\mathbf{H}$ on single $\pm 1/2$ disclinations. The plots show simulated (x, y) position in the form of dots, with brighter colors indicating later times, for various directions of the external field $\mathbf{H}$. All simulations use $|\mathbf{H}| = 0.5$ and $|\epsilon_H| = 1$. The trajectory of the defects matches that of the predicted velocity equation, Eq. (7.57).

analytically viable, such as in the case of twisted defects or in three dimensions.

7.6 Defect motion coupled to hydrodynamic flow

We now turn our attention to the case of coupling an imposed flow to nematic diffusive relaxation. We briefly discussed this in Sec. 6.3 where we derived the kinematic velocity equation and predicted the effect of advection of defects under a flow $\mathbf{u}$. Here we study specifically the case of an imposed shear flow with velocity

$$\mathbf{u}(x, y) = u_0 y \hat{\mathbf{x}} \tag{7.58}$$

where u_0 is the shear rate. This is a particularly simple flow to study theoretically since it automatically satisfies the Navier-Stokes equation (in the absence to back coupling to the nematic) and can be studied experimentally relatively simply [22]. Since this is the only flow we will consider in this dissertation, we will not concern ourselves with writing down the full Navier-Stokes system, and will instead focus on the time evolution equation for $\mathbf{Q}$ that follows from coupling the nematic to steady hydrodynamic degrees of freedom. We note that, as is standard in the realm of non-equilibrium dynamics, there are several models for the hydrodynamics of $\mathbf{Q}$ and no good agreement in the literature about which one should use [131–133]. Here we choose to analyze and employ numerically the Beris-Edwards model [134]:

$$\partial_t \mathbf{Q} = -\left(\mathbf{u}\cdot\nabla\right)\mathbf{Q} + \lambda\left[\mathbf{E}\mathbf{Q} + \mathbf{Q}\mathbf{E} + \frac{2}{3}\mathbf{E} - 2\left(\mathbf{Q} + \frac{1}{3}\mathbf{I}\right)\left(\mathbf{Q} : \nabla\mathbf{u}\right)\right] + \left[\mathbf{W}, \mathbf{Q}\right] - \frac{\delta F}{\delta \mathbf{Q}} \tag{7.59}$$

where $2\mathbf{E} = \nabla\mathbf{u} + \nabla\mathbf{u}^T$ is the strain rate tensor, $2\mathbf{W} = \nabla\mathbf{u} - \nabla\mathbf{u}^T$ is the vorticity tensor, λ is the "tumbling" parameter related to the tendency for the nematogens to align with the flow, and $[\mathbf{A}, \mathbf{B}] = \mathbf{A}\mathbf{B} - \mathbf{B}\mathbf{A}$ is the commutator of tensors $\mathbf{A}$ and $\mathbf{B}$. We choose this model because it is commonly employed in computational studies of active nematics in which disclinations play a primary role [24, 95, 135]. However, as we will show below, the qualitative predictions of the kinematic velocity are similar regardless of the hydrodynamic transport equation for $\mathbf{Q}$ chosen.

With the evolution of $\mathbf{Q}$ given by Eq. (7.59) we may compute the velocity of a disclination under shear flow. First, however, we note that in Eq. (7.59) we have already

discussed the effect of the first term (advection, see Sec. 6.3) and the last term (elastic relaxation, see previous sections in this chapter). Of the remaining terms, the only term that yields $\hat{\mathbf{\Omega}} \cdot \mathbf{g} \neq 0$ at the defect core is the term $(2/3)\lambda \mathbf{E}$. Therefore, the first prediction is that this is the only term arising from coupling to hydrodynamics that directly affects disclination motion. Of course, the flow may still indirectly affect the defect by perturbing the director configuration everywhere, $\tilde{\varphi}$ as we denoted earlier, which can then be analyzed by the methods of Sec. 7.2. However, in the frequent limit of small Ericksen number flows, the nematic configuration remains unaffected by the flow, and hence this is the only coupling to hydrodynamics that remains. We note that other models for the transport of $\mathbf{Q}$ have similar terms to lowest order in $\mathbf{Q}$ (e.g. compare the Beris-Edwards model above with the Qian-Sheng model of Ref. [131]) with the rest of the terms being higher order in $\mathbf{Q}$. Terms higher order in $\mathbf{Q}$ also yield $\hat{\mathbf{\Omega}} \cdot \mathbf{g} = 0$ and this is why *predictions* of the velocity from Eq. (6.13) do not qualitatively change for different models. Of course, numerical calculations using the full $\mathbf{Q}$-tensor do give different, model dependent results [132, 133].

To predict the velocity of disclinations under shear flow, we first obtain the rate of strain tensor as,

$$\mathbf{E} = \frac{u_0}{2} \left[\hat{\mathbf{x}} \otimes \hat{\mathbf{y}} + \hat{\mathbf{y}} \otimes \hat{\mathbf{x}} \right]. \tag{7.60}$$

Then, taking $\hat{\mathbf{n}}_0 = \hat{\mathbf{x}}$, the component of $\hat{\mathbf{\Omega}} \cdot \mathbf{g}$ resulting from the the shear flow is,

$$\hat{\mathbf{\Omega}} \cdot \mathbf{g} = -2m \frac{2\lambda u_0 S_N}{3a} \hat{\mathbf{x}}. \tag{7.61}$$

Note that the sign changes depending on the charge of the disclination. Combining this result with the velocity from advection (Eq. (6.19)) we find the predicted velocity of the defects under shear flow to be

$$\mathbf{v}(x, y) = 2u_0 y \hat{\mathbf{x}} - 2m \frac{4\lambda u_0 a}{3S_N} \hat{\mathbf{y}}. \tag{7.62}$$

The first term is simply advection of the defect by the flow field, while the second term stems from the tendency for the molecules to align with the flow. We note that, just as with the applied fields, the charge of the disclination determines the predicted motion. In particular, we find the same sorting behavior that was observed from the external

field in that positive charges move in the negative y direction while negative charges move in the positive direction.

Testing this numerically requires a bit more work than in the case of the applied field. We first derive the Beris-Edwards equations in a fully three-dimensional system for each degree of freedom of $\mathbf{Q}$ by comparing the time derivative of Eq. (2.23) with Eq. (7.59):

$$
\begin{aligned}
\dot{q_1} = -\lambda \Bigg[& \left(2q_1 + \frac{1}{\sqrt{3}}\right) g(\mathbf{q}, \nabla \mathbf{u}) - 2\partial_x u_x - \frac{\sqrt{3}}{2}(\partial_x u_y + \partial_y u_x) q_3 - \frac{\sqrt{3}}{2}(\partial_x u_z + \partial_z u_x) q_4 \\
& - \frac{1}{\sqrt{3}} \partial_x u_x \Bigg] - \frac{\sqrt{3}}{2} \left[(\partial_x u_y - \partial_y u_x) q_3 + (\partial_x u_z - \partial_z u_x) q_4 \right] - \frac{\sqrt{3}}{2} \frac{\delta F}{\delta q_1} \\
\dot{q_2} = -\lambda \Bigg[& 2q_2 g(\mathbf{q}, \nabla \mathbf{u}) - \frac{1}{2}(\partial_x u_y + \partial_y u_x) q_3 + \frac{1}{2}(\partial_x u_z + \partial_z u_x) q_4 - \partial_y u_y \left(-\frac{1}{\sqrt{3}} q_1 + q_2 \right) \\
& + \partial_z u_z \left(-\frac{1}{\sqrt{3}} q_1 - q_2 \right) - \frac{1}{3}(\partial_y u_y - \partial_z u_z) \Bigg] - \frac{1}{2} \left[(\partial_y u_x - \partial_x u_y) q_3 \right. \\
& \left. + (\partial_x u_z - \partial_z u_x) q_4 + 2(\partial_y u_z - \partial_z u_y) \right] - \frac{1}{2} \frac{\delta F}{\delta q_2} \\
\dot{q_3} = -\lambda \Bigg[& 2q_3 g(\mathbf{q}, \nabla \mathbf{u}) - (\partial_x u_x + \partial_y u_y) q_3 - \frac{1}{2}(\partial_y u_z + \partial_z u_y) q_4 - \frac{1}{2}(\partial_x u_z + \partial_z u_x) q_5 \\
& - \frac{1}{2}(\partial_x u_y + \partial_y u_x) \left(\frac{1}{\sqrt{3}} q_1 + q_2 \right) - \frac{1}{3}(\partial_x u_y + \partial_y u_x) \Bigg] \\
& - \frac{1}{2} \left[(\partial_x u_y - \partial_y u_x)(-\sqrt{3} q_1 + q_2) + (\partial_z u_y - \partial_y u_z) q_4 + (\partial_x u_z - \partial_z u_x) q_5 \right] - \frac{\delta F}{\delta q_3} \\
\dot{q_4} = -\lambda \Bigg[& 2q_4 g(\mathbf{q}, \nabla \mathbf{v}) - \frac{1}{2}(\partial_y u_z + \partial_z u_y) q_3 - (\partial_x u_x + \partial_z u_z) q_4 - \frac{1}{2}(\partial_x u_y + \partial_y u_x) q_5 \\
& - \frac{1}{2}(\partial_x u_z + \partial_z u_x) \left(\frac{1}{\sqrt{3}} q_1 - q_2 \right) - \frac{1}{3}(\partial_x u_z + \partial_z u_x) \Bigg] \\
& - \frac{1}{2} \left[(\partial_z u_x - \partial_x u_z)(\sqrt{3} q_1 + q_2) + (\partial_z u_y - \partial_y u_z) q_3 + (\partial_x u_y - \partial_y u_x) q_5 \right] - \frac{\delta F}{\delta q_4} \\
\dot{q_5} = -\lambda \Bigg[& 2q_5 g(\mathbf{q}, \nabla \mathbf{u}) - \frac{1}{2}(\partial_x u_z + \partial_z u_x) q_3 - \frac{1}{2}(\partial_x u_y + \partial_y u_x) q_4 - (\partial_y u_y + \partial_z u_z) q_5 \\
& + \frac{1}{\sqrt{3}}(\partial_y u_z + \partial_z u_y) q_1 - \frac{1}{3}(\partial_y u_z + \partial_z u_y) \Bigg] - \frac{1}{2} \left[2(\partial_z u_y - \partial_y u_z) q_2 \right. \\
& \left. + (\partial_z u_x - \partial_x u_z) q_3 + (\partial_y u_x - \partial_x u_y) q_4 \right] - \frac{\delta F}{\delta q_5}
\end{aligned}
\tag{7.63}
$$

where $\dot{q}_i = \partial_t q_i + (\mathbf{u}\cdot\nabla)q_i$ is the material time derivative and

$$g(\mathbf{q},\nabla\mathbf{u}) = \frac{1}{\sqrt{3}}(2\partial_x u_x - \partial_y u_y - \partial_z u_z)q_1 + (\partial_y u_y - \partial_z u_z)q_2 + (\partial_x u_y + \partial_y u_x)q_3 + (\partial_x u_z + \partial_z u_x)q_4 + (\partial_y u_z + \partial_z u_y)q_5. \quad (7.64)$$

We then use similar methods as described in Chapter 2 to discretize Eqs. (7.63) in time and space and solve the resulting system of equations using the finite element method for an imposed, static flow field $\mathbf{u}$.

In order to test the predictions of Eq. (7.62) we simulate the evolution of $\pm 1/2$ disclinations, which are initially located at $(x, y) = (0, 0)$, under the shear flow, Eq. (7.58). We use a three dimensional domain with standard tetrahedral finite elements such that there are $41 \times 41 \times 41$ vertices. We set $\Delta t = 0.1$, $\lambda = 1$, and $u_0 = 2$. While we use a three dimensional domain, there is no variation of either $\mathbf{Q}$ or $\mathbf{u}$ in the $\hat{\mathbf{z}}$ direction, and so it is essentially a two dimensional problem. Fig. 7.15a shows the results in the form of time slices of S and the director, while in Fig. 7.15b we show the trajectories of the defects over time in the form of (x, y) positions. The prediction of Eq. (7.62) is verified by the calculations: the direction of defect motion depends on its topological charge and is transverse to shear direction. We find that the $+1/2$ disclination has a component of its velocity in the $-\hat{\mathbf{y}}$ direction while the $-1/2$ disclination has a component of its velocity in the $+\hat{\mathbf{y}}$ direction. As with the applied field, the imposed shear flow enables sorting of defects based on their topological charge.

There is additional asymmetry in the figures that is caused by a second order effect in the shear flow. Because the flow is proportional to $\mathbf{Q}$, and hence S, there is a gradient in the director at the core of the defect because S is changing there. This yields a nonzero $\nabla\tilde{\varphi}$ which, as we have shown in Secs. 7.2, 7.3, and 7.4, results in defect motion. For this particular set of results, this causes a bias in the $+\hat{\mathbf{x}}$ direction, and it adds to the advection of the $-1/2$ disclination and opposes the advection of the $+1/2$ disclination leading to the asymmetry. This effect is visible primarily because the defects we consider have large core sizes relative to the shear gradient. Decreasing the core size or increasing the shear gradient reduces this effect, and hence the asymmetry might not be visible in experiments in which the shear is constant on the length scale of the core size, a [22,23].

In summary, in the last two sections we have presented some analytical predictions

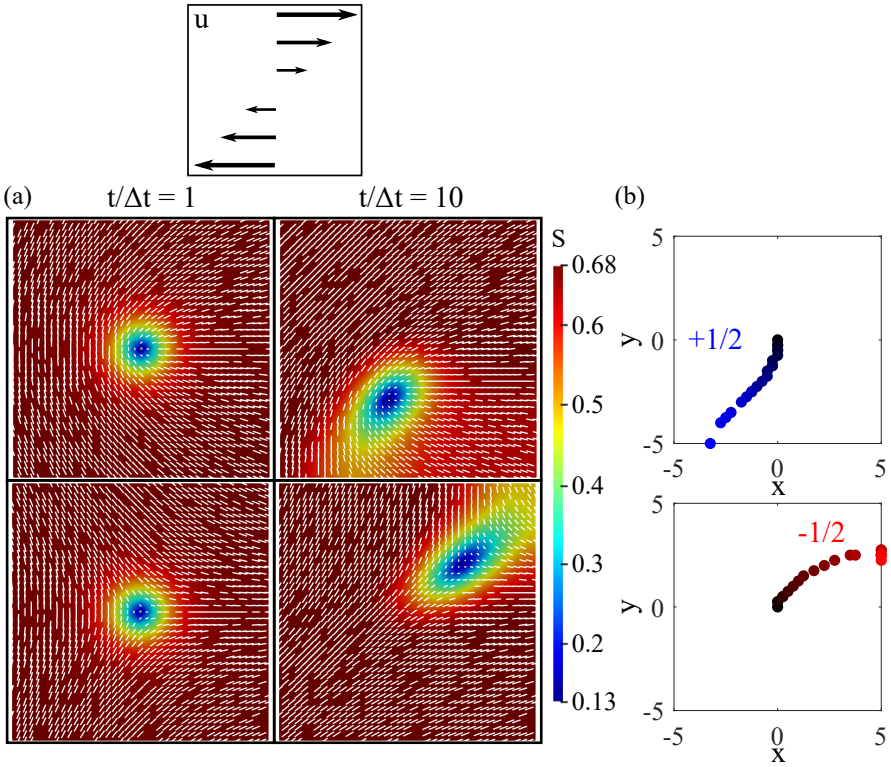

Figure 7.15: Effect of shear flow, $\mathbf{u}$ on $\pm 1/2$ disclinations. (a) Snapshots at iteration numbers $t/\Delta t = 1$, 10 for a $+1/2$ disclination and a $-1/2$ disclination. The colormap indicates the degree of ordering S while the white lines depict the director orientation. (b) Disclination (x, y) positions over time. Brighter dots indicate later times. There is a component of the velocity in the $\pm\hat{\mathbf{y}}$ direction depending on the sign of the disclination charge, as predicted by Eq. (7.62).

and numerical verification of the behavior of defects under external forces. In both the cases of an external, applied field and an imposed shear flow, the kinematic velocity of a disclination as derived in Chapter 6 agrees with the motion given by full **Q**-tensor numerical solution. Both effects have implications for control of defect motion in biological systems and in technological applications, as well in the understanding of disclination motion in active systems where flows are spontaneously generated by active forces.

7.7 Conclusion

In this chapter we have put to use the kinematic law giving the velocity of a disclination in Chapter 6 to predict and analyze their motion in various configurations. We have seen that the velocity equation may be used to give approximate analytical expressions for the velocity of disclinations that are consistent with the more complex numerical solutions in the **Q**-tensor representation. In this chapter, we have used results throughout this dissertation, from the computational theory of Chapter 2 to the analysis of anisotropic disclinations in Chapter 4, to the topological analysis of line disclinations in Chapter 5 to understand disclination motion. We have examined two dimensional disclination annihilation for the cases of optimal orientation and twisted disclinations. We have also seen how anisotropic elasticity can fundamentally change the behavior of these systems. Further, we have studied the annihilation or recombination of disclination lines and loops in three dimensional nematics, of which, there is little theoretical study in the literature. And finally we have studied some effects of coupling to external degrees of freedom and showed the efficacy of the predictions made by the kinematic velocity equation in these scenarios.

We mention that this work has implications for the study of large scale defect coarsening in both two dimensional and three dimensional nematics. Additionally, the behavior of active nematics is highly influenced by the behavior of disclinations, and hence an understanding of their motion is essential for an understanding of their long-time behavior. The research presented in this chapter will be the beginning of a much larger effort to describe disclination motion in both passive and active systems. Possible future extensions include adding active forces to the hydrodynamic model, and examining collective effects in systems comprising many disclinations, including active turbulence.

Some of this has already been undertaken in two dimensions [104], and hopefully the methods presented here will be of use to future studies in three dimensions.

Chapter 8

Conclusion

In this dissertation we have introduced new theoretical techniques as well as developed numerical methods to describe the nature and motion of both topological defects and two phase interfaces in nematic liquid crystals. A fundamental theme that emerges in the study of two phase tactoids and disclinations is the intrincate interplay between elasticity, anisotropy, geometry, and topology.

We have first developed a self-consistent field theory that remedies the known unboundedness of the classical Landau-de Gennes theory for elastically anisotropic nematic phases. We have demonstrated that the resulting numerical implementation can describe fully three dimensional configurations, and it is robust in the study of tactoid and disclination configurations with large anisotropic elasticity. We have shown that different terms in the anisotropic elastic energy can yield different structural and dynamic results in the form of anisotropic anchoring at interfaces, or anisotropic, biaxial order near the core of disclinations. This represents new advances for both experiments, looking to understand anisotropic morphologies in a wide variety of materials, and for liquid crystal theory in which many studies have neglected anisotropic elasticity to avoid the unboundedness of methods based on the Landau-de Gennes free energy. Our results quantitatively agree with experimental results, both for disclination configurations and two phase tactoids, in lyotropic chromonic liquid crystals.

We have also made theoretical advances in developing tools to identify disclinations when configurations are described in terms of the tensor order parameter $\mathbf{Q}$. We introduce a disclination density tensor that allows for a local classification of disclination

lines and loops in terms of both topology and geometry. This is important for both experiments and computational studies in which the tensor order parameter $\mathbf{Q}$ is available such as in studies of three dimensional defect coarsening in both active and passive systems. The interplay between elasticity and defect geometry will be more easily probed by the ability to identify the disclination line properties as given by this tensor.

Further, exact kinematic laws of disclination motion have been derived by way of conservation laws of topological charge. Disclination annihilation, as well as motion related to applied fields and flows, is shown to be heavily influenced by the geometry and topology of the disclination lines, as well as by anisotropic elasticity. The kinematic velocity law allows for an analytic understanding of these influences as well as analytic predictions of disclination motion based on simple approximations of its geometry.

8.1 Future Directions

We finish this chapter with some possible future directions for this research. First, as discussed in Secs. 2.3 and 2.8, different Hamiltonians may be used in the bulk free energy. An obvious extension of this work is to understand the differences in configurations yielded by different microscopic Hamiltonians such as the one introduced by Onsager. It has already been shown that the Onsager Hamiltonian may yield more exotic minimum energy configurations that include biaxiality [136]. Further, understanding the connection between the self-consistent field theory presented in Chapter 2 and the self-consistent field theories used in polymer physics [137] may yield a better understanding of the microscopic origins of various elastic terms, rather than the purely phenomenological approach used here.

As we showed in Chapter 4, the model of Chapter 2 works well to both quantitatively and qualitatively describe the anisotropoic structure of experimental systems, even when the elastic constants are constrained to their experimental values. We also showed that the disclination polarization, of which the active force in an active nematic is proportional to, changes qualitatively around defects with anisotropic elasticity. A possible extension of this work would be to use the self-consistent field theory to simulate defects in active nematics with anisotropic elasticity. It has already been shown experimentally

that defects in active nematic can exhibit signatures of elastic anisotropy [43]; moreover, in experiments of living liquid crystals the same chromonic liquid crystal studied in Chapter 4 are used, and hence elastic anisotropy is present in these experiments, although current theory does not take it into account [93]. Additionally, we were unable to quantitatively compare our results on surface defects on tactoids to experimental results. Comparing with experiments that cover a wide range of elastic constants would be a useful extension of the results of Chapter 3 (for example, in chromonics the elastic constants are dependent on concentration [5]). Domain coalescence, in both two and three dimensions, is also an interesting future avenue for research since this is the primary mechanism for disclination formation in nematics. Understanding the effects of domain morphology, anisotropy, and elasticity on this process is particularly valuable to those engineering materials synthesized from nematics.

Finally, we have discussed in Chapters 5, 6, and 7 how the disclination density tensor $\mathbf{D}$ and the kinematic velocity equation of Eq. (6.13) can be used as tools in future experimental, computational, and theoretical studies. Beyond this, an obvious extension of the methods of Chapter 5 is to use the disclination density tensor as a measure for liquid crystal Skyrmions, as these defects contain either double-twist and double-splay configurations. It is not yet clear if the methods of 6 may be used in a similar way to understand Skyrmion motion. Additionally, a major feature of disclination motion that was not considered in this dissertation is the time evolution of the rotation vector $\hat{\mathbf{\Omega}}$. A follow-up to this is important for a full understanding of the dynamics of both line and loop disclinations, particularly for active systems which show asymmetries in the numbers of wedge and twist disclinations [24]. Moreover, a follow-up study about the velocity equation predictions for an active nematic would be helpful in understanding the usefulness of this formalism for active nematics in general.

References

[1] P. G. de Gennes. *The Physics of Liquid Crystals.* Oxford University Press, 1975.

[2] B. I. Halperin and David R. Nelson. Theory of two-dimensional melting. *Phys. Rev. Lett.*, 41:121–124, 1978.

[3] Grace H. Zhang and David R. Nelson. Fractional defect charges in p-atic liquid crystals on cones. e-print arXiv:2201.11201v1 [cond-mat.soft], 2022.

[4] Pochi Yeh and Claire Gu. *Optics of Liquid Crystal Displays.* Wiley, 2009.

[5] Shuang Zhou, Krishna Neupane, Yuriy A. Nastishin, Alan R. Baldwin, Sergij V. Shiyanovskii, Oleg D. Lavrentovich, and Samuel Sprunt. Elasticity, viscocity, and orientational fluctuations of a lyotropic chromonic nematic liquid crystal disodium cromoglycate. *Soft Matter*, 10:6571, 2014.

[6] Chenhui Peng, Taras Turiv, Yubing Guo, Qi-Huo Wei, and Oleg D. Lavrentovich. Sorting and separation of microparticles by surface properties using liquid crystal-enabled electro-osmosis. *Liq. Cryst.*, 45:1936, 2018.

[7] P. M. Chaikin and T. C. Lubensky. *Principles of Condensed Matter Physics.* Cambridge University Press, 1995.

[8] J. Friedel and P. De Gennes. Boucles de disclination dans les cristaux liquides. *CR Acad. Sc. Paris B*, 268:257–259, 1969.

[9] L. M. Pismen. *Vortices in Nonlinear Fields.* Oxford University Press, 1999.

[10] Y. K. Kim, Sergij V. Shiyanovskii, and Oleg D. Lavrentovich. Morphogenesis of defects and tactoids during isotropic-nematic phase transition in self-assembled lyotropic chromonic liquid crystals. *J. Phys.: Condens. Matter*, 25:404202, 2013.

[11] Vida Jamali, Natnael Behabtu, Bohdan Senyuk, J. Alex Lee, Ivan I. Smalyukh, Paul van der Schoot, and Matteo Pasquali. Experimental realization of crossover in shape and director field of nematic tactoids. *Phys Rev. E*, 91:042507, 2015.

[12] H. Zocher. Über freiwillige strukturbildung in solen. (eine neue art anisotrop flüssiger medien.). *Zeitschrift für anorganische und allgemeine Chemie*, 147:91–110, 1925.

[13] Liquid crystaline substances from virus-infected plants. *Nature*, 138:1051–1052, 1936.

[14] A. V. Kaznacheev, M. M. Bogdanov, and S. A. Taraskin. The nature of prolate shape of tactoids in lyotropic inorganic liquid crystals. *J.E.T.P.*, 95:57–63, 2002.

[15] Shuang Zhou, Sergij V. Shiyanovskii, Heung-Shik Park, and Oleg D. Lavrentovich. Fine structure of the topological defect cores studied for disclinations in lyotropic chromonic liquid crystals. *Nat. Commun.*, 8:14974, 2017.

[16] P.J. Collings, A.J. Dickinson, and E.C. Smith. Molecular aggregation and chromonic liquid crystals. *Liquid Crystals*, 37:701–710, 2010.

[17] Peter J. Collings, Joshua N. Goldstein, Elizabeth J. Hamilton, Benjamin R. Mercado, Kenneth J. Nieser, and Margaret H. Regan. The nature of the assembly process in chromonic liquid crystals. *Liquid Crystal Reviews*, 3:1–27, 2015.

[18] Shuang Zhou, Yu. A. Nastishin, M. M. Omelchenko, L. Tortora, V. G. Nazarenko, O. P. Boiko, T. Ostapenko, T. Hu, C. C. Almasan, S. N. Sprunt, J. T. Gleeson, and O. D. Lavrentovich. Elasticity of lyotropic chromonic liquid crystals probed by director reorientation in a magnetic field. *Phys. Rev. Lett.*, 109:037801, 2012.

[19] Taewoo Lee, Rahul P. Trivedi, and Ivan I. Smalyukh. Multimodal nonlinear optical polarizing microscopy of long-range molecular order in liquid crystals. *Opt. Lett.*, 35(20):3447–3449.

[20] T. Ohzono, K. Katoh, and Ji Fukuda. Fluorescence microscopy reveals molecular localisation at line defects in nematic liquid crystals. *Sci. Rep.*, 6:36477, 2016.

[21] Yohei Zushi and Kazumasa A. Takeuchi. Scaling and spontaneous symmetry restoring in reconnecting nematic disclinations. e-print arXiv:2110.00442 [cond-mat.soft], 2021.

[22] Hend Baza, Taras Turiv, Bing-Xiang Li, Ruipeng Li, Benjamin M. Yavitt, Masafumi Fukuto, and Oleg D. Lavrentovich. Shear-induced polydomain structures of nematic lyotropic chromonic liquid crystal disodium cromoglycate. *Soft Matter*, 16:8565, 2020.

[23] Qing Zhang, Rui Zhang, Baoliang Ge, Zahid Yaqoob, Peter T. C. So, and Irmgard Bischofberger. Structures and topological defects in pressure-driven lyotropic chromonic liquid crystals. *Proceedings of the National Academy of Sciences*, 118:e2108361118, 2021.

[24] Guillaume Duclos, Raymond Adkins, Debarghya Banerjee, Matthew S. E. Peterson, Minu Varghese, Itamar Kolvin, Arvind Baskaran, Robert A. Pelcovits, Thomas R. Powers, Aparna Baskaran, Federico Toschi, Michael F. Hagan, Sebastian J. Streichan, Vincenzo Vitelli, Daniel A. Beller, and Zvonimir Dogic. Topological structure and dynamics of three-dimensional active nematics. *Science*, 367(6482):112–1124, 2020.

[25] F.C. Frank. On the theory of liquid crystals. *Discuss. Faraday Soc.*, 25:19, 1958.

[26] F. M. Leslie. Some constitutive equations for anisotropic fluids. *J. Mech. Appl. Math.*, 19:357, 1966.

[27] J. L. Ericksen. Liquid crystals with variable degree of orientation. *Arch. for Rational Mech. Anal.*, 113:97, 1991.

[28] Chiqun Zhang, Amit Acharya, Noel J. Walkington, and Oleg D. Lavrentovich. Computational modelling of tactoid dynamics in chromonic liquid crystals. *Liq. Cryst.*, 45:1084, 2018.

[29] N. Schopohl and T.J. Sluckin. Defect core structure in nematic liquid crystals. *Phys. Rev. Lett.*, 59:22, 1987.

[30] V. Popa-Nita, T. Sluckin, and A. Wheeler. Statics and kinematics at the nematic-isotropic interface: effects of biaxiality. *J. Phys. II (France)*, 7:1225, 1997.

[31] Egbert F. Gramsbergen, Lech Longa, and Wim H. de Jeu. Landau theory of the nematic-isotropic phase transition. *Physics Reports*, 135(4):195 – 257, 1986.

[32] W. Maier and A. Saupe. A simple molecular statistical theory of the nematic liquid-crystalline phase. *I. Z. Naturf.*, 14:882, 1959.

[33] Lars Onsager. The effects of shape on the interaction of colloidal particles. *Annals of the New York Academy of Sciences*, 51(4):627–659, 1949.

[34] J. Katriel, G. F. Kventsel, G. R. Luckhurst, and T.J. Sluckin. Free energies in the Landau and molecular field approaches. *Liq. Cryst.*, 1:337, 1986.

[35] L. Longa, D. Monselesan, and H. R. Trebin. An extension of the Landau-Ginzberg-de Gennes theory for liquid crystals. *Liq. Cryst.*, 2:769, 1987.

[36] J. M. Ball and A. Majumdar. Nematic liquid crystals: from Maier-Saupe to a continuum theory. *Mol. liq. Cryst.*, 525:1, 2010.

[37] Xingzhou Tang and Jonathan V. Selinger. Orientation of topological defects in 2d nematic liquid crystals. *Soft Matter*, 13:5481, 2017.

[38] Cheng Long, Xingzhou Tang, Robin L.B. Selinger, and Jonathan V. Selinger. Geometry and mechanics of disclination lines in 3d nematic liquid crystals. *Soft Matter*, 17:2265, 2021.

[39] B. I. Halperin. In Roger Balian, editor, *Physics of Defects*. North-Holland Pub. Co., 1981.

[40] Gene F. Mazenko and Robert A. Wickham. Ordering kinetics of defect structures. *Phys. Rev. E*, 57:2539, 1997.

[41] Gene F. Mazenko. Velocity distribution for strings in phase-ordering kinetics. *Phys. Rev. E*, 59:1574, 1999.

[42] Nigel J. Mottram and Christopher J.P. Newton. Introduction to Q-tensor theory. e-print arXiv:1409.3542v2 [cond-mat.soft], 2014.

[43] Rui Zhang, Nitin Kumar, Jennifer L. Ross, Margaret L. Gardel, and Juan J. de Pablo. Interplay of structure, elasticity, and dynamics in actin-based nematic materials. *Proceedings of the National Academy of Sciences*, 115(2):E124–E133, 2018.

[44] A. K. Sen and D. E. Sullivan. Landau-de Gennes theory of wetting and orientational transitions at a nematic-liquid–substrate interface. *Phys. Rev. A*, 35:1391, 1987.

[45] Jonathan V. Selinger. Interpretation of saddle-splay and the Oseen-Frank free energy in liquid crystals. *Liquid Crystals Reviews*, 6(2):129–142, 2018.

[46] T. C. Lubensky. Molecular description of nematic liquid crystals. *Phys. Rev. A*, 2:2497, 1970.

[47] Cody D. Schimming, Jorge Viñals, and Shawn W. Walker. Numerical method for the equilibrium configurations of a maier-saupe bulk potential in a q-tensor model of an anisotropic nematic liquid crystal. *J. Comp. Phys.*, 441:110441, 2021.

[48] Patricia Bauman and Daniel Phillips. Regularity and the behavior of eigenvalues for minimizers of a constrained Q-tensor energy for liquid crystals. *Calc. Var.*, 55:81, 1986.

[49] Jonathan V. Selinger. *Introduction to the Theory of Soft Matter*. Springer International Publishing, Switzerland, 2016.

[50] Apala Majumdar. Equilibrium order parameters of nematic liquid crystals in the landau-de gennes theory. *Eur. J. Appl. Math.*, 21:181–203, 2010.

[51] S. M. Wise, C. Wang, and J. S. Lowengrub. An energy-stable and convergent finite-difference scheme for the phase field crystal equation. *SIAM J. Numer. Anal.*, 47:2269–2288, 2009.

[52] Jia Zhao and Qi Wang. Semi-discrete energy-stable schemes for a tensor-based hydrodynamic model of nematic liquid crystal flows. *J. Sci. Comput.*, 68:1241–1266, 2016.

[53] Jinchao Xu, Yukun Li, Shuonan Wu, and Arthur Bousquet. On the stability and accuracy of partially and fully implicit schemes for phase field modeling. *Comput. Methods Appl. Mech. Eng.*, 345:826–853, 2019.

[54] Cody D. Schimming. Singularpotentialnematic. `https://github.com/schim111/SingularPotentialNematic`, 2022.

[55] William H. Press, Saul A. Teukolsky, William T. Vetterling, and Brian P. Flannery. *Numerical Recipes in C++ The Art of Scientific Computing*. Cambridge University Press, 2nd edition, 2002.

[56] Shawn W. Walker. Felicity: A matlab/c++ toolbox for developing finite element methods and simulation modeling. *SIAM J. Sci. Comput.*, 40:C234–C257, 2018.

[57] Yvan Notay. An aggregation-based algebraic multigrid method. *Electron. Trans. Numer. Anal.*, 37:123–146, 2010.

[58] Artem Napov and Yvan Notay. Algebraic analysis of aggregation-based multigrid. *Numer. Linear Algebra Appl.*, 18:539–564, 2011.

[59] Artem Napov and Yvan Notay. An algebraic multigrid method with guaranteed convergence rate. *SIAM J. Sci. Comput.*, 34:A1079–A1109, 2012.

[60] Yvan Notay. Aggregation-based algebraic multigrid for convection-diffusion equations. *SIAM J. Sci. Comput.*, 34:A2288–A2316, 2012.

[61] V.I. Lebedev and D. N. Laikov. A quadrature formula for the sphere of the 131st algebraic order of accuracy. *Dokl. Math.*, 59:477–481, 1999.

[62] Yuedong Gu and Nicholas L. Abbott. Observation of saturn-ring defects around solid microspheres in nematic liquid crystals. *Phys. Rev. Lett.*, 85:4719, 2000.

[63] Stan Alama, Lia Bronsard, and Xavier Lamy. Analytical description of the saturn-ring defect in nematic colloids. *Phys. Rev. E*, 93:012705, 2016.

[64] J. D. Bernal and I. Fankuchen. X-ray and crystallographic studies of plant virus preparations : I. introduction and preparation of specimens ii. modes of aggregation of the virus particles. *J. Gen. Physio.*, 25:111–126, 1941.

[65] A. S. Sonin. Inorganic lyotropic liquid crystals. *J. Mater. Chem.*, 8:2557–2574, 1998.

[66] Peter Prinsen and Paul van der Schoot. Shape and director-field transformation of tactoids. *Phys Rev. E*, 68:021701, 2003.

[67] P. Prinsen and P. van der Schoot. Continuous director-field transformation of nematic tactoids. *Eur. Phys. J. E*, 13:35–41, 2004.

[68] P. Prinsen and P. van der Schoot. Parity breaking in nematic tactoids. *J. Phys.: Condens. Matter*, 16:8835, 2004.

[69] Benjamin Wincure and Alejandro D. Rey. Interfacial nematodynamics of heterogeneous curved isotropic-nematic moving fronts. *J. Chem. Phys.*, 124:244906, 2006.

[70] R. M. W. van Bijnen, R. H. J. Otten, and P. van der Schoot. Texture and shape of two-dimensional domains of nematic liquid crystals. *Phys. Rev. E*, 86:051703, 2012.

[71] J. C. Everts, M. T. J. J. M. Punter, S. Samin, P. van der Schoot, and R. van Roij. A landau-de gennes theory for hard colloidal rods: Defects and tactoids. *J. Chem. Phys.*, 144:194901, 2016.

[72] Silvia Paparini and Epifanio G. Virga. Nematic tactoid population. *Phys. Rev. E*, 103:022707, 2021.

[73] Israel Lazo, Chenhui Peng, Jie Xiang, Sergij V. Shiyanovskii, and Oleg D. Lavrentovich. Liquid crystal-enabled electroosmosis through spatial charge separation in distorted regions as a novel mechanism of electrokinetics. *Nat. Commun.*, 5:5033, 2014.

[74] Chenhui Peng, Yubing Guo, Christopher Conklin, Jorge Viñals, Sergij Shiyanovskii, Qi-Huo Wei, and Oleg D. Lavrentovich. Liquid crystals with patterned molecular orientation as an electrolytic active medium. *Phys. Rev. E*, 92:052502, 2015.

[75] Alison E. Patteson, Arvind Gopinath, and Paulo E. Arratia. The propagation of active-passive interfaces in bacterial swarms. *Nat. Commun.*, 9:5373, 2018.

[76] Greta Babakhanova, Taras Turiv, Yubing Guo, Matthew Hendrikx, Qi-Huo Wei, Albert P.H.J. Schenning, Dirk J. Broer, and Oleg D. Lavrentovich. Liquid crystal elastomer coatings with programmed response of surface profile. *Nat. Commun.*, 9:456, 2018.

[77] Babak Vajdi Hokmabad, Kyle A. Baldwin, Carsten Krüger, Christian Bahr, and Corinna C. Maass. Topological stabilization and dynamics of self-propelling nematic shells. *Phys. Rev. Lett.*, 123:178003, 2019.

[78] Rodrigo C. V. Coelho, Nuno A. M. Araújo, and Margarida M. Telo da Gama. Propagation of active nematic-isotropic interfaces on substrates. *Soft Matter*, 16:4256, 2020.

[79] Bomi Lee, Jun-Seo Lee, Hyun-Jin Yoon, Seung-Ho Hong, and Song Jang-Kun. Generation and manipulation of isotropic droplets in nematic medium using switchable dielectrophoresis. *Phys. Rev. E*, 101:012704, 2020.

[80] Nicholas B. Ludwig, Kimberly Weirich, Eli Alster, Thomas A. Witten, Margaret L. Gardel, Kinjal Dasbiswas, and Suriyanarayanan Vaikuntanathan. Nucleation and shape dynamics of model nematic tactoids around adhesive colloids. *J. Chem. Phys.*, 152:084901, 2020.

[81] Andrew DeBenedictis and Timothy J. Atherton. Shape minimisation problems in liquid crystals. *Liquid Crystals*, 43(13-15):2352–2362, 2016, https://doi.org/10.1080/02678292.2016.1209699.

[82] Helmut R. Brand and Harald Pleiner. Nonlinear effects in the electrohydrodynamics of uniaxial nematic liquid crystals. *Phys. Rev. A.*, 35(7):3122, 1987.

[83] Hartmut L owen. A phase-field-crystal model for liquid crystals. *J. Phys. Consdens. Matter*, 22:364105, 2010.

[84] Nan Wang, Moneesh Upmanyu, and Alain Karma. Phase-field model of vapor-liquid-solid nanowire growth. *Phys. Rev. Materials*, 2:033402, 2018.

[85] Dmitry Golovaty, Young-Ki Kim, Oleg D. Lavrentovich, Michael Novack, and Peter Sternberg. Phase transitions in nematics: Textures with tacoids and disclinations. *Math. Model. Nat. Phenom.*, 15:8, 2020.

[86] Yubing Guo, Miao Jiang, Sajedeh Afghah, Chenhui Peng, Robin L. B. Selinger, Oleg D. Lavrentovich, and Qi-Huo Wei. Photopatterned designer disclination networks in nematic liquid crystals. *Adv. Optical Mater.*, 9:2100181, 2021.

[87] S. Meiboom, M. Sammon, and W. F. Brinkman. Lattice of disclinations: The structure of the blue phases of choloesteric liquid crystals. *Phys. Rev. A*, 27:438, 1982.

[88] Steven D. Hudson and Edwin L. Thomas. Frank elastic-constant anisotropy measured from transmission-electron-microscope images of disclinations. *Phys. Rev. Lett.*, 62:1993, 1989.

[89] Homin Shin, Mark J. Bowick, and Xiangjun Xing. Topological defects in spherical nematics. *Phys. Rev. Lett.*, 101:037802, 2008.

[90] M.C. Marchetti, J.F. Joanny, S. Ramaswamy, T.B. Liverpool, J. Prost, Madan Rao, and R. Aditi Simha. Hydrodynamics of soft active matter. *Rev. Mod. Phys.*, 85:1143, 2013.

[91] Cyrus Mostajeran. Curvature generation in nematic surfaces. *Phys. Rev. E*, 91:062405, 2015.

[92] Francisco Lòpez Jimènez, Norbert Stoop, Romain Lagrange, Jörn Dunkel, and Pedro M. Reis. Curvature-controlled defect localization in elastic surface crystals. *Phys. Rev. Lett.*, 116:104301, 2016.

[93] Mikhail M. Genkin, Andrey Sokolov, Oleg D. Lavrentovich, and Igor S. Aranson. Topological defects in a living nematic ensnare swimming bacteria. *Phys. Rev. X*, 7:011029, 2017.

[94] Thuan Beng Saw, Amin Doostmohammadi, Vincent Nier, Leyla Kocgozlu, Sumesh Thampi, Yusuke Toyama, Philippe Marcq, Chwee Teck Lim, Julia M. Yeomans, and Benoit Ladoux. Topological defects in epithelia govern cell death and extrusion. *Nature*, 544:212–216, 2017.

[95] Suraj Shankar, Sriram Ramaswamy, M. Cristina Marchetti, and Mark J. Bowick. Defect unbinding in active nematics. *Phys. Rev. Lett.*, 121:108002, 2018.

[96] Jack Binysh, Žiga Kos, Simon Čopar, Miha Ravnik, and Gareth P. Alexander. Three-dimensional active defect loops. *Phys. Rev. Lett.*, 124:088001, 2020.

[97] Taras Turiv, Jess Krieger, Greta Babakhanova, Hao Yu, Sergij V. Shiyanovskii, Qi-Huo Wei, Min-Ho Kim, and Oleg D. Lavrentovich. Topology control of human fibroblast cells monolayer by liquid crystal elastomer. *Science Advances*, 6(20), 2020.

[98] Katherine Copenhagen, Ricard Alert, Ned S. Wingreen, and Joshua W. Shaevitz. Topological defects promote layer formation in *Myxococcus xanthus* colonies. *Nat. Phys.*, 17:211–215, 2021.

[99] I. E. Dzyaloshinsky. Theory of disinclinations in liquid crystals. *Sov. Phys. JETP*, 31:773–780, 1970.

[100] Amin Doostmohammadi, Jordi Ignés-Mullol, Julia M. Yeomans, and Francesc Sagués. Active nematics. *Nat. Commun.*, 9:3246, 2018.

[101] Sriram Ramaswamy. The mechanics and statistics of active matter. *Annu. Rev. Condens. Matter Phys.*, 1:323, 2010.

[102] I. F. Lyuksyutov. Topological instability of singularities at small distances in nematics. *Sov. Phys. JETP*, 48:178, 1978.

[103] Suraj Shankar and M. Cristina Marchetti. Hydrodynamics of active defects: From order to chaos to defect ordering. *Phys. Rev. X*, 9:041047, 2019.

[104] Luiza Angheluta, Zhitao Chen, M. Cristina Marchetti, and Mark J. Bowick. The role of fluid flow in the dynamics of active nematic defects. *New J. Phys.*, 23:033009, 2021.

[105] Gareth P. Alexander, Bryan Gin-ge Chen, Elisabetta Matsumoto, and Randall D. Kamien. Colloquium: Disclination loops, point defects, and all that in nematic liquid crystals. *Rev. Mod. Phys.*, 84:497, 2012.

[106] F. Greco and G. Marrucci. Molecular structure of the hedgehog point defect in nematics. *Mol. Cryst. Liq. Cryst.*, 210:129–141, 1991.

[107] Sidney Coleman. *Aspects of Symmetry: Selected Erice Lectures*. Cambridge University Press, 1985.

[108] Arthur J. Vromans and Luca Giomi. Orientational properties of nematic disclinations. *Soft Matter*, 12:6490, 2016.

[109] D. J. G. Pearce and K. Kruse. Properties of twisted topological defects in 2d nematic liquid crystals. *Soft Matter*, 17:7408, 2021.

[110] Matthew L. Blow, Sumesh P. Thampi, and Julia M. Yeomans. Biphasic, lyotropic, active nematics. *Phys. Rev. Lett.*, 113:248303, 2014.

[111] D. Dell'Arciprete, M.L. Blow, A.T. Brown, F.D.C. Farrell, J. S. Lintuvuori, A. F. McVey, D. Marenduzzo, and W.C.K. Poon. A growing bacterial colony in two dimensions as an active nematic. *Nat. Commun.*, 9:4190, 2018.

[112] Mark J. Bowick, L. Chandar, E. A. Schiff, and Ajit M. Srivastava. The cosmological kibble mechanism in the laboratory: String formation in liquid crystals. *Science*, 263(5149):943–945, 1994.

[113] T. W. B. Kibble. Phase transitions and topological defects in the early universe. *Aust. J. Phys.*, 50:697, 1997.

[114] David C. Wright and N. David Mermin. Crystalline liquids: the blue phases. *Rev. Mod. Phys.*, 61:385–432, 1989.

[115] Jonathan V. Selinger. Director deformations, geometric frustration, and modulated phases in liquid crystals. *Annual Review of Condensed Matter Physics*, 13(1):49–71, 2022.

[116] Cheng Long and Jonathan V. Selinger. Coarse-grained theory for motion of solitons and skyrmions in liquid crystals. *Soft Matter*, 17:10437–10446, 2021.

[117] A Duzgun, C Nisoli, C J O Reichhardt, and C Reichhardt. Directed motion of liquid crystal skyrmions with oscillating fields. *New Journal of Physics*, 24(3):033033, 2022.

[118] Albert Fert, Nicolas Reyren, and Vincent Cros. Magnetic skyrmions: advances in physics and potential applications. *Nat. Rev. Mat.*, 2(17031), 2017.

[119] B Escaig. Dissociation and mechanical properties.dislocation splitting and the plastic glide process in crystals. *Journal de Physique Colleques*, 35:C7–151–C7–166, 1974.

[120] Alexander J.H. Houston and P. Alexander, Gareth. Defect loops in three-dimensional active nematics as active multipoles. e-print arXiv:2106.15424[cond-mat.soft], 2021.

[121] Géza Tóth, Colin Denniston, and J. M. Yeomans. Hydrodynamics of topological defects in nematic liquid crystals. *Phys. Rev. Lett.*, 88:105504, 2002.

[122] D. Svenšek and S. Žumer. Hydrodynamics of pair-annihilating disclination lines in nematic liquid crystals. *Phys. Rev. E*, 66:021712, 2002.

[123] Amin Doostmohammadi, Michael F. Adamer, Sumesh P. Thampi, and Julia M. Yeomans. Stabilization of active matter by flow-vortex lattices and defect ordering. *Nat. Commun.*, 7(10557), 2016.

[124] Fong Liu and Gene F. Mazenko. Defect-defect correlation in the dynamics of first-order phase transitions. *Phys. Rev. B*, 46:5963, 1992.

[125] Colin Denniston. Disclination dynamics in nematic liquid crystals. *Phys. Rev. B*, 54:6272–6275, 1996.

[126] Perry W. Ellis, Daniel J. G. Pearce, Ya-Wen Chang, Guillermo Goldsztein, Luca Giomi, and Alberto Fernandez-Nieves. Curvature-induced defect unbinding and dynamics in active nematic toroids. *Nature Physics*, 14:85–90, 2018.

[127] Angela Vella, Romuald Intartaglia, Christophe Blanc, Ivan I. Smalyukh, Oleg D. Lavrentovich, and Maurizio Nobili. Electric-field-induced deformation dynamics of a single nematic disclination. *Phys. Rev. E*, 71:061705, 2005.

[128] Holger Stark. Physics of colloidal dispersions in nematic liquid crystals. *Physics Reports*, 351:387–474, 2001.

[129] O. M. Tovkach, Christopher Conklin, M. Carme Calderer, Dmitry Golovaty, Oleg D. Lavrentovich, Jorge Viñals, and Noel Walkington. *Phys. Rev. Fluids*, 2:053302, 2017.

[130] P. E. Cladis, W. van Saarloos, P. L. Finn, and A. R. Kortan. Dynamics of line defects in nematic liquid crystals. *Phys. Rev. Lett.*, 58:222–225, 1987.

[131] Tiezheng Qian and Ping Sheng. Generalized hydrodynamic equations for nematic liquid crystals. *Phys. Rev. E*, 58:7475–7485, 1998.

[132] E. Vicente Alonso, A. A. Wheeler, and T. J. Sluckin. Nonlinear dynamics of a nematic liquid crystal in the presence of a shear flow. *Proc. R. Soc. A.*, 459:195–220, 2003.

[133] Adrian C. Murza, Antonio E. Teruel, and Arghir D. Zarnescu. Shear flow dynamics in the beris-edwards model of nematic liquid crystals. *Proc. R. Soc. A.*, 471:20170673, 2018.

[134] Antony N. Beris and Brian J. Edwards. *Thermodynamics of flowing systems.* Oxford University Press, 1994.

[135] Julia Yeomans. The hydrodynamics of active systems. e-print arXiv:1603.00194v1 [cond-mat.soft], 2016.

[136] Jianyuan Yin, Lei Zhang, and Pingwen Zhang. Solution landscape of the onsager model identifies non-axisymmetric critical points. *Physica D: Nonlinear Phenomena*, 430:133081, 2022.

[137] Glenn H. Fredrickson, Venkat Ganesan, and François Drolet. Field-theoretic computer simulation methods for polymers and complex fluids. *Macromolecules*, 35:16, 2002.